

SPACECRAFT TRAJECTORY DESIGN TECHNIQUES USING RESONANT
ORBITS

A Thesis

Submitted to the Faculty

of

Purdue University

by

Srianish Vutukuri

In Partial Fulfillment of the

Requirements for the Degree

of

Master of Science in Aeronautics and Astronautics

May 2018

Purdue University

West Lafayette, Indiana

THE PURDUE UNIVERSITY GRADUATE SCHOOL
STATEMENT OF THESIS APPROVAL

Professor Kathleen C. Howell, Chair

School of Aeronautics and Astronautics

Professor Carolin E. Frueh

School of Aeronautics and Astronautics

Professor David A. Spencer

School of Aeronautics and Astronautics

Approved by:

Professor Weinong Wayne Chen

Aeronautics and Astronautics Associate Head for Graduate Education

Dedicated to Mom, Dad and Ammarsh.

ACKNOWLEDGMENTS

I would like to thank my advisor first, Professor Kathleen Howell for giving me this fantastic opportunity to be a part of the Multi-Body Dynamics research group. You have always encouraged me to pursue the hard things and at the same time been my constant guiding force. You are an inspiration to me both personally and professionally.

I would like to extend my thanks to committee members, Professor David Spencer and Professor Carolin Frueh, for their valuable advice and feedback. A big thank you to Professor Micheal Grant, Professor James Longuski and Professor Sarag Saikia for continually motivating me in your classes.

My heartfelt thank you to all the group mates for your constant care and support throughout my time in the group. You have helped me to bring the best out of myself. I also want to immensely thank my friends both at Purdue and at home for being my best stress busters.

I would not have been here if it wasn't for my families endless love and support since my childhood. Thank you, Amma for all your sacrifices. Your strength will always drive me to become a better human being.

Last but not the least, I am ever grateful to the School of Aeronautics and Astronautics and NASA JSC NNX13AK60A grant for their exceptional facilities and financial support during my time at Purdue.

TABLE OF CONTENTS

	Page
LIST OF TABLES	vii
LIST OF FIGURES	viii
ABSTRACT	xii
1 INTRODUCTION	1
1.1 Problem Motivation and Goals	1
1.2 Previous Contributions	3
1.3 Thesis Overview	6
2 INTRODUCTION TO CIRCULAR RESTRICTED THREE BODY PROBLEM	9
2.1 The General n -Body Problem	9
2.2 The General and Relative Three Body Problem	13
2.3 Circular Restricted Three Body Problem (CR3BP)	15
2.4 Equations of Motion in the CR3BP	15
2.5 Integrals of Motion - Jacobi Constant	21
2.6 Libration Points - Equilibrium Solutions in the CR3BP	22
2.7 Forbidden Regions and Zero Velocity Surfaces	25
2.8 Coordinate Transformations	29
2.9 Stability of Equilibrium Points	31
3 NUMERICAL METHODS AND PERIODIC ORBITS	41
3.1 State Transition Matrix	41
3.2 Differential Corrections	44
3.3 Single Shooting or Simple Targeting Problem	46
3.4 Multiple Shooting Algorithm	48
3.5 Symmetric Properties in CR3BP	51
3.6 Symmetric Periodic Orbits	52
3.7 Continuation process	55
3.7.1 Natural Parameter Continuation	56
3.7.2 Pseudo-arclength Continuation	57
3.8 Stability of Periodic Orbits	59
3.9 Bifurcations	65
3.10 3D Periodic Orbit Families	66
4 RESONANT ORBITS AND POINCARÉ MAPS	71
4.1 Concept of Resonance	71

	Page
4.1.1 Resonances in Two-Body Model	73
4.1.2 Resonances in CR3BP	77
4.2 Stability and Bifurcations of 2D Resonant Orbits	82
4.3 Three Dimensional Resonances	87
4.4 Invariant Manifold Theory	88
4.4.1 Invariant Manifolds for Fixed points	88
4.4.2 Poincaré Maps	93
4.4.3 Invariant Manifolds for Periodic Orbits	96
4.4.4 Computation of Manifolds for Unstable Resonant Orbits	99
5 REFERENCE TRAJECTORY DESIGN IN EPHEMERIS MODEL	104
5.1 Resonant - Near Rectilinear Halo Orbits	104
5.2 Challenges in Ephemeris Trajectory Design	108
5.2.1 Quasi-periodic Trajectories in Ephemeris Model	109
5.2.2 Generating Nearby Reference Ephemeris Solutions	117
5.3 New Stacking Sequences in CR3BP	121
5.3.1 Alternative Stacking Sequence for Repeatable Behavior	121
5.3.2 Periapsis Control - a Non-homogeneous Stacking Sequence	122
6 TRANSFER DESIGN INCORPORATING RESONANT ORBITS : METHOD- OLOGY AND RESULTS	133
6.1 Representative NRHO - Departure Orbit	133
6.2 Representative DRO - Arrival Orbit	134
6.3 Theoretical Minimum Transfer Cost	135
6.4 Arc Blending Scheme - Transfer Design Process	139
6.5 Direct Transfers from NRHO to DRO	143
6.6 Transfers Incorporating Resonant Arcs	146
6.7 Transfers Incorporating Resonant Manifolds	148
6.8 Transfers Using Tangential Departure and Arrival Arcs	156
6.9 Designing Locally Optimal Transfers	163
6.10 Higher-Fidelity Transfers from NRHO to DRO	171
7 SUMMARY	182
7.1 Resonant Orbits and Manifolds in CR3BP	182
7.2 Reference Ephemeris Trajectory Design Using Resonant Orbits	183
7.3 Transfer Trajectory Design Using Resonant Orbits and Manifolds	184
7.4 Future Recommendations	184
REFERENCES	186

LIST OF TABLES

Table	Page
2.1 Characteristic quantities in the Earth-Moon and Sun-Earth system. . . .	18
2.2 Non-dimensional position coordinates of the libration points in the Earth-Moon and Sun-Earth systems	25
2.3 Value of Jacobi constant for libration points in the Earth-Moon and Sun-Earth systems.	26
3.1 Natural parameters of a representative L_1 Lyapunov orbit.	57
4.1 Two-Body orbital parameters of Moon.	73
6.1 9:2 L_2 synodic NRHO parameters.	134
6.2 Representative DRO parameters.	134
6.3 Transfer using 1:2 resonant arc, Jacobi constant history.	147
6.4 Transfer using 1:2 resonant arc, transfer costs and TOF.	151
6.5 Transfer using 2:3 resonant arc, transfer costs and TOF.	151
6.6 Transfer using 3:4 resonant arc, transfer costs and TOF.	154
6.7 Transfer using 4:3 resonant arc, transfer costs and TOF.	154
6.8 Transfer using 3:4 unstable resonant manifold, transfer costs and TOF. .	157
6.9 Transfer type A, transfer costs and TOF.	162
6.10 Transfer type A, Jacobi constant history.	162
6.11 Transfer type B, transfer costs and TOF.	163
6.12 Transfer type B, Jacobi constant history.	163
6.13 ΔV and TOF comparison - fixed time optimal transfer - Transfer type A.	169
6.14 ΔV and TOF comparison - variable time optimal transfer - Transfer type A.	169
6.15 ΔV and TOF comparison - fixed time optimal transfer -Transfer type B.	170
6.16 ΔV and TOF comparison - variable time optimal transfer - Transfer type B.	170

LIST OF FIGURES

Figure	Page
2.1 Definitions in the n -body problem.	10
2.2 Definition for position of particle P_i relative to particle P_q	12
2.3 Definitions in the three-body problem.	14
2.4 Definitions in the CR3BP.	17
2.5 Equilibrium points in the rotating frame of CR3BP.	24
2.6 ZVS and ZVC for $(C > C_{L_1})$ and $(C_{L_2} < C < C_{L_1})$	28
2.7 ZVS and ZVC for $(C_{L_3} < C < C_{L_2})$, $(C_{L_4} < C < C_{L_3})$ and $(C < C_{L_4})$	38
2.8 ZVC for $(C = C_{L_1})$, $(C = C_{L_2})$, ZVC $(C = C_{L_3})$ and ZVC $(C = C_{L_4})$	39
2.9 Orientation of rotating frame to the Inertial frame.	40
3.1 Illustration of Single shooting method.	49
3.2 Illustration of Multiple shooting method.	51
3.3 A symmetric, periodic L_1 Lyapunov orbit.	55
3.4 L_1 Lyapunov family.	59
3.5 Periodic orbit stability regions.	62
3.6 L_1 Lyapunov family - In-plane Stability index ν_1	64
3.7 L_1 Lyapunov family - Out-of-Plane stability index ν_3	64
3.8 Types of Bifurcations.	66
3.9 L_1 Lyapunov family - Halo family bifurcation.	67
3.10 L_1 Northern Halo family.	69
3.11 L_1 Northern Halo family projected on \hat{x} - \hat{z} plane.	69
4.1 Two-body 2:1 resonant orbit in the EM-inertial frame.	76
4.2 Two-body 2:1 resonant orbit in the EM-rotating frame.	76
4.3 2:1 Resonant orbit correction in the CR3BP.	81
4.4 2:1 Resonance family in the Earth-Moon system.	82

Figure	Page
4.5 1:1, 1:2, 1:3 and 1:4 planar resonant families.	83
4.6 2:1, 2:3, 3:1 and 3:2 planar resonant families.	84
4.7 3:4, 4:1 and 4:3 planar resonant families.	85
4.8 Stability Indices of 2:1 resonant family.	87
4.9 1:1, 1:2, 1:3 and 2:1 spatial resonant families.	89
4.10 2:3, 3:1 and 3:4 spatial resonant families.	90
4.11 Stable and unstable manifolds of an equilibrium point.	94
4.12 The Poincaré map.	96
4.13 Illustration of subsequent returns to a Poincaré map.	98
4.14 Stable and unstable eigenvectors at 20 fixed points.	102
4.15 Stable and unstable manifolds propagated for 3 resonant time periods (145 days).	103
4.16 1:2 Resonant manifolds - returns on Poincaré map $y = 0$ and $\dot{y} > 0$	103
5.1 Synodic and Sidereal configurations of the Moon.	105
5.2 L_1 and L_2 NRHO family in the Earth-Moon system.	106
5.3 Time periods of L_1 and L_2 NRHO family.	106
5.4 Stability Indices of L_1 NRHO family.	107
5.5 Stability Indices of L_2 NRHO family.	107
5.6 m:1 and m:2 Synodic resonances of L_2 NRHOs.	108
5.7 3:1 synodic southern L_2 NRHO in the CR3BP - Moon centered, Earth - Moon rotating frame view.	110
5.8 3:1 synodic southern L_2 NRHO in the CR3BP - Moon centered, Sun - Moon rotating frame view.	111
5.9 3:1 synodic southern L_2 NRHO in the CR3BP - Earth centered, Sun - Earth rotating frame view.	112
5.10 Twelve 3:1 synodic southern L_2 NRHOs stacked in the CR3BP - Barycentric, Earth - Moon rotating frame view.	113
5.11 Converged ephemeris trajectories from May 1 st , 2023 to May 16 th , 2023. . . .	115
5.12 Converged ephemeris trajectories from May 17 th , 2023 to May 31 st , 2023. . . .	116

Figure	Page
5.13 Quasi-periodic NRHOs computed on May 16 th and May 21 st - Earth-Moon rotating frame view.	117
5.14 Apse angles for quasi-periodic NRHOs computed on May 16 th and May 21 st - Earth-Moon rotating frame view.	118
5.15 periapsis radius variation for NRHOs computed on May 16 th and May 21 st	118
5.16 Ephemeris trajectory on May 16 th , 2023 in EM, SM, and SE rotating frames.	119
5.17 Ephemeris trajectory on May 21 st , 2023 in EM, SM and SE rotating frames.	119
5.18 Nearby reference trajectory with shifted periapsis.	120
5.19 Ephemeris trajectory comparison on May 16 th and May 21 st , 2023.	123
5.20 Alternative stacking sequence on May 16 th to remove phase difference.	124
5.21 Traditional stacking sequence on May 16 th , 2023.	125
5.22 Alternative stacking sequence on May 16 th , 2023.	125
5.23 Distance to Moon: Stacked NRHOs in CR3BP and Ephemeris trajectory on May 2 nd	128
5.24 Non-homogeneous stacking sequence.	130
5.25 Old and new ephemeris trajectories.	131
5.26 Old and new ephemeris trajectories - distance to Moon.	132
6.1 Representative NRHO and DRO.	135
6.2 9:2 synodic southern L_2 NRHO in the CR3BP - Moon centered, Sun - Moon rotating frame view.	136
6.3 9:2 synodic southern L_2 NRHO in the CR3BP - Earth centered, Sun - Earth rotating frame view.	137
6.4 Minimum energy to change Jacobi constant.	140
6.5 Theoretical Minimum Δv to jump from NRHO to DRO.	140
6.6 Arc blending scheme.	142
6.7 Tangential departures from NRHO to hyperplane $z=0$	144
6.8 Poincaé map $z = 0, \dot{z} > 0$	145
6.9 Direct transfer from NRHO to DRO.	145

Figure	Page
6.10 Potential resonant orbits for intermediate arcs.	149
6.11 Transfer incorporating 1:2 resonant arc - Poincaré map $z = 0, \dot{z} > 0$	149
6.12 Transfer between NRHO and DRO using 1:2 resonant arc.	150
6.13 Transfer between NRHO and DRO using 2:3 resonant arc.	152
6.14 Transfer between NRHO and DRO using 3:4 resonant arc.	153
6.15 Transfer between NRHO and DRO using 4:3 resonant arc.	155
6.16 Transfer using resonant manifold - Representative orbits.	157
6.17 Transfer using resonant manifold - Poincaré map for arrival arc.	158
6.18 Transfer using resonant manifold - Tangential departures from NRHO with $\Delta V = 20$ m/s.	158
6.19 Transfer using resonant manifold - Poincaré map for departure arc. . . .	159
6.20 Transfer between NRHO and DRO using 3:4 resonant arc.	160
6.21 Transfer type A - Poincaré map for initial guess.	164
6.22 Transfer type A.	165
6.23 Transfer type B - Poincaré map for initial guess - Distant plane change. .	166
6.24 Transfer type B - Distant plane change.	167
6.25 Fixed time optimized transfer - Transfer type A.	172
6.26 Variable time optimized transfer - Transfer type A.	173
6.27 Fixed time optimized transfer - Transfer type B.	174
6.28 Variable time optimized transfer - Transfer type B.	175
6.29 Variable time optimized transfer type A - ΔV vs ephemeris insertion epoch.	177
6.30 Variable time optimized transfer-type A - ephemeris converged trajectory.	179
6.31 Variable time optimized transfer-type A - ephemeris trajectory with re- duced ΔV	180
6.32 Variable time optimized transfer-type A - ephemeris trajectory with DRO free to vary.	181

ABSTRACT

Vutukuri, Srikanish. M.S.A.A, Purdue University, May 2018. Spacecraft Trajectory Design Techniques Using Resonant Orbits. Major Professor: Kathleen C. Howell.

Resonance phenomena are ubiquitous in the solar system. Historically, resonant orbits have been extensively studied to understand the long-term stability and formation of the solar system. In mission design, they have been employed as a mechanism for multiple planetary flyby trajectories and as a source for long-term orbital stability. However, resonance phenomena have not been fully explored as a tool for designing spacecraft trajectories in multi-body dynamical systems which include 1) constructing baseline ephemeris solutions with desired properties and 2) as transfer mechanisms connecting stable periodic orbits. In this investigation, the above goals are addressed within the context of Earth-Moon system by looking at two specific mission scenarios.

In general, a quasi-periodic ephemeris trajectory is constructed by employing a stacking process in which multiple revolutions of an identical periodic orbit in CR3BP are placed one behind another before transitioning them into the higher fidelity model. Depending upon the epoch, the resulting ephemeris trajectory may or may not satisfy all the desired mission parameters which include eclipse avoidance and periapsis conditions. To overcome this problem, a synodic resonant orbit in the cislunar space is used to develop an alternative, non-homogeneous stacking process to produce ephemeris trajectories with a better eclipse avoidance and periapsis control strategy. The second goal of this investigation is to explore the possibility of incorporating resonant arcs and their manifolds in the transfer design process to aid the transfer guess generation between stable periodic orbits with no natural dynamical structures. The applicability of this idea is demonstrated between two stable cislunar periodic orbits

by constructing various transfer scenarios incorporating resonant arcs and manifolds. Locally optimum transfers are generated in the CR3BP, and their practical validity is tested by transitioning them into a higher fidelity model. The techniques demonstrated to address the two goals are general and apply to other dynamical systems.

1. INTRODUCTION

In the past, several multi-body dynamical system techniques have been creatively applied to design novel, low cost, transfers to destinations which were not reachable via traditional design methods. An increasing number of libration point missions by leveraging the natural gravitational flow available in the form of multi-body solutions (periodic orbits and manifolds) are being conceived with potentially reduced propellant costs. One such family of multi-body periodic orbits which are ubiquitous in the solar system are resonant orbits. Historically, resonant orbits have been studied to understand the long-term stability and formation of the solar system. However, they have not been explored as a means for designing spacecraft trajectories. This investigation will examine the use of resonant orbits and their manifolds in constructing baseline trajectories with desired properties and as a transfer mechanism to move within the Circular Restricted Three-Body system.

1.1 Problem Motivation and Goals

In mission design, resonant orbits and manifolds are being employed as a mechanism for flyby trajectories and more recently as a source for long-term orbital stability. The dynamical environments of outer planets are comprised of multiple gravitational fields, and therefore the application of dynamical system techniques offer many advantages. The conceptual missions designed to explore the Jupiter system such as the Jupiter Icy Moons Orbiter (JIMO) [1] and the Jupiter Europa Orbiter (JEO) [2] make use of the multiple gravity fields of its several moons as well as low-thrust propulsion. The JIMO spacecraft is designed to explore the three large moons of Jupiter namely Callisto, Ganymede, and Europa by leveraging multiple gravity assists and undergoing efficient resonance transitions. The JEO mission is planned to insert a

spacecraft in orbit around Europa to investigate the presence of a liquid sub-surface ocean. Europa Orbit Insertion occurs after having encountered the moon multiple times, each time undergoing a resonance transition. Recent investigations have shown that the manifolds of unstable resonant orbits play an essential role in determining the resonance transitions which occur during multi-body gravitational flybys.

In the past, multi-body resonances in the Earth-Moon system having long-term stable characteristics were used as nominal mission trajectories. In 2008, Interstellar Boundary Explorer (IBEX) spacecraft [3] was launched into a high-altitude Earth orbit to collect information about the heliosphere and its boundary. The nominal trajectory was slightly unstable for estimating long-term station-keeping costs. Therefore, after the primary mission duration, the spacecraft was moved into a highly stable, more predictable, out-of-plane lunar-resonant orbit about the Earth while still meeting all the scientific requirements. In 2013, NASA selected the Transiting Exoplanet Survey Satellite (TESS) mission [4] to search for extra-terrestrial planets. The spacecraft will be placed in a highly stable Earth orbit in resonance with the Moon.

Resonant orbits and manifolds have not been fully explored as a tool for designing multi-body spacecraft trajectories. Therefore, the overarching goals in this investigation are 1) to use resonant orbits in constructing baseline ephemeris solutions with desired properties and 2) to use resonant orbits and manifolds as transfer mechanisms connecting non-resonant stable periodic orbits. In this investigation, the above aspects of trajectory design are addressed within the context of Earth-Moon system by looking at two specific mission scenarios. The work begins with the construction of planar and spatial resonant orbit families in the Circular restricted three-body problem (CR3BP). In general, a quasi-periodic ephemeris trajectory is constructed by employing a stacking process in which multiple revolutions of an identical periodic orbit in CR3BP are placed one behind another before transitioning them into the higher fidelity model. Depending upon the epoch, the resulting ephemeris solution

may or may not satisfy all the desired mission parameters which include eclipse avoidance and periapsis conditions. To overcome this problem, a synodic resonant orbit in the cislunar space is used to develop an alternative, non-homogeneous stacking process to produce ephemeris solutions with a better eclipse avoidance and periapsis control strategy.

The second goal of this investigation is to explore the possibility of incorporating resonant arcs and their manifolds in the transfer design process to aid the transfer guess generation between stable periodic orbits with no natural dynamical structures. The applicability of this idea is demonstrated between two stable cislunar periodic orbits by constructing various transfer scenarios incorporating resonant arcs and manifolds. Locally optimum transfers are generated in the CR3BP, and their practical validity is tested by transitioning them into a higher fidelity ephemeris model. The techniques demonstrated to address the two goals are general and apply to other dynamical systems.

1.2 Previous Contributions

The goals discussed in the previous section will be addressed by modeling the dynamics as a CR3BP. Many investigators have explored the CR3BP dynamical model in the past. In 1687 Sir Isaac Newton (1643-1727) published his most famous work titled *The Principia*, in which he attempted to describe the motion of n -bodies, governed by their mutual gravitational force of attraction [5]. However, his attempt to derive an analytical solution to the n -body problem was not successful. The next significant leap in answering this question was taken by Leonhard Euler (1707 - 1783) when he formulated a simplified version of a n -body model called the Circular Restricted Three Body Problem (CR3BP) [6]. Euler introduced a synodic (rotating) coordinate frame to describe the motion of the third body under the gravitational influence of two larger primaries. The view in the rotating frame helped to obtain use-

ful insight into the motion in a multi-body dynamical system. The first preliminary, constant periodic solutions to the CR3BP were found in 1772 when Joseph-Louis Lagrange (1736-1813) discovered two planar triangular equilibrium points, and Euler discovered three collinear planar equilibrium points in the CR3BP dynamical system. Equilibrium points are constant solutions to the CR3BP, and they appear to be fixed in the rotating frame of the primaries. In 1836, Carl Gustav Jacobi leveraged the rotating frame view to introduce an integral of the equations of motion for the CR3BP called the Jacobi integral or Jacobi constant [7]. Even though an integral of motion was found, an analytical solution to the CR3BP was not possible, yet the Jacobi integral proved significant in making qualitative conclusions about the motion of the third body and helped to further the understanding about the multi-body dynamical system. These qualitative conclusions of the motion of the third body using the Jacobi constant was shown by Hill in 1878 [8]. He introduced bounding surfaces/curves called the Zero Velocity Surfaces/Curves which bound the motion of the third body for a given value of the Jacobi constant associated with the system.

A significant leap towards a numerical approach to understanding the CR3BP was taken by Henry Poincaré in 1881 when he introduced the concept of Poincaré map [7, 9]. This technique helped to decrease the complexity of the dynamical system by transforming the analysis of the continuous system to a discrete system. In the latter half of the 20th century, advancements in computational resources significantly increased the capability of numerically exploring the CR3BP. Much of the latest developments in the CR3BP is made possible by the application of various numerical techniques. Trajectory correction in the CR3BP or any non-linear dynamical model, in general, is equivalent to solving a boundary value problem by repeatedly correcting many initial value problems. Various correction algorithms were shown by Keller [10], Roberts and Shipman [11, 12] when they developed different shooting formulations to solve boundary value problems. The existence of an infinite number of particular, periodic solutions of the CR3BP was shown to exist in 1881 by

Poincaré [9]. But their computation was only possible during the latter half of the 20th century by the application of differential correction techniques [13]. The first mission to utilize low energy, dynamical structures in the multi-body system as the mission trajectory was the International Sun-Earth Explorer-3 (ISEE-3) spacecraft which was sent to the Sun-Earth L_1 halo orbit in 1978 [14]. Since then many missions leveraging multi-body dynamical structures have been accomplished. Some of them include ARTEMIS, SOHO, ACE, Genesis, WIND and WAMP [15, 16].

Traditionally resonant orbits have been studied in the context of planetary flybys. In almost all the planetary flyby trajectories, some form of resonance transition is incorporated. Naturally occurring heteroclinic resonance transitions are observed to happen in the solar system for the Jupiter family of comets such as Gehrels 3, Oterma and Helin-Roman - Crockett [17]. These comets frequently transition between the 3:2 and 2:3 resonances, sometimes temporarily being captured by Jupiter. During 2000, this phenomenon was theoretically proven in a planar perspective by Koon, Lo, Marsden, and Ross when they showed that the invariant manifolds of the two resonant orbits and the Lyapunov orbits in the Sun-Jupiter system are responsible for the resonance transfer and capture around Europa [17–19]. In 2001, Howell, Marchand, and Lo proved the phenomenon to occur numerically in three dimensions [17, 20]. In 2010, Vaquero explored the relationship between planar unstable resonant orbits by studying the interaction of their invariant manifold structures [21]. Recently in 2011, a stable, spatial resonant orbit about the Earth was considered for an extended mission trajectory for the spacecraft IBEX [3]. In 2013, NASA announced the TESS mission which will search for exo-planets and is currently scheduled to launch in 2018 into a stable 2:1 periodic resonant orbit around Earth [4]. In 2013, Vaquero demonstrated that resonant orbits and their manifolds could be utilized as transfer mechanisms between periodic orbits in the CR3BP [22]. More specifically, Vaquero and Howell designed trajectories that transition between exterior and interior resonant orbits using unstable and stable resonance manifolds in the Saturn-Titan system [23]. A

transfer scenario to access the stable orbit of Hyperion was also demonstrated using the unstable resonant manifolds of an exterior 3:5 resonant orbit and an interior 5:4 resonant orbit [23]. Using various planar and spatial resonant orbits and their associated manifolds, Vaquero and Howell designed novel, lost cost transfers from LEO to planar and three-dimensional libration point orbits [24]. A grand tour of all the planar libration points was also demonstrated using the unstable manifolds of a 4:3 resonant orbit [22].

Other orbit families of interest in this work are the Near Rectilinear Halo Orbits (NRHOs) and Distant Retrograde Orbits (DROs). Halo orbits are three-dimensional periodic orbits around the collinear libration points. When seen from Earth, in the Earth-Moon line of sight they seem to have a 'Halo' like appearance around the Moon. Hence the name Halo orbit was coined by Farquhar in 1968 [25]. In 1979, Breakwell and Brown demonstrated the existence of Halo orbit families about the L_1 and L_2 libration points [26]. Howell extended the families into other systems and characterized the L_3 Halo family [27]. In 1983, Howell and Breakwell developed approximations for 'Almost Rectilinear Halo Orbits,' which are now called Near Rectilinear Halo Orbits (NRHOs) and helped to gain additional insight about these stable orbits in the Halo family [26]. More accurate characterization of the L_1 and L_2 Halo orbits in the Earth-Moon system was carried out by Zimovan in 2017 [28]. Several authors investigated designing transfers to and from NRHOs to other cislunar locations. Some of them include Capdevila [29], Folta et al [30], Loucks et al [31], Whitley and Martinez [32] and Zimovan [28].

1.3 Thesis Overview

The present work includes the following chapters:

- **Chapter 2:** This chapter starts with the discussion of the general n-body problem followed by the Relative Three Body problem. To obtain a deeper

insight into multi-body dynamical behavior the concept of Circular Restricted Three Body Problem (CR3BP) is introduced. Equations of motion for the CR3BP dynamical model are derived followed by the introduction of an integral of motion called the Jacobi integral. Preliminary constant solutions to the CR3BP are identified. They are named as Equilibrium points or Libration points. The Jacobi integral is used to introduce Forbidden regions or Zero Velocity Surfaces which qualitatively indicate the domain of possible realm of motion of the third body in the dynamical system. Coordinate transformations are presented to convert the rotating frame view to an inertial view to gain additional insight into the motion of the third particle. Finally, the chapter ends with a discussion on the concept of linear stability analysis for equilibrium points.

- **Chapter 3:** Several numerical techniques for trajectory corrections are developed in this chapter. The concept of State Transition Matrix (STM) is introduced which forms the fundamental basis for any differential corrections process. Single and Multiple shooting differential correction algorithms are formulated. Mirror theorem is presented in the context of the CR3BP which is later utilized as the essential property for generating symmetric periodic orbits about the collinear libration points. Natural parameter and Pseudo-arclength continuation schemes are implemented to create periodic orbit families about the collinear libration point orbits. The concept of linear stability for periodic orbits is presented by the introduction of a particular matrix called the Monodromy matrix. The theory of bifurcations in the context of CR3BP is explained and is applied to the planar Lyapunov periodic families to generate spatial periodic orbits.
- **Chapter 4:** This chapter presents a thorough background about the concept and construction of resonant orbits in both the two-body and the CR3BP. The fundamentals of the invariant manifold theory are discussed and a technique

to numerically generate manifolds for unstable resonant orbits is presented. Poincaré mapping technique is introduced and applied in the context of resonant orbits.

- **Chapter 5:** In this chapter, the behavior of quasi-periodic trajectories in the higher fidelity models is explained using NRHOs. The problems encountered by the traditional stacking sequence regarding eclipsing properties and periapsis conditions is highlighted, and a remedy is presented using a synodic resonant NRHO. An alternative non-homogeneous stacking sequence is developed and investigated, and are applied to CR3BP trajectories while transitioning into the ephemeris model to generate baseline solutions with a better eclipse avoidance and periapsis control strategy.
- **Chapter 6:** In this chapter, various spatial transfers scenarios between a representative NRHO and a DRO are designed using resonant orbits and associated manifold structures. The concept of theoretical minimum ΔV is introduced which helps in evaluating the efficiency of the transfer. Locally optimal transfers are generated and transitioned into the higher fidelity ephemeris model to assess the practical transfer costs and time of flight.
- **Chapter 7:** In this chapter, a summary of the present work is presented followed by some of the key outcomes. In the end, potential expansion of the current research work is discussed in the future recommendations section.

2. INTRODUCTION TO CIRCULAR RESTRICTED THREE BODY PROBLEM

The n -body gravitational model represents the most general and accurate representation of the solar system. Having a clear understanding of the dynamical interaction of multiple bodies under their respective gravitational fields is vital before introducing the Circular Restricted Three Body Problem (CR3BP) and three-body resonances. Therefore, this chapter begins with the discussion about the general n -body problem. It will be followed by the two-body problem and the three-body problem which are special cases of the general n -body problem. In the preliminary two-body case the motion of two particles under the influence of their mutual gravitational forces is analyzed. Likewise, in the three-body model, the movement of three particles interacting in the combined gravity field is studied. Just by adding another particle to the two-body problem, the three-body problem becomes very complicated to analyze. Hence, to simplify the three-body problem and to get a better understanding of the dynamics of a particle under the influence of two other gravitational bodies a CR3BP is developed. Equations of motion for the third body in the CR3BP are derived, which in turn help in the development of a useful, qualitative technique to determine the bounds on the motion of the third body. Finally, this chapter concludes with the computation and linear stability analysis of various equilibrium solutions in the CR3BP.

2.1 The General n -Body Problem

The n -body problem is the most general gravitational model in which the motion of n , ($n > 3$) particles (in both position and velocities) are analyzed under the influence of their mutual gravitational fields. A representative set up of an n -body

model is shown in Figure 2.1. Point O indicates the origin of the inertial reference frame represented by three orthonormal \hat{X} , \hat{Y} and \hat{Z} axes which complete the right hand rule. The hat symbol indicates a unit vector. All the n bodies are modeled as centrobaric point masses and named as $P_1, P_2, \dots, P_i, P_n$ and P_q . Their masses are labeled as $m_1, m_2, \dots, m_i, m_n$ and m_q respectively. The position vectors of the particles from the origin are given as $\bar{r}_1, \bar{r}_2, \dots, \bar{r}_i, \bar{r}_n$ and \bar{r}_q respectively. The bar symbol indicates a vector notation.

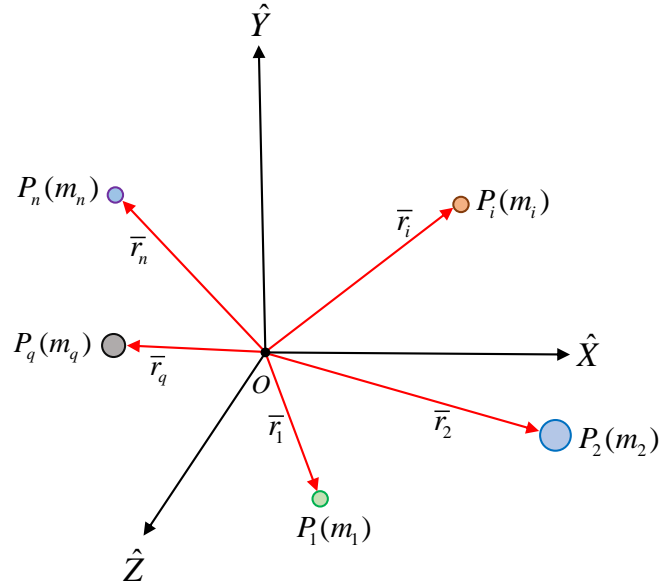


Figure 2.1. Definitions in the n -body problem.

According to Newton's law of gravity [5] the net force on particle P_i is given by,

$$\bar{F}_i = -Gm_i \sum_{\substack{j=1 \\ j \neq i}}^n \frac{m_j}{r_{ji}^3} \bar{r}_{ji} \quad (2.1)$$

In equation (2.1), G is the universal gravitational constant, m_i is the mass of the particle P_i and \bar{r}_{ji} is the radius vector from particle P_j to particle P_i . Now, applying Newton's second law of motion [5] to particle P_i , assuming that the mass is constant

and the observer is in an inertial frame located at a stationary base point O the equation of motion is written as,

$$m_i \frac{d^2 \bar{r}_i}{dt^2} = -G \sum_{\substack{j=1 \\ j \neq i}}^n \frac{m_i m_j}{r_{ji}^3} \bar{r}_{ji} \quad (2.2)$$

Where \bar{r}_i is the position vector of the particle P_i from O . This second-order vector differential equation is broken down into six first-order scalar differential equations in position and velocity along the three orthogonal directions of the coordinate system. These six states in position and velocity represent the degrees of freedom of a particle in the n -body dynamical model. The equations are nonlinear and coupled. As every particle is associated with a second-order vector differential equation of motion, the total number of scalar first-order differential equations in the n -body dynamical system is $6n$. To solve these set of $6n$ scalar differential equations, $6n$ integrals of motion are required, but to this day only ten integrals of motion are known to exist. The Principle of Conservation holds true for linear momentum, angular momentum, and energy of the n -body system which gives rise to the ten known integrals. Even in the simplest two-body model, closed-form solutions corresponding to the twelve scalar first-order differential equations of motion cannot be obtained as sufficient integrals of motion are not available.

An alternative approach to study the motion of the particles is to know how they move relative to each other. The position of particle P_i with respect to another particle P_q is represented by a position vector \bar{r}_{qi} and is more useful than the radius vector \bar{r}_i alone as shown in Figure 2.2. Newton's second law of motion [5] cannot be applied directly to the relative motion, as the new base point particle P_q is not inertially fixed. The equation of motion governing the new dependent variable \bar{r}_{qi} , i.e., $\ddot{\bar{r}}_{qi}$ is obtained by individually applying Newton's law to both the particles P_i and P_q with respect to the base point O and subtracting them appropriately. In the

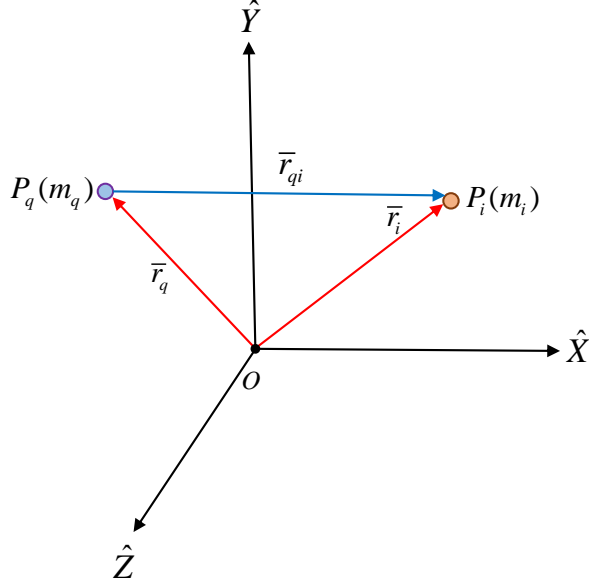


Figure 2.2. Definition for position of particle P_i relative to particle P_q .

relative n -body problem the equation of motion of particle P_i relative to particle P_q is thus,

$$\bar{r}_{qi}'' + G \frac{(m_j + m_q)}{r_{qi}^3} \bar{r}_{qi} = G \sum_{\substack{j=1 \\ j \neq i, q}}^n m_j \left(\frac{\bar{r}_{ij}}{r_{ij}^3} - \frac{\bar{r}_{qj}}{r_{qj}^3} \right) \quad (2.3)$$

In equation (2.3) double primes denote the derivative with respect to dimensional time. The term on the left is called the Dominant term as it captures the direct gravitational interaction of particle P_q and P_i . The two terms on the right are the Direct and Indirect perturbing terms which relate to the gravitational interaction of the remaining particles with the particle P_i and P_q respectively. When there are just two bodies in the dynamical system, the equation of motion for a relative two-body formulation is written as follows,

$$\bar{r}_{qi}'' + G \frac{(m_j + m_q)}{r_{qi}^3} \bar{r}_{qi} = 0 \quad (2.4)$$

Notice that there are no additional perturbing bodies and hence perturbing terms on the right side of equation (2.4) are zero. Closed form solution for this second order differential equation which governs the motion of a relative formulation of two bodies exists. The particle P_i can only take one of circular, elliptical, parabolic or hyperbolic paths relative to particle P_q . Adding just one more point mass to this relative problem, i.e., having ($n \geq 3$) the closed form solutions ceases to exist. In fact, the two-body relative motion is virtually the only problem in celestial mechanics with a closed form solution.

2.2 The General and Relative Three Body Problem

Consider a general three-body problem with particles P_1 , P_2 and P_3 having masses m_1 , m_2 and m_3 respectively as shown in Figure 2.3. Applying Newton's second law [5], the differential equation of motion for particle P_1 with respect to an inertially fixed base point O under the gravitational influence of the particles P_2 and P_3 similar to equation (2.1) is written as,

$$m_3 \bar{r}''_3 = -G \frac{m_3 m_1}{r_{13}^3} \bar{r}_{13} - G \frac{m_3 m_2}{r_{23}^3} \bar{r}_{23} \quad (2.5)$$

Corresponding equations of motion can be written for particles P_2 and P_3 . As previously shown, solving for all the position and velocity vectors for three particles requires 18 integrals of motion, but only ten are available. Hence closed-form solutions for the general three-body problem do not exist.

The problem is simplified by considering the relative three-body problem in which the motion of particle P_3 is observed with respect to particle P_1 and P_2 . The equation of motion of particle P_3 relative to P_1 , with particle P_2 acting as a perturbing body is written as,

$$\bar{r}''_{13} + G \frac{(m_3 + m_1)}{r_{13}^3} \bar{r}_{13} = G m_2 \left(\frac{\bar{r}_{32}}{r_{32}^3} - \frac{\bar{r}_{12}}{r_{12}^3} \right) \quad (2.6)$$

Similarly the equation of motion of particle P_3 relative to P_2 with particle P_1 acting as a perturbing body is written as,

$$\bar{r}_{23}'' + G \frac{(m_3 + m_2)}{r_{23}^3} \bar{r}_{23} = Gm_1 \left(\frac{\bar{r}_{31}}{r_{31}^3} - \frac{\bar{r}_{21}}{r_{21}^3} \right) \quad (2.7)$$

A total of 12 integrals of motion are required to solve the two second-order, vector relative differential equations of motion in equations (2.6) and (2.7). But, as only ten integrals are available, the relative three-body problem is also rendered solution less. By further simplification of the relative three-body problem, significant insights into the motion of particle P_3 are obtained. These simplifications lead to the Restricted Three Body Problem.

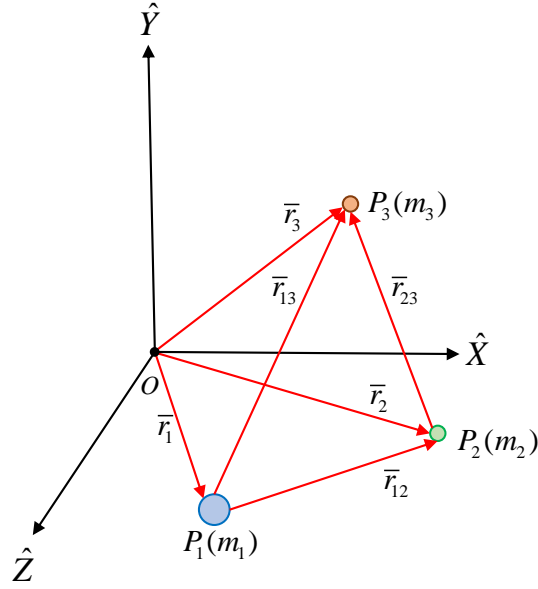


Figure 2.3. Definitions in the three-body problem.

2.3 Circular Restricted Three Body Problem (CR3BP)

The following assumptions applied to the general three-body problem dramatically reduces the complexity and helps to make the problem more tractable, thus formulating the Circular Restricted Three Body Problem.

1. The mass of particle P_3 is assumed to be infinitesimally small relative to particles P_1 and P_2 . This assumption is reasonable for practical purposes when particle P_3 is modeled as a comet or spacecraft under the influence of larger bodies like planets, moons and the Sun. This simplification implies that the particle P_3 does not have any gravitational influence on the particles P_1 and P_2 and thus their motion remains unaffected by P_3 .
2. If particle P_3 does not influence the motion of particles P_1 and P_2 , then P_1 and P_2 represents an isolated two-body system. Solutions to the relative two-body motion of particles P_1 and P_2 exist as conics. For many applications, the solution is a closed conic, i.e., a circle or an ellipse. P_1 and P_2 are named as the Primary system. P_1 is arbitrarily labeled as the larger primary, and it has the larger mass. P_2 is the smaller primary and has the smaller mass. P_3 is the particle of interest and is called the Secondary particle.
3. The simplest two-body relative motion for primary particles P_1 and P_2 is circular, and they are assumed to move in circular orbits with respect to the center of mass of the primary system. The conic motion of P_1 and P_2 is further restricted to be planar. However, the motion of P_3 is allowed to be in three dimensions.

2.4 Equations of Motion in the CR3BP

Non-dimensionalizing the equations of motion and formulating them in a rotating coordinate frame are perhaps the two most significant steps towards gaining a greater insight into the three-body problem. Non-dimensionalizing the equations make them applicable for any primary mass system like Sun-Earth, Earth-Moon and so on. It

also helps to normalize the differences in the order of magnitudes for distances and velocities, thus helping with numerical integration which will be widely used for the rest of the analysis. Formulating the equations in the rotating coordinate frame helps to establish equilibrium solutions and other periodic orbits in the dynamical system.

The setup for the CR3BP is shown in Figure 2.4. The particles P_1 and P_2 represent the larger and the smaller primaries respectively. The third particle of interest whose motion is being analyzed is shown as P_3 . The mass of the three particles are labeled as m_1 , m_2 and m_3 respectively. The primaries rotate about their barycenter B in a circular fashion in the \hat{X} - \hat{Y} plane. The inertial reference frame is represented by the rectangular coordinate system \hat{X} , \hat{Y} and \hat{Z} centered at B . A rectangular rotating coordinate system is defined whose \hat{x} -axis is always parallel to a line joining the primaries. θ denotes the orientation of the rotating frame with respect to the inertial frame at any instant of time. The rate of change of θ , i.e., θ' is the angular velocity of the rotating frame which in this case is constant for the circular orbits of primaries and is equal to the mean motion, N . Both the inertial \hat{Z} and rotational \hat{z} axes are parallel to the angular velocity of the primary system. The position vectors to the particles P_1 , P_2 and P_3 from B are given as \bar{D}_1 , \bar{D}_2 and \bar{P} respectively and the relative position vectors of particle P_3 from P_1 and P_2 are given as \bar{D} and \bar{P} respectively. For non-dimensionalizing the states in the equations of motion, three characteristic quantities are defined. The characteristic length, **lstar**, is defined as the distance between the two primaries. The characteristic mass, **mstar**, is the sum of masses of the two primaries. The characteristic time, **tstar** is the orbital period of the system primaries. The following symbols are used for the characteristic quantities.

$$l^* = \|\bar{r}_1\| + \|\bar{r}_2\| \quad (2.8)$$

$$m^* = m_1 + m_2 \quad (2.9)$$

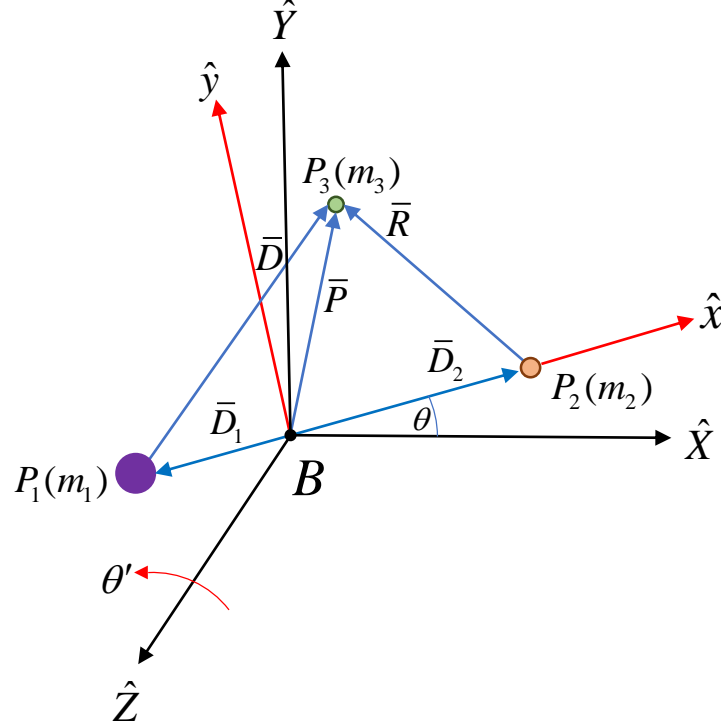


Figure 2.4. Definitions in the CR3BP.

$$t^* = \left[\frac{l^{*3}}{Gm^*} \right] \quad (2.10)$$

Using these characteristic quantities, other useful parameters are non-dimensionalized as follows,

$$\tilde{G} = \frac{Gl^{*3}}{m^*t^{*2}} = 1 \quad (2.11)$$

Where G is the universal gravitational constant. \tilde{G} in equation (2.11) represents the non-dimensionalized universal gravitational constant, which is equal to 1. The mean motion of the primary system N , is also non-dimensionalized and it turns out to be $\vartheta=1$,

$$\vartheta = Nt^* = \left(\frac{Gm^*}{l^{*3}} \right)^{1/2} \left(\frac{l^{*3}}{Gm^*} \right)^{1/2} = 1 \quad (2.12)$$

Another parameter of importance is defined as the mass fraction μ which is associated with the mass ratios of the two primaries P_1 and P_2 and is defined as,

$$\mu = \frac{m_2}{m_1 + m_2} = \frac{m_2}{m^*} \quad (2.13)$$

Table (2.1) below shows the values of the characteristic quantities in the Earth-Moon and the Sun-Earth systems for comparison. Applying Newton's second law [5] to

Table 2.1. Characteristic quantities in the Earth-Moon and Sun-Earth system.

System	m^* [kg]	l^* [km]	t^* [sec]	μ
Earth-Moon	6.046804×10^{24}	3.844000×10^5	3.751903×10^5	1.215059×10^{-2}
Sun-Earth	1.988800×10^{30}	1.496500×10^8	5.025263×10^6	3.003486×10^{-6}

the particle of interest P_3 , the vector differential equation in the inertial frame with respect to the base point B is written as,

$$m_3 \bar{P}'' = -\frac{Gm_3m_1}{D^3} \bar{D} - \frac{Gm_3m_2}{R^3} \bar{R} \quad (2.14)$$

The position vectors \bar{P} , \bar{D} and \bar{R} are non-dimensionalized using the characteristic parameters from equations (2.8) - (2.11) and written as $\bar{\rho}$, \bar{d} , and \bar{r} respectively.

$$\bar{\rho} = \frac{\bar{P}}{l^*}, \bar{d} = \frac{\bar{D}}{l^*}, \bar{r} = \frac{\bar{R}}{l^*}, \tau = \frac{t}{t^*} \quad (2.15)$$

Converting all the terms of equation (2.14) into their non-dimensional form results in the following expression,

$$\ddot{\bar{\rho}} = -\frac{(1-\mu)\bar{d}}{\bar{d}^3} - \frac{\mu\bar{r}}{\bar{r}^3} \quad (2.16)$$

Note that the dots indicate the derivatives with respect to non-dimensional time τ and primes indicate the derivatives with respect to the dimensional time t , both relative to an inertial reference frame centered at the barycenter of the system.

The acceleration of the third particle P_3 is also derived from the Basic Kinematic Equations(BKE) expressed in the rotating frame coordinates by the following steps. First, distance to particle P_3 is expressed in terms of non-dimensional coordinates x , y and z defined in the rotating frame as,

$$\bar{\rho} = \frac{\bar{P}}{l^*} = x\hat{x} + y\hat{y} + z\hat{z} \quad (2.17)$$

The velocity of the particle P_3 in the inertial frame is expressed as,

$$\bar{\rho}' = \frac{{}^I d\bar{\rho}}{d\tau} = \frac{{}^R d\bar{\rho}}{d\tau} + {}^I\bar{\omega}^R \times \bar{\rho} \quad (2.18)$$

Once again using BKE with equation (2.18) the acceleration of particle P_3 in the inertial frame with respect to base point B is given by,

$$\bar{\rho}'' = \frac{{}^I d^2\bar{\rho}}{d\tau^2} = \frac{{}^R d^2\bar{\rho}}{d\tau^2} + 2{}^I\bar{\omega}^R \times \bar{\rho}' + {}^I\bar{\omega}^R \times ({}^I\bar{\omega}^R \times \bar{\rho}) \quad (2.19)$$

Where ${}^I\bar{\omega}^R = n\hat{z}$ is the angular velocity of the rotating frame \hat{x} - \hat{y} - \hat{z} with respect to the inertial frame \hat{X} - \hat{Y} - \hat{Z} . Substituting the value of $\bar{\rho}$ from equation (2.17) into equation (2.19), the acceleration of particle P_3 in the inertial frame expressed as rotational coordinates is,

$$\bar{\rho}'' = (\ddot{x} - 2\vartheta\dot{y} - \vartheta^2x)\hat{x} + (\ddot{y} + 2\vartheta\dot{x} - \vartheta^2y)\hat{y} + \ddot{z}\hat{z} \quad (2.20)$$

Equations (2.16) and (2.20), both represent the acceleration of particle P_3 in terms of the rotating coordinates in the inertial reference frame centered at the barycenter B . The scalar components of both the equations are equated to obtain three scalar second order differential equations for the CR3BP as follows,

$$\ddot{x} - 2\vartheta\dot{y} - \vartheta^2x = -\frac{(1-\mu)(x+\mu)}{d^3} - \frac{\mu}{r^3}(x-1+\mu) \quad (2.21)$$

$$\ddot{y} + 2\vartheta\dot{x} - \vartheta^2y = -\frac{(1-\mu)}{d^3}y - \frac{\mu}{r^3}y \quad (2.22)$$

$$\ddot{z} = -\frac{(1-\mu)}{d^3}z - \frac{\mu}{r^3}z \quad (2.23)$$

Where the magnitudes of d and r are calculated as,

$$d = \sqrt{(x+\mu)^2 + y^2 + z^2} \quad (2.24)$$

$$r = \sqrt{(x-1+\mu)^2 + y^2 + z^2} \quad (2.25)$$

The three scalar second-order differential equations, i.e., equations (2.21)-(2.23) are broken down into six scalar first-order differential equations which represent the derivatives of the non-dimensional states of motion of particle P_3 as observed in a rotating frame centered at the base point B . They are generally represented as $\dot{\bar{X}} = \bar{F}(\bar{X}, \tau)$, where the six dimensional state vector \bar{X} and \bar{F} are expressed as,

$$\bar{X} = \begin{bmatrix} x \\ y \\ z \\ \dot{x} \\ \dot{y} \\ \dot{z} \end{bmatrix} = \begin{bmatrix} x_1 \\ x_2 \\ x_3 \\ x_4 \\ x_5 \\ x_6 \end{bmatrix} \quad (2.26)$$

$$\bar{F} = \begin{bmatrix} x_4 \\ x_5 \\ x_6 \\ 2\vartheta x_5 + \vartheta^2 x_1 - \frac{(1-\mu)(x_1+\mu)}{d^3} - \frac{\mu}{r^3}(x_1-1+\mu) \\ -2\vartheta x_4 + \vartheta^2 x_2 - \frac{(1-\mu)}{d^3}x_2 - \frac{\mu}{r^3}x_2 \\ -\frac{(1-\mu)}{d^3}x_3 - \frac{\mu}{r^3}x_3 \end{bmatrix} \quad (2.27)$$

The equations of motion in the CR3BP are autonomous as the non-dimensional time τ does not explicitly appear in \bar{F} .

2.5 Integrals of Motion - Jacobi Constant

The equations of motion in the rotating frame are alternatively written in terms of Pseudopotential function [7]. The Pseudopotential function, U^* , is defined as,

$$U^* = \frac{1-\mu}{d} + \frac{\mu}{r} + \frac{1}{2}\vartheta^2(x^2 + y^2) \quad (2.28)$$

Equations of motion, i.e., equations (2.21)-(2.23) formulated in terms of Pseudo Potential are written as,

$$\ddot{x} - 2\vartheta\dot{y} = \frac{\partial U^*}{\partial x} \quad (2.29)$$

$$\ddot{y} - 2\vartheta\dot{x} = \frac{\partial U^*}{\partial y} \quad (2.30)$$

$$\ddot{z} = \frac{\partial U^*}{\partial z} \quad (2.31)$$

Since the system comprises of conservative forces, an energy or energy-like quantity may be found to be constant in the rotating frame. The constant is found by taking the dot product of the equations (2.29)-(2.31) and the rotating velocity vector, $\dot{\vec{\rho}} = \dot{x}\hat{x} + \dot{y}\hat{y} + \dot{z}\hat{z}$. Summing up the resulting scalar expressions gives,

$$\dot{x}\ddot{x} + \dot{y}\ddot{y} + \dot{z}\ddot{z} = \frac{\partial U^*}{\partial x}\dot{x} + \frac{\partial U^*}{\partial y}\dot{y} + \frac{\partial U^*}{\partial z}\dot{z} \quad (2.32)$$

Since U^* is only a function of position the expression on the right hand side of equation (2.32) equals total derivative $\frac{\partial U^*}{\partial \tau}$. Then integrating the equation (2.32) with respect to non-dimensional time τ yields the following integration constant C ,

$$\frac{1}{2}(\dot{x}^2 + \dot{y}^2 + \dot{z}^2) = U^* - \frac{C}{2} \quad (2.33)$$

Rearranging the coefficients in equation (2.33) gives the following expression to define the Jacobi constant or the Jacobi Integral of Motion, as C ,

$$C = 2U^* - V^2 \quad (2.34)$$

Note here that V is the velocity in the rotating frame. To find analytical solutions for the CR3BP, six integrals of motion are required. Since only one integral of motion, the Jacobi integral, has been known to exist, the equations of motion cannot be solved analytically. But equations (2.26)-(2.27) are numerically propagated to understand the behavior of the secondary particle P_3 in the dynamical system. For a given initial condition of particle P_3 which comprises three non-dimensional positions and velocities along the coordinate axes, the Jacobi constant of the system remains fixed for an indefinite amount of time. It only changes by altering the energy of the system, which happens whenever a ΔV is imparted by performing a maneuver. Jacobi constant plays a vital role in the numerical propagation of the equations of motion by checking the numerical stability as well as in the dimensional reduction of the problem.

2.6 Libration Points - Equilibrium Solutions in the CR3BP

Equilibrium solutions are the preliminary, particular solutions of any dynamical system. They represent the states of the system which when attained stay constant with time. Looking for equilibrium states in the CR3BP is equivalent to finding the rotating position and velocity state components whose derivatives are zero for all times. In equations (2.29)-(2.31), if $\dot{\rho} = \ddot{\rho} = 0$, then velocity and acceleration relative to the rotating frame is zero indefinitely and the particle P_3 does not move with respect to the rotating frame. By substituting the above conditions into the equations of motion, the equilibrium states are evaluated by setting the gradient of the pseudo-potential function equal to zero as,

$$\frac{\partial U^*}{\partial x} = \frac{\partial U^*}{\partial y} = \frac{\partial U^*}{\partial z} = 0 \quad (2.35)$$

Here, U^* is the pseudo-potential function defined in equation (2.28). There are five equilibrium points in the CR3BP. Two of them were first computed by Joseph Lagrange in 1772 and hence are also called Lagrange points or Libration points [7]. The locations of the five equilibrium points in the CR3BP are shown in figure (2.5). All the points lie in the plane of motion of the primaries, i.e., all the points have an out of plane component position $z = 0$. The three collinear points namely L_1 , L_2 and L_3 lie along the \hat{x} -axis and the remaining two points namely L_4 and L_5 form equilateral triangles with the primaries and are therefore called equilateral libration points. Libration point L_1 always lies in between the larger and the smaller primary on the \hat{x} -axis. Libration point L_2 always lies beyond the smaller primary on the positive side of \hat{x} -axis. Libration point L_3 always lies beyond the larger primary on the negative side of the \hat{x} -axis. The equilateral point L_4 has a positive y component and the equilateral point L_5 has a negative y component. Also, γ_1 , γ_2 and γ_3 represent the distances of the collinear libration points to their nearest primaries. The locations of the three collinear points is evaluated by expanding the partial $\frac{\partial U^*}{\partial x} = 0$ in equation (2.35), i.e.,

$$x - \frac{(1 - \mu)(x + \mu)}{d^3} - \frac{\mu(x - 1 + \mu)}{r^3} = 0 \quad (2.36)$$

where d and r are distances of the third body from the primaries given by equations (2.24) and (2.25) respectively. By substituting the three different x coordinates for $L_1 = (1 - \mu - \gamma_1)$, $L_2 = (1 - \mu + \gamma_2)$ and $L_3 = (-\mu - \gamma_3)$ and noting that $y = 0$ and $z = 0$ for all three collinear points three fifth degree polynomials are obtained as follows,

$$\begin{aligned} \gamma_1^5 + \gamma_1^4(\mu - 3) + \gamma_1^3(3 - 2\mu) - \gamma_1^2(\mu) + \gamma_1(2\mu) - \mu &= 0 \\ \gamma_2^5 + \gamma_2^4(3 - \mu) + \gamma_2^3(3 - 2\mu) - \gamma_2^2(-\mu) + \gamma_2(-2\mu) - \mu &= 0 \\ \gamma_3^5 + \gamma_3^4(2 + \mu) + \gamma_3^3(1 + 2\mu) - \gamma_3^2(\mu - 1) + \gamma_3(2\mu - 2) - (1 - \mu) &= 0 \end{aligned} \quad (2.37)$$

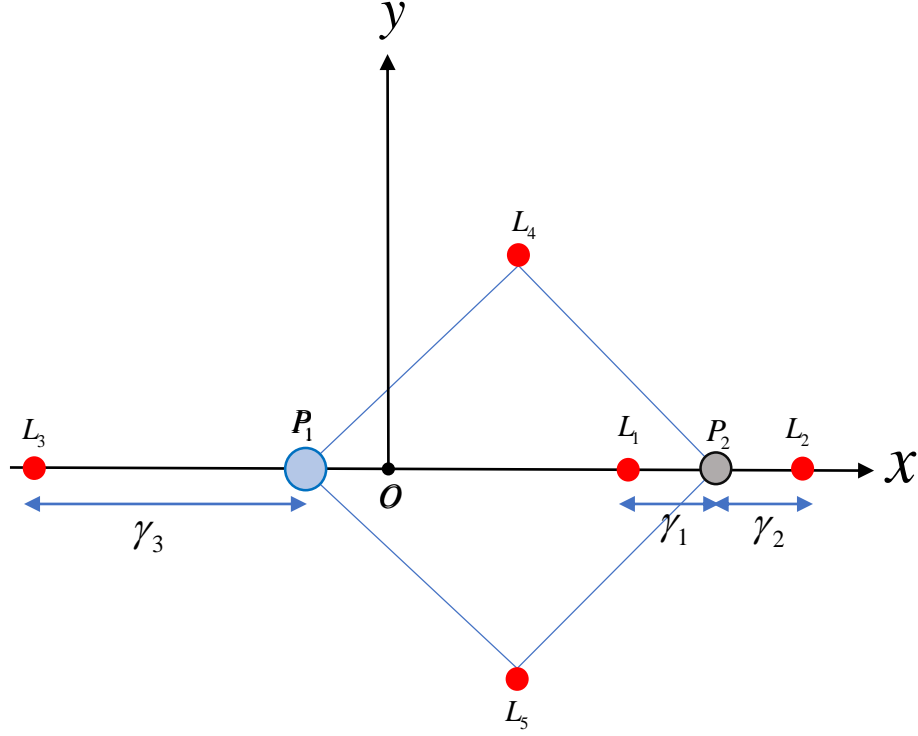


Figure 2.5. Equilibrium points in the rotating frame of CR3BP.

The real roots of the above polynomials are obtained by solving them using a Newton-Raphson's algorithm which give the positions for the three collinear libration points. Further in equation (2.35), substituting $\frac{\partial U^*}{\partial y} = 0$, the following expression is obtained,

$$y \left(1 - \frac{(1-\mu)}{d^3} - \frac{\mu}{r^3} \right) = 0 \quad (2.38)$$

Assuming $y \neq 0$ equation (2.38) will be satisfied only if the term in the paranthesis is equal to zero, i.e.,

$$\left(1 - \frac{(1-\mu)}{d^3} - \frac{\mu}{r^3} \right) = 0 \quad (2.39)$$

On substituting equation (2.39) into equation (2.36), results in $d = r$. Putting this back into equation (2.39) results in $d = r = 1$. This corresponds to two symmetric points which form two equilateral triangles with primaries P_1 and P_2 . The coordinates

of equilibrium points in the Earth-Moon and Sun-Earth systems are show in the table (2.2) below.

Table 2.2. Non-dimensional position coordinates of the libration points in the Earth-Moon and Sun-Earth systems

Equilibrium Point	Earth-Moon [n.d]	Sun-Earth [n.d]
$L_1(x, y, z)$	(0.836915, 0, 0)	(0.990027, 0, 0)
$L_2(x, y, z)$	(1.155682, 0, 0)	(1.010034, 0, 0)
$L_3(x, y, z)$	(−1.005063, 0, 0)	(−1.000001, 0, 0)
$L_4(x, y, z)$	(0.487849, 0.866025, 0)	(0.499997, 0.866025, 0)
$L_5(x, y, z)$	(0.487849, −0.866025, 0)	(0.499997, −0.866025, 0)

2.7 Forbidden Regions and Zero Velocity Surfaces

The introduction of Jacobi constant and libration points help to understand important qualitative aspects about the CR3BP. Given a Jacobi constant for the system, it is possible to define forbidden regions or Zero Velocity Surfaces as the regions inside which the motion of the secondary body is not physically possible [33]. Consider again the expression for the Jacobi constant in equation (2.34). If the velocity of the secondary body with respect to the rotating frame is zero then the following expression is obtained,

$$x^2 + y^2 + \frac{2}{d}(1 - \mu) + \frac{2}{r}\mu = C \quad (2.40)$$

Equation (2.40) represents a surface in 3D space, i.e., for a given value of Jacobi constant C , infinite combinations of rotating x , y and z coordiantes satisfy this equation. The terms on the left are always positive since x^2 and y^2 are always positive and terms $\frac{2}{d}(1 - \mu) > 0$ and $\frac{2}{r}\mu > 0$ because d and r are distances and $0 < \mu < 1$. Thus, at this surface where the secondary particle has a zero relative velocity, Jacobi constant is always positive. When the secondary body is outside the Zero Velocity Surface, it's

velocity is positive and hence its motion in this region is physically possible. On the Zero Velocity Surface the secondary body has zero velocity, but still, has a non-zero acceleration. Inside the Zero Velocity Surface the secondary body has an imaginary velocity which is not physically attainable and hence its motion in this region is practically non-existent throughout the time evolution of any initial condition. For equilibrium points both the rotating velocity and rotating acceleration are together zero. A secondary body at any of the equilibrium points is therefore associated with a specific Jacobi constant which is obtained from equation (2.34). Jacobi constants of libration points for the Earth-Moon and Sun-Earth systems are shown in the table (2.3) below.

Table 2.3. Value of Jacobi constant for libration points in the Earth-Moon and Sun-Earth systems.

System	L_1	L_2	L_3	L_4	L_5
Earth-Moon	3.188341	3.172160	3.012147	2.987997	2.987997
Sun-Earth	3.00089	3.000887	3.000003	2.999997	2.999997

The libration points lie on the Zero Velocity Surfaces at their respective Jacobi constants. At a lower Jacobi constant value they lie outside the surface, and at a higher Jacobi constant value, they lie inside the surface. The Zero Velocity Surfaces are dynamic and change with the Jacobi constant of the system. Consider the Earth-Moon system. The Jacobi constants of the equilibrium solutions are seen in the table (2.3). For a C value larger than C_{L_1} the Zero Velocity Surface is shown in figure 2.6(a). The projection of this surface onto the \hat{x} - \hat{y} plane is shown in figure 2.6(b) and is termed as the Zero Velocity Curve. The region inside the ZVS and ZVC is bounded by three distinct surfaces. For larger values of d and r , the surface is cylindrical with its axis of symmetry parallel to the \hat{z} -axis. For smaller d and r , i.e., closer to primaries, the surface is in the form of small ovoids encircling the primaries. As

a consequence, when the third body is in the vicinity of the primaries, it remains bounded indefinitely, and it cannot escape the system as it cannot pass through the ZVS or ZVC.

As the C value decreases the outer cylinder shrinks in size and the smaller inner ovoids about the primaries increase in size. The effect is captured on the corresponding ZVC. At $C = C_{L_1}$ both the inner curves of the ZVC meet at the libration point L_1 as seen in the figure 2.8(a). Upon further decreasing C , i.e., for $C_{L_2} < C < C_{L_1}$ the region between the two primaries now opens up as seen in figure 2.6(c) and 2.6(d). Trajectories which begin close to one of the primaries are no longer bounded and is possible to move towards the other primary by passing through the corridor. Further decreasing C reduces the size of the outer ZVC and opens up the inner ZVC until they meet at libration point L_2 when $C = C_{L_2}$ as shown in the figure 2.8(b). When $C_{L_3} < C < C_{L_2}$ the right side of the ZVC take off from the \hat{x} -axis and creates a gateway to the exterior region beyond the outer most surface as shown in figure 2.7(a) and 2.7(b). When $C = C_{L_3}$, the outer and inner ZVC at the left end intersect at libration point L_3 as seen in figure 2.8(c). For $C_{L_4} < C < C_{L_3}$ the ZVC get separated and take off completely from the \hat{x} -axis enclosing only the L_4 and L_5 points as shown in figure 2.7(c) and 2.7(d). The exterior region is now open from the left side of the larger primary. At $C = C_{L_4}/C_{L_5}$ the ZVCs shrink and only intersect exactly at the two Equilateral libration points. For $C < C_{L_4}/C_{L_5}$ ZVCs no longer exist on the \hat{x} - \hat{y} plane as shown in figure 2.7(f). This does not mean that the forbidden region has disappeared. Large forbidden regions which are symmetric about the plane of primaries still exist above and below the \hat{x} - \hat{y} plane in 3D space as shown in figure 2.7(e). The whole of \hat{x} - \hat{y} plane is now open for trajectories to traverse freely.

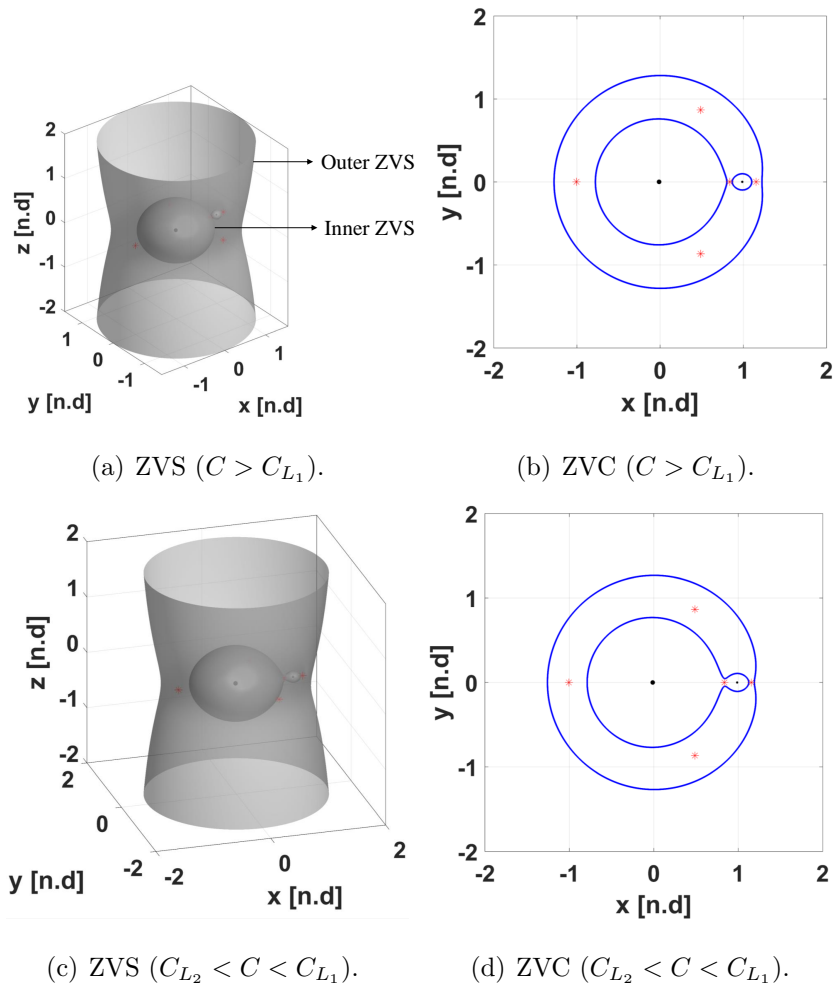


Figure 2.6. ZVS and ZVC for ($C > C_{L_1}$) and ($C_{L_2} < C < C_{L_1}$).

2.8 Coordinate Transformations

Having derived the equations of motion in the rotating frame, numerical propagation and preliminary trajectory design and analysis are also performed in the rotating frame of the primaries in the following chapters. But it is often beneficial to convert the trajectories into an inertial reference frame with respect to either one of the primaries. The conversion offers a useful perspective for practical mission design purposes, especially when the trajectories need to be analyzed in higher fidelity ephemeris models. Frame transformations are performed with a Direction Cosine Matrix (DCM). Recall that the rotating frame has a non-dimensional, constant angular velocity $\vartheta = 1$ with respect to the inertial frame centered at the barycenter. At any given non-dimensional time τ , the orientation of the rotating frame with respect to the inertial frame is given by $\theta = \vartheta \times \tau$, as seen in figure 2.9. The position vector of the secondary particle with respect to the barycenter is expressed in both the rotating and inertial coordinates as,

$$\bar{\rho}_{in} = X\hat{X} + Y\hat{Y} + Z\hat{Z} \quad (2.41)$$

$$\bar{\rho}_{rot} = x\hat{x} + y\hat{y} + z\hat{z} \quad (2.42)$$

By applying appropriate trigonometric transformations the inertial position coordinates in terms of rotational coordinates are expressed as,

$$\begin{aligned} X &= x \cos(\tau - \tau_0) - y \sin(\tau - \tau_0) \\ Y &= x \sin(\tau - \tau_0) + y \cos(\tau - \tau_0) \\ Z &= z \end{aligned} \quad (2.43)$$

The position transformation is captured in a DCM form as follows,

$$\begin{bmatrix} \hat{X} \\ \hat{Y} \\ \hat{Z} \end{bmatrix} = {}^I C^R(\tau) \begin{bmatrix} \hat{x} \\ \hat{y} \\ \hat{z} \end{bmatrix} \quad (2.44)$$

where, the matrix ${}^I C^R$ is written as,

$${}^I C^R(\tau) = \begin{bmatrix} \cos(\tau - \tau_0) & -\sin(\tau - \tau_0) & 0 \\ \sin(\tau - \tau_0) & \cos(\tau - \tau_0) & 0 \\ 0 & 0 & 1 \end{bmatrix} \quad (2.45)$$

Transforming velocities from the rotating frame to inertial frame is possible by applying the Basic Kinematic Equation. Taking the derivatives of equations (2.41) and (2.42) with respect to an inertial frame results in the following,

$$\dot{\rho}_{in} = \dot{X}\hat{X} + \dot{Y}\hat{Y} + \dot{Z}\hat{Z} \quad (2.46)$$

$$\dot{\rho}_{in} = (\dot{x} - \vartheta y)\hat{x} + (\dot{y} + \vartheta x)\hat{y} + \dot{z}\hat{z} \quad (2.47)$$

Both the position and velocity transformation is captured into a single 6×6 matrix by clubbing the above transformations to yield,

$$\begin{bmatrix} X \\ Y \\ Z \\ \dot{X} \\ \dot{Y} \\ \dot{Z} \end{bmatrix} = \begin{bmatrix} {}^I C^R(\tau) & 0_{3 \times 3} \\ \dot{C}(\tau) & {}^I C^R(\tau) \end{bmatrix} \begin{bmatrix} x \\ y \\ z \\ \dot{x} \\ \dot{y} \\ \dot{z} \end{bmatrix} \quad (2.48)$$

where sub matrix ${}^I C^R$ is defined in equation (2.45) and sub matrix $\dot{C}(\tau)$ is defined as,

$$\dot{C}(\tau) = \begin{bmatrix} -\sin(\tau - \tau_0) & -\cos(\tau - \tau_0) & 0 \\ \cos(\tau - \tau_0) & -\sin(\tau - \tau_0) & 0 \\ 0 & 0 & 0 \end{bmatrix} \quad (2.49)$$

The DCM is only an explicit function of the non-dimensional time. The inverse of the DCM in equation (2.48) converts the inertial coordinates to rotational coordinates.

2.9 Stability of Equilibrium Points

The five equilibrium points represent constant, particular solutions in the CR3BP. Lyapunov stability criteria is employed to assess the stability of these points by conducting eigenvalue analysis of the linear variational equations, obtained by linearizing the dynamical system about these points [7]. Linear stability analysis helps in understanding the nature of motion in the close vicinity of the libration points. Depending upon the real or imaginary form of the eigenvalues, the Lyapunov stability criteria for a linearized dynamical model is defined as follows:

1. Complex Eigenvalues

- All negative real parts – The equilibrium point is asymptotically stable.
- At least one root with positive real part – The equilibrium point is unstable.

Above criteria are also valid for repeated complex eigenvalues.

2. Purely Imaginary Eigenvalues

- Distinct roots – Oscillatory bounded motion and equilibrium point is marginally stable.
- Repeated roots – Solution may contain both periodic and secular terms, and hence equilibrium point is unstable.

3. Purely Real roots

- All roots negative – equilibrium point is stable.
- At least one root positive – equilibrium point is unstable.

Above criteria are also valid for repeated purely real eigenvalues.

Let the equilibrium points be represented by coordinates $L(a, b, c)$. Adding infinitesimal variations ξ , η and ψ along x , y and z directions the perturbed states relative to $L(a, b, c)$ are written as,

$$\begin{aligned}x &= a + \xi \\y &= b + \eta \\z &= c + \psi\end{aligned}\tag{2.50}$$

Taking the higher order derivatives of the perturbed states results in,

$$\begin{aligned}\dot{x} &= \dot{\xi} \\\dot{y} &= \dot{\eta} \\\dot{z} &= \dot{\psi} \\\ddot{x} &= \ddot{\xi} \\\ddot{y} &= \ddot{\eta} \\\ddot{z} &= \ddot{\psi}\end{aligned}\tag{2.51}$$

Observe in equation (2.51) the derivatives of a , b , c are zero as the positions of the equilibrium points are constant in the CR3BP. Linearizing the nonlinear differential equations in equations (2.29)-(2.31) using Taylor series expansions and neglecting the higher order terms about equilibrium points L_i result in the following second order linear variational equations expressed as,

$$\ddot{\xi} - 2\dot{\eta} = U^*_{xx}\xi + U^*_{xy}\eta + U^*_{xz}\psi\tag{2.52}$$

$$\ddot{\eta} + 2\dot{\xi} = U^*_{yx}\xi + U^*_{yy}\eta + U^*_{yz}\psi\tag{2.53}$$

$$\ddot{\psi} = U^*_{zx}\xi + U^*_{zy}\eta + U^*_{zz}\psi\tag{2.54}$$

The partials in the above equations (2.52)-(2.54) are calculated as follows,

$$U^*_{xx} = \frac{\partial^2 U^*}{\partial x^2} = 1 - \frac{(1-\mu)}{d^3} + \frac{3(1-\mu)(x+\mu)^2}{d^5} - \frac{\mu}{r^3} + \frac{3\mu(x-1+\mu)^2}{r^5} \quad (2.55)$$

$$U^*_{yy} = \frac{\partial^2 U^*}{\partial y^2} = 1 - \frac{(1-\mu)}{d^3} + \frac{3(1-\mu)y^2}{d^5} - \frac{\mu}{r^3} + \frac{3\mu y^2}{r^5} \quad (2.56)$$

$$U^*_{zz} = \frac{\partial^2 U^*}{\partial z^2} = -\frac{(1-\mu)}{d^3} + \frac{3(1-\mu)z^2}{d^5} - \frac{\mu}{r^3} + \frac{3\mu z^2}{r^5} \quad (2.57)$$

$$U^*_{xy} = \frac{\partial^2 U^*}{\partial x \partial y} = U^*_{yx} = \frac{3(1-\mu)(x+\mu)y}{d^5} + \frac{3\mu(x-1+\mu)y}{r^5} \quad (2.58)$$

$$U^*_{xz} = \frac{\partial^2 U^*}{\partial x \partial z} = U^*_{zx} = \frac{3(1-\mu)(x+\mu)z}{d^5} + \frac{3\mu(x-1+\mu)z}{r^5} \quad (2.59)$$

$$U^*_{yz} = \frac{\partial^2 U^*}{\partial y \partial z} = U^*_{zy} = \frac{3(1-\mu)zy}{d^5} + \frac{3\mu zy}{r^5} \quad (2.60)$$

As all the partials in the above equations (2.55)-(2.60) are evaluated at L_i , they are constant values and since all L_i are planar, the z component for all $L_i = 0$. Making these substitutions into equations (2.52)-(2.54) results in a simplified form of linear variational equations about L_i , given as,

$$\ddot{\xi} - 2\dot{\eta} = U^*_{xx}\xi + U^*_{xy}\eta \quad (2.61)$$

$$\ddot{\eta} + 2\dot{\xi} = U^*_{yx}\xi + U^*_{yy}\eta \quad (2.62)$$

$$\ddot{\psi} = U^*_{zz}\psi \quad (2.63)$$

It is observed from the above linearized equations (2.61)-(2.63) that the in-plane and out of plane motion is decoupled. Thus, it is possible to separately perform the analysis in and out of the rotating plane of the primaries. The second order ordinary

differential equation in equation (2.63) is a simple harmonic oscillator, and its general solution is known to be sinusoidal. Thus a general solution exists as,

$$\psi = A_1 \cos(v\tau) + A_2 \sin(v\tau) \quad (2.64)$$

Where $v = \sqrt{|U_{zz}|_{L_i}}$ is the out of plane frequency and A_1 and A_2 are coefficients determined from initial conditions. At libration points L_4 and L_5 , $U^*_{zz} = -1$, which implies that the $v = 1$, i.e., the angular velocity of a small oscillation along \hat{z} -axis is same as mean motion of primaries. This has been confirmed with the discovery of the Trojan asteroids at Sun-Jupiter L_4 and L_5 locations, which have the same period of small oscillations perpendicular to the ecliptic as the orbital period of Jupiter. As the eigenvalues of the equation (2.63) are imaginary the out of plane linear motion is marginally stable, and therefore stability of the non-linear system cannot be predicted. The stability of the in-plane motion is explored by analyzing the eigenvalues of the linear system described by the equations (2.61) and (2.62). The two second-order coupled linear differential equations is written as four first-order coupled linear differential equations of the form $\dot{\bar{X}} = A\bar{X}$, where $\bar{X} = \begin{bmatrix} \xi & \eta & \dot{\xi} & \dot{\eta} \end{bmatrix}^T$ and A is the system matrix expressed as,

$$A = \begin{bmatrix} 0 & 0 & 1 & 0 \\ 0 & 0 & 0 & 1 \\ U^*_{xx} & U^*_{xy} & 0 & 2 \\ U^*_{yx} & U^*_{yy} & -2 & 0 \end{bmatrix} \quad (2.65)$$

Here the system coefficient matrix A is constant when computed at the equilibrium points L_i . The partial derivatives in the matrix A are computed using equations (2.55)-(2.60). The general solution to this linear system is expressed as,

$$\xi = \sum_{i=1}^4 a_i e^{\lambda_i t} \quad (2.66)$$

$$\eta = \sum_{i=1}^4 b_i e^{\lambda_i t} \quad (2.67)$$

Where a_i and b_i are constants of integration (b_i depend on a_i) and λ_i are roots of the characteristic determinant of matrix A . Expanding the characteristic determinant results in the following fourth order polynomial,

$$\lambda^4 + (4 - U_{xx}^* - U_{yy}^*)\lambda^2 + (U_{xx}^*U_{yy}^* - U_{yx}^*U_{xy}^*) = 0 \quad (2.68)$$

Consider the collinear libration points L_1 , L_2 and L_3 . As they lie on the \hat{x} -axis $y_{L_i} = z_{L_i} = 0$. Substituting these values in the partials of equation (2.68) results in $U_{xy}^* = 0$, $U_{xx}^* > 0$ and $U_{yy}^* < 0$. The characteristic roots of the equation (2.68) are given as,

$$\lambda_{1,2} = \pm \sqrt{\Lambda_1} \quad (2.69)$$

$$\lambda_{3,4} = \pm \sqrt{\Lambda_2} \quad (2.70)$$

Where coefficients Λ_1 , Λ_2 expressed as,

$$\Lambda_{1,2} = -\beta_1 \pm (\beta_1^2 + \beta_2^2)^{\frac{1}{2}} \quad (2.71)$$

Coefficients β_1 and β_2 are given as,

$$\beta_1 = 2 - \frac{U_{xx}^* + U_{yy}^*}{2} \quad (2.72)$$

$$\beta_2 = -U_{xx}^*U_{yy}^* \quad (2.73)$$

Two of the eigenvalues given by equation (2.69) and (2.70) are real and the other two eigenvalues are imaginary. As at least one of the real eigenvalues has a positive real part, by the definition of Lyapunov stability the collinear libration points L_1 , L_2 and L_3 are unstable. However, in the vicinity of the collinear libration points by appropriate choice of initial conditions it is possible to erase unstable eigenmodes in the linear system, which results in a bounded periodic elliptical motion about L_i , with semi-major and semi-minor axes parallel to \hat{y} -axis and \hat{x} -axis respectively. The

same initial conditions may not be periodic in the non-linear model, but it is possible to numerically compute periodic solutions about the libration points using the linear periodic ellipses as the initial guess.

Now, consider the planar stability for the equilateral libration points. At L_4 and L_5 the value of coordinates are $x = \mu - 0.5$, $y = \pm \frac{\sqrt{3}}{2}$ and $z = 0$. Substituting these values into the characteristic equation (2.68) results in the following expression,

$$\lambda^4 + \lambda^2 + \frac{27}{4}\mu(1 - \mu) = 0 \quad (2.74)$$

The characteristic roots of the system are given by,

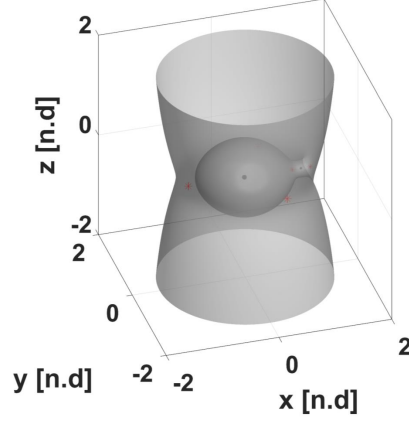
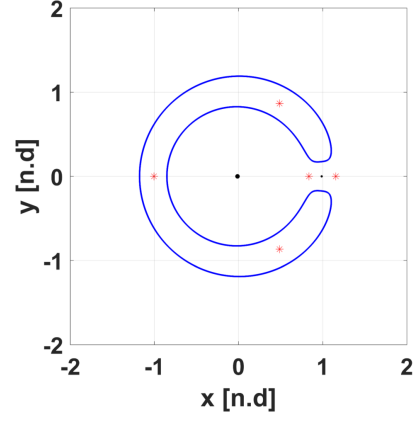
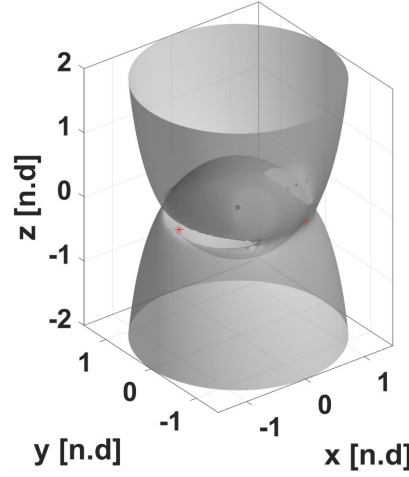
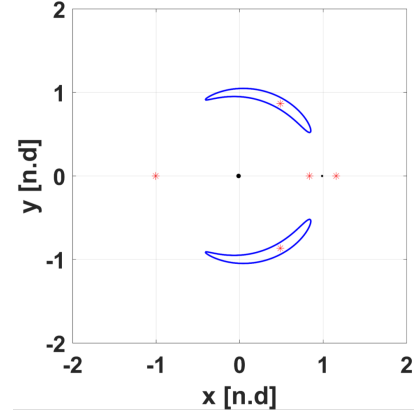
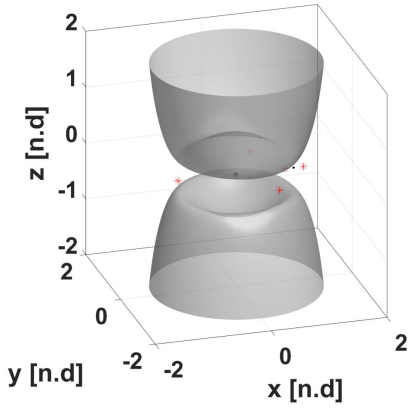
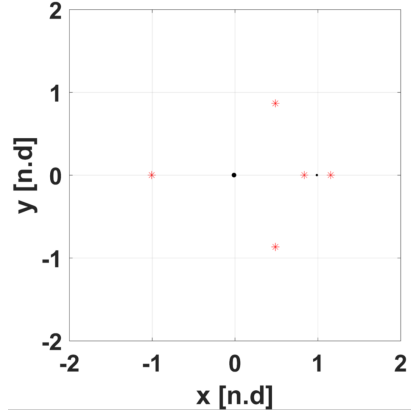
$$\lambda_{1,2,3,4} = \pm \sqrt{\Lambda_{1,2}} \quad (2.75)$$

Where Λ is given by,

$$\Lambda_{1,2} = \frac{1}{2} \left\{ -1 \pm [1 - 27\mu(1 - \mu)]^{1/2} \right\} \quad (2.76)$$

The eigenvalues are seen to be a function of μ . The real or complex nature of the eigenvalues switches at a critical value of $\mu_0 = 0.03852$. Hence, three regions of μ are considered. When $0 \leq \mu < \mu_0$, all four eigenvalues are imaginary, and the linear system is marginally stable. The four imaginary eigenvalues usually correspond to two different frequencies s_1 and s_1 . The motion is bounded and is the superposition of two harmonic oscillations having the above frequencies. One frequency corresponds to the long period motion, and the other corresponds to a short period oscillation. By appropriate choice of initial conditions, it is possible to eliminate the coefficients of a certain frequency, and the resulting motion will be an ellipse with its minor and major axes tilted with respect to the \hat{x} and \hat{y} axes. As the linear system is marginally stable, the stability of the non-linear system cannot be concluded. Just as in the collinear libration points, the same initial conditions may not result in a periodic elliptical motion in the non-linear model, but it is possible to numerically compute

periodic solutions about the libration points using the linear periodic ellipses as the initial guess. In the second region when $\mu = \mu_0$, results in imaginary eigenvalues of equal frequencies. L_4 and L_5 are stable in a linear sense, but conclusions cannot be drawn about the non-linear behavior. In the final region where $\mu > \mu_0$, eigenvalues turn out to be imaginary with two eigenvalues having a negative real part and the remaining eigenvalues having a positive real part. This renders the linear system unstable. Similar to previous cases a wise selection of initial conditions will eliminate the unstable eigenvalues, and the solution will approach asymptotically spiraling towards $L_{4/5}$. But in general planar motion about the L_4 and L_5 points in this region is stable.

(a) ZVS ($C_{L_3} < C < C_{L_2}$).(b) ZVC ($C_{L_3} < C < C_{L_2}$).(c) ZVS ($C_{L_4} < C < C_{L_3}$).(d) ZVC ($C_{L_4} < C < C_{L_3}$).(e) ZVS ($C < C_{L_4}$).(f) ZVC ($C < C_{L_4}$).Figure 2.7. ZVS and ZVC for ($C_{L_3} < C < C_{L_2}$), ($C_{L_4} < C < C_{L_3}$) and ($C < C_{L_4}$).

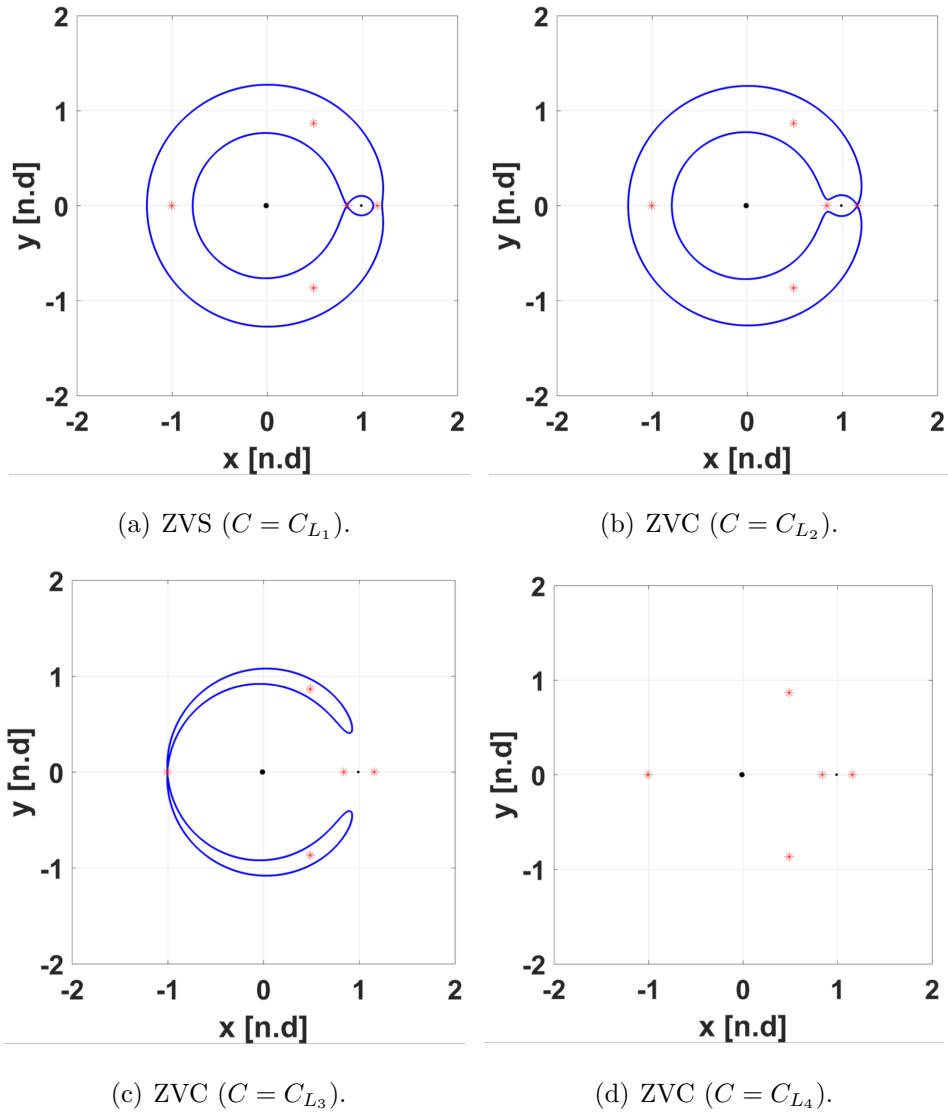


Figure 2.8. ZVC for ($C = C_{L_1}$), ($C = C_{L_2}$), ZVC ($C = C_{L_3}$) and ZVC ($C = C_{L_4}$).

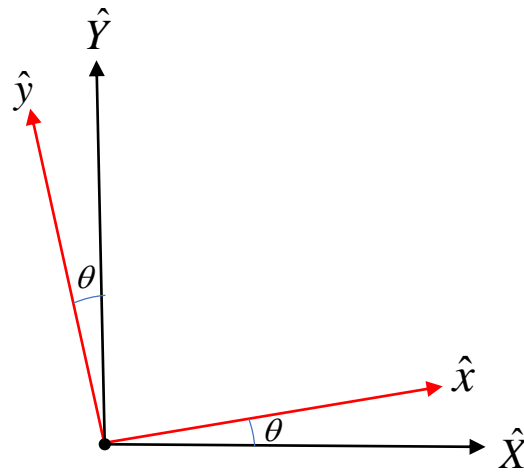


Figure 2.9. Orientation of rotating frame to the Inertial frame.

3. NUMERICAL METHODS AND PERIODIC ORBITS

As closed-form solutions cannot be analytically obtained in the CR3BP, numerical methods are efficiently used for searching and computing several periodic and quasi-periodic solutions. Numerical techniques also form the fundamental tools for trajectory design in the later part of this work. In this chapter, the concept of State Transition Matrix (STM) is introduced, which forms the basis for many linear differential correction algorithms. A general formulation of a differential corrections process is outlined and is followed by two widely used correction processes namely the Single shooting and Multiple shooting techniques. Mirror theorem is introduced which forms the motivation for developing the algorithm to compute symmetric periodic orbits in the CR3BP. Natural parameter and Pseudo-Arclength continuation techniques are presented which are essential in extending the families of periodic orbits and transfer trajectories. And finally the concept of stability is introduced for periodic orbits in the CR3BP and criteria for bifurcations to other periodic solutions is also laid down.

3.1 State Transition Matrix

Numerically integrating the EOMs to study the time evolution of a particular initial condition, may not necessarily reveal the dynamics and time evolution of neighboring trajectories originating from nearby initial conditions. Quite often, it is useful to learn about trajectories close to nominal/reference trajectory that is being integrated. Sometimes the desired trajectory may lie close to the nominal/reference trajectory, and satisfies a certain two-point boundary value problem (TPBVP) in the sense that it has a set of desired initial and final states. One painstaking way to find the desired nearby trajectory is to integrate several initial conditions until the final

conditions are satisfied. An alternative method is a standard way to obtain information about all nearby trajectories at the same time. It relies on the use of variational equations and the State Transition Matix (STM). STM is widely used in the CR3BP to compute trajectories that satisfy a TPBVP, in computing periodic orbits and also analyzing their stability.

Consider the first-order form of nonlinear equations of motion represented by equation (2.3). By integrating an initial condition \bar{X}_0 for a non-dimensional time τ , a particular reference solution $\bar{X}_n(\tau)$ is obtained for the nonlinear equations. Nearby desired trajectory to the reference solution is written as,

$$\bar{X}(\tau) = \bar{X}_n(\tau) + \delta\bar{X}(\tau) \quad (3.1)$$

Here, in equation (3.1) $\bar{X}(\tau)$ indicates the nearby desired trajectory and $\delta\bar{X}(\tau)$ corresponds to the variation with respect to the reference trajectory. Variational equations are obtained by substituting equation (3.1) into the nonlinear system given by equations (2.3) and by expanding them using Taylor series about the reference trajectory. By neglecting the higher order terms the following variational equations are obtained,

$$\delta\dot{\bar{X}} = A(\tau)\delta\bar{X} \quad (3.2)$$

here, $A(\tau)$ is the system Jacobian matrix and $\delta\bar{X}(\tau) = [\delta x \ \delta y \ \delta z \ \delta \dot{x} \ \delta \dot{y} \ \delta \dot{z}]^T$.

The equation (3.2) is written in matrix form as,

$$\begin{bmatrix} \delta \dot{x} \\ \delta \dot{y} \\ \delta \dot{z} \\ \delta \ddot{x} \\ \delta \ddot{y} \\ \delta \ddot{z} \end{bmatrix} = \begin{bmatrix} 0 & 0 & 0 & 1 & 0 & 0 \\ 0 & 0 & 0 & 0 & 1 & 0 \\ 0 & 0 & 0 & 0 & 0 & 1 \\ U^*_{xx} & U^*_{xy} & U^*_{xz} & 0 & 2 & 0 \\ U^*_{yx} & U^*_{yy} & U^*_{yz} & -2 & 0 & 0 \\ U^*_{zx} & U^*_{zy} & U^*_{zz} & 0 & 0 & 0 \end{bmatrix} \begin{bmatrix} \delta x \\ \delta y \\ \delta z \\ \delta \dot{x} \\ \delta \dot{y} \\ \delta \dot{z} \end{bmatrix} \quad (3.3)$$

The partial derivatives in the matrix $A(\tau)$ are computed using equations (2.55)-(2.60) and are evaluated along the reference trajectory. Hence, $A(\tau)$ is not a constant matrix, but a function of the state on the reference trajectory. The general solution to equation (3.2) takes the form,

$$\delta \bar{X}(\tau) = \Phi(\tau, \tau_0) \delta \bar{X}_0 \quad (3.4)$$

Where $\Phi(\tau, \tau_0)$ is the first-order 6×6 matrix STM and the $\delta \bar{X}_0$ is the six element initial variation from a given initial condition associated with the reference trajectory. As both the system Jacobi matrix and the STM are time dependent, they are propagated by the following matrix differential equation along the reference trajectory,

$$\dot{\Phi}(\tau, \tau_0) = A(\tau) \Phi(\tau, \tau_0) \quad (3.5)$$

From equation (3.4) at time $\tau = 0$, $\Phi(\tau_0, \tau_0) = I_{6 \times 6}$. Equation (3.5) corresponds to 36 scalar differential equations which corresponds to each element of the STM.

STM is also alternatively viewed as the derivative of the states at non-dimensional time τ with respect to the initial condition at τ_0 . It is also called the Sensitivity matrix as it contains information about the sensitivities of the final state(at time τ) to variations in the initial state(at time τ_0). By this definition it is written as,

$$\begin{bmatrix} \delta x_f \\ \delta y_f \\ \delta z_f \\ \delta \dot{x}_f \\ \delta \dot{y}_f \\ \delta \dot{z}_f \end{bmatrix} = \begin{bmatrix} \frac{\partial x}{\partial x_0} & \frac{\partial x}{\partial y_0} & \frac{\partial x}{\partial z_0} & \frac{\partial x}{\partial \dot{x}_0} & \frac{\partial x}{\partial \dot{y}_0} & \frac{\partial x}{\partial \dot{z}_0} \\ \frac{\partial y}{\partial x_0} & \frac{\partial y}{\partial y_0} & \frac{\partial y}{\partial z_0} & \frac{\partial y}{\partial \dot{x}_0} & \frac{\partial y}{\partial \dot{y}_0} & \frac{\partial y}{\partial \dot{z}_0} \\ \frac{\partial z}{\partial x_0} & \frac{\partial z}{\partial y_0} & \frac{\partial z}{\partial z_0} & \frac{\partial z}{\partial \dot{x}_0} & \frac{\partial z}{\partial \dot{y}_0} & \frac{\partial z}{\partial \dot{z}_0} \\ \frac{\partial \dot{x}}{\partial x_0} & \frac{\partial \dot{x}}{\partial y_0} & \frac{\partial \dot{x}}{\partial z_0} & \frac{\partial \dot{x}}{\partial \dot{x}_0} & \frac{\partial \dot{x}}{\partial \dot{y}_0} & \frac{\partial \dot{x}}{\partial \dot{z}_0} \\ \frac{\partial \dot{y}}{\partial x_0} & \frac{\partial \dot{y}}{\partial y_0} & \frac{\partial \dot{y}}{\partial z_0} & \frac{\partial \dot{y}}{\partial \dot{x}_0} & \frac{\partial \dot{y}}{\partial \dot{y}_0} & \frac{\partial \dot{y}}{\partial \dot{z}_0} \\ \frac{\partial \dot{z}}{\partial x_0} & \frac{\partial \dot{z}}{\partial y_0} & \frac{\partial \dot{z}}{\partial z_0} & \frac{\partial \dot{z}}{\partial \dot{x}_0} & \frac{\partial \dot{z}}{\partial \dot{y}_0} & \frac{\partial \dot{z}}{\partial \dot{z}_0} \end{bmatrix} \begin{bmatrix} \delta x_0 \\ \delta y_0 \\ \delta z_0 \\ \delta \dot{x}_0 \\ \delta \dot{y}_0 \\ \delta \dot{z}_0 \end{bmatrix} \quad (3.6)$$

Along with the six non-linear differential equations, the 36 elements of the first-order STM are numerically integrated with a typical numerical simulation of the CR3BP and used in various differential correction algorithms.

3.2 Differential Corrections

Computation of periodic orbits, quasi-periodic trajectories and transfer trajectories in the CR3BP is typically similar to solving two-point boundary value problems along with meeting specific state constraints along the trajectory. Various kinds of differential correction algorithms are employed to solve these problems. In this investigation, differential corrections formulated as single and multiple shooting schemes are used as the principal algorithms for trajectory design. These shooting schemes are well known as multi-dimensional Newton-Raphson's methods. Any differential correction process has two main matrices:

1. **Free Variable Matrix** : A vector consisting of n design variables of the problem which vary freely to satisfy a set of given constraints. Typically, free variables include positions, velocities, integration times, epoch times and slack variables.
2. **Constraint Matrix** : A vector consisting of m constraint equations that needs to be satisfied by the propagated trajectory. Any mission constraint is usually expressed in terms of free variables of the trajectory. Typical constraints include position and velocity constraints, apse constraint, time of flight, ΔV or altitude constraints and so on.

The correction process boils down to finding the appropriate free variable matrix \bar{X} close to the initial guess \bar{X}^0 which satisfies the constraint matrix, i.e., $\bar{F}(\bar{X}) = 0$. For this, the constraint vector is expanded using Taylor series about the initial free variable vector,

$$\bar{F}(\bar{X}) = \bar{F}(\bar{X}^0) + \frac{\partial \bar{F}(\bar{X}^0)}{\partial \bar{X}^0}(\bar{X} - \bar{X}^0) + \dots \quad (3.7)$$

Here $\frac{\partial \bar{F}(\bar{X}^0)}{\partial \bar{X}^0}$ is an $m \times n$ Jacobian matrix which is made up of partial derivatives of the constraint vector with respect to the free variables. Neglecting the higher order terms the following expression is obtained,

$$\bar{F}(\bar{X}) = \bar{F}(\bar{X}^0) + DF(\bar{X}^0)(\bar{X} - \bar{X}^0) \quad (3.8)$$

As at the desired free variable the constraint vector $\bar{F}(\bar{X}) = 0$, the update equation for the corrections process takes the form,

$$\bar{X}^{j+1} = \bar{X}^j - DF(\bar{X}^j)^{-1} \bar{F}(\bar{X}^j) \quad (3.9)$$

Where \bar{X}^j is the current iteration value of the free variable vector, \bar{X}^{j+1} is the next iteration of the free variable vector, $\bar{F}(\bar{X}^j)$ is the value of the current constraint vector evaluated at the current design variable \bar{X}^j . The Jacobian $DF(\bar{X}^j)$ is evaluated from the current $\bar{F}(\bar{X}^j)$ and \bar{X}^j . The iterations are stopped when the Euclidean norm of the constraint vector $\|\bar{F}(\bar{X}^{j+1})\|_2$ is less than an acceptable tolerance of 10^{-12} , i.e., $\|\bar{F}(\bar{X}^{j+1})\|_2 < 10^{-12}$.

When the number of design variables n equals the constraint equations m , the update equation (3.9) is used. Sometimes, the number of design variables n are more than the constraint equations m which leads to infinitely many solutions. In such an under-determined system a minimum norm solution is sought and the new update equation is given as,

$$\bar{X}^{j+1} = \bar{X}^j - DF(\bar{X}^j)^T (DF(\bar{X}^j)DF(\bar{X}^j)^T)^{-1} \bar{F}(\bar{X}^j) \quad (3.10)$$

This yields a solution \bar{X} that is as close as possible to the initial design variable \bar{X}^0 . On some occasions, having fewer design variables than the constraint equations often leads to no solution. In such an over-determined system a least squares solution is desired and the new update equation is given to be,

$$\bar{X}^{j+1} = \bar{X}^j - (DF(\bar{X}^j)^T DF(\bar{X}^j))^{-1} DF(\bar{X}^j)^T \bar{F}(\bar{X}^j) \quad (3.11)$$

The corrections process formulated form the basis for different kinds of targeting algorithms. The two most extensively used methods are the Single Shooting and the Multiple Shooting techniques. The following sections explain the two in more detail.

3.3 Single Shooting or Simple Targeting Problem

The essence of a single shooting differential correction process is captured by a simple targeting problem. It is an elementary correction process in which the goal is to find a nearby solution to a reference trajectory which satisfies certain initial and final state conditions. Consider a reference trajectory shown in figure 3.1. It starts with the initial conditions $\bar{x}(t_0)$ and is propagated for a time T , using the nonlinear equations of motion given in equation (2.26) - (2.27) to attain the final conditions $\bar{x}(t_0 + T)$. Let there exist a target final state $\bar{x}_d(t_0 + T)$ in the vicinity of the current final condition. The simple targeting problem is now to find a nearby trajectory which reaches the new final desired state by appropriately modifying the initial conditions and the propagation time. The iteration scheme developed in the previous section is used to formulate the corrections process. First, the free variable vector is formulated and is comprised of initial conditions and the propagation time of the reference trajectory, written as,

$$\bar{x}(t_0) = \begin{bmatrix} x(t_0) \\ y(t_0) \\ z(t_0) \\ \dot{x}(t_0) \\ \dot{y}(t_0) \\ \dot{z}(t_0) \\ T \end{bmatrix} \quad (3.12)$$

Depending on the problem scenario sometimes some of the initial conditions or propagation time are not allowed to vary. In such cases, the fixed conditions are not included in the free variable vector. For example, if the initial positions are not allowed to vary then the free variable vector is modified as,

$$\bar{x}(t_0) = \begin{bmatrix} \dot{x}(t_0) \\ \dot{y}(t_0) \\ \dot{z}(t_0) \\ T \end{bmatrix} \quad (3.13)$$

Next, the constraint vector is formulated by including all the scalar constraint equations for the trajectory. As the trajectory must reach a target final condition $\bar{x}_d(t_0+T)$ the constraint vector is written as,

$$\bar{F}(\bar{x}_d(t_0+T)) = \begin{bmatrix} x_d(t_0+T) - x_d \\ y_d(t_0+T) - y_d \\ z_d(t_0+T) - z_d \\ \dot{x}_d(t_0+T) - \dot{x}_d \\ \dot{y}_d(t_0+T) - \dot{y}_d \\ \dot{z}_d(t_0+T) - \dot{z}_d \end{bmatrix} = 0 \quad (3.14)$$

Here $\bar{x}_d(t_0+T)$ are the states obtained by propagating the initial condition $\bar{x}(t_0)$ for a time T using the nonlinear equations of motion, i.e., equation (2.26) - (2.27). Sometimes, the target final conditions may apply only to a subset of the final states of the trajectory. In such cases, the free final conditions are not included in the constraint vector. For example, if only final positions are to be targeted, then the modified constraint vector is written as,

$$\bar{F}(\bar{x}_d(t_0+T)) = \begin{bmatrix} x_d(t_0+T) - x_d \\ y_d(t_0+T) - y_d \\ z_d(t_0+T) - z_d \end{bmatrix} = 0 \quad (3.15)$$

The next crucial step is to calculate the Jacobian matrix which is made up of partial derivatives of the constraint vector with respect to the free variables. By this definition, the Jacobian matrix for the free variable and the constraint vectors in equation (3.13) - (3.15) respectively is written as,

$$DF(\bar{x}(t_0 + T)) = \begin{bmatrix} \frac{\partial x(t_0+T)}{\partial \dot{x}(t_0)} & \frac{\partial x(t_0+T)}{\partial \dot{y}(t_0)} & \frac{\partial x(t_0+T)}{\partial \dot{z}(t_0)} & \frac{\partial x(t_0+T)}{\partial T} \\ \frac{\partial y(t_0+T)}{\partial \dot{x}(t_0)} & \frac{\partial y(t_0+T)}{\partial \dot{y}(t_0)} & \frac{\partial y(t_0+T)}{\partial \dot{z}(t_0)} & \frac{\partial y(t_0+T)}{\partial T} \\ \frac{\partial z(t_0+T)}{\partial \dot{x}(t_0)} & \frac{\partial z(t_0+T)}{\partial \dot{y}(t_0)} & \frac{\partial z(t_0+T)}{\partial \dot{z}(t_0)} & \frac{\partial z(t_0+T)}{\partial T} \end{bmatrix} \quad (3.16)$$

Note that the elements in the first three columns of the DF matrix quantify the sensitivity of the final states with respect to the initial states and thus are elements of the STM. The elements in the last column of the DF matrix indicate the sensitivity of propagation time on the final states and hence are the time derivatives of the final states. The DF matrix is evaluated straightforwardly as,

$$DF(\bar{x}(t_0 + T)) = \begin{bmatrix} \Phi_{14} & \Phi_{15} & \Phi_{16} & \dot{x}(t_0 + T) \\ \Phi_{24} & \Phi_{25} & \Phi_{26} & \dot{y}(t_0 + T) \\ \Phi_{34} & \Phi_{35} & \Phi_{36} & \dot{z}(t_0 + T) \end{bmatrix} \quad (3.17)$$

Depending upon the number of free variables and the elements of constraint vector one of the three iteration schemes in equations (3.9), (3.10) and (3.11) is used as the update equation during the differential corrections process. The iteration process is repeated until the norm of the constraint vector $\|\bar{F}(\bar{x}(t_0 + T))\|_2$, is less than an acceptable tolerance value of 10^{-12} . If the integration time is a free variable, the corrections scheme is labeled variable time shooting process and if the integration time is fixed then it is termed as fixed time shooting process.

3.4 Multiple Shooting Algorithm

When the reference solution lies in a highly sensitive, nonlinear region or has longer integration times, single shooting method often takes a lot of iterations or does not converge to the desired free variables. In such circumstances multiple shooting method is more robust in tackling such conditions. It is essentially applying several single shooting methods parallelly along the trajectory to meet the design constraints. An important first step in this process is to discretized the trajectory into $(n - 1)$ smaller segments or sub-arcs separated by n patch points or nodes. Consider a reference

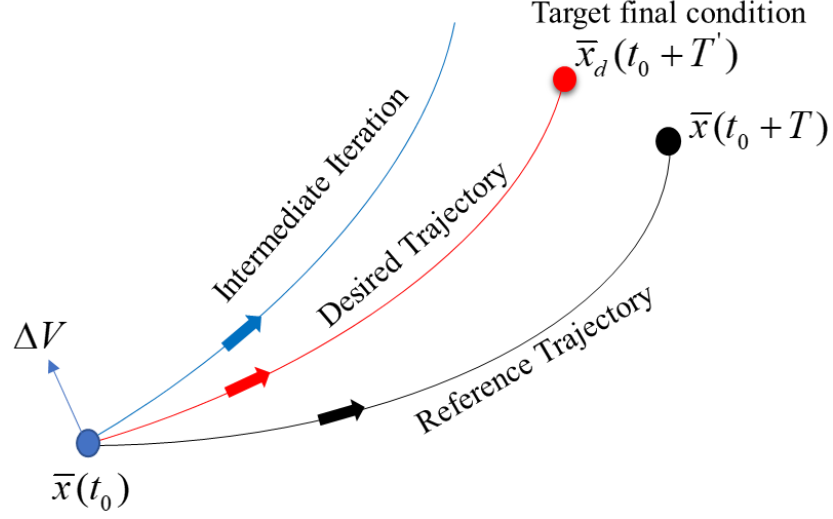


Figure 3.1. Illustration of Single shooting method.

trajectory broken down by n patch points into $n - 1$ sub arcs as seen in figure 3.2. Here \bar{x}_i^0 represents the initial state vector along a sub-arc. The integration time from \bar{x}_n^0 to the next patch point is T_n . The final state of a sub-arc after integration is written as $\bar{x}_n^f(\tau_n, T_n)$. Similar to the single shooting method, a targeting algorithm is written using a multiple shooting scheme. First, the design vector is formulated as the set of all the (n) initial conditions and sub-arc propagation times. Thus the free variable design vector is written as,

$$\bar{X} = \begin{bmatrix} \bar{x}_1^0 \\ \vdots \\ \bar{x}_n^0 \\ T_1 \\ \vdots \\ T_{n-1} \end{bmatrix} \quad (3.18)$$

Sometimes, when few of the design variables are fixed, they may be omitted from the design vector or added to the constraint vector. Next, the constraint vector is formulated by including all the scalar constraint equations for the trajectory. Many

times the sub-arcs are desired to be continuous in their states after the corrections process. Hence continuity constraints are first introduced by ensuring the states at the end of the sub-arcs to match the initial conditions of the patch points of the next sub-arc. If a maneuver is introduced at a patch point, only the position constraints are ensured between the end point of the previous sub-arc and the desired patch point. Finally, other design constraints are appended to the continuity constraints to complete the constraint vector. A typical constraint vector takes the form,

$$\bar{F}(\bar{X}) = \begin{bmatrix} \bar{x}_1^f(\tau_1, T_1) - \bar{x}_2^0 \\ \bar{x}_2^f(\tau_2, T_2) - \bar{x}_3^0 \\ \vdots \\ \bar{x}_{n-1}^f(\tau_{n-1}, T_{n-1}) - \bar{x}_n^0 \end{bmatrix} \quad (3.19)$$

The next step is to calculate the Jacobian matrix, DF which is made up of partial derivatives of the constraint vector with respect to the free variables. By this definition the DF matrix for the free variable and the constraint vectors in equation (3.18) and (3.19) respectively is written as,

$$DF(\bar{X}) = \begin{bmatrix} \frac{\partial \bar{x}_1^f(\tau_1, T_1)}{\partial \bar{x}_1^0} & -\frac{\partial \bar{x}_2^0}{\partial \bar{x}_2^0} & 0 & 0 & \frac{\partial \bar{x}_1^f(\tau_1, T_1)}{\partial T_1} & 0 & 0 \\ 0 & \frac{\partial \bar{x}_2^f(\tau_2, T_2)}{\partial \bar{x}_2^0} & \ddots & \vdots & 0 & \ddots & \vdots \\ \vdots & \ddots & \ddots & \vdots & \vdots & \ddots & \vdots \\ 0 & 0 & \frac{\partial \bar{x}_{n-1}^f(\tau_{n-1}, T_{n-1})}{\partial \bar{x}_{n-1}^0} & -\frac{\partial \bar{x}_n^0}{\partial \bar{x}_n^0} & 0 & 0 & \frac{\partial \bar{x}_{n-1}^f(\tau_{n-1}, T_{n-1})}{\partial T_{n-1}} \end{bmatrix} \quad (3.20)$$

Note that some of the elements in the DF matrix correspond to elements of the STMs belonging to the sub-arcs. Remaining elements of the DF matrix correspond to the time derivatives of states at the endpoints of the sub-arcs. The DF matrix is evaluated straightforwardly as,

$$DF(\bar{X}) = \begin{bmatrix} \Phi_1 & -I_{6 \times 6} & 0 & 0 & \dot{\bar{x}}_1^f(\tau_1, T_1) & 0 & 0 \\ 0 & \Phi_2 & \ddots & \vdots & 0 & \ddots & \vdots \\ \vdots & \ddots & \ddots & \vdots & \vdots & \ddots & \vdots \\ 0 & 0 & \Phi_{n-1} & -I_{6 \times 6} & 0 & 0 & \dot{\bar{x}}_{n-1}^f(\tau_{n-1}, T_{n-1}) \end{bmatrix} \quad (3.21)$$

Depending upon the number of free variables and the elements in the constraint vector one of the three iteration schemes in equations (3.9), (3.10) and (3.11) are used for the differential corrections process. The iteration process is repeated until the norm of the constraint vector $\bar{F}(\bar{X})$, is less than an acceptable tolerance value of 10^{-12} . Throughout this investigation, a variable time multiple shooting algorithm is used to compute periodic orbits and design trajectories.

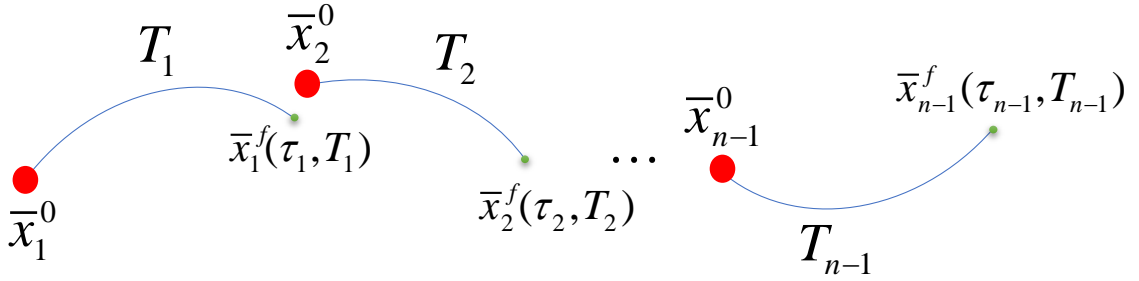


Figure 3.2. Illustration of Multiple shooting method.

3.5 Symmetric Properties in CR3BP

Consider a solution to the CR3BP given by $x = x(t)$, $y = y(t)$ and $z = z(t)$, which is obtained by integrating an arbitrary initial condition $\bar{X}_0 = \begin{bmatrix} x_0 & y_0 & z_0 & \dot{x}_0 & \dot{y}_0 & \dot{z}_0 \end{bmatrix}^T$ for a time t . A mirror image of the initial condition \bar{X}_0 about the \hat{x} - \hat{z} plane exists and is given to be $\bar{X}'_0 = \begin{bmatrix} x_0 & -y_0 & z_0 & -\dot{x}_0 & \dot{y}_0 & -\dot{z}_0 \end{bmatrix}^T$. When evolved backwards in time \bar{X}'_0 produces a trajectory $x = x(-t)$, $y = -y(-t)$ and $z = z(-t)$ which is the mirror image of the original trajectory about the \hat{x} - \hat{z} plane and also satisfies the nonlinear differential equations of motion. This is verified by making the following

substitutions $t = -t$, $x = x$, $y = -y$ and $z = z$ into equations (2.29)-(2.31) and simplification to arrive at the following set of equations,

$$\frac{d^2 x'}{dt'^2} = -2 \frac{dy'}{dt'} + \frac{\partial U^*}{\partial x'} \quad (3.22)$$

$$\frac{d^2 y'}{dt'^2} = 2 \frac{dx'}{dt'} + \frac{\partial U^*}{\partial y'} \quad (3.23)$$

$$\frac{d^2 z'}{dt'^2} = \frac{\partial U^*}{\partial z'} \quad (3.24)$$

Thus, the mirror trajectory when substituted into the EOM's leave them unchanged. One of the consequence of the symmetry property is the Mirror theorem.

The **Mirror theorem** states that if n point masses are acted upon by their mutual gravitational forces, and at a certain epoch, each radius vector from the center of mass of the system is perpendicular to every velocity vector, then the orbit of each point mass after the epoch is a mirror image of its orbit prior to that epoch. Such a configuration of radius and velocity vectors is called a Mirror configuration [34]. Roy and Ovenden used this theorem to say that if in two separate instances a mirror configuration occurs, then the orbits are periodic. That is if the secondary particle crosses the \hat{x} - \hat{z} plane perpendicularly at two different points then its trajectory is periodic. This fact forms the basis for numerical computation of symmetric periodic orbits about the libration points in the CR3BP.

3.6 Symmetric Periodic Orbits

Recall that by careful selection of certain initial conditions, periodic and oscillatory solutions to the linearized equations of motion about the libration points exist. But when the same initial conditions are evolved using the nonlinear dynamical equations the solution no longer stays periodic. Nevertheless, periodic solutions for the nonlinear model in the close vicinity of the initial conditions are numerically found by the

application of Mirror theorem and a targeting algorithm as discussed in the previous sections. The preliminary planar periodic orbits about the libration points are called the Lyapunov families of periodic orbits. Consider the libration point L_1 . In general, the L_1 point is considered unstable as it has both unstable and stable eigenvalues for the linearized system. By a careful selection of initial conditions about this point, it is possible only to retain the stable oscillatory eigenvalues to produce elliptical periodic orbits in the linear dynamical regime. Such an initial condition is given as,

$$\bar{x}_0 = \begin{Bmatrix} x_0 & 0 & 0 & 0 & \dot{y}_0 & 0 \end{Bmatrix} \quad (3.25)$$

When the above initial condition is integrated using the nonlinear differential equations for a period equal to that of the linear orbit, it results in nonperiodic trajectory with a non-perpendicular \hat{x} -axis crossing. According to the Mirror theorem, if a nearby initial condition is found which makes the nonlinear trajectory cross the \hat{x} -axis perpendicularly at the two crossings then it will represent a periodic solution. As a consequence, only half of the trajectory will be considered as the initial guess for the differential corrections process to target two perpendicular crossings at the \hat{x} -axis. The initial condition for the guess is given in equation (3.25), which starts at \hat{x} -axis perpendicularly in a retrograde direction to the primaries. A periodic orbit which starts at the same x -coordinate is desired. Therefore, the design vector only consists of the velocity state in \hat{y} -direction and the integration time written as,

$$\bar{X} = \begin{Bmatrix} \dot{y}_0 \\ T \end{Bmatrix} \quad (3.26)$$

Position state in x_0 and velocity \dot{x}_0 (to ensure perpendicular crossing) are fixed states in the correction process. The constraint vector ensures that the trajectory crosses the \hat{x} -axis perpendicularly at the final point on the trajectory. Thus it is written as,

$$\bar{F}(\bar{X}) = \begin{Bmatrix} \dot{x}_F \\ y_F \end{Bmatrix} \quad (3.27)$$

The Jacobian or the DF matrix is expressed using the design and the constrain vectors as the following,

$$D\bar{F}(\bar{X}) = \begin{bmatrix} \frac{\partial \dot{x}_F}{\partial \dot{y}_0} & \frac{\partial \dot{x}_F}{\partial T} \\ \frac{\partial \dot{y}_F}{\partial \dot{y}_0} & \frac{\partial \dot{y}_F}{\partial T} \end{bmatrix} \quad (3.28)$$

As the number of constraints are equal to the number of design variables equation (3.9) is used for the iteration process. To demonstrate the process consider a non-dimensional initial condition close to the L_1 equilibrium point given by,

$$\bar{x}_0 = \left\{ 0.835915 \quad 0 \quad 0 \quad 0 \quad 0.008372 \quad 0 \right\} \quad (3.29)$$

and the halftime period of the linear elliptical orbit is $T = 1.359022$ non-dimensional units. Now, applying the single shooting scheme as discussed above results in a Lyapunov periodic orbit as shown in figure 3.3 with the new initial conditions,

$$\bar{x}_0^{corrected} = \left\{ 0.835915 \quad 0 \quad 0 \quad 0 \quad 0.008435 \quad 0 \right\} \quad (3.30)$$

and the new half time period of the periodic orbit is $T = 1.345895$ non-dimensional units. Notice that the corrected Lyapunov orbit has the same \hat{x} -coordinate as the initial guess.

Alternatively, for every iteration during the differential corrections process the trajectory is propagated until the intersection occurs with the \hat{x} -axis, i.e., automatically $y_F = 0$ for the propagated time during every iteration. This helps to remove time from the design variable and the new design variable is just the velocity \dot{y} . The modified constraint vector is $\dot{x}_F = 0$ as the trajectory is always integrated till $y_F = 0$ during every iteration. Both the approaches are equivalent. The iteration process is continued until the norm of the constraint vector is less than an acceptable tolerance level of 10^{-12} . The final trajectory of the correction process represents half of the L_1 planar Lyapunov orbit which is a retrograde periodic orbit at the same x -coordinate as X_0 , i.e., the initial guess. The other half of the periodic orbit is obtained by reflect-

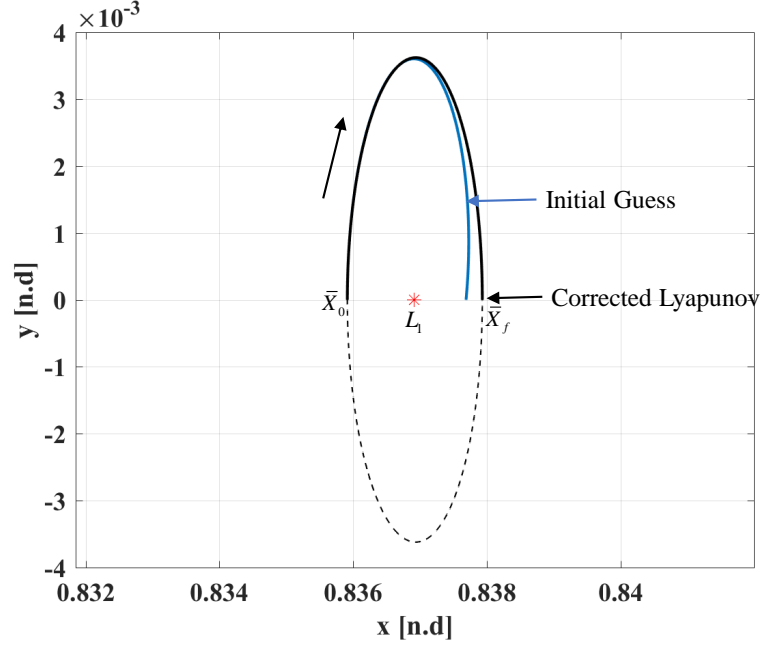


Figure 3.3. A symmetric, periodic L_1 Lyapunov orbit.

ing the converged trajectory about the \hat{x} -axis. This periodic orbit is only one among infinitely many members of the Lyapunov family. Other members of the family are obtained by various continuation algorithms. Different three-dimensional periodic orbits also exist which originate from the Lyapunov family, and will be discussed in later sections.

3.7 Continuation process

From the previous section, the periodic L_1 Lyapunov orbit obtained by differential corrections process is a particular solution to the CR3BP. It is one among infinitely many periodic orbits which belong to L_1 Lyapunov family. In a more general sense isolated periodic orbits are not found in the CR3BP. Periodic orbits always exist as families and originate about the libration points or primaries. All the orbits in a family evolve smoothly over various natural parameters which characterize the orbits such a time period, Jacobi constant, stability and excursions in various directions.

This smooth evolution of various parameters are leveraged to compute other members of the families by incorporating them into the differential corrections process. This method of generating new members of a family from an existing periodic orbit is called Continuation process. The simplest form of continuation is accomplished by evolving the natural parameters of the orbit family, and there is also a more robust method termed as the Pseudo-arclength process which is widely used in the later analysis.

3.7.1 Natural Parameter Continuation

Natural Parameter Continuation is an elementary continuation process. It makes use of the fact that natural parameters in the family of periodic orbits evolve smoothly. It is implemented in the following way. First, a periodic orbit is computed using a simple differential corrections process. For example, consider the previous section. An L_1 Lyapunov orbit with the following natural parameters as shown in table 3.1 is computed using a simple targeting algorithm and mirror theorem as shown in figure 3.3. Then, one of the natural parameters is changed by a small amount and added to the constraint vector. In this case, the positive crossing on the \hat{x} -axis is chosen as the natural parameter and is decreased by a small amount $\beta = 0.001$. This changes the initial condition. The trajectory propagated using the new initial condition for the same time period as the base periodic orbit fails to produce a periodic trajectory. This forms the initial guess in the corrections process. Any one of the single or multiple shooting targeting schemes is applied to converge to a new nearby periodic solution, which is characterized by the new natural parameter, as it is included in the constraint vector. Using the newly converged periodic orbit as the new guess, the process is repeated to evolve new members of the periodic family. Even though the algorithm seems straightforward, there are a few challenges associated with this process. Sometimes, the evolution of the natural parameters is non-intuitive, and thus a step in an incorrect direction may not lead to convergence. Also, depending

Table 3.1. Natural parameters of a representative L_1 Lyapunov orbit.

Natural Parameter	Value (n.d)
Positive \hat{x} -axis crossing	0.835915
Negative \hat{x} -axis crossing	0.837932
Positive \hat{x} -axis crossing velocity	0.008435
Negative \hat{x} -axis crossing velocity	−0.00847
Half Time Period	1.345895
Jacobi Constant	3.188281

upon the sensitivity of the dynamical region the step size β may vary significantly compared to other non-sensitive dynamical regions within the family. Therefore, there is no fixed size for the step length β and is to be chosen based on experience.

3.7.2 Pseudo-arclength Continuation

Pseudo-arclength Continuation is a more robust process [35]. All the free variables associated with periodic orbits in a family may or may not evolve smoothly. Pseudo-arclength helps to step along the tangential direction of evolution of free variables towards the next orbit in a family. Hence, prior knowledge about the evolution of the free variables is not required. Larger and accurate step sizes is taken which leads to faster convergence and fewer iterations. But a step size in Pseudo-arclength technique has no physical significance as a change in all the free variables happens at once as opposed to a single variable in natural parameter continuation. Hence, there is less intuition about the distances between solutions computed using this algorithm.

To implement any continuation process, a converged base periodic orbit is necessary. Let the free variable vector of the periodic orbit be represented by \bar{X}_{i-1}^* satisfying the constraints $\bar{F}(\bar{X}_{i-1}^*) = 0$. The linear approximation of the tangent to

the family of periodic orbits at the free variable vector \bar{X}_{i-1}^* is given by the null vector of the Jacobian matrix for the converged solution as $\Delta\bar{X}_{i-1}^* = N(DF(\bar{X}_{i-1}^*))$. All the free variables are then incremented simultaneously along the tangent by a step length Δs . This creates a new set of design variables, \bar{X}_i^* as,

$$\bar{X}_i = \bar{X}_{i-1}^* + \Delta s \Delta\bar{X}_{i-1}^* \quad (3.31)$$

When the initial conditions given by equation (3.31) are propagated, it forms the non-periodic initial guess for the next corrections process. A Pseudo-arclength constraint is additionally incorporated into the constraint vector to ensure that the new periodic orbit is at the step length Δs along the tangent to the family at the previous design variable \bar{X}_{i-1}^* . Thus the new constraint vector for the corrections process is written as,

$$(\bar{X}_i - \bar{X}_{i-1}^*)^T \Delta\bar{X}_{i-1}^* - \Delta s = 0 \quad (3.32)$$

The new augmented DF matrix with the augmented constraint vector in equation (3.32) is given by,

$$\bar{G}(\bar{X}_i) = \begin{bmatrix} \bar{F}(\bar{X}_i) \\ (\bar{X}_i - \bar{X}_{i-1}^*)^T \Delta\bar{X}_{i-1}^* - \Delta s = 0 \end{bmatrix} = \bar{0} \quad (3.33)$$

Once all the matrices are formulated, depending upon the number of free variables and constraints one of the differential corrections schemes in equations (3.9) - (3.11) is used to produce the next periodic orbit in the family with free variables \bar{X}_i^* . This process is continued to generate the other L_1 family orbits as shown in figure 3.4 by updating the base periodic orbit with the newest member of the family. The color bar on the right indicates the Jacobi constant for the computed orbits. Close to the libration point, the Lyapunov orbits have a Jacobi constant similar to the L_1 libration point. As the orbits get bigger and as they move closer towards the Earth, the Jacobi constant decreases, i.e., the energy of the orbits increases. This technique coupled

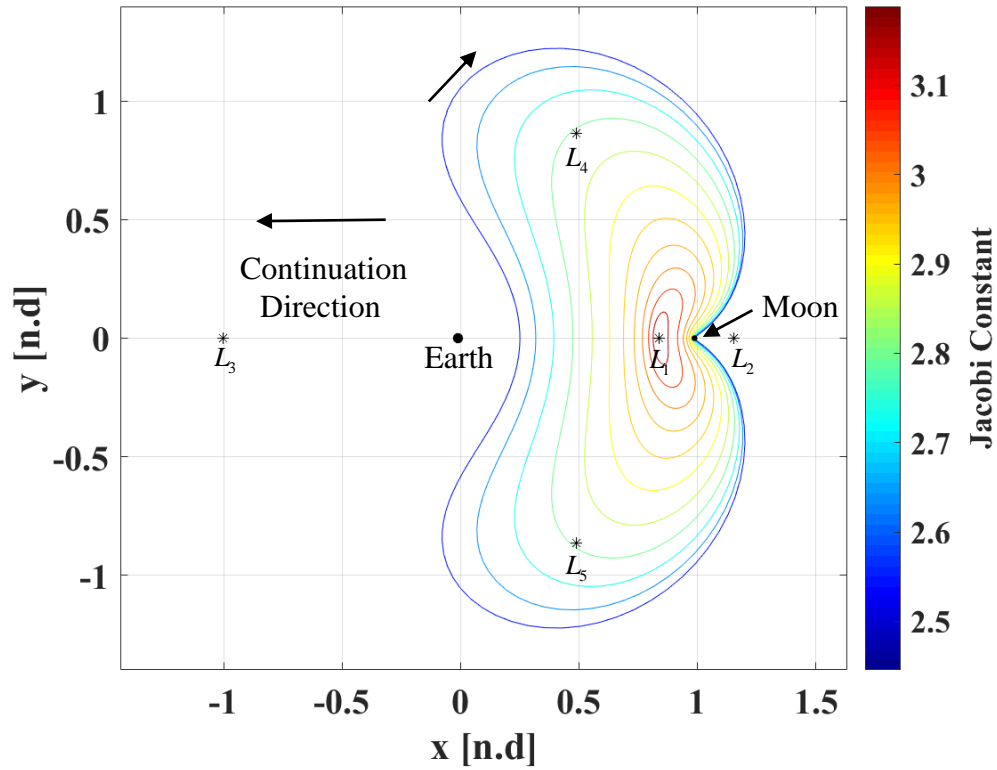


Figure 3.4. L_1 Lyapunov family.

with a multiple shooting algorithm is used in the remaining part of this analysis to generate all the periodic orbit families.

3.8 Stability of Periodic Orbits

In the previous chapter Lyapunov stability criteria was used to determine the linear stability of equilibrium points which are constant, particular solutions to the CR3BP. The equations of motion were linearized about the libration points and stability was assessed by analyzing the eigenvalues of the linearized system. In this chapter, another kind of particular solution to the CR3BP, i.e., periodic orbits have been computed. Very often in mission design, periodic orbits of certain characteristics are widely used as the final destination orbits for spacecraft missions around other

planets and moons. These periodic orbits are called the stable periodic orbits as the spacecraft once placed in this orbit will remain in its vicinity for a considerably long time even in the ephemeris model. Also the station keeping costs associated with maintaining a spacecraft close to such an orbit is extremely low when compared to an unstable periodic orbit. But recently even unstable periodic orbits have become a very important mechanism for low energy transfers as they possess stable and unstable manifolds which on many occasions help the spacecraft to reach a desired location at a lower cost compared to traditional transfers. Also detecting bifurcations, which is crucial to identify new periodic families is done by analyzing the change in the stability of a periodic orbit family. Hence identifying the stability of a periodic orbit is a very useful design consideration.

Eigenvalues of the Monodromy matrix, $\Phi(t_0 + T, t_0)$, which is a special form of the STM computed over exactly one time period of the periodic orbit [33], are used to assess the linear stability. The computation of the monodromy matrix and its associated eigenvalues are independent of the starting point on the periodic orbit and hence remain the same for all the points on the periodic orbit. Any point on the periodic orbit where the monodromy matrix is calculated is termed as a fixed point, as the periodic orbit always returns to the same states indefinitely after every time period. As the CR3BP is a Hamiltonian time-invariant system, the Lyapunov theorem states that all the six eigenvalues of monodromy matrix always appear in reciprocal pairs [36]. For periodic orbits in CR3BP, there is always a pair of trivial eigenvalues equal to one. The other two pairs of eigenvalues either take real or complex values. As the eigenvalues always appear in reciprocal pairs, the complex pair of eigenvalues is possible only if they lie on a unit circle. The following stability criteria is used to define the stability of periodic orbits:

- **Unstable Eigenvalues:** If any one of the eigenvalue has a magnitude greater than one, i.e., $|\lambda_i| > 1$ then it is termed as an unstable eigenvalue. This implies that after one time period of the periodic orbit, a state on an unstable eigen-

vector corresponding to the monodromy matrix of the fixed point diverges away from the fixed point along the unstable eigenvector by a factor of $|\lambda_i|$.

- **Stable Eigenvalues:** If an eigenvalue has a magnitude less than one, i.e., $|\lambda_i| < 1$, then it is called a stable eigenvalue. This means that after one time period of the periodic orbit, a state on a stable eigenvector corresponding to the monodromy matrix of the fixed point arrives closer to the fixed point along the stable eigenvector by a factor of $|\lambda_i|$.
- **Marginally Stable Eigenvalues:** If the magnitude of the eigenvalue is equal to one, i.e., $|\lambda_i| = 1$, then it indicates marginal stability.

A periodic orbit is deemed unstable if the magnitude of at least one eigenvalue is greater than one. A periodic orbit is deemed stable if the magnitudes of all the eigenvalues are less than one. And finally, a periodic orbit is said to be marginally stable if the magnitudes of all the eigenvalues of the monodromy matrix are equal to one. Because eigenvalues are reciprocal in the CR3BP, every stable eigenvalue is accompanied by a corresponding unstable eigenvalue. Hence in the CR3BP only unstable and marginally stable periodic orbits are known to exist. The stability regions are depicted with the help of a diagram shown in figure 3.5. Eigenvalues only lie on the unit circle or the real axis. Unstable eigenvalues lie on the real axis beyond the unit circle on both sides. Marginally stable eigenvalues lie on the unit circle, and the stable eigenvalues lie on the real axis inside the unit circle.

Another simplified term called the stability index is introduced to represent the stability of the periodic orbits. It is defined as follows,

$$\nu = \frac{1}{2}(\lambda_i + \frac{1}{\lambda_i}) \quad (3.34)$$

Where λ_i corresponds to the eigenvalue of the monodromy matrix. Any periodic orbit is associated with three stability indices corresponding to the three reciprocal pairs of eigenvalues. Therefore unstable periodic orbits have one of the stability indices

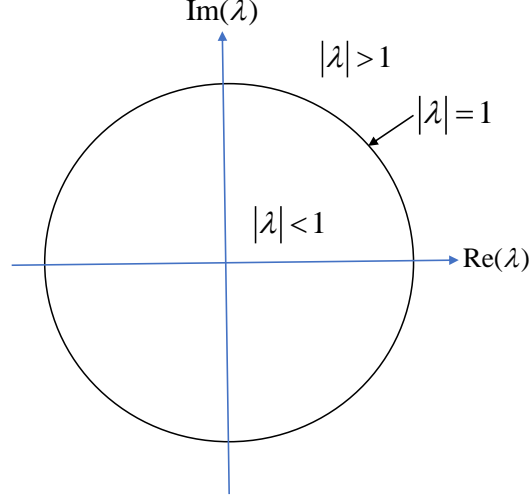


Figure 3.5. Periodic orbit stability regions.

greater than one and marginally stable periodic orbits have all the stability indices equal to one. Let us consider the Lyapunov orbit constructed in section 3.6. A point on the periodic orbit where it crosses the \hat{x} -axis in the positive direction is chosen to be the fixed point for the computation of the monodromy matrix. The value of the monodromy matrix is given as follows,

$$\Phi(t_0+T, t_0) = \begin{bmatrix} 1585.228539 & -277.71404 & 0 & 415.445474 & 186.418073 & 0 \\ -711.937507 & 125.615431 & 0 & -186.418073 & -83.774963 & 0 \\ 0 & 0 & 0.984538 & 0 & 0 & -0.078030 \\ 4626.347507 & -809.782991 & 0 & 1212.392392 & 544.387581 & 0 \\ -2109.443224 & 369.783773 & 0 & -553.176906 & -247.220716 & 0 \\ 0 & 0 & 0.393240 & 0 & 0 & 0.984538 \end{bmatrix} \quad (3.35)$$

The eigenvalues of the monodromy matrix are computed to be,

$$\begin{aligned}
\lambda_1 &= 2674.015272 \\
\lambda_2 &= 0.000374 \\
\lambda_3 &= 1 \\
\lambda_4 &= 1 \\
\lambda_5 &= 0.984538 + 0.175170i \\
\lambda_6 &= 0.984538 - 0.175170i
\end{aligned} \tag{3.36}$$

As expected two eigenvalues are equal to one which indicates that the orbit is periodic and it belongs to a family of Lyapunov orbits. Two eigenvalues are real with one being greater than one and the other being less than one. The remaining two eigenvalues are complex conjugates and lie on the unit circle. Thus the three stability indices are given as,

$$\begin{aligned}
v_1 &= 1337.007823 \\
v_2 &= 1 \\
v_3 &= 0.984538
\end{aligned} \tag{3.37}$$

Hence, according to the linear stability criteria, the Lyapunov period orbit is unstable. Now the stability of all the Lyapunov periodic orbits computed in the previous section is calculated, and their stability index is computed and plotted with respect to their positive \hat{x} -axis crossing in figure 3.6 and 3.7. From these figures, it is observed that the in-plane stability index ν_1 first decreases with x reaches a local minimum and then starts increasing. It never crosses the stability bounds $+/-1$ indicated by blue lines. On the other hand, the out of plane stability index ν_3 initially increases reaches a maximum and then continuously decreases for the rest of x -coordinates. Also, stability index ν_3 crosses the stability boundary thrice, two times at $+1$ and one time at -1 . The trivial stability index ν_2 is always equal to one for all the periodic orbits in the family.

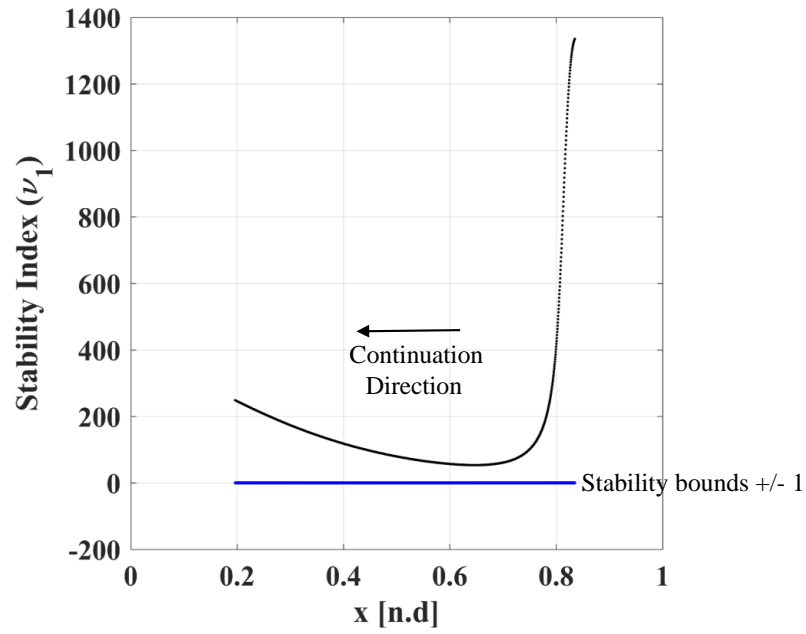


Figure 3.6. L_1 Lyapunov family - In-plane Stability index ν_1 .

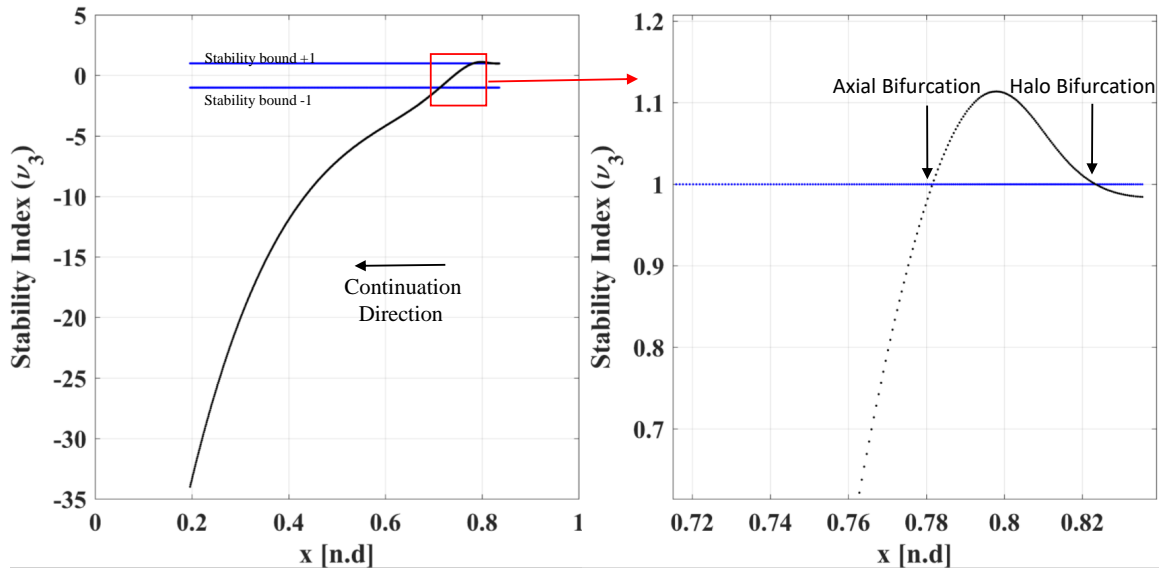


Figure 3.7. L_1 Lyapunov family - Out-of-Plane stability index ν_3 .

3.9 Bifurcations

Consider the family of L_1 Lyapunov orbits in figure 3.4. The stability indices are plotted in the figures 3.6 and 3.7. Orbits within the family are unstable as one of their stability index ν_1 is always greater than one. As the energy of the Lyapunov family increases, i.e., as the size of the family increases, at one particular \hat{x} -axis positive crossing, the stability index ν_3 changes from being marginally stable to unstable as the stability index of the corresponding pair of eigenvalues crosses the boundary on unit circle at one. This qualitative change in the stability of the eigenvalues within a periodic family is called a Bifurcation [37]. The implication of bifurcation is that new periodic orbit family may arise from the bifurcation point or an existing periodic orbit family may end at a bifurcation point. Depending upon the direction of change of the stability index two types of bifurcations are predominantly identified in CR3BP. They are tangent bifurcations and period multiplying bifurcations.

- **Tangent Bifurcation:** When the stability index of a pair of eigenvalues crosses $\nu = 1$, then it is termed as a Tangent Bifurcation. In Figure 3.7 tangent bifurcations occur at points indicated by arrows, i.e., the Halo and Axial bifurcations. On the corresponding stability diagram in figure 3.8(a) the eigenvalues cross the unit circle at $x = 1$, i.e., they jump from the unit circle to the real axis or vice versa. Usually, new periodic families emerge from the existing family when such a bifurcation is encountered. This is the most dominant bifurcation encountered in the following chapters.
- **Period Multiplying Bifurcation:** At the location where period multiplying(m) bifurcation takes place periodic orbits of period mq intersect the orbit family of period q . They are indicated when the stability index of the eigenvalues cross the $(m - 1)$ th complex root of unity as indicated in figure 3.8(b). More details about this bifurcation are discussed by Bosanac [37].

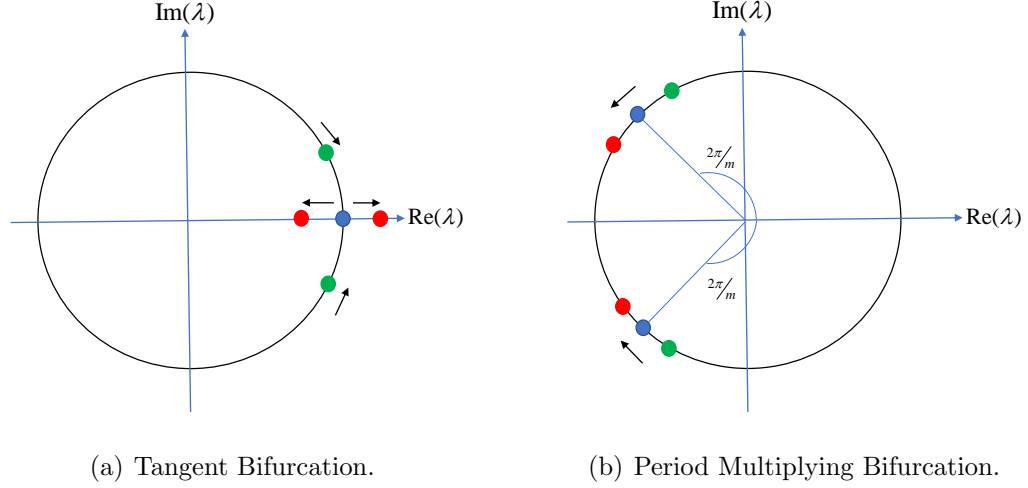


Figure 3.8. Types of Bifurcations.

3.10 3D Periodic Orbit Families

The CR3BP has several spatial, 3D periodic orbits in addition to the planar, 2D periodic orbits computed and shown in the section 3.7.2, in the vicinity of the libration points. Halo orbits are one such kind which originates from the first bifurcation point of the Lyapunov orbits as seen in figure 3.9. The bifurcating orbit is thus common to both the Halo and Lyapunov families. They were first discovered by Robert Farquhar in 1968. Since then a lot of researchers have contributed to numerically computing and extending the families to their full size around the three Libration points L_1 , L_2 and L_3 . Space missions like International Sun-Earth Explorer 3 (ISEE 3) [14] and Solar and Heliospheric Observatory (SOHO) [38] have used L_1 Halo orbits as the primary mission trajectory. The term halo was coined because most of these orbits have a continuous earth coverage from the far side of the moon and appear to revolve around the moon in the form of a halo when viewed in the Earth-Moon direction [25].

Halo orbits are symmetric about the \hat{x} - \hat{z} plane. Therefore, similar to Lyapunov families, they are numerically computed using the Mirror theorem as discussed previously. Consider once again the L_1 Lyapunov family. Starting from the first orbit close

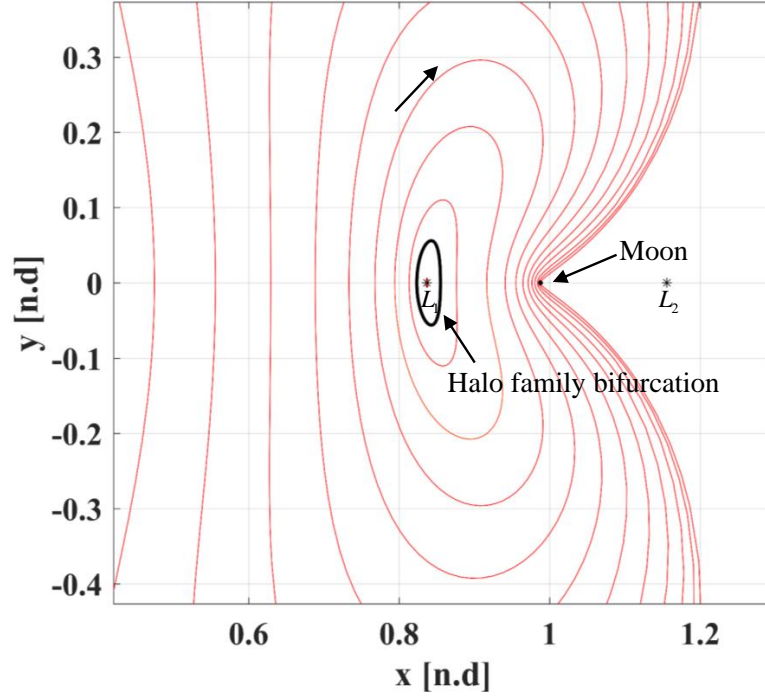


Figure 3.9. L_1 Lyapunov family - Halo family bifurcation.

to L_1 Libration point, a pseudo-arclength continuation is used to generate guesses for new members of the family and a multiple shooting technique is employed to differentially correct the guess to a periodic trajectory. While implementing the pseudo-arclength process, a new guess is obtained by moving along the tangential direction to a previously converged Lyapunov orbit. This is done by stepping along the null vector of the DF matrix as shown in equation (3.31). At the Halo orbit bifurcation point in figure 3.9 there are two directions in which the Lyapunov orbit can move and hence there are two null vectors of the DF matrix in the pseudo-arclength method at the bifurcating orbit. Obtaining the exact bifurcating orbit is not numerically possible hence a bisection method is used to get as close as possible. There are two tangential directions in this orbit given by the two null vectors of the DF matrix. One tangent is in the direction of the Lyapunov family, and the other tangent is in the direction of the Halo family. The tangent vector along the Halo family has non zero components in the spatial \hat{z} -direction and the tangent vector along the Lyapunov family has zero

components in the spatial direction. Halo orbits close to the bifurcating point have approximately the same time periods as the Lyapunov bifurcating orbit. The initial conditions for the first halo orbit are obtained by incrementing the free variable design matrix of the bifurcating Lyapunov family along the halo family direction by a scalar value $\Delta\bar{X}$. The step are taken in two possible directions on the tangent vector. Moving along the positive \hat{z} -direction results in a Northern Halo family and stepping along the negative \hat{z} -direction results in a Southern Halo family.

As Mirror theorem is used to correct the halo orbits, the initial condition is propagated for half the time period of the Lyapunov orbit at the bifurcation point. The resulting orbit is not periodic, and it forms the guess for the differential corrections process. The next important step is to formulate the constraint vector. As the Halo orbit crosses perpendicularly at the \hat{x} - \hat{z} plane the y , \dot{z} and \dot{x} components at the first and the last point on the trajectory have to be zero. Also, similar to Lyapunov orbits the halo orbits are computed by fixing one of the initial variables x_0 or z_0 at the \hat{x} - \hat{z} plane crossing. On implementing the corrections process, the initial guess converges to the desired Halo Orbit with initial conditions of the type,

$$\bar{x}_0 = \left\{ x_0 \quad 0 \quad z_0 \quad 0 \quad \dot{y}_0 \quad 0 \right\} \quad (3.38)$$

During the formulation of the initial guess, if the step along the tangent was taken in the opposite direction then a Southern Halo orbit is obtained with the following initial conditions,

$$\bar{x}_0 = \left\{ x_0 \quad 0 \quad -z_0 \quad 0 \quad \dot{y}_0 \quad 0 \right\} \quad (3.39)$$

Notice that only the z component in the initial conditions is opposite to each other. The rest of the components are the same, and hence the energy of the orbits or their Jacobi constants are equal. Once a Northern/Southern halo orbit is computed other members of the halo family are extended similar to the Lyapunov family by a pseudo-arclength continuation method and are shown in the figure 3.10 and 3.11. The Halo orbits first start closer to the libration point and are nearly planar. As the family

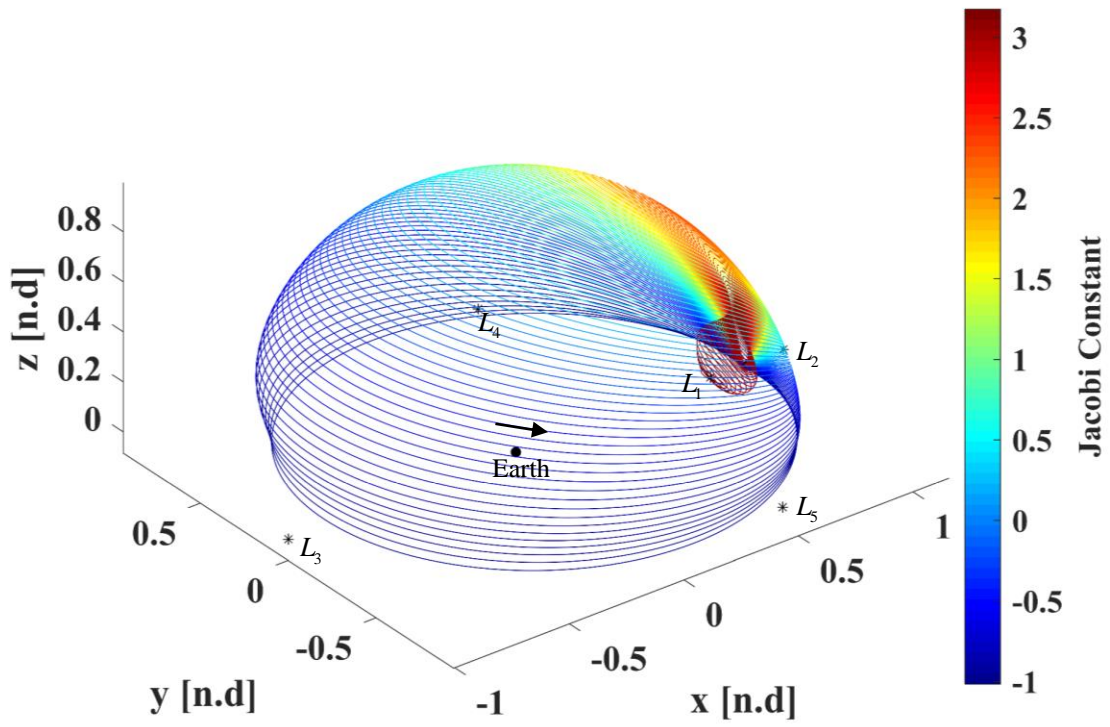


Figure 3.10. L_1 Northern Halo family.

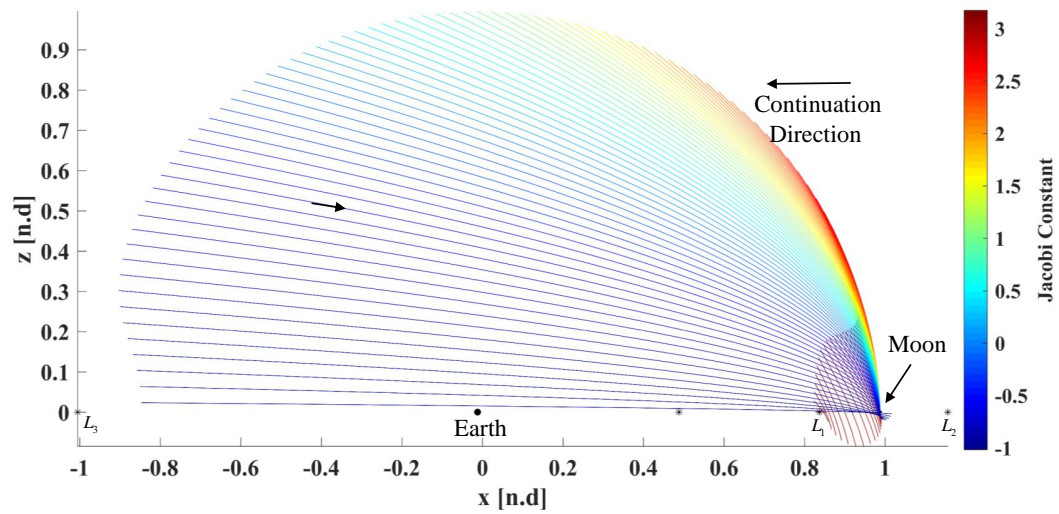


Figure 3.11. L_1 Northern Halo family projected on \hat{x} - \hat{z} plane.

grows, the halo orbits become more out of plane, and they reach a point when they are almost rectilinear and predominantly exist in the \hat{y} - \hat{z} plane. These highly out of plane Halo orbits are called Near Rectilinear Halo Orbits. On further extension the Halo orbits grow larger and go all the way across to the larger primary and connect to the Southern Halo family. Halo orbits have been found to exist around the other collinear libration points and across all values of μ . A similar technique is used to generate the L_2 and L_3 halo families. Halo orbits are being increasingly considered for various practical mission design applications.

4. RESONANT ORBITS AND POINCARÉ MAPS

One of the primary foci of this investigation is to explore the use of resonant orbits and their manifolds as a tool for multi-body trajectory design. This chapter gives the necessary background in resonant orbits. The concept of resonances is introduced in the two-body problem. Then, two types of resonant orbits in CR3BP are discussed followed by techniques to compute various resonant families. Stability of resonant orbits is analyzed which will help in detecting bifurcations and spatial resonances. Invariant manifold theory will be introduced for both equilibrium points and unstable periodic orbits. Numerical techniques for the computation of manifolds for unstable resonant orbits is described. And finally, a preliminary design technique for dimensional reduction in the CR3BP in the form of Poincaré mapping technique will be described.

4.1 Concept of Resonance

Resonant phenomena are ubiquitous in the solar system. They appear in both the Sun-Planet and Planet-Moon models throughout the solar system in various forms. Typically, the following types of resonances are observed:

- **Orbit-Orbit Resonances** (Mean-motion or Laplace Resonance): Consider two bodies A and B of arbitrary masses rotating around a common central body. Let the orbital time periods of the two bodies be given as T_A and T_B respectively. A mean-motion resonance is said to exist between the two bodies whenever their time periods are in a simple integer ratio of $p : q$ [39]. Here p corresponds to the orbital period of body B and q corresponds to the orbital period of body A. In other words, p relates to the frequency of rotation of body A and q relates to the frequency of rotation of body B around the central body.

In the solar system, an example of this kind of resonance is observed in the Sun-Pluto-Neptune system. Pluto and Neptune are in a 2:3 orbital resonance about the Sun. This indicates that Pluto revolves around the sun two times, at the same time during which Neptune completes three revolutions around the Sun. Depending upon the configuration of the two bodies, mean-motion resonance can stabilize or destabilize the system. When mean-motion resonance occurs between three or more bodies it is termed as the Laplace resonance. In the solar system a very famous example of Laplace resonance is the Io-Europa-Ganymede motion around Jupiter. The three moons are in a simple mean-motion resonance ratio of 4:2:1. The ratio means that Io which is the closest moon to Jupiter completes four revolutions around Jupiter at the same time during which Europa completes two revolutions and Ganymede completes one orbital revolution around Jupiter respectively.

- **Spin-Orbit Resonance:** This type of resonance occurs when there exists a simple integer ratio between the time period of rotation and the orbital time period corresponding to a single body [39]. The most popular example is the Moon, which has a spin-orbit resonance ratio of 1:1. This means that the time taken by the moon to complete one rotation about its spin axis is equivalent to the time taken by it to complete one orbital revolution around the Earth. Because of this phenomenon, Moon is tidally locked to the Earth and only one side of the Moon faces the Earth at any given time.
- **Secular Resonance:** This type of resonance occurs when the precession of two orbits(perihelion or ascending node) are in an integer ratio with each other [39]. Over long durations a secular resonance will change the eccentricity and inclination of the small body in resonance with the larger body.

In this investigation Orbit-Orbit resonances are first described in the two-body problem. The two-body resonances are then used as initial guesses to compute corresponding resonances in the CR3BP, but with a slightly modified definition.

4.1.1 Resonances in Two-Body Model

Consider the relative Earth-Moon two-body dynamical system. Mass of the moon is considered to be negligible with respect to the Earth and hence does not influence the motion of the Earth. Moon is assumed to move in a circular orbit, with Earth at the center with the following two-body orbital parameters as shown in table 4.1. Now, consider a spacecraft in the system to be in a $p : q$ mean-motion resonance

Table 4.1. Two-Body orbital parameters of Moon.

Parameter	Value
Semi-major axis (a)	385692.5 km
Orbital Eccentricity	0
Orbital Inclination	0 degrees
Sidereal Time period (T_q)	27.59 days
Gravitational Parameter (GM_{2B})	398600.43 km ³ /s ²

with the Moon. This implies that the spacecraft completes p revolutions around the Earth at the same time that the Moon takes to complete q orbital revolutions. This is written in the following way,

$$\frac{p}{q} = \frac{n_p}{n_q} = \frac{\frac{1}{T_p}}{\frac{1}{T_q}} = \frac{T_q}{T_p} \quad (4.1)$$

where n_p and n_q are mean motions of the satellite and the Moon respectively. Thus the resonance ratio $p : q$ is nothing but the inverse ratio of orbital periods of the Moon and the satellite. From the two-body equations, mean motion of a conic is only a function of its semi-major axis and is written as,

$$n = \sqrt{\frac{GM_{2B}}{a^3}} \quad (4.2)$$

where G is the universal gravitational constant, M_{2B} is the mass of the central body and a is the semi-major axis of the secondary body. Substituting equation 4.2 into

equation 4.1 gives the relationship between the semi-major axis of the spacecraft and the moon in a $p : q$ resonance to be,

$$\frac{n_p}{n_q} = \sqrt{\frac{a_q^3}{a_p^3}} = \frac{T_q}{T_p} \quad (4.3)$$

As the semi-major axis of the Moon is known, substituting it in equation 4.3 results in the equation for the semi-major axis of the spacecraft and is given as,

$$a_p = \left(\frac{T_p^2 a_q^3}{T_q^2} \right)^{\frac{1}{3}} \quad (4.4)$$

Now consider a spacecraft which is in a 2:1 mean motion resonance with the Moon. According to equation 4.4, this resonance is feasible if the semi-major axis of the spacecraft is 242971.05 km . Once the semi-major axis is known, the initial condition for the corresponding elliptical trajectory of the spacecraft with Earth at one of its focus can be chosen in an infinite number of ways. For the purposes of simplification, it is assumed without loss of generality that the spacecraft always starts from the \hat{x} axis at an apse location, i.e., either from a state of periapsis or apoapsis, and has the same angular momentum direction as the Moon. Let the spacecraft begin at a distance 115707.75 km ($0.3 \times a_{Moon}$) on the \hat{x} axis which is in between the Earth and the Moon. The above assumptions results in a simplified initial condition for the spacecraft,

$$\begin{aligned} X_0(km) &= 115707.75 \\ Y_0(km) &= 0 \\ \dot{X}_0(km/s) &= 0 \\ \dot{Y}_0(km/s) &= V_p \end{aligned} \quad (4.5)$$

The starting location of the spacecraft is a periapsis since its distance from the earth X_0 is less than its semi-major axis a . The velocity of the spacecraft at the periapsis V_p is calculated by the following two-body relation,

$$V_p = \sqrt{2(GM)_{2B} \left(\frac{1}{X_0} - \frac{1}{2a} \right)} \quad (4.6)$$

The eccentricity and the semiperimeter of the conic traced by the spacecraft is further found using the following equations,

$$p = a(1 - e^2) \quad (4.7)$$

$$X_0 = \frac{p}{1 + e} \quad (4.8)$$

The combined orbital parameters of the spacecraft are non-dimensionalized using the two-body characteristic quantities, and the orbit corresponds to an ellipse as shown in the inertial frame indicated by the red color in figure 4.1. Notice, the spacecraft has the same direction of angular momentum as the Moon along the positive \hat{z} -direction. When the spacecraft starts at another location on the \hat{X} axis, the eccentricity of its elliptic trajectory changes but its time period and semi-major axis remain unaltered. This is because in the two-body problem the spacecraft needs to have a constant time period of $T_p = T_q/2$ in order to stay in 2 : 1 resonance with the Moon.

Observing the motion of the spacecraft in the Earth-Moon rotating frame helps in obtaining a better insight into the problem. The rotating frame has the \hat{x} -axis in the Earth-Moon direction, \hat{z} -axis points in the direction of angular momentum and \hat{y} -axis completes the right-hand rule. Using the direction cosine matrix developed in equation 2.48, the inertial 2:1 resonant spacecraft trajectory as seen in figure 4.1 is converted into the Earth-Moon rotating frame and appears in figure 4.2. Earth and the Moon are indicated at the x -coordinates 0 and 1 respectively. The view in the rotating frame highlights the conjunctions between Earth, spacecraft and the Moon [39]. A conjunction occurs whenever all the three bodies fall along the same line. In the rotating frame, this happens whenever the spacecraft intersects the \hat{x} -axis. Since at $t = 0$ both the spacecraft and the Moon start on the \hat{X} -axis in the inertial frame, they correspond to a conjunction and are seen to be aligned along the

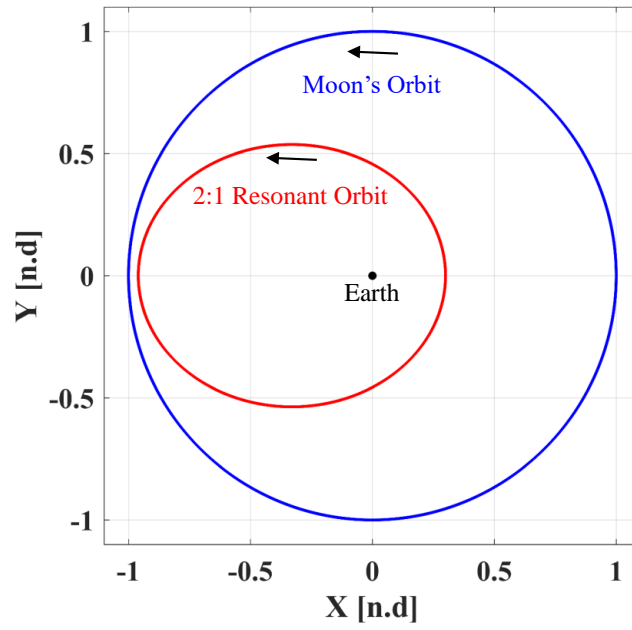


Figure 4.1. Two-body 2:1 resonant orbit in the EM-inertial frame.

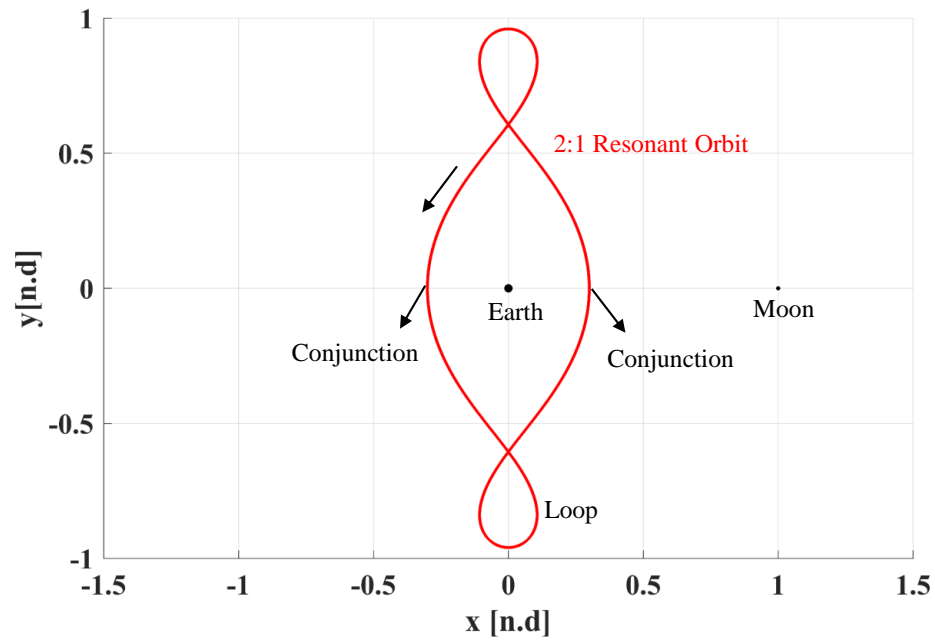


Figure 4.2. Two-body 2:1 resonant orbit in the EM-rotating frame.

\hat{x} -axis in the rotating frame. One unique feature which is observed in the rotating frame is the formation of loops, which occur due to the changes in the relative angular velocity between the spacecraft and the rotating frame. The number of loops indicate the integer p in the resonance ratio $p : q$. In the above example of a 2:1 mean-motion, two loops are observed in the rotating frame. In general, resonances are broadly classified into two kinds:

- **Exterior Resonances:** Have an integer ratio of $p : q$ such that $p < q$. The spacecraft spends a majority of the time outside the vicinity of the Moon as it has a larger orbital period/semi-major axis compared to the Moon.
- **Interior Resonances:** Have an integer ratio of $p : q$ such that $p > q$. The spacecraft spends a majority of the time inside the orbit of the Moon as it has a smaller orbital period/semi-major axis compared to the Moon.

4.1.2 Resonances in CR3BP

In the CR3BP, due to the gravitational influence of both the larger and the smaller primaries, both the definition and computation of resonant orbits is not similar to the two-body model. The initial conditions, which seed a resonant periodic orbit in the two-body model, when propagated in the CR3BP dynamical system does not necessarily produce a periodic orbit. Applying a differential corrections process on the non-periodic trajectory produces a periodic orbit with a time period approximately equal to that of the two-body resonant orbit. The corrected periodic orbit is the two-body equivalent resonant orbit in the CR3BP. Thus, the ratio of the time periods is not a simple integer but an approximate rational number [22]. Like any other periodic orbit in the CR3BP, the resonant orbit also belongs to a family of periodic orbits. These resonant periodic families are computed using a numerical continuation scheme. The next section describes the method for computing resonant families in CR3BP, assessing their stability and identifying bifurcations to generate spatial resonant orbits. The second category of resonant orbits found in the CR3BP is the

libration point periodic orbits which are in resonance with the smaller primary. In the Earth-Moon system, specific libration point orbits (LPOs) are in resonance with either the synodic or sidereal time-period of the Moon. These libration point orbit resonances will be discussed in the next chapter.

Two-body Equivalent Resonances in CR3BP

Recall the Earth-Moon two body dynamical system. The Moon is assumed to be massless and therefore does not perturb the resonant orbit. This causes the resonant orbit to have a constant time period and thereby the resonance ratio remains an exact integer. In the CR3BP, the smaller primary has a gravitational influence on the third body and thus perturbs its motion. Therefore, when the initial conditions of the two-body resonant orbit are integrated using the nonlinear equations of motion in the CR3BP for one resonant time period, the resulting solution is no longer a closed periodic trajectory. The steps implemented to generate a periodic resonant orbit in the CR3BP are as follows:

1. In the two-body model, a $p : q$ resonant orbit is computed in the inertial frame with the dimensional initial conditions of the type,

$$\bar{X}_0^I = \left\{ X_0 \text{ km} \quad 0 \quad 0 \quad 0 \quad \dot{Y}_0 \text{ km/s} \quad 0 \right\}$$
as discussed in subsection 4.1.1. Note that in the two-body inertial frame the Earth is at the origin.
2. In the two-body model, transform the dimensional states from the inertial frame to the rotating frame using the DCM in equation (2.48). Note that in the two-body rotating frame Earth is at the origin.
3. Convert the dimensional, two-body, rotational initial conditions to the three-body equivalent rotational, non-dimensional states by multiplying them with the CR3BP characteristic quantities in equation (2.8) - (2.10) and shifting the coordinates such that the Earth-Moon barycenter is at the origin.

4. Propagate the three-body equivalent, non-dimensional, rotating frame initial conditions of the resonant orbit using the nonlinear equations of motion of the CR3BP for exactly one time period of the resonant orbit.
5. It is observed that even though the trajectory maintains its shape, it is no longer periodic and does not cross the \hat{x} -axis perpendicularly. Similar to other symmetric periodic orbits in the CR3BP, Mirror theorem is used to target two perpendicular crossing at \hat{x} -axis to generate a periodic trajectory. Therefore, only half of the propagated trajectory is considered as the initial guess during the differential corrections process.
6. As a part of the multiple shooting corrections process, discretize the trajectory into sub-arcs by distributing patch points along the trajectory. Once the trajectory is discretized formulate the necessary free variables and constraint vectors to target perpendicular crossings at the beginning and the end of the initial guess trajectory.
7. The complete $p : q$ resonant periodic orbit is obtained in the CR3BP by reflecting the corrected trajectory about the \hat{x} -axis.

The time period of the resulting resonant periodic orbit in the CR3BP is approximately equal to the actual time period of the resonant orbit in the two-body model and therefore the ratio $p : q$ is no longer a perfect integer. Sometimes depending upon the resonance type, the orbit crosses the \hat{x} -axis multiple times. In such situations the perpendicular crossings must be suitably targeted at the right locations on the trajectory.

To illustrate the above algorithm consider the 2:1 resonant orbit discussed in section 4.1.1. The dimensional initial conditions for the orbit in the inertial frame in the two-body model are as follows,

$$\bar{X}_0^I = \left\{ 115707.75 \text{ km} \quad 0 \quad 0 \quad 0 \quad 2.291125 \text{ km/s} \quad 0 \right\} \quad (4.9)$$

Theses conditions when converted to dimensional, rotating frame coordinates in the two-body model using the DCM in equation (2.48) results in,

$$\bar{X}_0^R = \left\{ 115707.75 \text{ km} \quad 0 \quad 0 \quad 0 \quad 1.198146 \text{ km/s} \quad 0 \right\} \quad (4.10)$$

In the next step, the conditions in 4.10 are converted to the CR3BP equivalent, rotating, non-dimensional coordinates as the following,

$$\bar{x}_0^R = \left\{ 0.287849 \quad 0 \quad 0 \quad 0 \quad 1.941817 \quad 0 \right\} \quad (4.11)$$

Notice that in the initial condition given by equation (4.11) the x -coordinate starts at a value less than 0.3 as the barycenter is now located at the origin. Propagating these initial conditions in the CR3BP using the nonlinear equations of motion for half of the original time period results in a black colored trajectory shown in figure 4.3. Observe that the trajectory does not cross the \hat{x} -axis perpendicularly. Now, discretize the trajectory into sub-arcs by distributing patch points along it. A variable time multiple shooting differential corrections algorithm, discussed in the previous chapter is implemented to target perpendicular crossings at the two ends of the trajectory. The corrected nearby trajectory at the same x -coordinate is plotted in red. Notice that the corrected trajectory crosses the \hat{x} -axis perpendicularly and is slightly shifted compared to the initial guess. The non-dimensional, rotational initial conditions of the corrected orbit in the CR3BP are as follows,

$$\bar{x}_{corrected}^R = \left\{ 0.287849 \quad 0 \quad 0 \quad 0 \quad 1.937458 \quad 0 \right\} \quad (4.12)$$

Observe that in the corrected initial condition in equation (4.12), the \dot{y} velocity changes slightly compared to the value in equation (4.11). The resonance ratio is now calculated as,

$$\frac{p}{q} = \frac{T_{Moon}(n.d)}{T_{CR3BP-Resonance}(n.d)} = \frac{2\pi}{3.123303} = 2.011712 \quad (4.13)$$

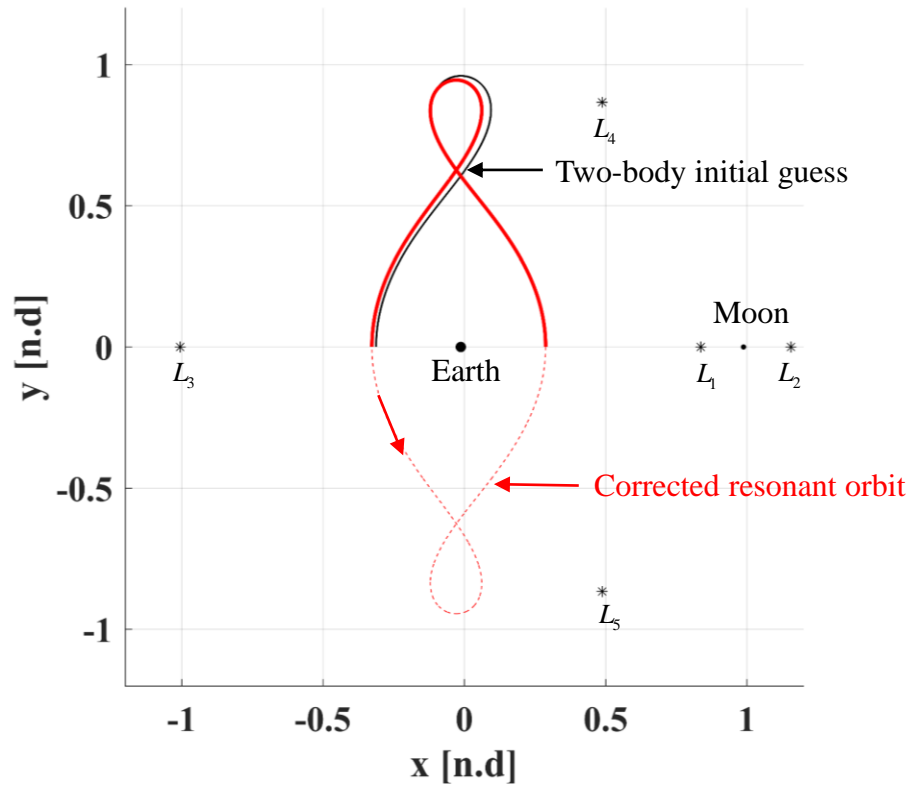


Figure 4.3. 2:1 Resonant orbit correction in the CR3BP.

The new resonance ratio it is not an integer but very close to two. This implies that the time period of the 2:1 resonant orbit in the CR3BP is slightly lesser than the two-body model. Recall that in the CR3BP a single periodic orbit cannot exist in isolation. It belongs to a whole family of periodic orbits which share similar characteristics. Like the Lyapunov families computed in section 3.7.2, pseudo-arclength continuation scheme is used to generate the 2:1 resonant family and is shown in the figure 4.4.

Other examples of exterior and interior resonant orbits in the Earth-Moon model are shown in the figures 4.5 - 4.7. The above algorithm is very robust in generating various exterior and interior resonant orbits alike in different CR3BP systems. A

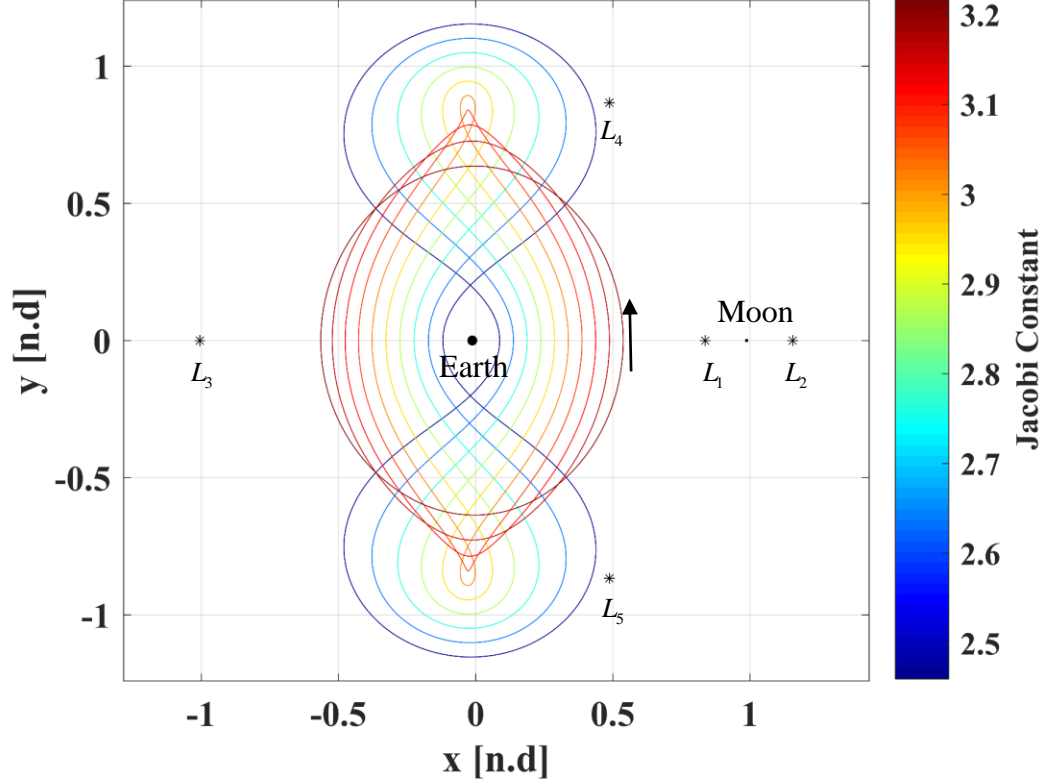
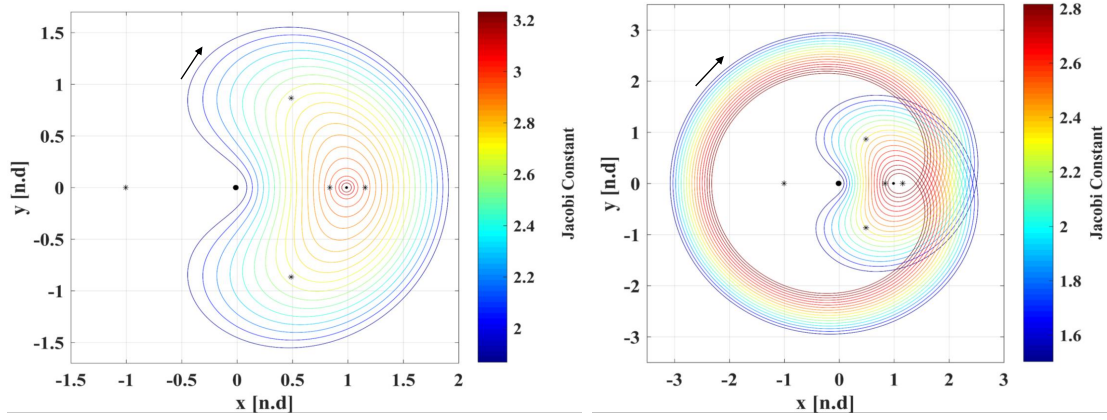


Figure 4.4. 2:1 Resonance family in the Earth-Moon system.

useful alternative technique to generate resonant orbits is to implement a natural parameter continuation process by increasing the mass parameter μ from the two body model, where $\mu = 0$, to the desired μ value of the system. After computing the resonant orbits in the CR3BP, the next important step is it to understand their dynamical behavior and assess their stability.

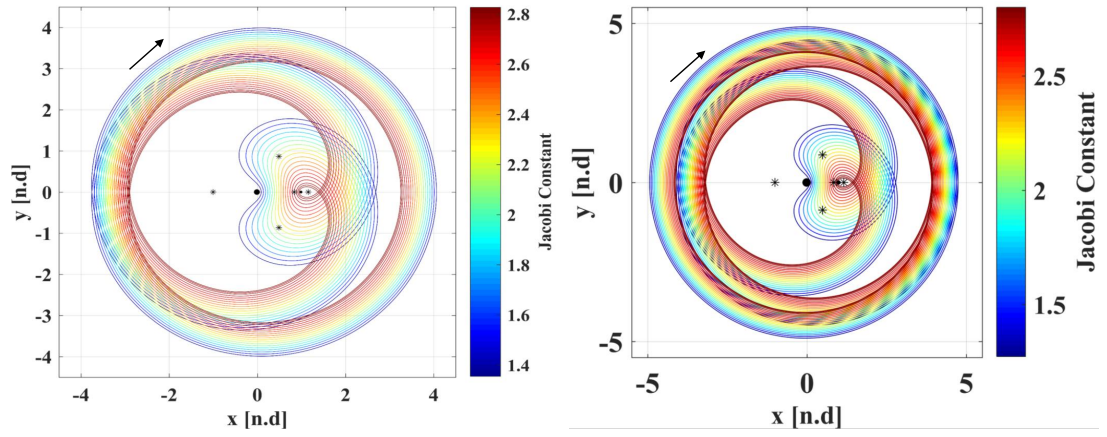
4.2 Stability and Bifurcations of 2D Resonant Orbits

Resonant orbits are used for various purposes in a mission design scenario. Whenever a repeatable behavior is desired in the ephemeris model, stable resonant orbits have been used as primary mission trajectories in the IBEX [3] and the TESS missions [4]. More recently, manifolds of unstable resonant orbits are being leveraged to



(a) 1:1 Resonance.

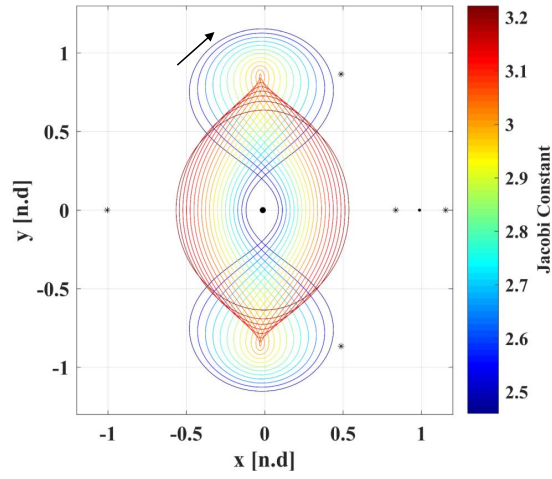
(b) 1:2 Resonance.



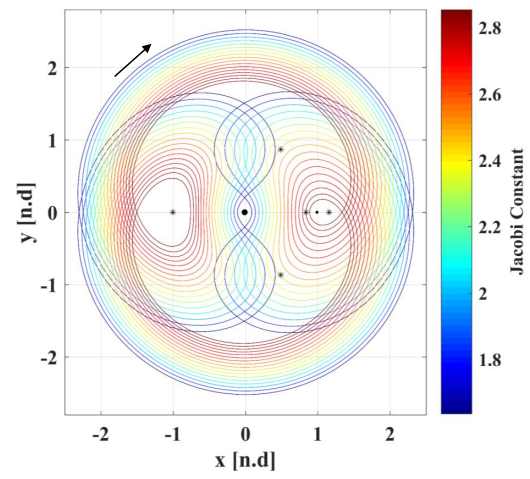
(c) 1:3 Resonance.

(d) 1:4 Resonance.

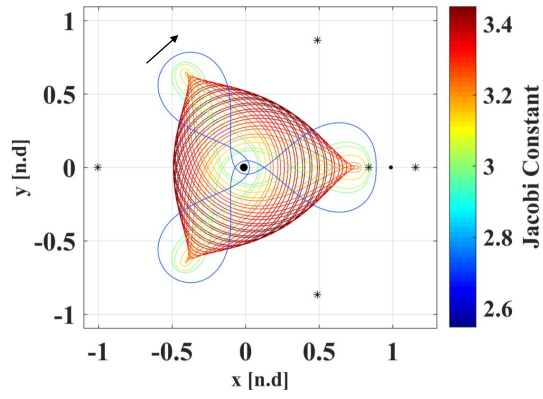
Figure 4.5. 1:1, 1:2, 1:3 and 1:4 planar resonant families.



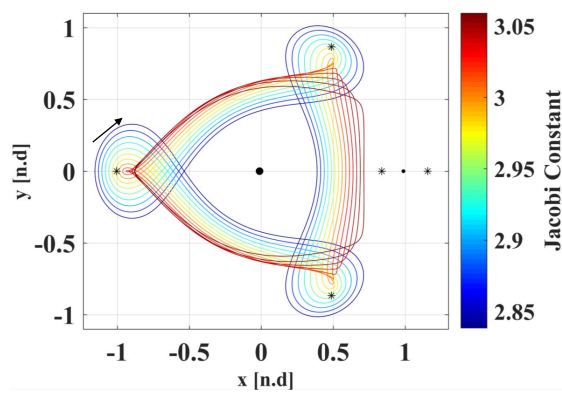
(a) 2:1 Resonance.



(b) 2:3 Resonance.

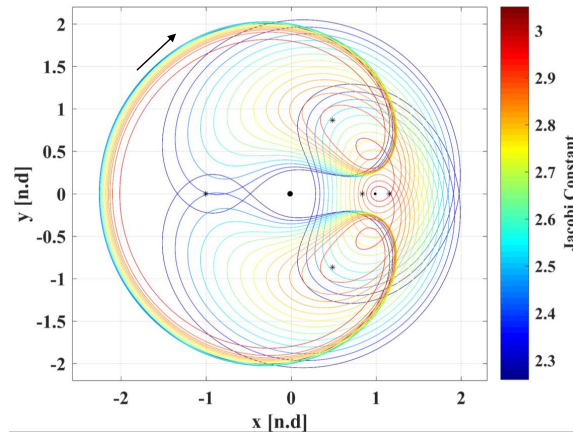


(c) 3:1 Resonance.

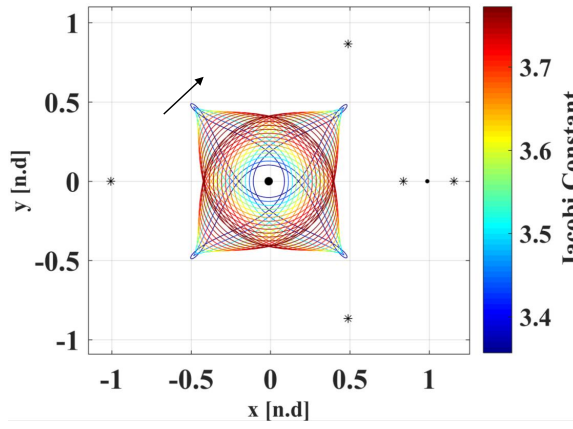


(d) 3:2 Resonance.

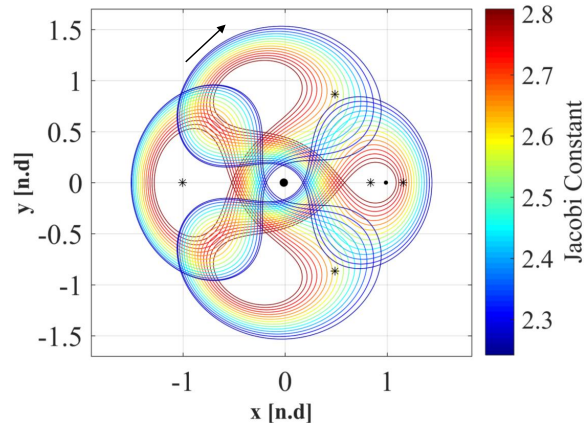
Figure 4.6. 2:1, 2:3, 3:1 and 3:2 planar resonant families.



(a) 3:4 Resonance.



(b) 4:1 Resonance.



(c) 4:3 Resonance.

Figure 4.7. 3:4, 4:1 and 4:3 planar resonant families.

design novel, low energy transfers to various regions within the three-body system. Unlike the manifolds of unstable Lyapunov orbits, the manifolds of resonant orbits will be shown to spread across all five libration point regions. The unstable resonant manifolds also undergo resonance transitions, i.e., they jump from one resonant orbit to another via heteroclinic connections [40]. The Europa-Orbiter trajectory utilizes this phenomenon by closely following the invariant manifolds associated with the 3 : 4 resonant orbit and transitions to a 5 : 6 resonant orbit during a flyby with Europa [41].

The linear stability of resonant orbits is analyzed in a similar way to the Lyapunov orbits discussed in section 3.8. Monodromy matrix is calculated using the STM by integrating the EOMs for exactly one time period of the resonant orbit. Eigenvalues of the computed monodromy matrix are examined and the linear stability is inferred using the periodic orbit stability criteria discussed in section 3.8. Consider the 2:1 resonant orbit in the Earth-Moon CR3BP shown in figure 4.3. The eigenvalues of the monodromy matrix are calculated to be the following,

$$\begin{aligned}
 \lambda_1 &= 0.803070 + 0.595885i \\
 \lambda_2 &= 0.803070 - 0.595885i \\
 \lambda_3 &= 1 \\
 \lambda_4 &= 1 \\
 \lambda_5 &= 0.999426 + 0.033881i \\
 \lambda_6 &= 0.999426 - 0.033881i
 \end{aligned} \tag{4.14}$$

From the above values, notice that being a periodic orbit, two of the eigenvalues are equal to one and the remaining eigenvalues are reciprocal pairs and lie on the unit circle. The stability indices for the pairs of eigenvalues are calculated to be,

$$\begin{aligned}
 v_1 &= 0.803070 \\
 v_2 &= 1 \\
 v_3 &= 0.999426
 \end{aligned} \tag{4.15}$$

As both the stability indices are less than one, and the corresponding magnitudes of eigenvalues are equal to one, the representative resonant orbit is marginally stable. Stability of the family of resonant orbits are analyzed in the similar way. The evolution of the stability for the 2:1 resonance family is plotted in figure 4.8. The in-plane stability index ν_1 is always less than one. The out of plane stability index ν_2 crosses the stability boundary twice. The stability changes occurring at these boundaries indicate a tangent bifurcation as shown in the section 3.9. A spatial resonant family evolves at the bifurcation point in a similar way to that of Halo orbits from a Lyapunov family.

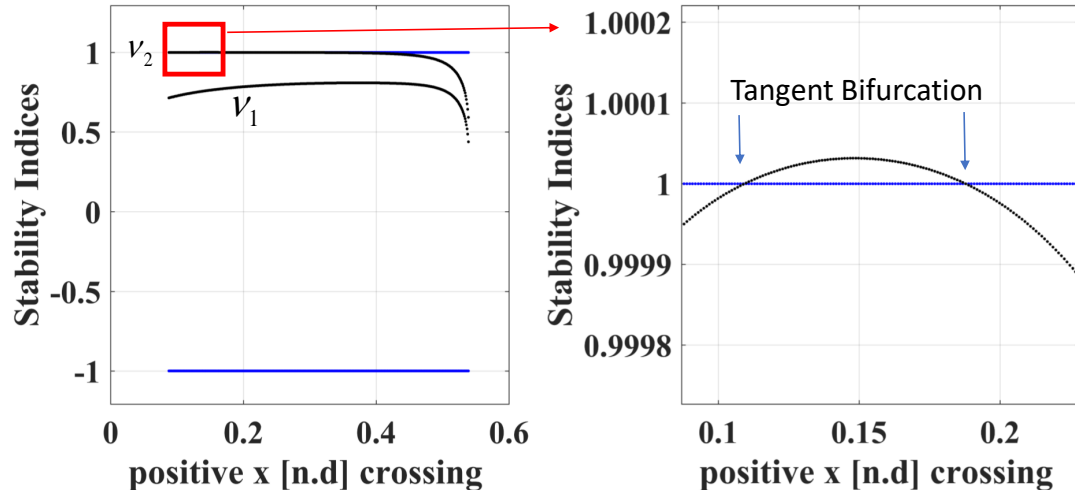


Figure 4.8. Stability Indices of 2:1 resonant family.

4.3 Three Dimensional Resonances

Recall that Halo orbits are three-dimensional periodic orbits emerging from the tangent bifurcations of Lyapunov families. Likewise, three-dimensional resonant orbits emerge from the tangent bifurcation locations on a planar resonant family along the \hat{z} direction. A procedure adopted for the computation of Halo orbits is similarly implemented to generate three dimensional northern/southern resonant orbits. Figures 4.9 - 4.10 represents such 3D southern resonant orbits in the Earth-Moon system.

Northern resonant orbits step off in the positive \hat{z} direction while the southern resonant orbits step off in the negative \hat{z} direction from the tangent bifurcation locations on the planar resonant orbits.

4.4 Invariant Manifold Theory

Solutions to the differential equations of a dynamical system are analyzed in two ways. A first way is a classical approach wherein individual trajectories and their properties corresponding to specific initial conditions are analyzed. This approach does not reveal much information about the global dynamical behavior of the system. The second way is a global, geometrical approach which is based on the phase portrait of a dynamical system. Equilibrium points, periodic orbits, quasi-periodic trajectories, and chaos are four fundamental reference solutions observed in the CR3BP. Linear stability analysis helps to predict the flow of nearby states, in the vicinity of the reference solutions. Both the structure and geometry of phase space of a dynamical system is therefore investigated by considering the reference solution and its associated local flow. The type of local flow nearby the reference solutions are related to the invariant manifold structures surrounding them. Invariant manifold theory for equilibrium points and periodic orbits are detailed in the following sections.

4.4.1 Invariant Manifolds for Fixed points

Consider the equilibrium solutions L_i with the states \bar{x}_L . The phase portrait of the dynamical flow near L_i , i.e., evolution of trajectories with initial conditions near \bar{x}_L , $\bar{x} = \bar{x}_L + \Delta\bar{x}$ is obtained by linearizing the differential equations about the libration point L_i . The linearized system of equations about L_i is given as,

$$\delta\dot{\bar{x}}(\tau) = A\delta\bar{x}(\tau) \quad (4.16)$$

where A is the Jacobian matrix evaluated at the libration point L_i , and is a constant. The behavior of local flow about these points is defined by the characteristic mul-

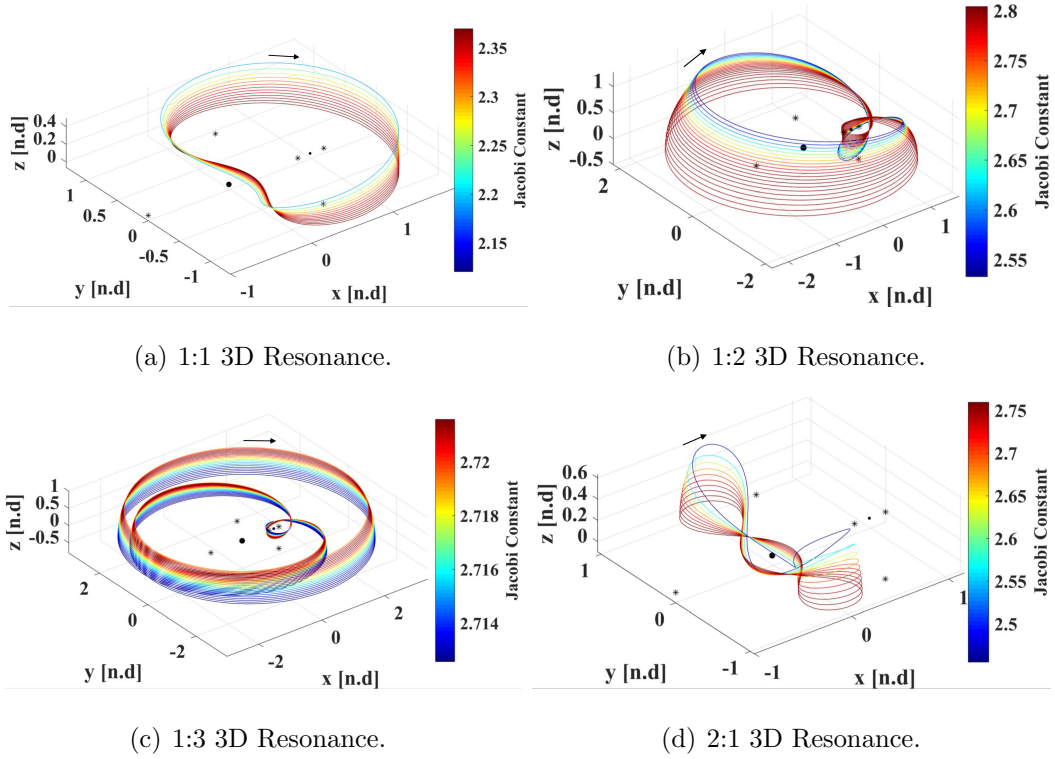
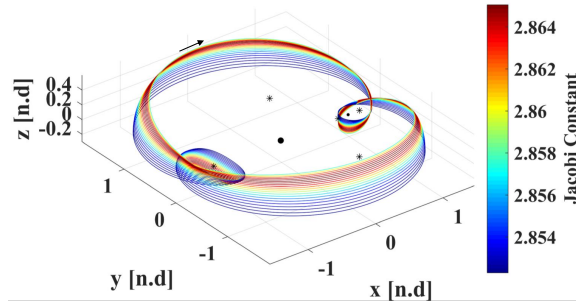
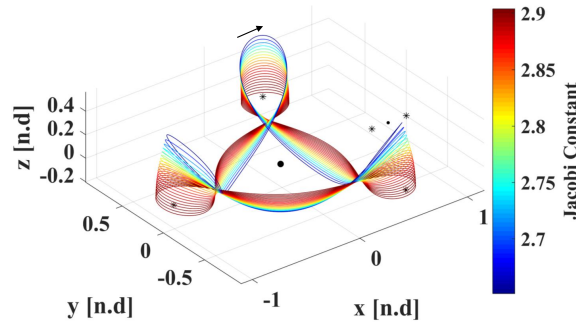


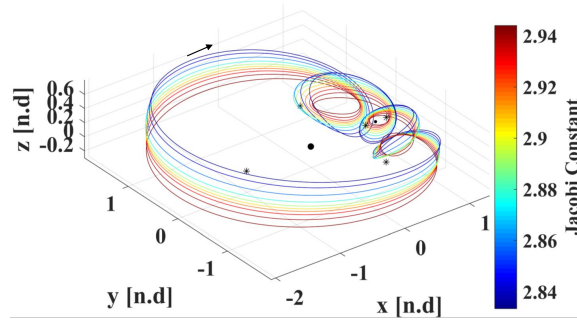
Figure 4.9. 1:1, 1:2, 1:3 and 2:1 spatial resonant families.



(a) 2:3 3D Resonance.



(b) 3:1 3D Resonance.



(c) 3:4 3D Resonance.

Figure 4.10. 2:3, 3:1 and 3:4 spatial resonant families.

multipliers or the eigenvalues of the Jacobian matrix. Assuming there exist n distinct eigenvalues of A that corresponds to n linearly independent eigenvectors which span \mathbb{R}^n , the general solution of initial conditions nearby the libration point is written as,

$$\delta\bar{x}(\tau) = \sum_{j=1}^n c_j e^{\lambda_j(t-t_0)} \bar{v}_j \quad (4.17)$$

where coefficients c_j are determined from the initial state. Linear stability of the libration point is evaluated by analyzing the form of the eigenvalues in the following manner:

1. **Real part of $\lambda_j < 0$ for all λ_j :** Sufficiently small perturbations in the states about the libration points tend to zero as $t \rightarrow \infty$ and the libration point is termed stable.
2. **Real part of $\lambda_j > 0$ for all λ_j :** Any small perturbation about the libration point grows as $t \rightarrow \infty$, and the trajectory eventually escapes the vicinity of the libration point. Hence it is termed an unstable equilibrium point.
3. If λ_i and λ_j exist such that the real parts are both greater and less than zero, then L_i is non-stable, and the point is termed as a saddle point. The small perturbation about L_i escapes the vicinity if the coefficients associated with the unstable eigenvalues are not equal to zero.

Stable or unstable equilibrium points with no complex eigenvalues are termed as nodes. And equilibrium points are called Hyperbolic if all of its eigenvalues possess non-zero real parts [42, 43]. Out of the n distinct eigenvalues of matrix A , let there exist n_s stable eigenvalues, n_u unstable eigenvalues and n_c eigenvalues with zero real parts such that,

$$n = n_s + n_u + n_c \quad (4.18)$$

where n corresponds to the number of states of the dynamical system. Then the eigenvectors associated with each λ are linearly independent, and hence span \mathbb{R}^n . Therefore \mathbb{R}^n is represented in terms of three fundamental subspaces E^s , E^u and E^c . These

three subspaces are called the invariant subspaces of the corresponding linearized system. The term invariant means that when equilibrium states are perturbed along one of the directions of eigenvector subspace, i.e., \bar{v}_s , \bar{v}_u or \bar{v}_c corresponding to the eigenvalues λ_s , λ_u or λ_c respectively, the perturbed states when propagated linearly will remain in the subspace as $t \rightarrow \infty / -\infty$ [44]. This concept is also extended to the nonlinear system, leading to some important definitions:

- **Local stable manifold:** is the set of all initial conditions in the neighbourhood of the libration point L_i at \bar{x}_L , such that the trajectories initiated at these states using the nonlinear differential equations asymptotically approach \bar{x}_L as $t \rightarrow \infty$.
- **Local unstable manifold:** is the set of all initial conditions in the neighbourhood of the libration point L_i at \bar{x}_L such that trajectories initiated at these states using the nonlinear differential equations asymptotically approach \bar{x}_L as $t \rightarrow -\infty$.
- **Local center manifold:** is the set of all initial conditions in the neighbourhood of the libration point L_i at \bar{x}_L such that the trajectories initiated at these states using the nonlinear differential equations neither grow nor decay relative to \bar{x}_L both as $t \rightarrow \infty$ and $t \rightarrow -\infty$.

The relationship between the nonlinear local manifolds and the linear subspaces is given by the stable and center manifold theorems.

Stable Manifold Theorem : Suppose $\dot{\bar{x}}(\tau) = \bar{f}(\bar{x}(\tau))$ possesses a hyperbolic equilibrium point \bar{x}_{eq} . Then, there exists local stable and unstable manifolds of same dimension n_s and n_u as that of the linear eigenspaces E^s and E^u of the linearized system and tangent to E^s and E^u at \bar{x}_{eq} . These local stable and unstable manifolds, $W_{loc}^s(\bar{x}_{eq})$, $W_{loc}^u(\bar{x}_{eq})$ are as smooth as function f [44].

To illustrate the above theorem, consider figure 4.11. \bar{x}_{eq} represents a hyperbolic equilibrium point of a 2D first-order system with two distinct eigenvalues. Eigenvec-

tors \bar{v}_s, \bar{v}_u span the linear stable and unstable subspaces E^s and E^u . Together they form a vector basis in \mathfrak{R}^n . Stable subspace E^s is shown as a line segment along \bar{v}_s and $-\bar{v}_s$. Unstable subspace E^u is defined as the line segment along \bar{v}_u and $-\bar{v}_u$. Local stable and unstable manifolds, $W_{loc}^s(\bar{x}_{eq}), W_{loc}^u(\bar{x}_{eq})$ are seen to be tangent to E^s and E^u respectively at the equilibrium point \bar{x}_{eq} . Global analogs W^s and W^u for the local invariant manifolds $W_{loc}^s(\bar{x}_{eq})$ and $W_{loc}^u(\bar{x}_{eq})$ respectively are generated by propagating the local stable manifolds backward in time and local unstable manifolds forward in time. When \bar{x}_{eq} is a non-hyperbolic equilibrium point, n_s, n_u and n_c are all non-zero. In this case the structure of the local flow is given by the center manifold theorem.

Center Manifold Theorem : Suppose $\dot{\bar{x}}(\tau) = \bar{f}(\bar{x}(\tau))$ posses a non-hyperbolic equilibrium point. Then there exists stable and unstable manifolds W^s and W^u tangent to linear subspaces E^s and E^u and a center manifold W^c tangent to linear center subspace E^c at \bar{x}_{eq} . The manifolds W^s, W^u and W^c are all invariant for the flow \bar{f} . The stable and unstable manifolds are unique but W^c may not be. Initial conditions in W^c neither grow nor decay with time relative to \bar{x}_{eq} . Periodic orbits and quasi periodic trajectories are examples of types of motion that might exist in W^c near \bar{x}_{eq} [44].

4.4.2 Poincaré Maps

Two main types of dynamical systems exist. The first kind are systems of differential equations of the form,

$$\dot{\bar{x}} = \bar{f}(\bar{x}, t) \quad (4.19)$$

an the second kind are maps or mappings of the form,

$$\bar{x}_{n+1} = \bar{f}(\bar{x}_n) \quad (4.20)$$

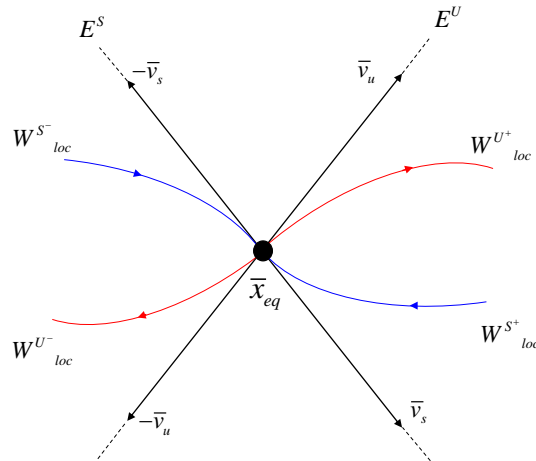


Figure 4.11. Stable and unstable manifolds of an equilibrium point.

Maps describe the time evolution of a state \bar{x} at discrete time intervals $t = n(\text{integer})$. Both the dynamical systems are deterministic in nature. Properties of generic dynamical systems that are described by differential equations can be effectively represented by maps on a Poincaré surface of section. Henry Poincaré first utilized this concept in his studies of the CR3BP. He simplified the study of a chaotic, nonlinear continuous time system to the study of an associated discrete time system in the form of maps [9]. This technique offers the following advantages:

1. **Reduction of dimension:** Converting the continuous time system to a Poincaré map eliminates at least one state variable in the problem resulting in the study of a lower dimensional system.
2. **Better understanding of global dynamics:** In lower dimensional problems, numerically computed Poincaré maps provide an insightful and sometimes, dramatic display of the global dynamics of a system.
3. **Conceptual clarity:** Concepts that may be somewhat cumbersome to state for ordinary differential equations may be succinctly stated for the associated Poincaré map.

The phase space and general dynamics near a reference solution in a CR3BP such as a periodic orbit can be explored using a Poincaré map. Consider an autonomous system defined in n -dimensional phase space as \mathbb{R}^n with an initial condition \bar{x}_0 . The vector field \bar{f} generates a flow $\bar{x}(\bar{x}_0, t)$ or $\varphi_t(\bar{x}_0)$. The mapping $\bar{K}(\bar{x}, t)$ defines a solution curve, orbit, or a trajectory corresponding to the differential equation based at \bar{x}_0 . In phase space, define an $(n - 1)$ dimensional hyperplane Σ such that the flow is transverse to Σ , that is, the trajectory has some component normal to Σ . Now, consider a periodic orbit Γ and assume a state \bar{x}^* lies on it. Hence by definition, Σ is an $(n - 1)$ dimensional hyperplane transversal to Γ at \bar{x}^* . Since \bar{x}^* lies on a periodic orbit, trajectory or flow through \bar{x}^* comes back to \bar{x}^* again in time T , where T is the time period of the periodic orbit. Trajectories that start on Γ in a sufficiently small neighborhood of \bar{x}^* will intersect again, in approximately T time units, in the vicinity of \bar{x}^* . So the flow φ_t and Γ define "mapping" P of some neighborhood of \bar{x}^* ($U \subset \Sigma$) onto another neighborhood ($V \subset \Sigma$), of \bar{x}^* . This mapping P is said to be the Poincaré mapping about the periodic orbit Γ at \bar{x}^* and is represented as,

$$P(\bar{x}_0) = \bar{x}(\bar{x}_0) \quad (4.21)$$

Where $\bar{x}(\bar{x}_0)$ is the state vector that results from the application of the nonlinear map to \bar{x}_0 , i.e., until it intersects the hyperplane Σ . Frequently hyperplane is defined in the configuration space as $x = \text{constant}$, $y = \text{constant}$ or $z = \text{constant}$. Note from the figure 4.12 that the trajectory starting at \bar{x}_0 also crosses the hyperplane at $t = T/2$ but in an opposite direction. If the point \bar{x}_0 is on a periodic orbit, i.e., if $\bar{x}_0 = \bar{x}^*$ then the map $P : \Sigma \rightarrow \Sigma$ repeatedly maps \bar{x}^* onto itself as,

$$P(\bar{x}^*) = \bar{x}^* \quad (4.22)$$

This means that the first return of the initial condition \bar{x}^* comes back to the same state after exactly one time period T on the hyperplane Σ . This state on the hyperplane of the periodic orbit \bar{x}^* is termed as a fixed point. Therefore periodic orbits can be represented by fixed points on a Poincaré map and thus a continuous time system

is reduced to a discrete time system. A special map called a Stroboscopic map is defined which is a result of observing or sampling the flow of a system at periodic time intervals. A linear stroboscopic map, with sampling time T relative to the fixed point on a periodic orbit having time period T allows examining the stability properties of the fixed point and therefore the stability properties of the periodic orbit as discussed previously. Eigenvalues of the monodromy matrix which is a result of linearizing the stroboscopic map ($DP(\bar{x}^*) = \Phi(T, 0)$), is used to analyze the linear stability properties of the periodic orbit. In the next sections, Poincaré maps of resonant manifolds are discussed in the context of periodic resonant orbits.

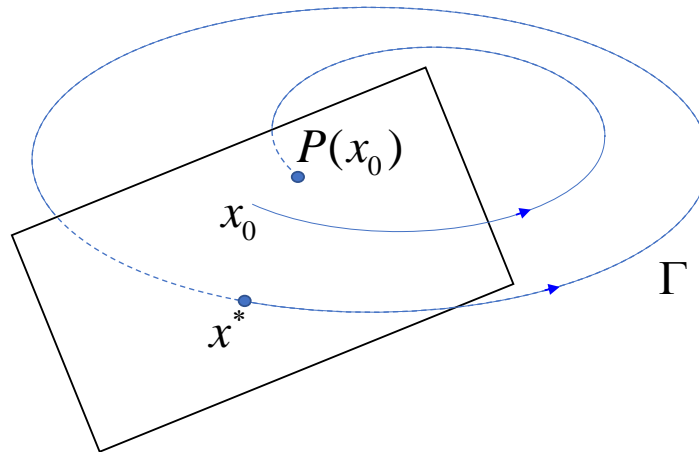


Figure 4.12. The Poincaré map.

4.4.3 Invariant Manifolds for Periodic Orbits

Similar to equilibrium points, invariant manifolds and subspaces also exist for periodic orbits. Consider an autonomous system $\dot{\bar{x}} = \bar{f}(\bar{x})$. Let Γ represent a periodic orbit. In the phase space associated with Γ , hyperplane Σ is defined at \bar{x}_0 such that the flow is transverse to Σ , i.e., trajectory has some component normal to Σ as shown in figure 4.12. As seen in the previous section the first return of the trajectory

passing through Σ with normal component parallel to that of the initial intersection defines a nonlinear map $P : \Sigma \rightarrow \Sigma$ given as,

$$P(\bar{x}_0) = \bar{x}(\bar{x}_0) \quad (4.23)$$

Where \bar{x} is the state vector that results from an application of nonlinear map to \bar{x}_0 . If \bar{x}_0 lies on a periodic orbit then, $\bar{x}_0 = \bar{x}^*$. So P repeatedly maps \bar{x}^* onto itself. Therefore $P^j(\bar{x}^*) = \bar{x}^*$, where j indicates the j^{th} intersection of Σ . Linearizing the Stroboscopic Poincaré map relative to the fixed point allows examining the stability properties of the fixed point using a monodromy matrix and thus the stability properties of the periodic orbit. Consider an initial state \bar{x} close to the state \bar{x}^* of the periodic orbit on the hyperplane Σ . Integrate the state \bar{x}^* and form a one-sided map until the trajectory crosses the hyperplane n times in the same direction. Three different cases may arise. In the first case represented in figure 4.13 the returns on the hyperplane keep coming closer to the fixed point \bar{x}^* with every iteration. This type of behavior signifies a stable periodic orbit. In the second case represented in figure 4.13 the returns keep moving further away from the fixed point \bar{x}^* with every iteration. This type of behavior signifies an unstable periodic orbit. In the third case represented by figure 4.13 the returns neither move away nor come close to the fixed point \bar{x}^* and thus signifies a marginally stable periodic orbit. The returns of the trajectories in figure 4.13 represent the stable $W^s(\bar{x}^*)$, unstable $W^u(\bar{x}^*)$ and center $W^c(\bar{x}^*)$ manifolds associated with fixed point \bar{x}^* . The manifolds of the fixed point are thus $(n - 1)$ dimensional and are not trajectories but instead collection of returns onto the hyperplane Σ from a nearby perturbation. Every state on a periodic orbit is a fixed point, and every fixed point on the periodic orbit is used to compute the corresponding stable and unstable manifolds, by placing the surface Σ transverse to the flow at different points along the periodic orbit. All the manifolds combined at all the fixed points on the periodic orbit form n dimensional stable $W^s(\Gamma)$, unstable $W^u(\Gamma)$ and center manifold $W^c(\Gamma)$ surfaces for the periodic orbit. The stable mani-

fold theorem for periodic orbits states the dimensions of these subspaces [43].

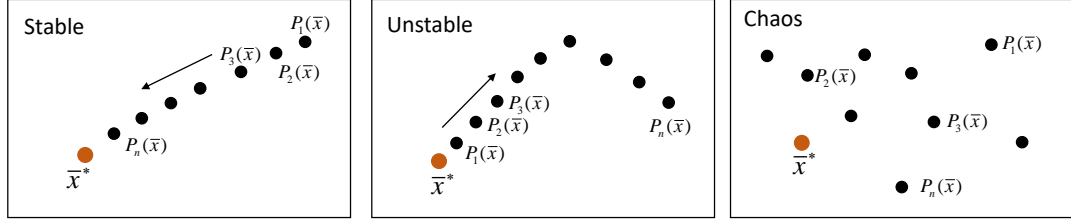


Figure 4.13. Illustration of subsequent returns to a Poincaré map.

Stable Manifold Theorem for Periodic Orbit: Let an open subset of \mathfrak{R}^n contain a periodic orbit $\Gamma : \bar{x} = \gamma(\tau)$ of period T . Let φ_t be the flow and $\gamma(\tau) = \varphi_\tau(\bar{x}^*)$. If k characteristic exponents of $\gamma(\tau)$ have a negative real part where $0 \leq k \leq n - 1$ and $n - k - 1$ of them have a positive real part, then there is a $\delta > 0$ such that the stable manifold of Γ given as,

$S(\Gamma) = \{\bar{x} \in N_\delta(\Gamma) \mid d(\varphi_\tau(\bar{x}), \Gamma) \rightarrow 0 \text{ as } \tau \rightarrow \infty \text{ and } \varphi_\tau(\bar{x}) \in N_\delta(\Gamma) \text{ for all } \tau \geq 0\}$ is a $(k + 1)^{th}$ dimensional, differentiable manifold which is positively invariant under the flow φ_τ , and the unstable manifold of Γ given as,

$U(\Gamma) = \{\bar{x} \in N_\delta(\Gamma) \mid d(\varphi_\tau(\bar{x}), \Gamma) \rightarrow 0 \text{ as } \tau \rightarrow -\infty \text{ and } \varphi_\tau(\bar{x}) \in N_\delta(\Gamma) \text{ for all } \tau \leq 0\}$ is an $(n - k)^{th}$ -dimensional, differentiable manifold which is negatively invariant under the flow φ_τ . Further the stable and unstable manifolds of Γ intersect transversely in Γ . If the dimension of the stable and unstable manifolds for the fixed points are represented by n_s and n_u respectively, then the stable and unstable manifolds associated with the periodic orbits Γ represented by $W^s(\Gamma)$ and $W^u(\Gamma)$ have dimensions $n_s + 1$ and $n_u + 1$ respectively. The dimensions are always one higher than that of the fixed points [44].

4.4.4 Computation of Manifolds for Unstable Resonant Orbits

Stable and unstable manifolds are useful for trajectory design as they indicate natural dynamical flow that is going out or into a periodic orbit Γ . Thus acquiring the states of a stable manifold would eventually lead to the periodic orbit Γ or states of an unstable manifold would lead to a location which is away from the periodic orbit Γ when integrated forwards in time, i.e., as $t \rightarrow \infty$. Stable and unstable local manifolds of a fixed point on the periodic orbit are computed similarly to equilibrium points. The local unstable manifold W_{loc}^u is tangential to the unstable subspace E^u at the fixed point \bar{x}^* and the local stable manifold W_{loc}^s is tangential to the stable subspace E^s at the fixed point \bar{x}^* . The stable and unstable subspaces lie along the eigenvectors corresponding to the stable ($|\lambda| < 1$) and unstable ($|\lambda| > 1$) eigenvalues of the monodromy matrix computed at fixed point \bar{x}^* . Global stable and unstable manifolds of the fixed point are then computed by integrating the nearby initial conditions on the stable and unstable subspaces backward and forward in time respectively. But the real interest for periodic orbits Γ are the stable and unstable manifolds of the periodic orbit and not the fixed point. The Stable manifolds of the periodic orbit are the surface formed by the collection of the stable global manifolds at infinitely many fixed points on the periodic orbit. Likewise unstable manifolds of the periodic orbit are the surface formed by the collection of the unstable global manifolds at infinitely many fixed points on the periodic orbit. Numerically it is not possible to generate the manifold surface for infinitely many fixed points on the periodic orbit. Hence the following algorithm is used to generate manifold surfaces for periodic orbits:

1. Periodic orbit Γ is discretized into n fixed points.
2. At each fixed point, monodromy matrix $\Phi(T, 0)$ is computed, and its eigenvalues are evaluated. Stable and unstable eigenvectors corresponding to the eigenvalues form the linear stable and unstable eigenvector spaces for fixed points.

3. At each fixed point, global stable and unstable manifolds are computed by stepping off onto the stable and unstable linear eigenvector spaces and integrating backward and forward in time respectively.
4. The step off initial conditions for the global stable and unstable manifolds at a fixed point is obtained by,

$$\bar{x}_{u^\pm/s^\pm} = \bar{x}^* \pm l\bar{v}_{u/s} \quad (4.24)$$

where l is the offset in the direction of the unstable or stable eigenvector. If l is too big then the computed \bar{x}_{u^\pm/s^\pm} is not a good approximation. If l is too small, the trajectory spends a long time near the fixed point and affects the integration accuracy. One option to select the value of l is to give it a physical meaning in terms of distance by rephrasing the equation in the following way,

$$\bar{x}_{u^\pm/s^\pm} = \bar{x}^* \pm d \cdot \frac{\bar{v}_{u/s}}{\sqrt{x_{u/s}^2 + y_{u/s}^2 + z_{u/s}^2}} \quad (4.25)$$

The value d , now represents a distance from the fixed point and the unstable and stable eigenvectors are defined as $\bar{v}_{u/s} = \begin{bmatrix} x_{u/s} & y_{u/s} & z_{u/s} & \dot{x}_{u/s} & \dot{y}_{u/s} & \dot{z}_{u/s} \end{bmatrix}^T$.

5. The collection of all the manifolds at the n fixed points represent the stable and unstable manifold surfaces of the periodic orbit Γ .

To implement the above algorithm, consider an unstable 1:2 resonant orbit with the following non-dimensional rotating frame initial conditions as shown below,

$$\bar{x}_0^R = \left\{ \begin{bmatrix} 0.887849 & 0 & 0 & 0 & 0.640766 & 0 \end{bmatrix} \right\} \quad (4.26)$$

The eigenvalues of the monodromy matrix at the initial condition are as follows,

$$\begin{aligned}
\lambda_1 &= -52.206173 \\
\lambda_2 &= -0.019155 \\
\lambda_3 &= 1 \\
\lambda_4 &= 1 \\
\lambda_5 &= 1.457532 \\
\lambda_6 &= 0.686090
\end{aligned} \tag{4.27}$$

λ_1 and λ_2 represent the in-plane eigenvalues corresponding to the unstable and stable eigenvectors. In the Earth-Moon system, a step off distance of 40 km is a reasonable value used in the past literature [22]. As an illustration, the stable and unstable eigenvectors for 20 fixed points distributed equally in time across the resonant orbit is shown in figure 4.14. The red vectors indicate unstable eigenvectors, and blue vectors indicate stable eigenvectors. Integrating the manifolds at all the fixed points for three resonant time periods or 145 days results in the global manifold surfaces as seen in figure 4.15. Stable manifolds are represented using blue trajectories and unstable manifolds are represented by red trajectories. Notice that the manifolds for the resonant orbits are highly tangled. They generally pass close to other resonances and spread across different regions in the CR3BP. Manifolds in this form are not fruitful for trajectory design purposes as they do not offer any significant insight. Poincaré mapping of the manifolds gives them more structure and helps to uncover the hidden relations between the resonant orbit, its manifolds and other dynamical structures in the configuration space. A common hyperplane used to form a Poincaré map for the manifolds is $y = 0$. The map can be single-sided or a double-sided depending upon the direction of crossings of the manifolds. The crossings on the map are recorded in two ways. The first way is to record all the crossing of the manifolds with the hyperplane in the desired direction for a fixed amount of integration time period. The second way is to record the first m number of crossings of the manifolds with the hyperplane in the desired direction. In order to demonstrate this process, a Poincaré mapping of the stable and unstable manifolds integrated for 145 days on $y = 0$ and $\dot{y} > 0$ is

shown in the figure 4.16. A clear structure in the returns of the stable and unstable manifolds is noticed. The red dots indicate the returns of the unstable manifold and the blue dots indicate the returns of the stable manifolds. The intersections between the stable and unstable manifolds correspond to homoclinic connections.

The resonant families and Poincaré mapping techniques demonstrated in this chapter will be utilized to answer the fundamental question of using resonant orbits and their manifolds in the transfer, initial guess generation process between stable periodic orbits by incorporating them as intermediate arcs.

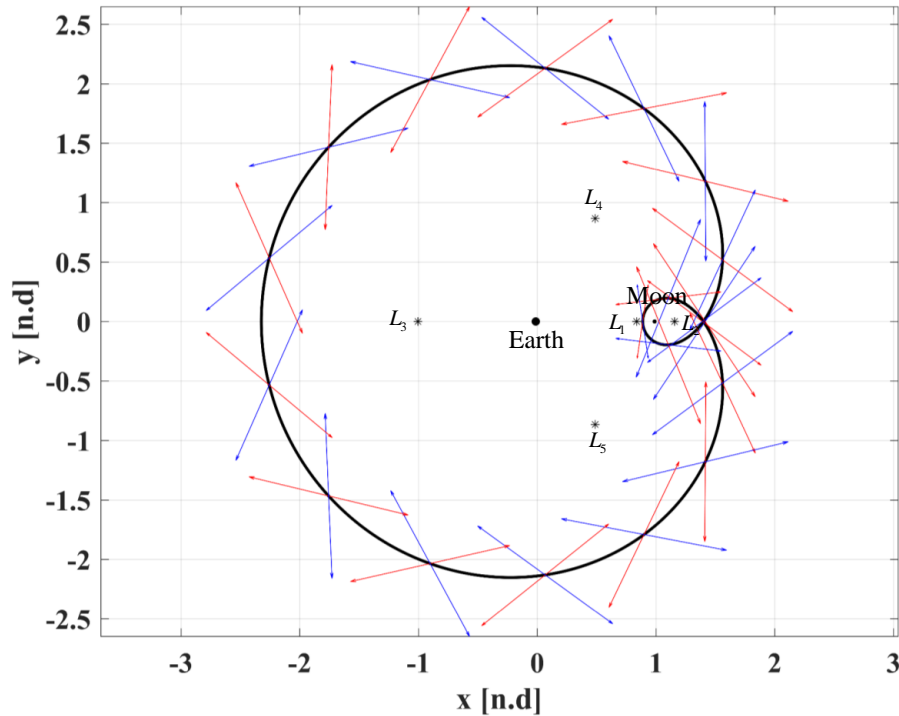


Figure 4.14. Stable and unstable eigenvectors at 20 fixed points.

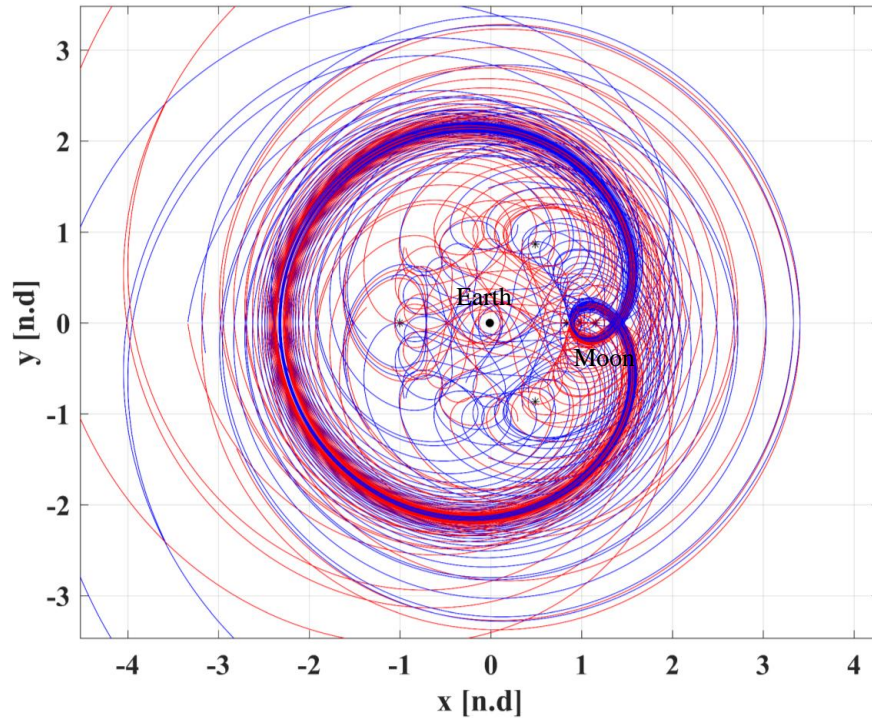


Figure 4.15. Stable and unstable manifolds propagated for 3 resonant time periods (145 days).

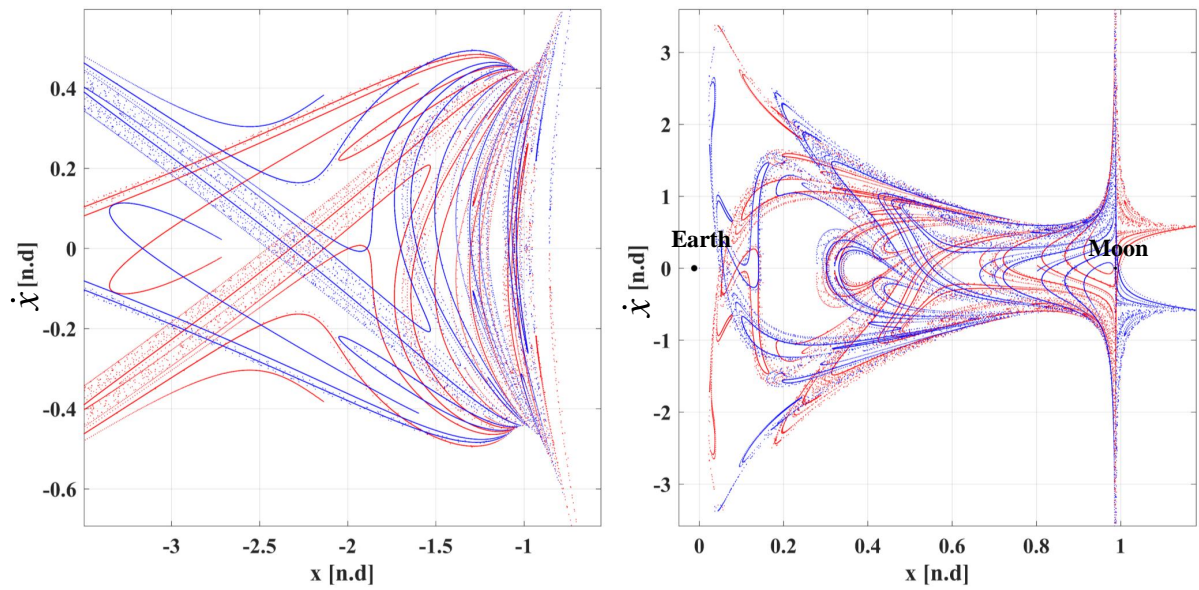


Figure 4.16. 1:2 Resonant manifolds - returns on Poincaré map $y = 0$ and $\dot{y} > 0$.

5. REFERENCE TRAJECTORY DESIGN IN EPHEMERIS MODEL

In the previous chapter, both planar and spatial resonant orbits have been shown to exist in the CR3BP based upon their existence in the two-body dynamical model. Invariant manifolds and Poincaré mapping techniques have been developed, which will be used as the primary design methodology to construct trajectories in the multibody systems. Another type of resonant orbits which are found in the CR3BP are the libration point periodic orbits which are in resonance with the smaller primary. In the Earth-Moon system, the libration point orbits (LPOs) are in resonance with either the synodic or sidereal time-period of the Moon. A synodic period of the Moon is defined as the time taken by the Moon to revolve around the Earth and return to the same position relative to the Sun. The Sidereal period of the Moon is defined as the time taken by the Moon to orbit 360° around the Earth relative to the fixed stars. The synodic and sidereal period of the Moon is approximately 29.532 days and 27.322 days respectively. Figure 5.1 illustrates the difference between the synodic and sidereal time-periods of the Moon.

5.1 Resonant - Near Rectilinear Halo Orbits

One category of LPOs of interest are the halo orbit families. The current investigation will focus on a specific subset of the halo families known as the L_1 and L_2 Near Rectilinear Halo Orbits which largely exist in the \hat{y} - \hat{z} plane. They possess several ideal characteristics making them suitable for staging orbits in the cislunar space. Many of the NRHOs are stable or almost stable in a linear sense and retain their fundamental characteristics and NRHO like rectilinear motion even when transitioned into a higher fidelity ephemeris model. Some of the NRHOs possess favorable resonant

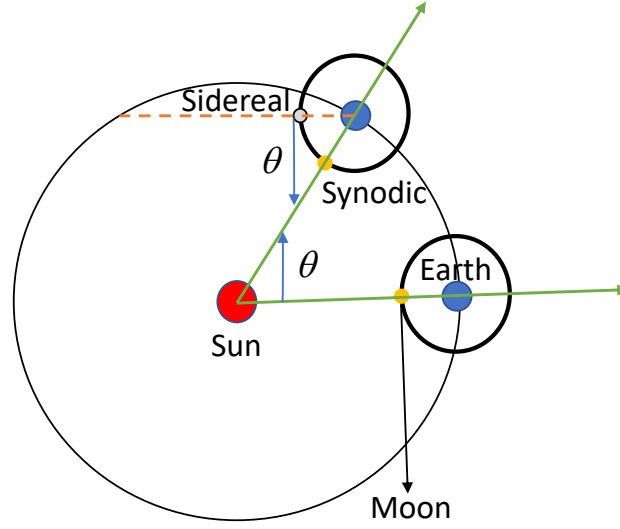


Figure 5.1. Synodic and Sidereal configurations of the Moon.

properties with the Moon which make them an ideal choice to satisfy specific mission operational constraints like avoiding eclipses and periapsis conditions. Consider the figure 5.2 which shows the subsets of L_1 and L_2 halo orbits. The colors of the orbits indicate the Jacobi constants and are indicated by the color bar. At L_1 the first halo orbit is almost planar, and as the family continues, they grow largely out of the plane and almost exist in the \hat{y} - \hat{z} plane. Similar behavior is observed for L_2 NRHOs. Both L_1 and L_2 NRHOs can be effectively characterized by their periapsis radius, stability indices, Jacobi constants and time periods. Figures 5.3 - 5.5 show various relationships between the parameters stated above. The typical time periods of NRHOs vary from 1 to 2 weeks. Stability index ν_1 for both the NRHOs lie between the stability boundaries. Stability index ν_2 for both the NRHOs with smaller periapsis radii lie between the stability boundaries, but quickly become unstable for larger periapsis radii. An in-depth analysis regarding the NRHO stability characteristics is given by Zimovan [45]. Within the L_2 NRHOs, the orbits which have a synodic resonance ratio of type $m:1$ and $m:2$ with the Moon are shown in figure 5.6. Two specific orbits of interest having a synodic resonance ratio of 3:1 and 9:2 respectively are chosen and are highlighted by a red dot in the plots.

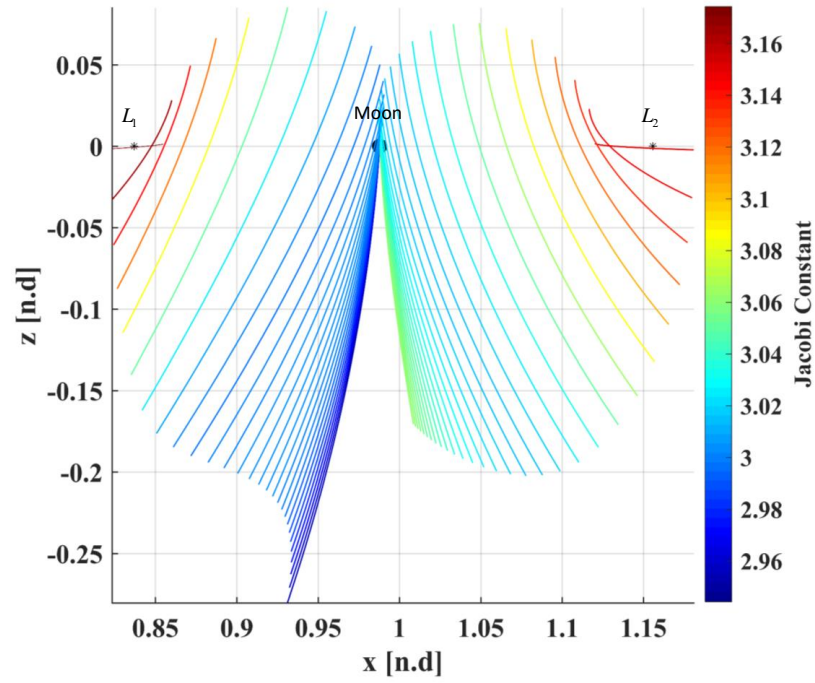


Figure 5.2. L_1 and L_2 NRHO family in the Earth-Moon system.

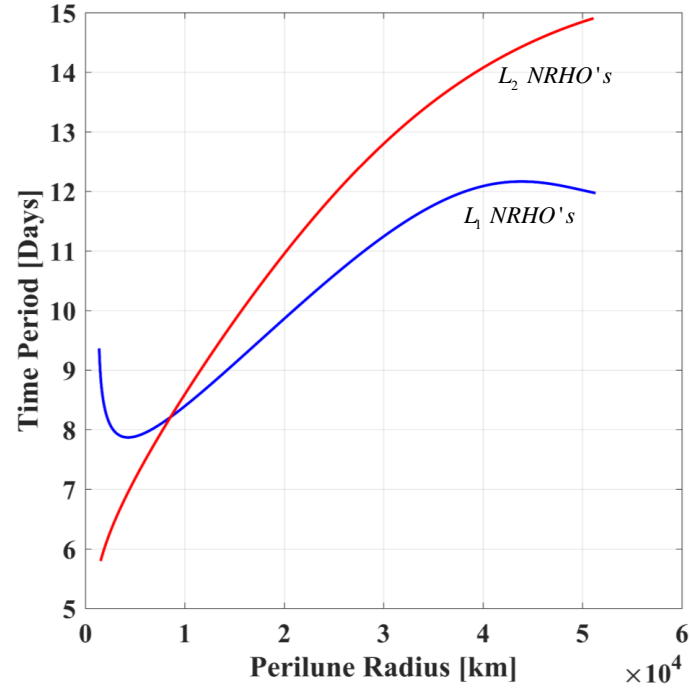


Figure 5.3. Time periods of L_1 and L_2 NRHO family.

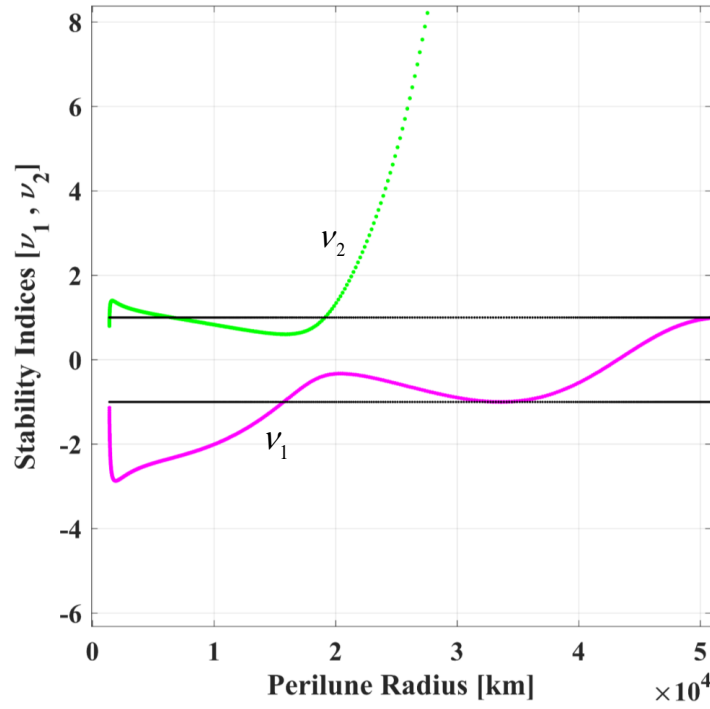


Figure 5.4. Stability Indices of L_1 NRHO family.

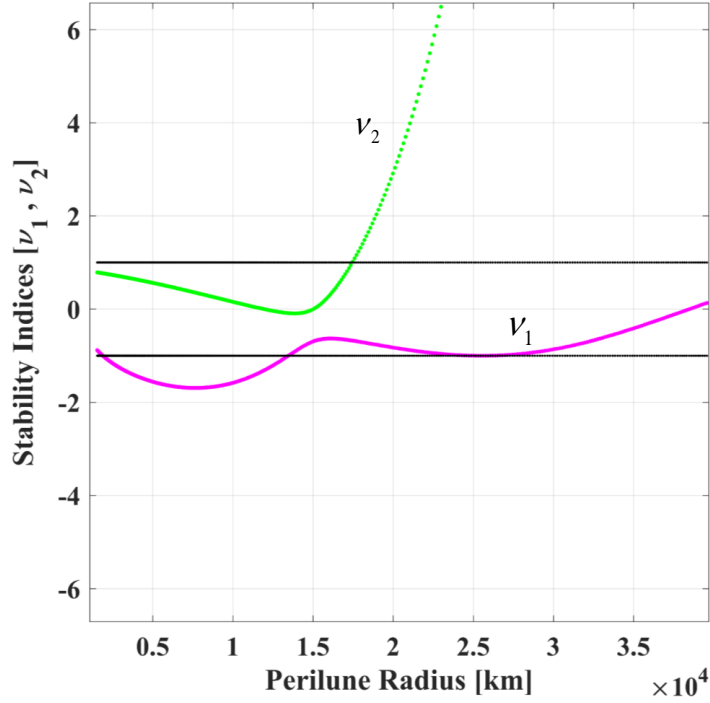


Figure 5.5. Stability Indices of L_2 NRHO family.

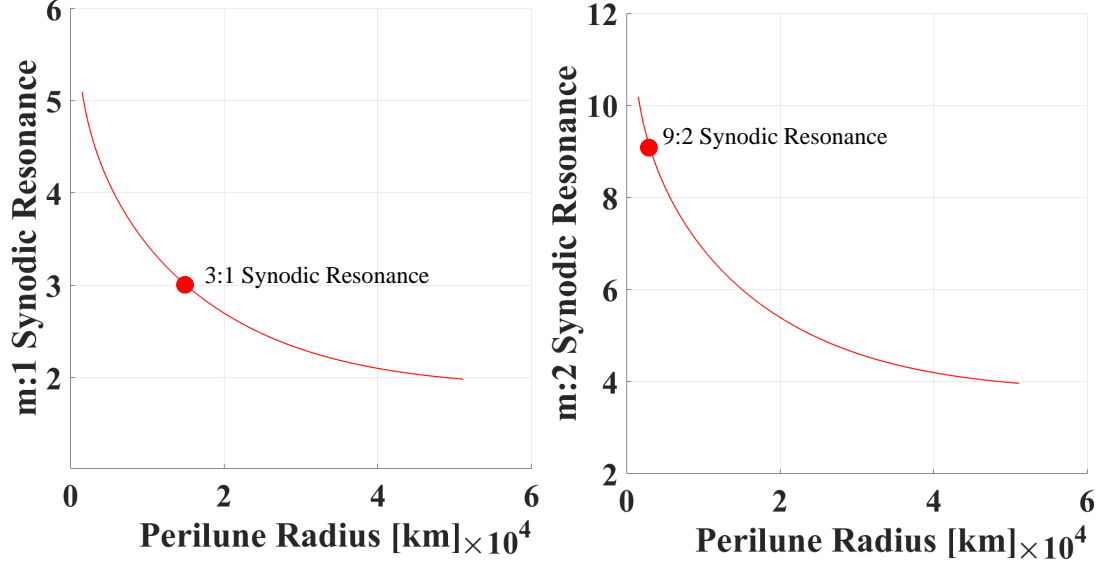


Figure 5.6. m:1 and m:2 Synodic resonances of L_2 NRHOs.

5.2 Challenges in Ephemeris Trajectory Design

To practically validate the design process, the solutions generated in the CR3BP are subjected to a higher fidelity analysis by transitioning them into an ephemeris model. One such scenario where analysis of higher fidelity solutions is extremely critical is the generation of long-term baseline trajectories for staging purposes. Trajectories in the higher fidelity ephemeris models are generated by appropriately transitioning periodic orbits from the CR3BP into the ephemeris model. Periodic orbits exist as quasi-periodic trajectories in the higher fidelity model. As the ephemeris model is non-autonomous in nature, the quasi-periodic solution that is converged using the same set of CR3BP periodic orbits will be dependent upon the ephemeris transition epoch. This poses a challenge especially when the periodic orbits considered are being utilized for long-term staging purposes. Orbit parameters of the quasi-periodic trajectories like eclipse avoidance and periapsis conditions will now become a function of the ephemeris transition date. Hence a careful selection of the ephemeris insertion epoch is warranted. A 3:1 L_2 southern synodic NRHO is cur-

rently being considered as a potential long-term staging orbit in the cislunar space due to its eclipse avoidance properties. A 3:1 synodic NRHO would mean that the time taken to complete three revolutions of the NRHO is same as one synodic period of the Moon. Figure 5.7 illustrates three 3:1 L_2 southern synodic NRHOs stacked one after the other starting from the periapsis on the \hat{x} - \hat{z} plane in the CR3BP, centered at the Moon. The time period of the orbit is approximately 9.844 days and has a periapsis radius of about 14,689 km. When the same stack of orbits is viewed in the Sun-Moon rotating frame, the eclipse avoidance property is clearly highlighted in figure 5.8. Here, the \hat{x} -axis represents the Sun-Moon direction and the stacked orbits do not pass through the line of eclipse due to the Moon. Similarly, eclipses due to Earth are known by observing the trajectory in the Sun-Earth rotating frame as seen in figure 5.9. Here, the Sun-Earth direction, i.e., the \hat{x} -axis is the direction of eclipses caused due to Earth. Methods to evaluate the duration of eclipses has been shown previously by Zimovan [28]. The effect of epoch date upon ephemeris transition are studied in this context.

5.2.1 Quasi-periodic Trajectories in Ephemeris Model

A traditional stacking sequence is employed to transition periodic orbits in the CR3BP to higher fidelity ephemeris models on any chosen epoch date. In this process, a desired number of identical periodic orbits are stacked one after another starting from a fixed state on the first orbit until the time period of the stacked trajectories roughly equals the mission duration. Once the orbits are stacked, they are further divided into sub-arcs by distributing patch points to facilitate convergence in the higher fidelity model. To demonstrate this process twelve 3:1 L_2 Southern Synodic NRHOs are stacked one after another in the CR3BP until the total time amounts to approximately 118.13 days. The starting point on the stacked trajectory is arbitrarily chosen to lie on the \hat{x} - \hat{z} plane, i.e., the periapsis of the NRHO. Once the orbits are stacked, they are further split into sub-arcs by distributing patch points along

each orbit as shown in figure 5.10. For this analysis, ten patch points are equally distributed in time on a single NRHO thereby splitting it into ten sub-arcs. Adaptive Trajectory Design software developed at Purdue University is utilized to apply a multiple shooting differential corrections process to facilitate convergence in the ephemeris model [46]. The design variable matrix consists of all the states in position and velocity associated with the patch points and the sub-arc integration times. An Earth-Moon ephemeris model with Sun as the perturbing body is considered, and a position and velocity continuity is ensured across all the patch points during the corrections process. The Julian day associated with the first patch point of the corrected trajectory corresponds to the ephemeris insertion epoch.

To investigate the impact of the epoch on the convergence in ephemeris model, the same set of stacked orbits are transitioned and corrected on each day of May 2023. Figure 4.2 and Figure 4.3 represent the converged ephemeris trajectories in

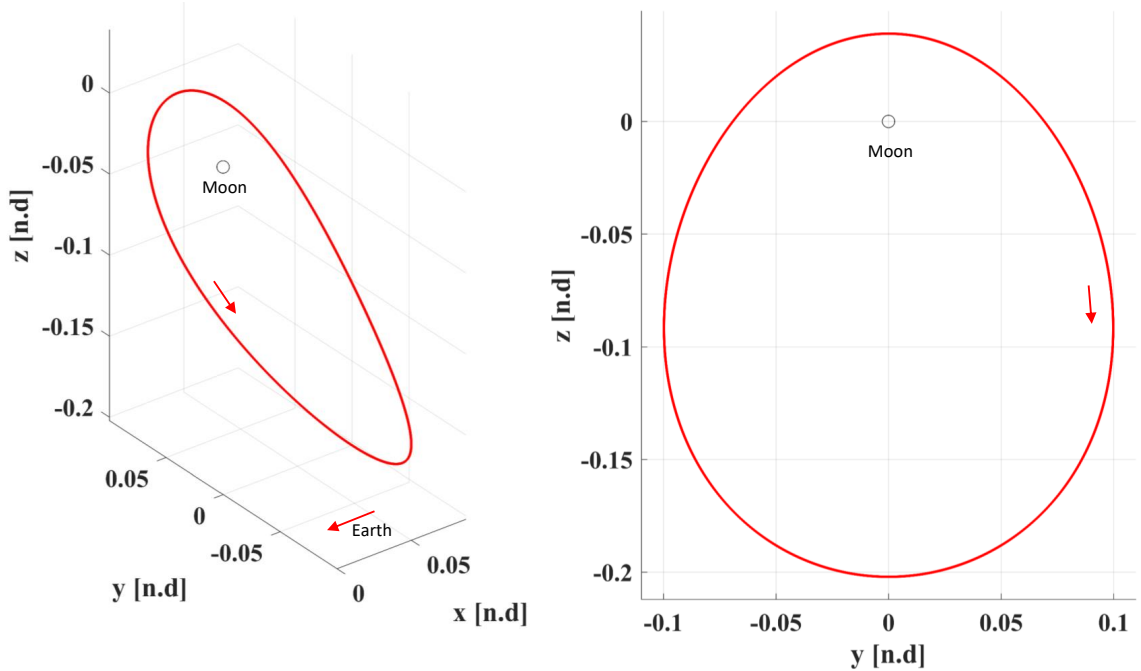


Figure 5.7. 3:1 synodic southern L_2 NRHO in the CR3BP - Moon centered, Earth - Moon rotating frame view.

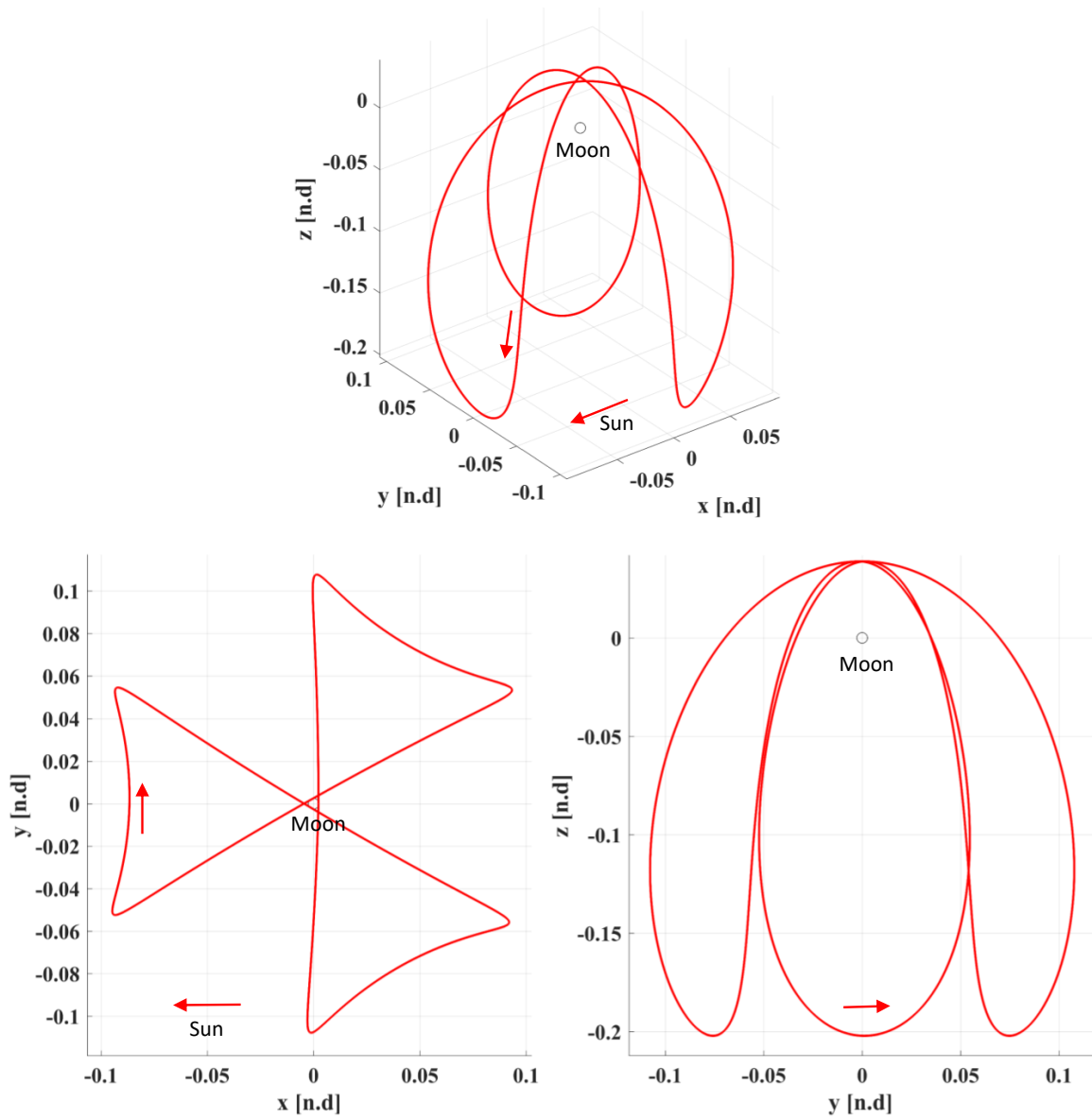


Figure 5.8. 3:1 synodic southern L_2 NRHO in the CR3BP - Moon centered, Sun - Moon rotating frame view.

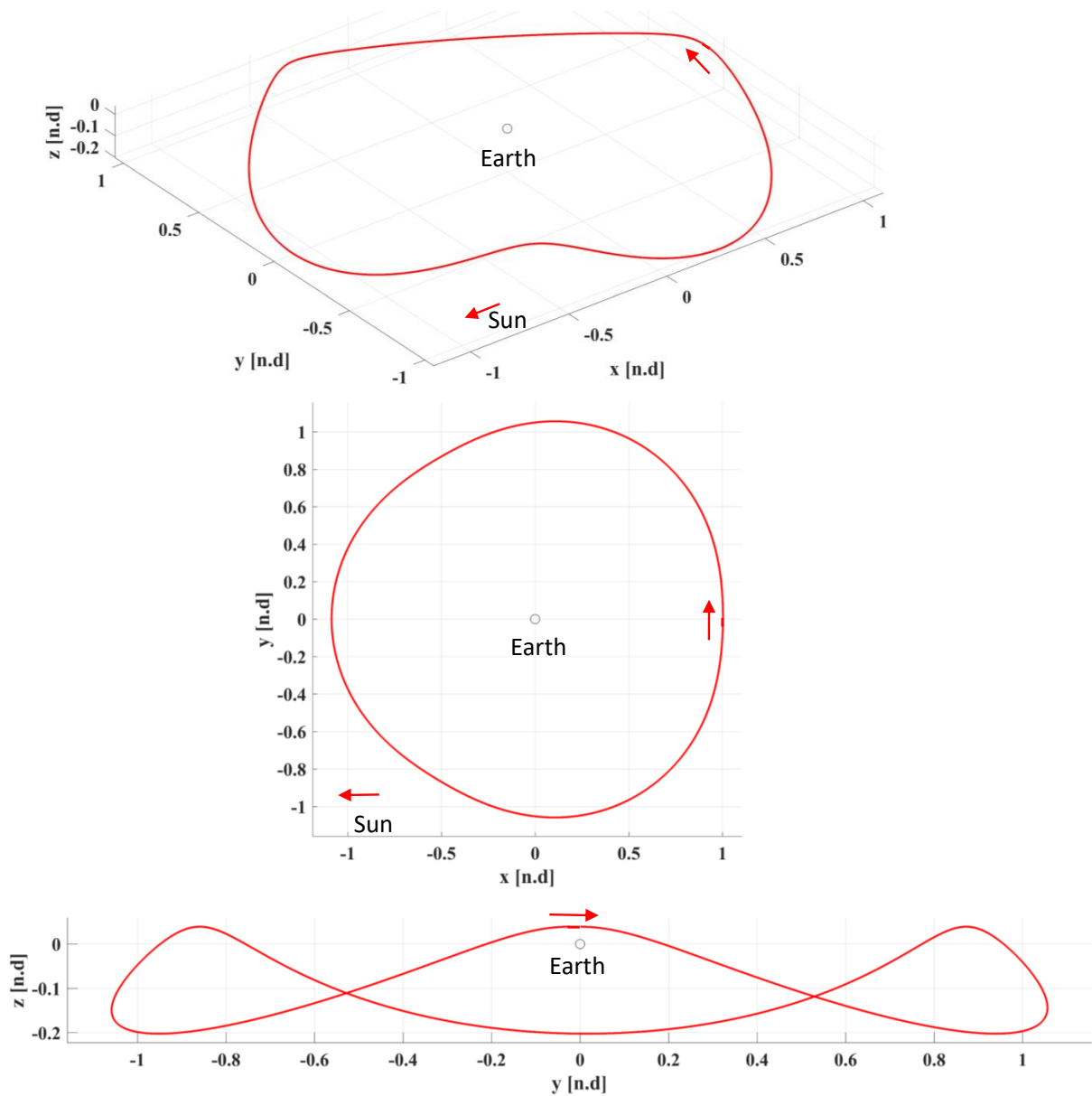


Figure 5.9. 3:1 synodic southern L_2 NRHO in the CR3BP - Earth centered, Sun - Earth rotating frame view.

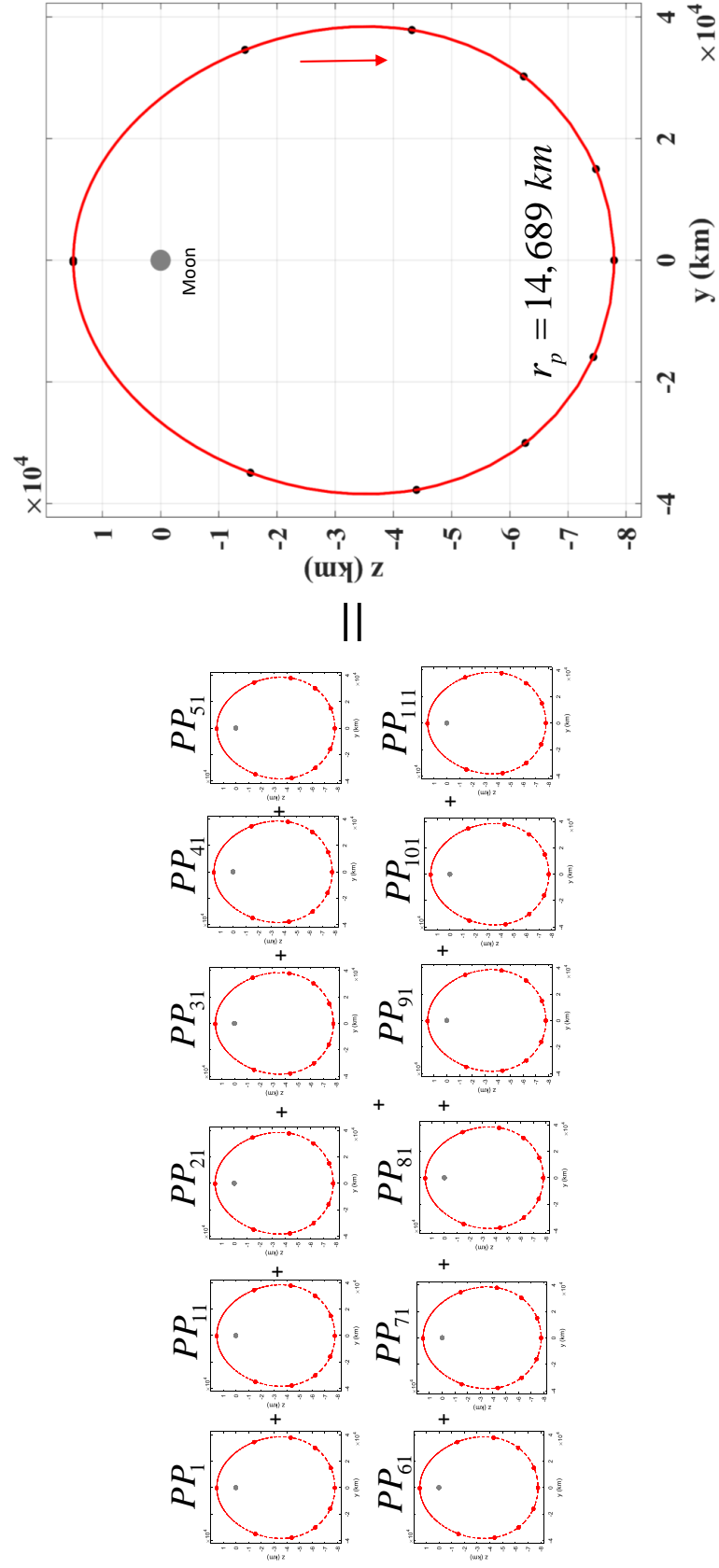


Figure 5.10. Twelve 3:1 synodic southern L_2 NRHOs stacked in the CR3BP - Barycentric, Earth - Moon rotating frame view.

May 2023. Clearly, an interesting convergence pattern is observed. A series of tightly or loosely converged trajectories are visible across the month. The pattern approximately repeats every 9 to 10 days which is roughly equal to the time period of the synodic NRHO. Also, the 3:1 synodic resonance is visible on the days with tighter or repeatable behavior. While on some other days, the solutions are more dispersed and have a less repeatable structure which distorts the visual appearance of the resonance in the converged trajectories.

An apse angle (ω) is introduced to quantify the "tightness" or "looseness" of a quasi-periodic trajectory [28]. An apse angle is defined as the deviation of periapsis of each orbit in the converged ephemeris trajectory relative to the corresponding periapsis in the CR3BP model. The argument of periapsis for all the periodic NRHOs stacked in the CR3BP is 90^0 . Then the apse angle corresponding to each periapsis in the ephemeris trajectory is obtained by the following equation,

$$\varpi = \omega - \frac{\pi}{2} \quad (5.1)$$

where ω represents the osculating argument of periapsis for the quasi-periodic NRHO's in the ephemeris model.

Consider two representative epochs on May 16th and May 21st. The apse angles for the quasi-periodic trajectories are plotted in figure 5.14. Visually trajectory on May 16th appears to have a larger spread compared to the trajectory on May 21st as seen in figure 5.13. Even though the resonance is not visible on May 16th, apse angle plots highlight the angles occurring in sets of three, indicating the 3:1 synodic resonance ratio on both the epoch dates. Additionally, periapsis radius varies, and its difference with respect to the CR3BP model is shown in figure 5.15. It is seen that the deviation in periapsis radius of the tighter trajectory on May 21st is much lesser than that of the loosely spread trajectory on May 16th. Further insight is obtained by looking at the two trajectories in the Sun-Moon and the Sun-Earth rotating frames.

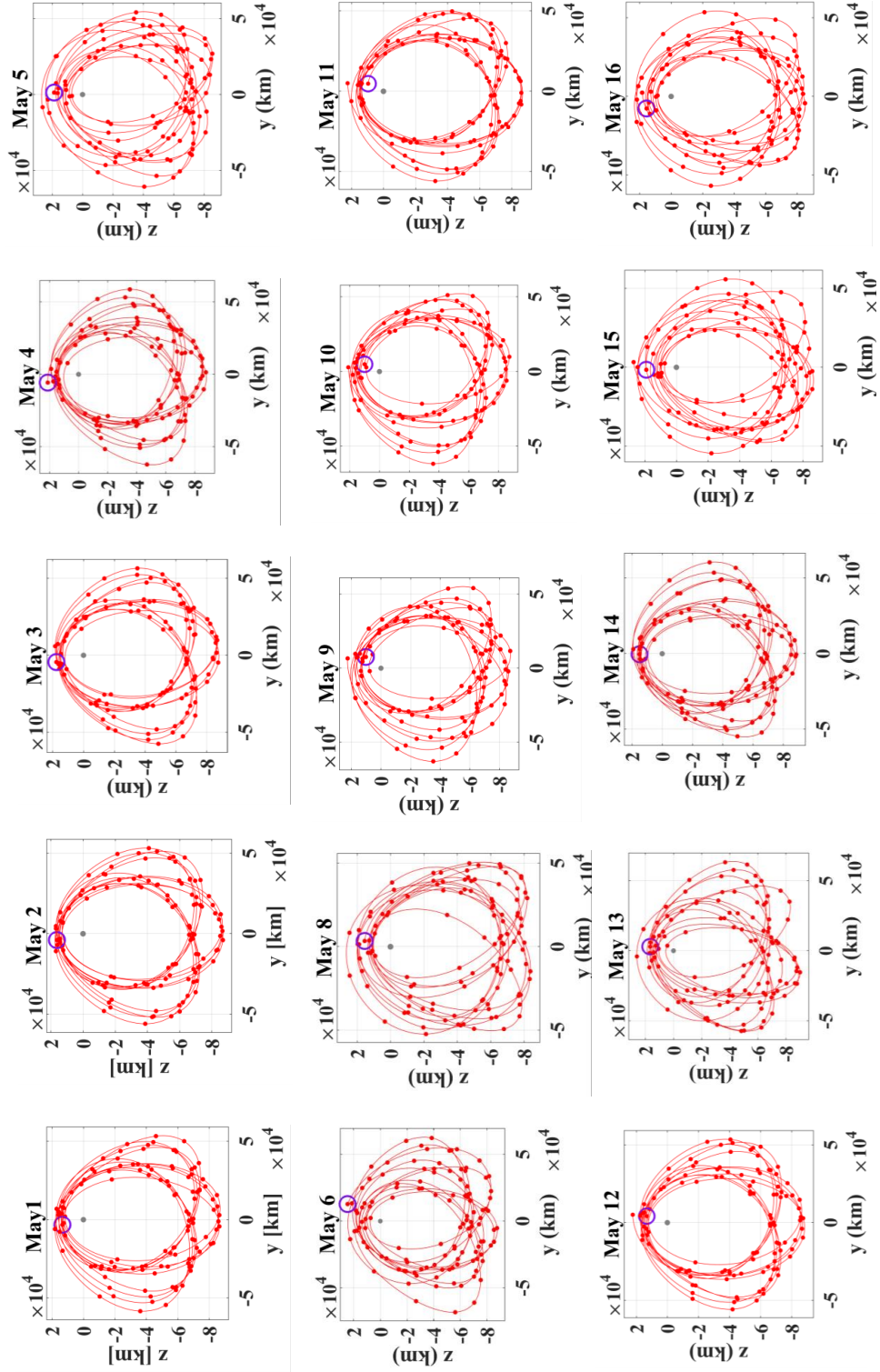


Figure 5.11. Converged ephemeris trajectories from May 1st, 2023 to May 16th, 2023.

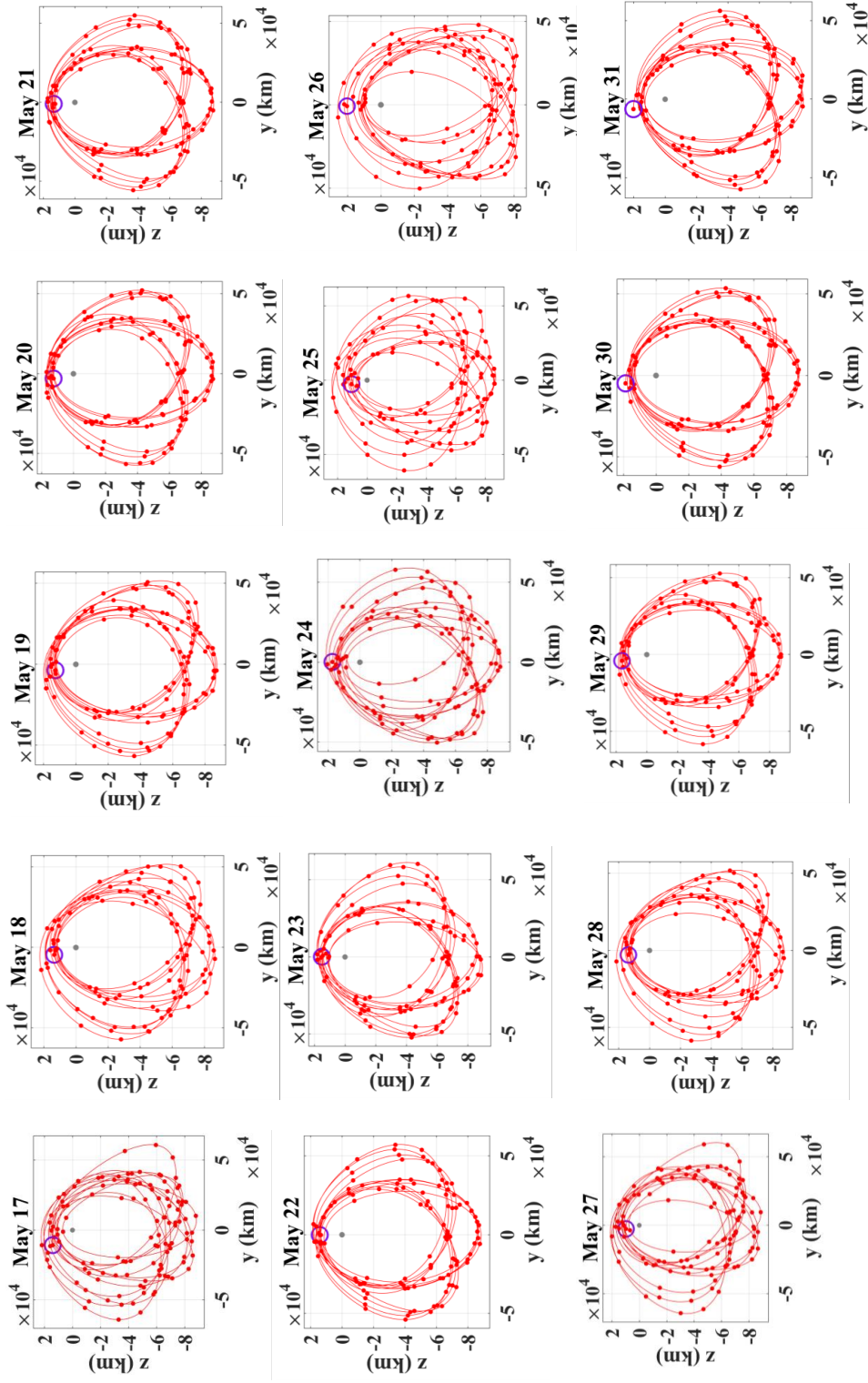


Figure 5.12. Converged ephemeris trajectories from May 17th, 2023 to May 31st, 2023.

Figure 5.16 and figure 5.17 represent the two trajectories in Sun-Moon and the Sun-Earth rotating frames. The usefulness of repeatability in the quasi-periodic trajectory on May 21st is seen by its ability to avoid eclipses due to the Earth and the Moon when compared to the trajectory on May 16th. Therefore, one of the challenges in generating desired quasi-periodic trajectories is that by adopting the same stacking sequence may or may not produce the anticipated solution on all the epoch dates.

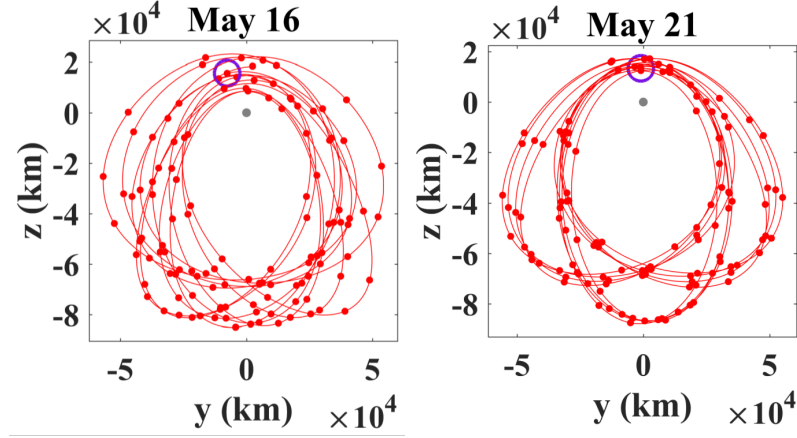


Figure 5.13. Quasi-periodic NRHOs computed on May 16th and May 21st - Earth-Moon rotating frame view.

5.2.2 Generating Nearby Reference Ephemeris Solutions

Consider the figure 5.18 which indicates a part of an ephemeris NRHO shown by a red line whose distance to the Moon is plotted on the \hat{y} -axis and the corresponding epoch is plotted on the \hat{x} -axis. A spacecraft on this trajectory may encounter eclipses of short durations, especially near the periapsis regions (Sun-Earth and Sun-Moon rotating plane) of the trajectory. Previous studies have shown that maximum eclipse durations on an NRHO typically are in the range of 1-2 hours due to Moon and 4-5 hours due to the Earth [47]. Eclipses are generally avoided by performing a phase shift maneuver in advance, to shift the epoch of the target periapsis in the eclipse region by a certain number of hours. This delays or advances the arrival of the spacecraft

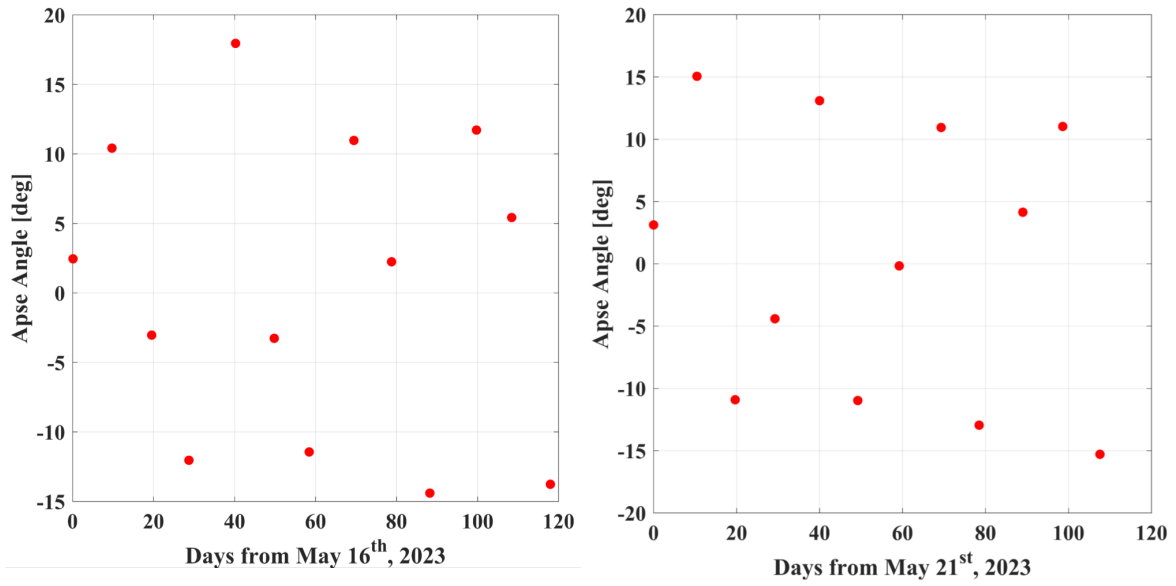


Figure 5.14. Apse angles for quasi-periodic NRHOs computed on May 16th and May 21st - Earth-Moon rotating frame view.

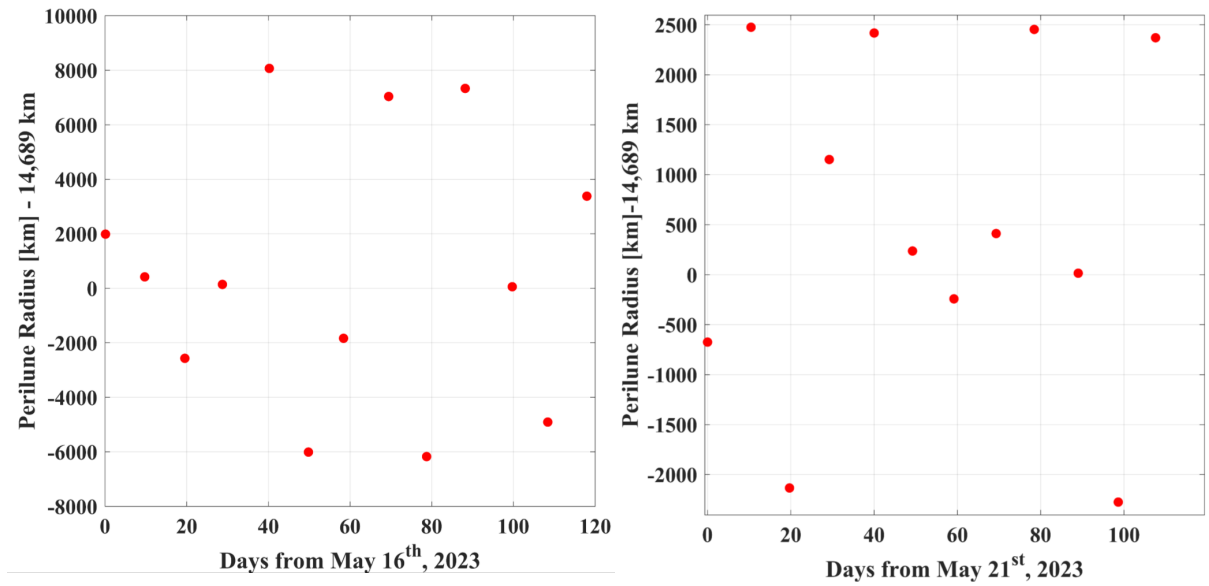


Figure 5.15. periapsis radius variation for NRHOs computed on May 16th and May 21st.

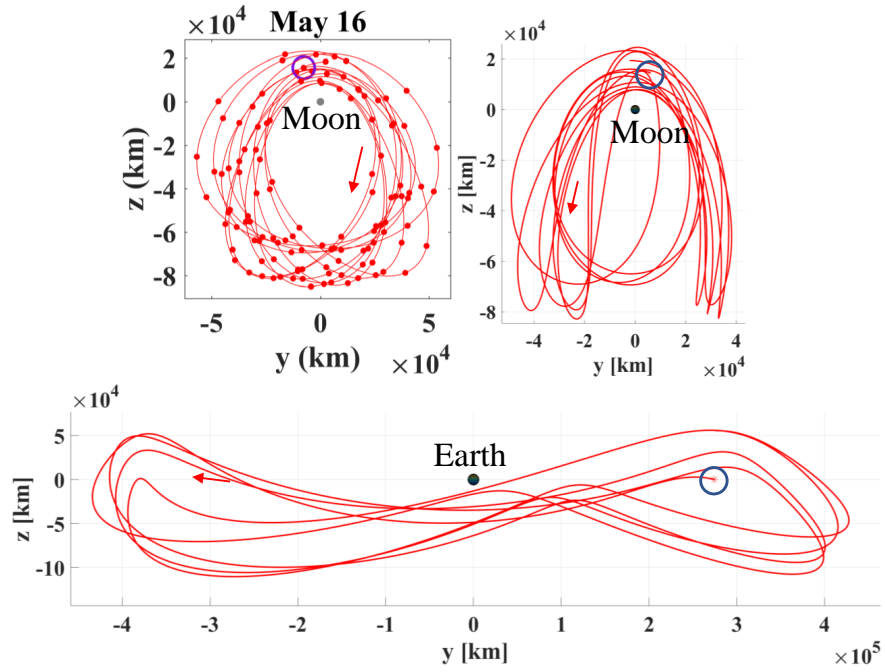


Figure 5.16. Ephemeris trajectory on May 16th, 2023 in EM, SM, and SE rotating frames.

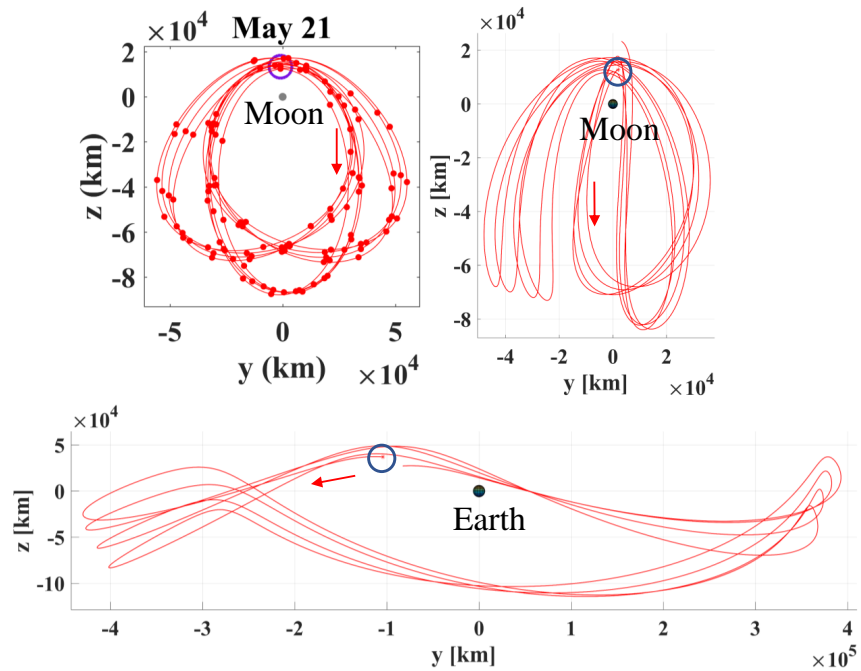


Figure 5.17. Ephemeris trajectory on May 21st, 2023 in EM, SM and SE rotating frames.

into the eclipse region and helps to avoid it partially or completely. This is equivalent to generating a new reference trajectory starting from the maneuver location, whose periapsis is now shifted with respect to the original trajectory to avoid the eclipse as shown with the green line in the plot. Sometimes a new ephemeris trajectory which avoids the eclipse is generated by altering the ephemeris solution subject to an optimization algorithm. If multiple periapsis epochs are targeted at once, then this process may become expensive and may not lead to convergence. Moreover, for conducting preliminary design studies and analysis, several nearby quasi-periodic trajectories may be required with different periapsis epoch and radii constraints. Therefore, one of the challenges is to design a reliable method to generate nearby reference solutions with a better periapsis control to a known baseline trajectory.

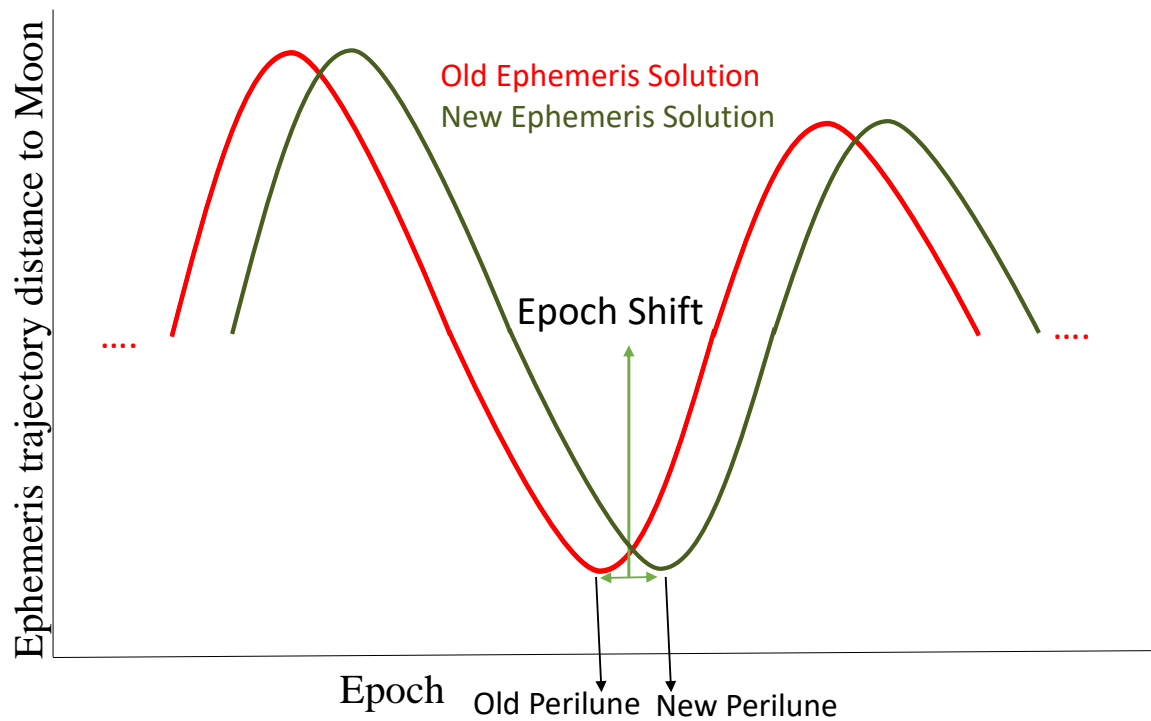


Figure 5.18. Nearby reference trajectory with shifted periapsis.

5.3 New Stacking Sequences in CR3BP

5.3.1 Alternative Stacking Sequence for Repeatable Behavior

One goal of this investigation is to produce repeatable and tightly converged ephemeris trajectories irrespective of the ephemeris insertion epoch. This is useful to retain the favorable properties exhibited by the "tighter" formations of the synodic resonant trajectories in the higher fidelity model. In the ephemeris model, two different epoch dates correspond to two entirely different dynamical environments. The implication of this is that the same initial guess in the CR3BP converges to two different solutions on the two epoch dates in the ephemeris model. From the previous section consider two quasi-periodic 3:1 L_2 Southern Synodic NRHOs on May 16th, 2023 and on a nearby epoch May 21st, 2023 formed from the same traditionally stacked NRHOs in the CR3BP. By altering the stacking sequence of the NRHOs starting on May 16th, it is possible to converge to a "tighter" quasi-periodic formation, like the one starting on May 21st. To accomplish this the traditionally stacked NRHOs on the two epochs in the CR3BP are compared with each other by plotting their distances to the Moon as seen in figure 5.19. The blue line indicates the stacked orbits on May 16th, while the red line indicates the stacked orbits on May 21st. Clearly, a phase difference is noticed between the two lines. To converge to an ephemeris trajectory which looks like May 21st, the initial guess on May 16th is modified such that the phase difference between the two trajectories is nullified. This is realized by propagating the initial state on the stacked orbits of May 21st backward in time until it reaches May 16th as shown by the green line in figure 5.20. The starting point on the green line corresponds to a different location on the NRHO as seen in figure 5.22. Therefore, stacking the NRHOs as a combination of the green and the red line removes the phase difference between the two initial guesses starting on the two different epoch dates. This is equivalent to including a partial arc of the NRHO (of time-period five days) as the first orbit in the stacking process followed by the traditionally stacked orbits starting from the \hat{x} - \hat{z} plane. Transitioning the newly stacked orbits which starts at

a different NRHO location on May 16th, will converge to a quasi-periodic solution which retains the synodic structure. Applying the differential corrections process to the newly stacked orbit on May 16th results in the trajectory as shown in figure 5.22. The first patch point is now not close to the periapsis but starts at a location indicated by a blue marker near the apoapsis region. For comparison, trajectories converged using the old and the modified stacking sequence on May 16th are shown in figure 5.21 and figure 5.22. The blue markers indicate the first patch point on the trajectories. It is visually clear that the converged trajectory due to the new stacking sequence is "tighter" and less spread apart compared to the older method and retains the synodic behavior. The Sun-Earth and the Sun-Moon rotating frame views corresponding to the old and new stacking sequences are also shown in the plots. The trajectory attained using the old stacking sequence remains non-repetitive and has a large spread in the Sun-Moon and Sun-Earth rotating frames. Clearly, it is more prone to eclipses due to the Earth and the Moon. The trajectory obtained using the new stacking sequence remains in a synodic, less spread out formation in the Sun-Moon and Sun-Earth rotating frames and is generally less prone to eclipses due to the "wide gaps" along the line of shadow, i.e., \hat{x} -axis. This method can be used on any epoch date and for any NRHO provided there is a nearby tighter baseline trajectory. This technique is also useful to converge trajectories on days which usually do not show convergence with the traditional stacking method.

5.3.2 Periapsis Control - a Non-homogeneous Stacking Sequence

Previous studies have shown that eclipse durations on an NRHO typically are in the range of 1-2 hours due to Moon and 4-5 hours due to the Earth [47]. Eclipses are generally avoided by performing a phase shift maneuver in advance, to shift the epoch of the periapsis in the eclipse region by a certain number of hours. This delays or advances the arrival of the spacecraft into the eclipse region and helps to avoid the eclipse partially or completely. This is equivalent to generating a new reference tra-

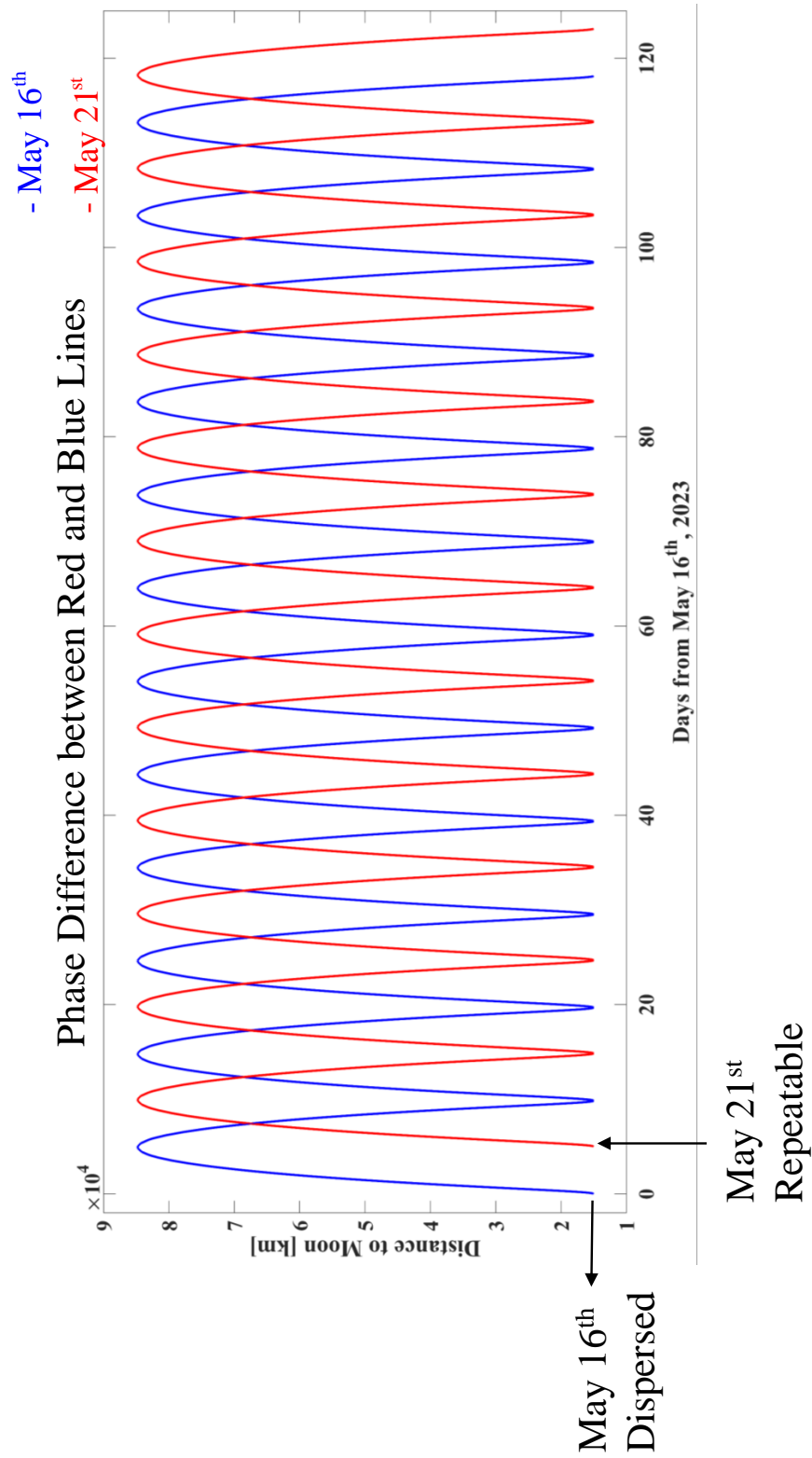


Figure 5.19. Ephemeris trajectory comparison on May 16th and May 21st, 2023.

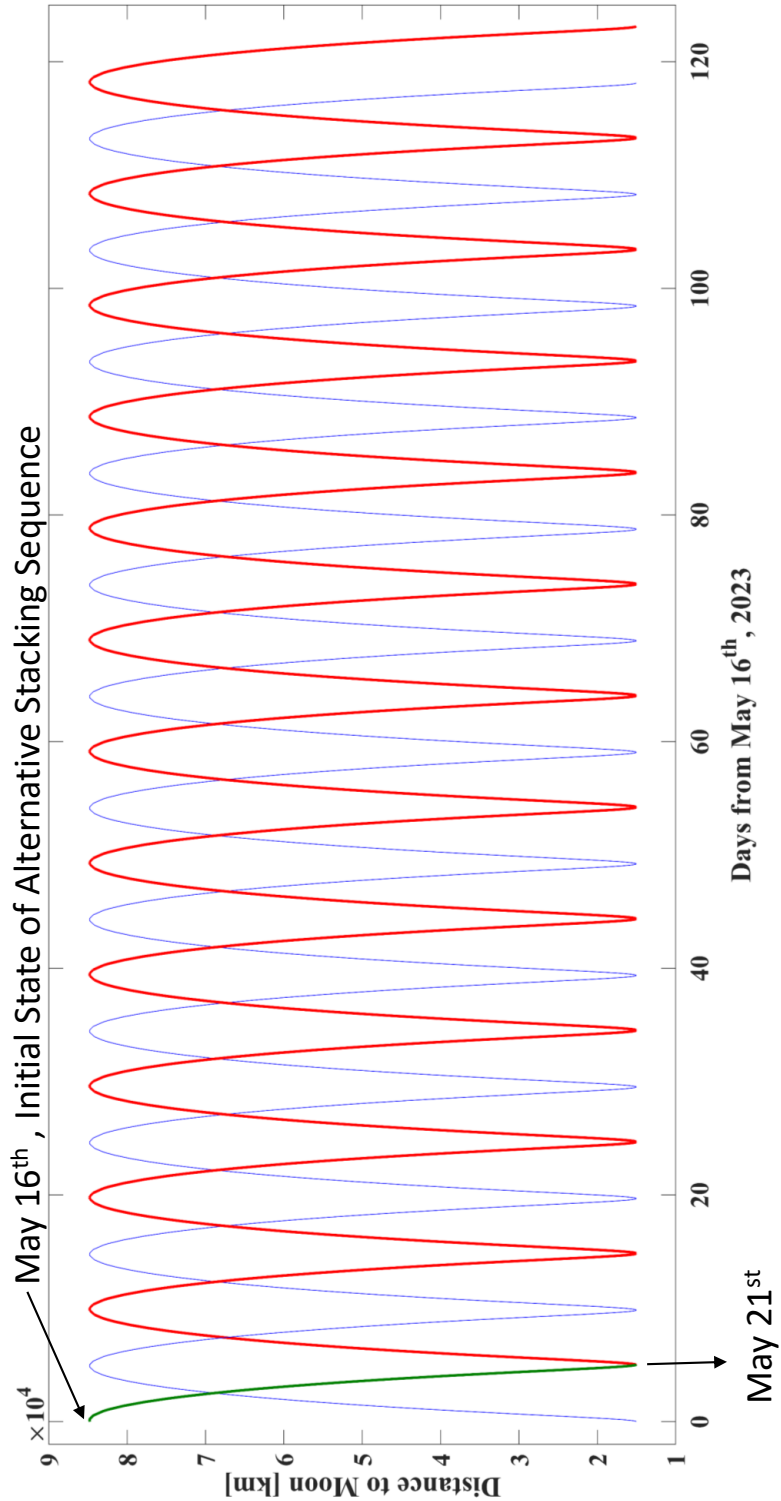


Figure 5.20. Alternative stacking sequence on May 16th to remove phase difference.

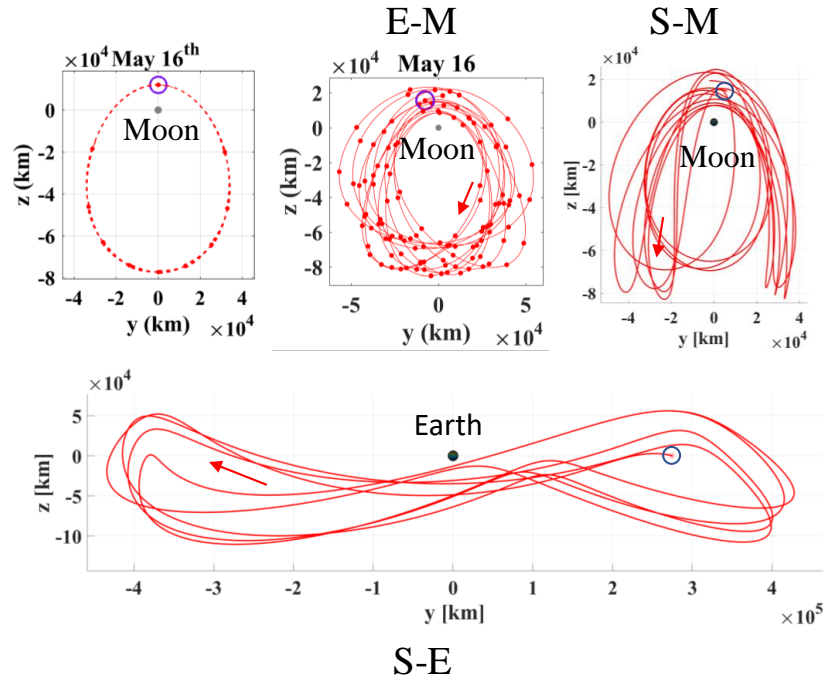


Figure 5.21. Traditional stacking sequence on May 16th, 2023.

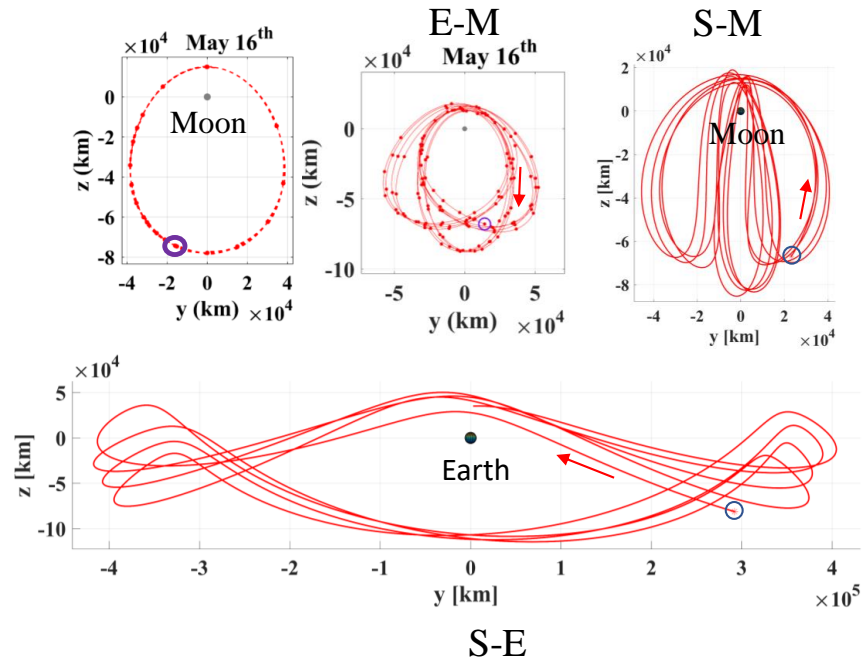


Figure 5.22. Alternative stacking sequence on May 16th, 2023.

jectory starting from the maneuver location, whose periapsis is shifted with respect to the original trajectory to avoid the eclipse. The goal of this part of the investigation is to generate a new reference trajectory by employing a non-homogeneous stacking sequence to have a better periapsis control while maintaining the less spread out, synodic ephemeris convergence on any epoch date.

Consider the traditional stacking sequence from the previous section in which L_2 NRHOs are stacked one after another starting from the periapsis location on the \hat{x} - \hat{y} plane. When transitioned into the higher fidelity ephemeris model, the quasi-periodic NRHO generated on May 2nd is less spread out and tighter compared to the nearby epoch dates as seen in figure 5.11. Before transitioning into the ephemeris model, the stacked initial guess in the CR3BP is seen in figure 5.10. When transitioned into a higher fidelity model the periapsis of the ephemeris solution will no longer occur at the original periapsis locations of the stacked CR3BP trajectory. Instead, the new periapsis of the ephemeris trajectory occurs in the close vicinity to the periapsis patch points of the CR3BP. To illustrate this point, consider the figure 5.23 . Starting from the epoch date of May 2nd the distance of the traditionally stacked NRHOs to the Moon in the CR3BP model is shown as a blue line. As expected in the CR3BP the apoapsis and periapsis distances are equal. All the patch points on the trajectory are marked with blue dots on the curve. The distance of the corresponding ephemeris trajectory starting on the same epoch date is shown as a red line. Patch points of the ephemeris trajectory are added to the curve with red dots. It is immediately clear from the plot that even though both the trajectories begin from the same epoch, there is a noticeable phase difference between the two trajectories. The periapsis of the ephemeris solution are shown as green dots on the red line and occur close to the CR3BP periapsis patch points. For illustration, a hypothetical eclipse event is assumed to take place when the spacecraft arrives close to the sixth ephemeris periapsis. Eclipse can be completely avoided if the arrival time at the sixth periapsis is either advanced or delayed by an amount greater than the eclipse duration. To

demonstrate this example, a delay of 6 hours in arrival at the 6th ephemeris periapsis is planned. This is achieved by generating a new ephemeris trajectory which starts at the same epoch date, i.e., May 2nd, but arrives at the 6th periapsis later than the original ephemeris trajectory by 6 hours. This is equivalent to generating a new reference trajectory by performing a phase shift maneuver to escape the eclipse. A non-homogeneous stacking sequence is explored in the CR3BP by implementing the following steps to generate the new reference trajectory which will potentially avoid the eclipse.

Step 1: Calculate the new epoch of the target periapsis:

In the present example, the target periapsis of the ephemeris trajectory whose epoch is to be delayed by 6 hours is the 6th ephemeris periapsis which occurs at a time $t = 49.134064$ days from the ephemeris insertion date on May 2nd. The region near the 6th periapsis of the ephemeris trajectory is seen in figure 5.23. The green and blue dots indicate the 6th ephemeris periapsis and the 6th CR3BP periapsis respectively. The goal is to generate a nearby ephemeris solution whose 6th periapsis is delayed by 6 hours. Hence the new epoch of the targeted periapsis corresponds to the following number of days after the insertion epoch,

$$t_{target} = \left(49.134064 + \frac{6}{24} \right) \text{ days} \quad (5.2)$$

Step 2: Calculate the time difference between the new epoch of target periapsis and the corresponding CR3BP periapsis:

In the figure 5.23, the green dot indicates the 6th periapsis of the reference ephemeris trajectory, the blue dot indicates the 6th perilapsis of the CR3BP trajectory and the green dot on the black dotted line indicates the new 6th periapsis of the desired ephemeris trajectory (whose epoch has been calculated in step 1 as t_{target}). In this step the difference between the epoch of the 6th CR3BP periapsis and

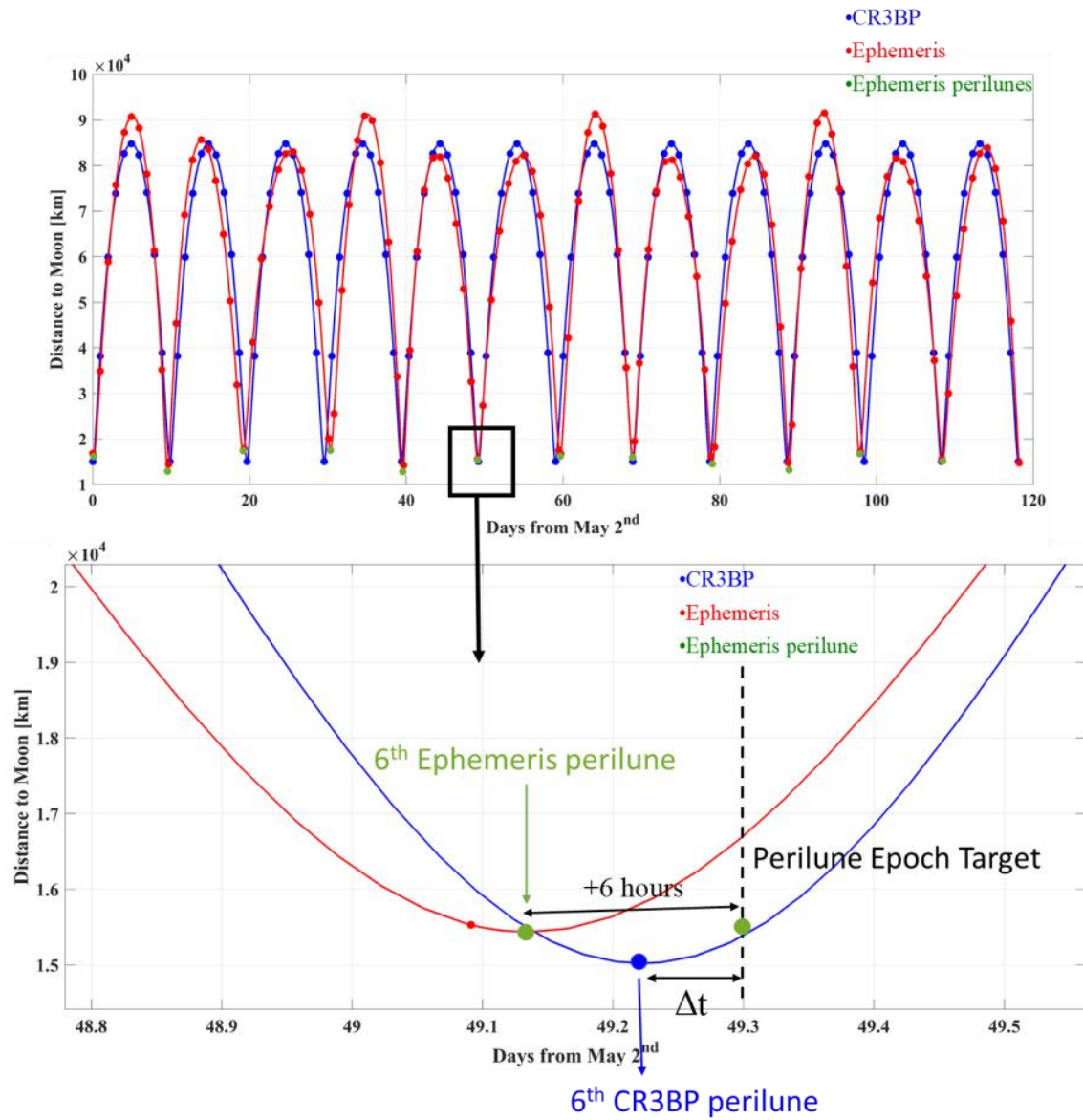


Figure 5.23. Distance to Moon: Stacked NRHOs in CR3BP and Ephemeris trajectory on May 2nd.

the new epoch of the targeted periapsis is calculated, which will be used in the next step to alter the stacking sequence. The difference is calculated as follows,

$$\Delta t = t_{target} - t_{CR3BP} = \left(49.134064 + \frac{6}{24} - 49.22000 \right) \text{ days} \quad (5.3)$$

Step 3: Use the Δt to generate an alternative stacking sequence:

The Δt calculated in the previous step is equal to 3.937536 hours. The eclipsing epoch lies in between the 5th and the 6th NRHOs in the stacking sequence. These orbits are replaced by a set of new nearby NRHOs whose time periods are equal to the following,

$$5^{th} \text{ NRHO} = (9.844 + \Delta t) \text{ days} \quad (5.4)$$

$$6^{th} \text{ NRHO} = (9.844 - \Delta t) \text{ days} \quad (5.5)$$

The new 5th NRHO delays the epoch of the 6th CR3BP periapsis to match the target epoch and the new 6th NRHO maintains the overall time-period of the stacked orbits to be equal to the original stacked trajectories. Since non-identical NRHOs are included into the stacking sequence, it is termed as a non-homogeneous stacking process and is shown in figure 5.24.

Step 4: Transition the non-homogeneous stacked trajectories into ephemeris model:

In the final step, transition the modified stacked trajectories in figure 5.24, into the ephemeris model and apply the necessary constraints on the patch points during the corrections process. In the current example, the 6th periapsis of the non-homogeneous CR3BP stack is associated with the target epoch, and therefore it is maintained upon ephemeris transition by constraining its epoch and periapsis condition. The epoch of the first state on the ephemeris trajectory may or may not be constrained but to compare it with the original ephemeris trajectory it is constrained in the current

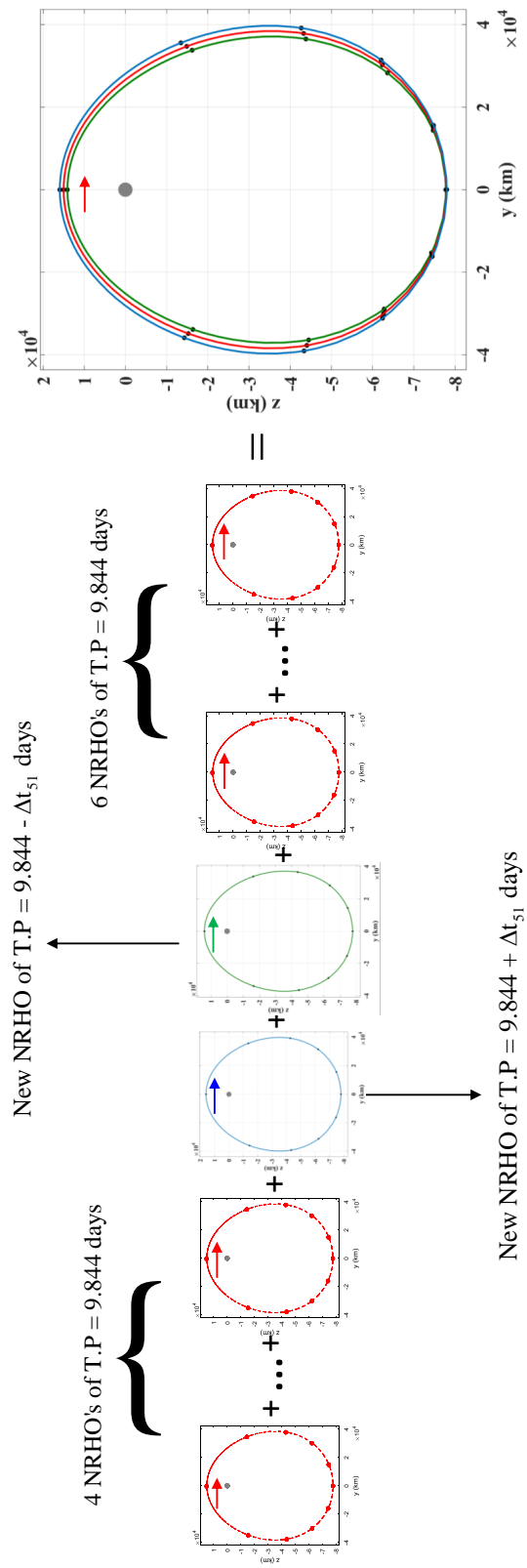


Figure 5.24. Non-homogeneous stacking sequence.

example. The newly converged ephemeris trajectory is plotted together with the original trajectory in figure 5.25. The new and the old ephemeris trajectories are marked in cyan and red colors respectively. To compare the two trajectories their distances to the Moon with respect to their epochs are plotted in figure 5.26. The new trajectory occurs in close vicinity to the original trajectory. The 6th periapsis of the new ephemeris solution is exactly delayed by 6 hours compared to the original solution. Therefore at the time of the eclipse, the spacecraft would be at a different location when compared to the original ephemeris trajectory. Also, note that, within the current implementation, the phase shift for other periapsis and their nearby patch points is purely a by-product of the corrections process. The converged trajectory retains the less spread out nature and has a tighter appearance and is shown in figure 5.25.

The Non-homogeneous stacking sequence can be employed to shift the epochs associated with multiple periapsis in the ephemeris trajectory thereby avoiding potential eclipses in a reliable way. It can also be effectively used to control the periapsis radius of the target periapsis by making an informed selection of periodic orbits, that formulate the stacking sequence.

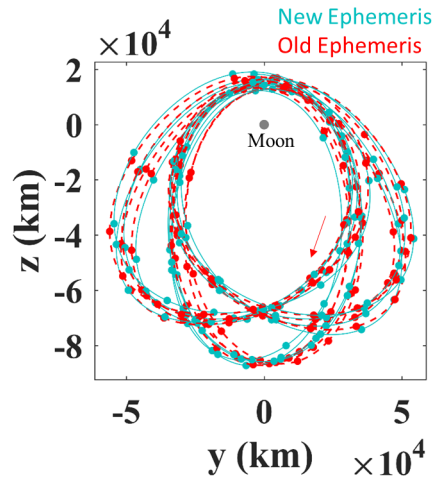


Figure 5.25. Old and new ephemeris trajectories.

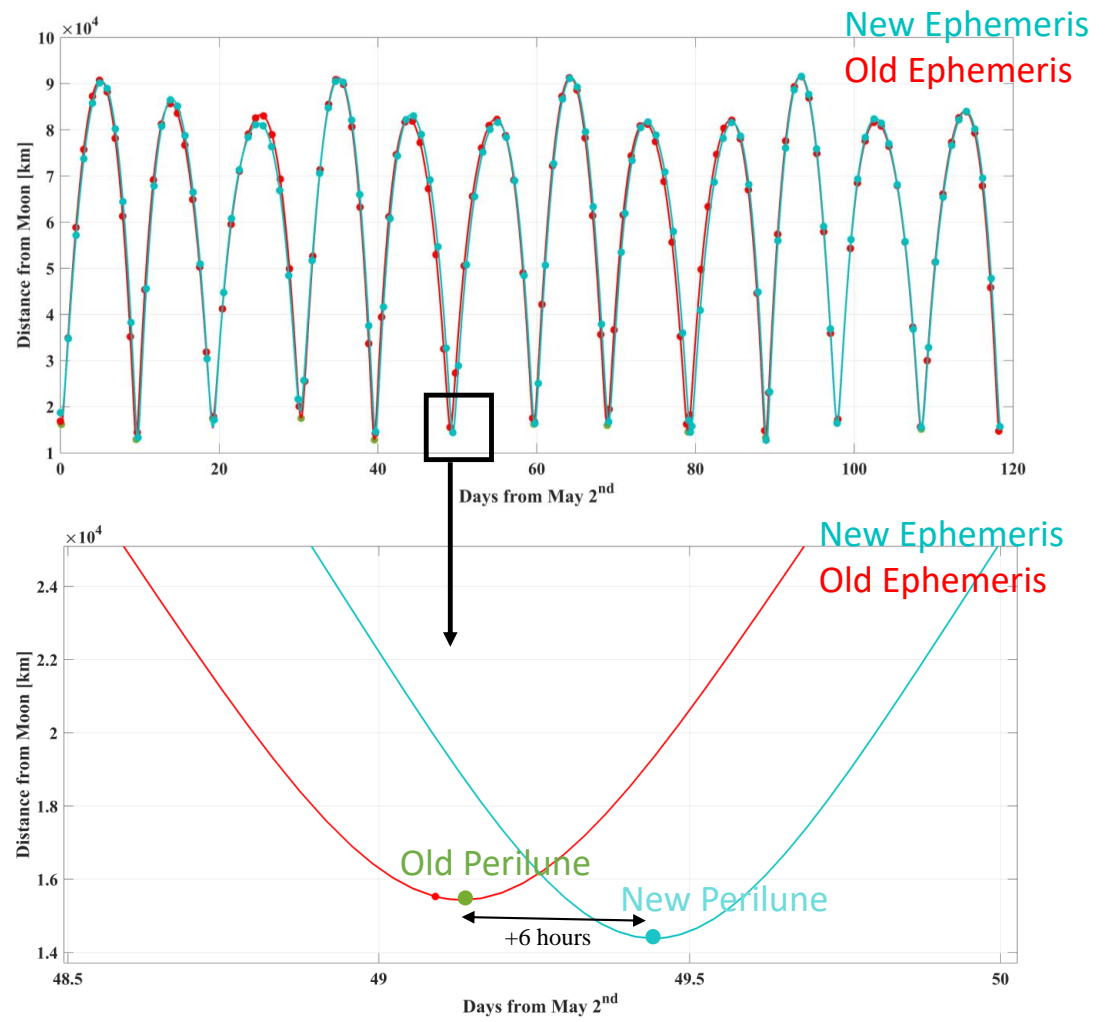


Figure 5.26. Old and new ephemeris trajectories - distance to Moon.

6. TRANSFER DESIGN INCORPORATING RESONANT ORBITS : METHODOLOGY AND RESULTS

In the previous chapter, an alternative stacking sequence has been demonstrated to consistently converge NRHOs in the CR3BP model to less spread out quasi-periodic ephemeris trajectories, irrespective of the epoch dates. An eclipse avoidance strategy was also described in which a new nearby reference trajectory was generated, in which a target periapsis lying in the potential eclipse zone was shifted outside by altering its epoch time. This chapter explores various transfer scenarios between two cislunar periodic orbits, namely a representative NRHO and a Distant Retrograde Orbit (DRO), primarily using resonant orbits and manifolds as intermediate arcs. First, the representative NRHO and the DRO are selected followed by describing the design methodology adopted to produce various transfer options between them. The results of various transfers will be presented and will be locally optimized using a direct optimization technique. The optimized trajectories will be transitioned into the ephemeris model using Adaptive Trajectory Design software to assess the impact of higher fidelity on the geometry and transfer cost [46].

6.1 Representative NRHO - Departure Orbit

NRHOs which have a synodic resonance ratio with the Moon have been studied in the past as an efficient way to avoid eclipses for long duration staging activities [45]. Out of the various NRHO's computed in the section 5.1, for the rest of the analysis an L_2 9:2 southern synodic resonant orbit is considered as the departure orbit and is shown in the figure 6.1. The ratio indicates that the orbit completes nine revolutions around the Moon at the same time the Moon takes to complete two synodic time periods around the Earth. The resonance ratio becomes more distinct when the

trajectory is viewed in the Sun-Moon and the Sun-Earth rotating frames as seen in the figure 6.2 and 6.3. The natural parameters of the periodic orbit are given in the table 6.1.

Table 6.1. 9:2 L_2 synodic NRHO parameters.

Parameter	Value
Periapse radius	3153 km
Apoapse radius	71,230 km
Jacobi constant	3.047189
Time period (T_q)	6.56 days

6.2 Representative DRO - Arrival Orbit

DROs are a stable, planar periodic family extending from the neighborhood around the Moon with a smaller periapsis radius, all the way up to the Earth with large periapsis radius, moving in a retrograde direction in the CR3BP. For the rest of the analysis, the DRO orbit with the following natural parameters as shown in table 6.2 is used as the destination orbit for all the transfer scenarios. The representative DRO is shown in the figure 6.1.

Table 6.2. Representative DRO parameters.

Parameter	Value
Periapse radius	64658 km
Jacobi constant	2.937908
Time period (T_q)	12.72 days

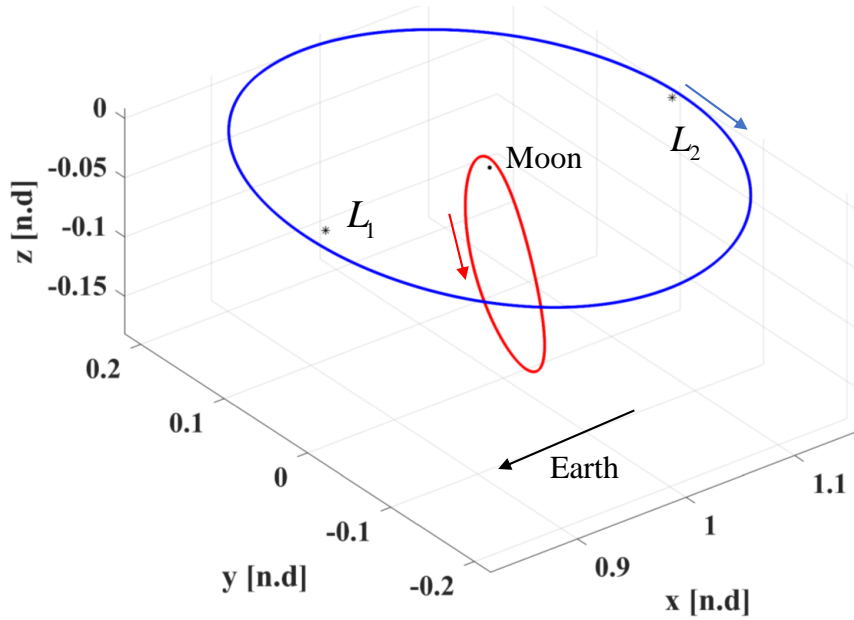


Figure 6.1. Representative NRHO and DRO.

6.3 Theoretical Minimum Transfer Cost

A change in the Jacobi constant associated with the CR3BP model is achieved by performing a maneuver at a given location on a trajectory. By changing the Jacobi constant, the spacecraft jumps on to a different arc. This is particularly useful for a transfer scenario between two stable periodic orbits where free of cost, heteroclinic connections are not possible due to the lack of manifolds. Performing a finite burn is the only way to jump off from the departure stable orbit or connect to the stable arrival orbit. Consider for instance a spacecraft located on the departure orbit of Jacobi constant C_1 as seen in figure 6.4 shown as a blue trajectory. Performing a burn of magnitude ΔV at an angle θ with respect to the original velocity places the spacecraft onto another arc with Jacobi constant C_2 shown as a dotted black trajectory. Notice that the two arcs have a common point in the configuration space at the burn location. From equation (2.34) the Jacobi constant expression for the departure stable orbit is written as,

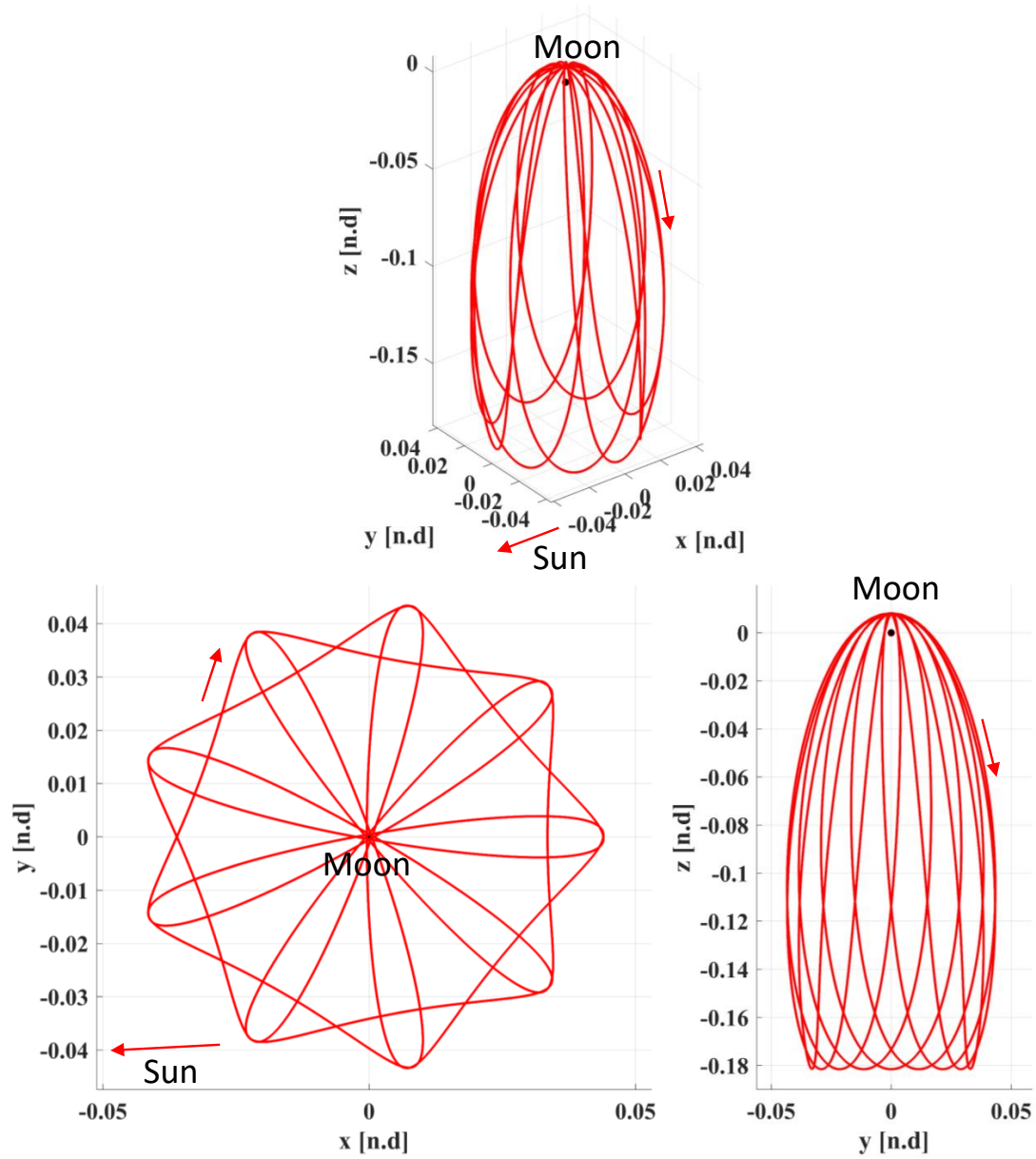


Figure 6.2. 9:2 synodic southern L_2 NRHO in the CR3BP - Moon centered, Sun - Moon rotating frame view.

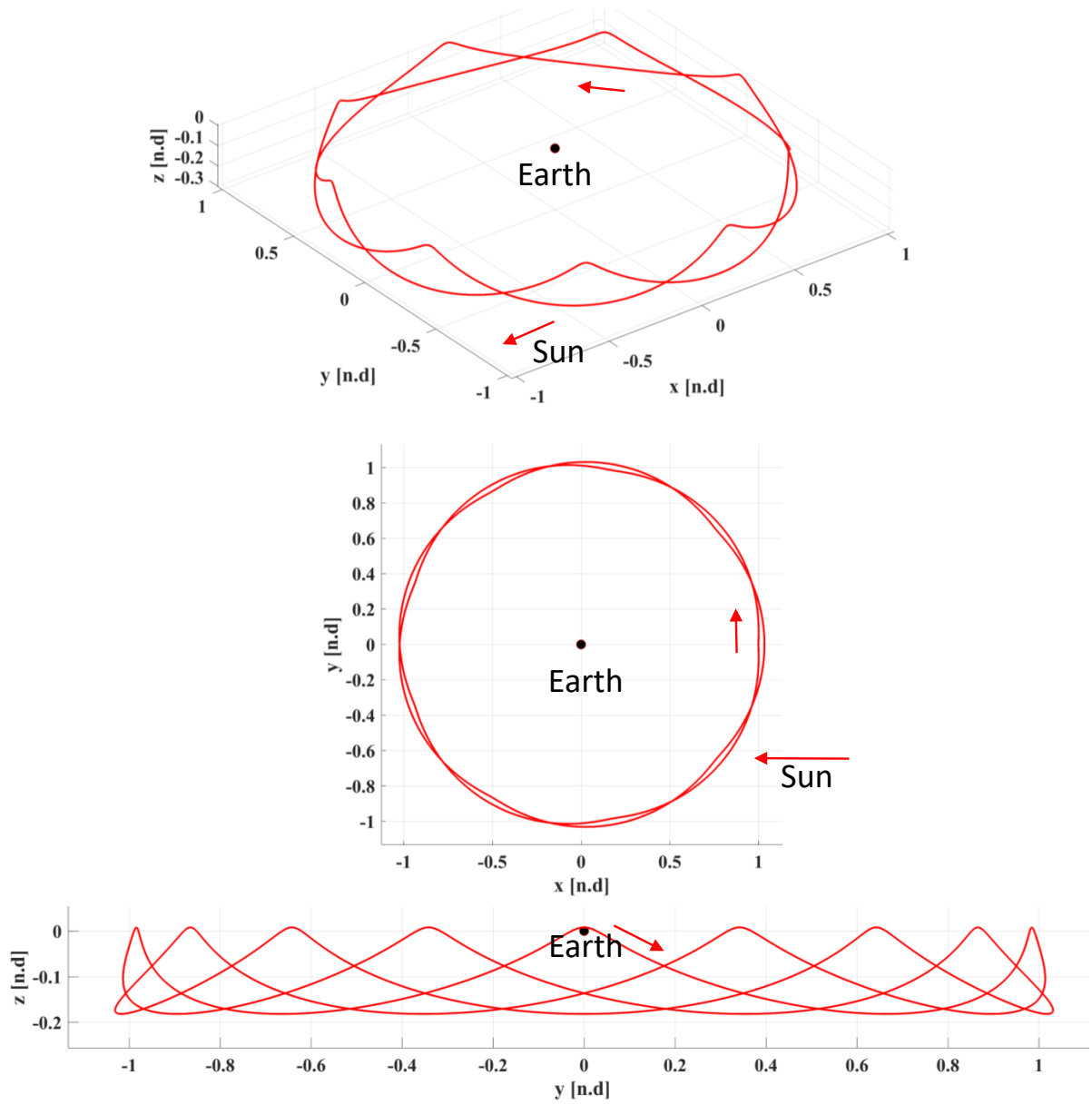


Figure 6.3. 9:2 synodic southern L_2 NRHO in the CR3BP - Earth centered, Sun - Earth rotating frame view.

$$C_1 = 2U_1^* - v_1^2 \quad (6.1)$$

Similarly the Jacobi constant expression for the second arc is,

$$C_2 = 2U_2^* - v_2^2 \quad (6.2)$$

At the departure point U_1^* is equal to U_2^* in equations (6.1) and (6.2). The difference in Jacobi constants is evaluated as follows,

$$\Delta C = C_1 - C_2 = v_2^2 - v_1^2 \quad (6.3)$$

The change in velocity for the maneuver is calculated using the expression,

$$\|\Delta \bar{v}\| = \Delta v = \sqrt{v_1^2 + v_2^2 - 2v_1v_2 \cos \theta} \quad (6.4)$$

The change in velocity in equation (6.4) is minimized when $\cos \theta = 1$. Substituting this back into equation (6.4) yields the minimum velocity change to jump from Jacobi constant C_1 to Jacobi constant C_2 ,

$$\min \Delta v = \sqrt{v_1^2 + v_2^2 - 2v_1v_2} \quad (6.5)$$

Substituting equation (6.5) into equation (6.3) results in an expression for minimum energy change between two Jacobi constants and a given initial velocity as,

$$\min \Delta v = \sqrt{2v_1^2 + \Delta C - 2v_1 \sqrt{\Delta C + v_1^2}} \quad (6.6)$$

Equation (6.6) corresponds to a tangential burn from the departure point. This implies that to jump from a Jacobi constant C_1 to C_2 , departing tangentially from the first arc corresponds to the lowest Δv . In the case of planar transfers for tangential departures, lower difference in Jacobi constant corresponds to lower Δv values. When a directional change in the velocity is required or when there is a plane change maneuver, the minimum energy change is non-zero in spite of the initial and final Jacobi

constants being the same.

For a transfer scenario between the representative departure NRHO and the arrival DRO in figure 6.1, the minimum energy change required to jump from the Jacobi constant of the NRHO to the Jacobi constant of the DRO from various locations on the NRHO is computed using the equation (6.6) and plotted in the figure 6.5. The minimum energy change or the minimum Δv required to depart from the periapsis region of the NRHO is significantly smaller than that needed to leave from its apoapsis region. This is because in equation (6.6), it is seen that larger initial velocities require smaller Δv for departure. Therefore, as the velocity near periapsis region is higher than the velocity near the apoapsis regions of the NRHO, the Δv needed to cause the fixed change in the Jacobi constant is smaller at the periapsis region. Minimum energy change is useful because it serves as a good reference value for comparing the transfer costs obtained in the various transfer scenarios which will be discussed in the coming sections.

6.4 Arc Blending Scheme - Transfer Design Process

The idea of incorporating manifolds to construct a low cost, novel transfer scenarios between two destinations in CR3BP is well established. In this regard, a lot of past research was focused on generating transfers between unstable periodic orbits in the CR3BP. Unstable periodic orbits have natural dynamical structures in the form of stable and unstable manifolds, which are leveraged to depart and arrive at a periodic orbit with almost a negligible cost. Haapala has developed new ways of representing Poincaré maps in lower as well as higher dimensions, using which she generated a catalog of free and low energy trajectories between several planar and spatial unstable libration point orbits in the Earth-Moon system [48]. On the other hand designing transfers between stable periodic orbits is often challenging due to the lack of natural dynamical structures. Vaquero and Howell have demonstrated

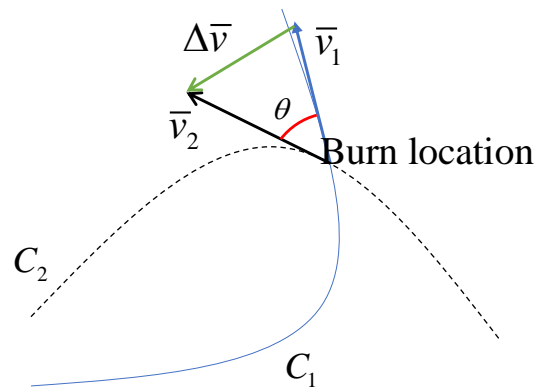


Figure 6.4. Minimum energy to change Jacobi constant.

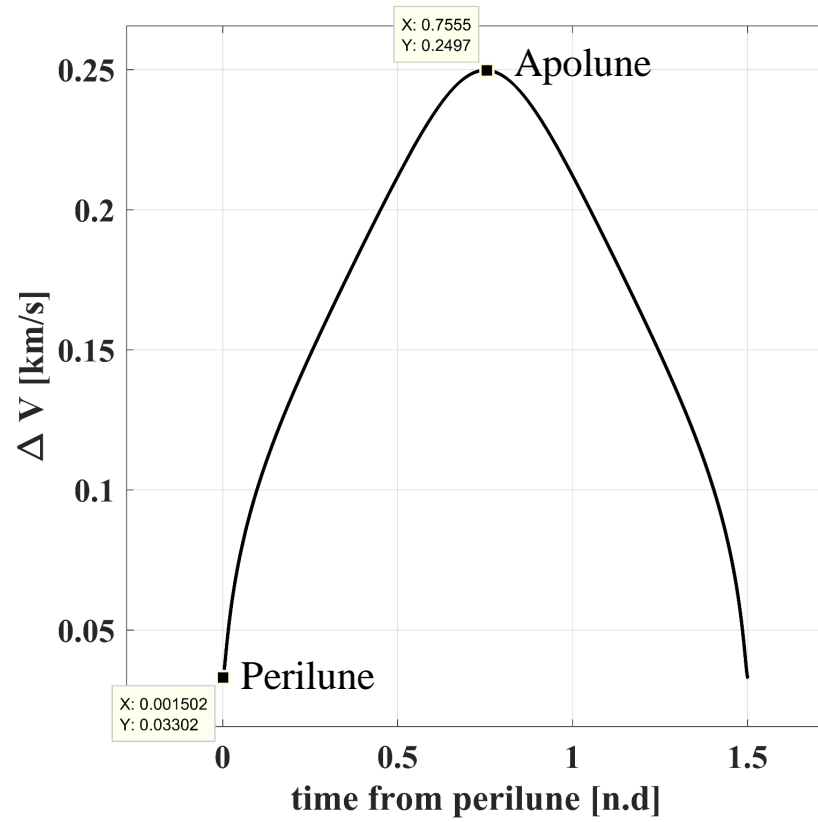


Figure 6.5. Theoretical Minimum Δv to jump from NRHO to DRO.

an innovative design strategy, in which arcs and manifolds of stable and unstable resonant periodic orbits were incorporated into the transfer design scenario by using them as intermediate transfer arcs for linking the stable/unstable departure and destination orbits [22]. Vaquero used this transfer strategy to access the stable orbit of Hyperion in the Saturnian system by leveraging the unstable manifolds of a 3:4 unstable resonant orbit [23]. She has incorporated resonant orbits and their manifolds into the transfer strategy for designing transfers from LEO to several planar and spatial Lyapunov periodic orbits in the Earth-Moon system [24]. The versatility of the resonant orbits and their natural dynamical structures were highlighted by using the manifolds associated with a 4:3 resonant orbit to design a grand libration point orbit tour around the five equilibrium points [22]. In the present context of generating transfers between cislunar stable periodic orbits, more recently Capdevila contributed to the infrastructure of a network of transfer trajectories connecting stable regions in the cislunar space specifically between LEO, DROs, NRHOs and L_4 and L_5 Short Period Orbits [29]. Zimovan created impulsive transfer solutions from a 4:1 synodic southern L_2 NRHO to several DROs by utilizing a multi-dimensional Poincaré map constructed using tangential departures from the apoapsis location on the NRHO and also manifolds of period-3-DROs [28]. The goal for this work is to explore and develop a systematic method for designing transfers between two stable cislunar periodic orbits namely from a representative NRHO to a DRO incorporating resonant arcs and manifolds into the transfer process.

Throughout the various transfer scenarios, a variety of Poincaré maps are utilized to come up with initial guesses for the intermediate arcs of a transfer. The intermediate arcs will be comprised of resonant arcs, resonant stable or unstable manifolds, tangential departures or tangential arrival arcs. This is accomplished in the CR3BP by selecting the desired intersections on the Poincaré map and integrating the selected initial conditions to form a discontinuous set of intermediate trajectories. The intermediate arcs are then carefully stacked to start at the departure orbit and end

at the arrival orbit as seen in the figure 6.6. Patch points are distributed along the intermediate arcs, thereby forming sub-arcs and necessary constraints such as periapsis, ΔV and TOF are introduced at the patch points during the corrections process. From the initial guess, a continuous transfer trajectory in position and velocity is obtained by implementing a multiple shooting differential corrections process. When a maneuver is introduced at a patch point, only the position continuity is ensured. Once a continuous transfer is generated, a direct optimization technique is applied to produce a locally optimal transfer. As a final step, the optimal trajectory is transitioned into the higher fidelity ephemeris model using ATD to evaluate the practical transfer costs. In summary, identifying the intermediate arcs and blending them to obtain a transfer trajectory is the goal. In the coming sections a variety of transfer scenarios between the representative 9:2 L_2 southern synodic NRHO to the DRO are computed using the above transfer design process.

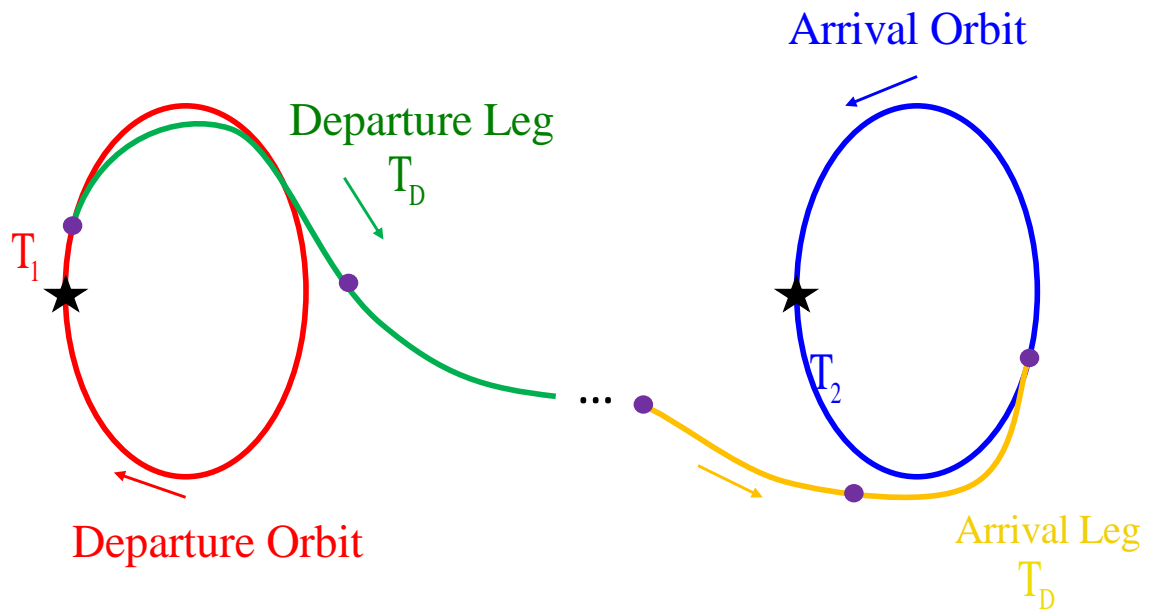


Figure 6.6. Arc blending scheme.

6.5 Direct Transfers from NRHO to DRO

A direct transfer is a single intermediate arc which departs from the NRHO and connects to the DRO. There are two burns in the transfer, one at the departure point on the NRHO and the other at the arrival location on the DRO. The search for a direct transfer begins with the discretization of the departure orbit, i.e., the NRHO. At the discretized states on the NRHO, tangential burns are performed along the direction of velocity, to jump from the Jacobi constant of the NRHO to a Jacobi constant of the representative DRO with a Δv given by equation (6.6). The new states are then integrated forwards in time until they intersect the hyperplane $z = 0$ for the first time as represented in the figure 6.7. All the intersections of the tangential departures with the hyperplane and their respective integration times are recorded and plotted on the Poincaré section given by the \hat{x} - \hat{y} plane as seen in the figure 6.8. The dots represent the intersections of the tangential departures from NRHO with the Poincaré section. The color bar on the right indicates the out of plane \dot{z} -velocity and the arrows on the section represent the magnitude and direction of the in-plane velocity. The representative DRO is also plotted on the Poincaré section. Tangential intersections on the map which come close to the DRO corresponds to a potential direct transfer and is shown in a red boxed area. Three such transfers are possible at the locations A, B and C on the DRO. For this transfer scenario, without the loss of generality, the location C is considered as the target arrival state on the DRO. The tangential intersection on the Poincaré map closest to the DRO is selected and integrated backward in time to the departure point on the NRHO. This forms the intermediate arc of the transfer. There is a slight discontinuity in states between the last state of the intermediate arc and the arrival location on the DRO. Sufficient patch points are distributed across the intermediate arc, and the position constraints are ensured at the first and the last state of the trajectory to match the NRHO and DRO at their departure and arrival target states respectively. As there are no maneuvers in between the intermediate arc continuity between all the patch points is ensured,

and a multiple shooting differential corrections process is applied to result in a direct transfer which starts on the NRHO and arrives at the DRO and is shown in the figure 6.9. For the converged trajectory the departure ΔV_d is 0.250 km/s and the arrival ΔV_a is 0.387 km/s . The total ΔV_t and total time of flight of the transfer are 0.637 km/s and 3.92 days respectively. The minimum theoretical transfer cost from the departure location is 0.258 km/s, but it takes a significantly higher ΔV due to the large plane change maneuver to arrive at the planar DRO from an almost perpendicular NRHO. It is to be noted that the solution is not optimal and is just one of the infinitely many direct transfers possible between the two orbits. Nevertheless, it will serve as a baseline trajectory and a good starting point to generate the remaining transfer scenarios.

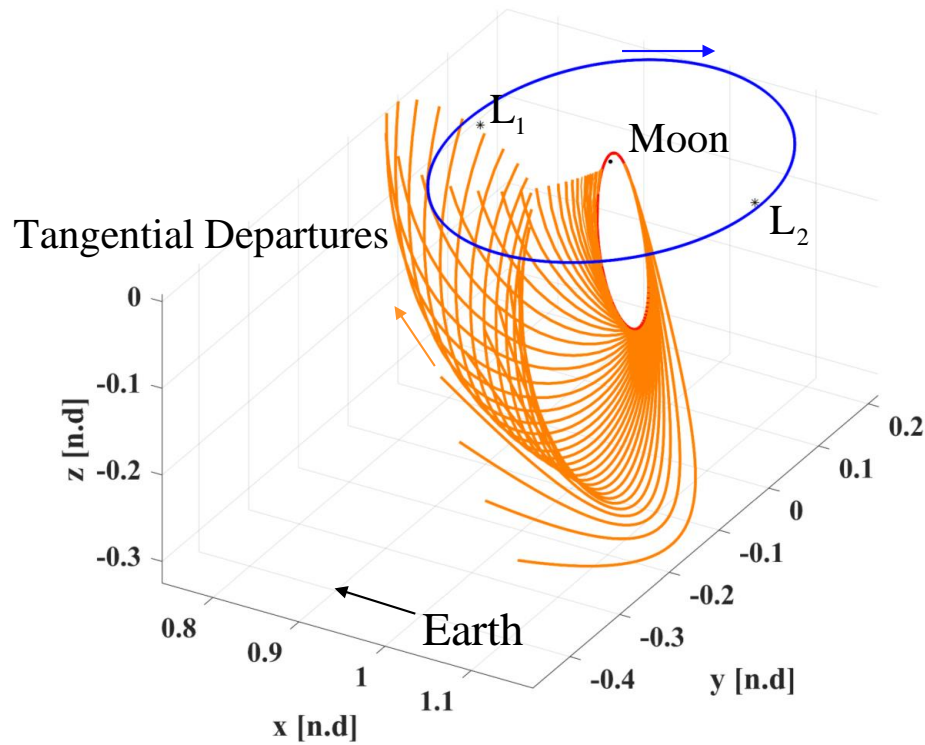


Figure 6.7. Tangential departures from NRHO to hyperplane $z=0$.

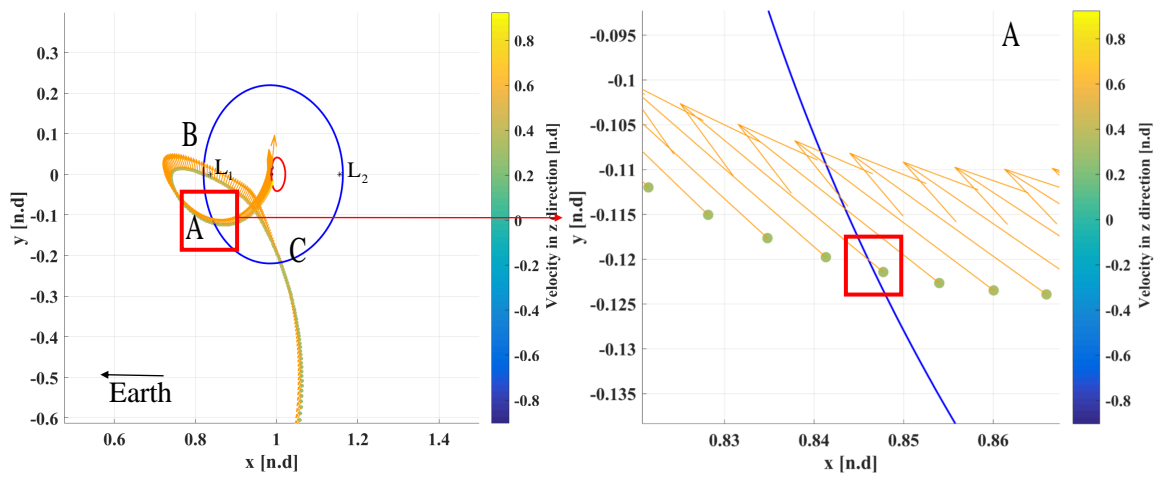
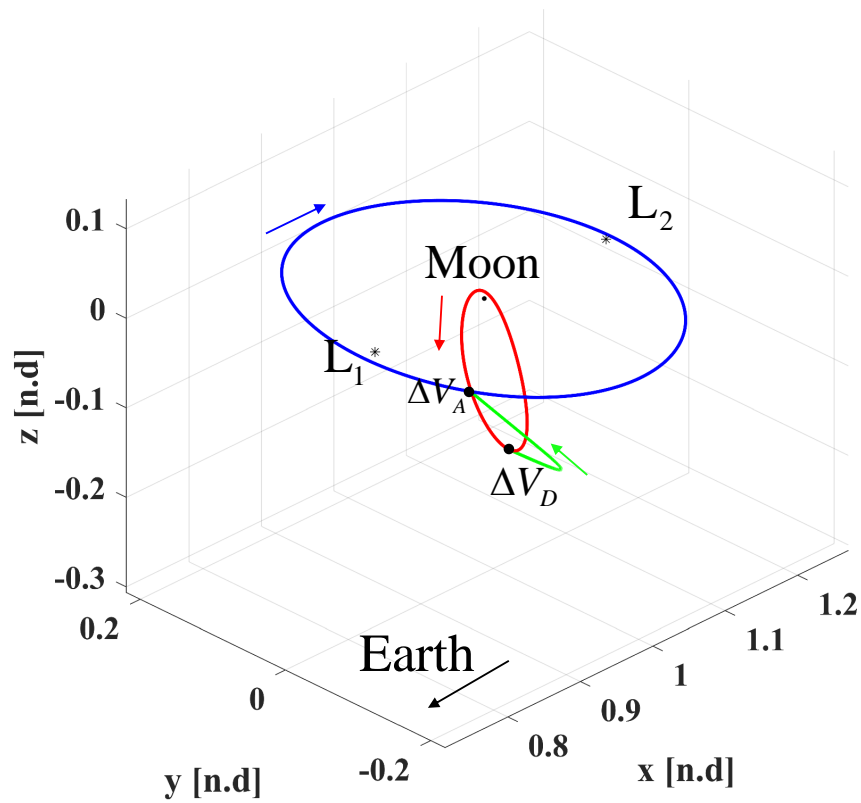
Figure 6.8. Poincaré map $z = 0$, $\dot{z} > 0$.

Figure 6.9. Direct transfer from NRHO to DRO.

6.6 Transfers Incorporating Resonant Arcs

In this transfer scenario, a section of a resonant orbit is incorporated as an intermediate arc in a transfer between the representative NRHO and the DRO. The selection of the intermediate resonant orbit is based upon its intersection with the DRO at its positive \hat{x} -axis crossing. This intersection condition is chosen because all the members of the DRO family and resonant orbits have perpendicular crossings along the \hat{x} -axis. There are multiple resonant orbits which cross the \hat{x} -axis perpendicularly with $\dot{y} > 0$ at the same location as the representative DRO. A plot showing the Jacobi constants for the 1:2, 2:3 and 3:4 exterior resonant orbits and their \hat{x} -axis crossings with $\dot{y} > 0$ is shown in the figure 6.10. The destination DRO is also represented in the plot with an asterisk mark. Notice that at the same \hat{x} -axis crossing the Jacobi constant of the 1:2 resonant orbit is the smallest and the Jacobi constant of the 3:4 resonant orbit is the largest. The J.C of the DRO is greater than the three resonant arcs at the desired \hat{x} -axis crossing. Without the loss of generality, a 1:2 resonant orbit is chosen as the intermediate resonant arc. Choosing another resonant orbit will not change the design methodology but may change the TOF and ΔV of the transfer. Figure 6.11 represents both the 1:2 resonant orbit and the representative DRO plotted together. As expected the resonant orbit and the DRO cross the \hat{x} -axis at the same location. This is useful because staying on the resonant orbit will bring a spacecraft close to the vicinity of the DRO and is inserted into the DRO by performing a necessary maneuver at the \hat{x} -axis crossing, i.e., the common intersection point of the DRO and the resonant orbit. To obtain the departure leg, tangential maneuvers are performed at the discretized states on the NRHO, to jump to a Jacobi constant of the intermediate orbit, i.e., the 1:2 resonant orbit, with magnitudes of the burns given by equation (6.6). The new states are then integrated forwards in time until they intersect the hyperplane $z = 0$ and $\dot{z} > 0$ for the first time. All the intersections of the tangential departures with the hyperplane and their respective integration times are recorded and plotted on the Poincaré section given by the \hat{x} - \hat{y}

plane as seen in the figure 6.11. The dots represent the intersections of the tangential departures from NRHO with the \hat{x} - \hat{y} plane. The color bar on the right indicates the out of plane \hat{z} -velocity and the arrows on the section represent the magnitude and direction of the in-plane velocity. The representative DRO and the 1:2 Resonant orbit is also plotted on the Poincaré section. Tangential intersections on the Poincaré map which come close to the resonant orbit corresponds to a potential departure leg. One such point at A is selected and integrated backwards in time to the departure point on the NRHO, which forms the departure leg of the transfer. The arrival leg of the transfer is the arc of the 1:2 resonant orbit which starts at point A and ends at the positive \hat{x} -axis crossing at point B. The two intermediate arcs form the initial guess for the corrections process. Patch points are distributed along the two intermediate arcs and continuity in both the position and velocity is ensured individually within each leg. Maneuvers are introduced at departure patch point on the NRHO, intermediate patch point which connects the two legs and the arrival patch point on the DRO. A multiple shooting algorithm is used to blend the two intermediate arcs to form a continuous trajectory which departs from a certain location on NRHO and arrives at the \hat{x} -axis crossing of the DRO and is shown in figure 6.12. The three ΔV 's and the TOF of the trajectory is given in the table 6.4. It is to be noted that the solution is not optimal. One indicator of the efficiency of the transfer is the variation of Jacobi constants across the intermediate arcs. In the transfer computed using the 1:2 resonant arc the Jacobi constant changes in the manner as shown in table 6.3.

Table 6.3. Transfer using 1:2 resonant arc, Jacobi constant history.

Parameter	Jacobi constant
Departure orbit (NRHO)	3.047189
Departure arc (Tangential departure)	2.761475
Arrival arc (1:2 resonant arc)	2.761326
Arrival orbit (DRO)	2.937908

From table 6.3, the Jacobi constants of the intermediate arcs are lesser than the departure and the final orbits. This makes the transfer inefficient. More efficient transfers are sought by ensuring that the Jacobi constants of the intermediate arcs lie between the departure and arrival orbits. Different transfer options exist with the use of other intermediate resonant arcs. In figures 6.13 and 6.14 two new transfers using 2:3 and 3:4 resonant orbits are shown. Tables 6.5 and 6.8 shows the ΔV and TOF of the corresponding transfers. A 4:3 internal resonant orbit is also used by connecting to the DRO on the \hat{x} -axis at the negative crossing. The transfer is shown in figure 6.15. Table 6.7 indicates the total ΔV and TOF for this transfer. All the four transfer scenarios have unique transfer geometries with varying transfer costs and TOF.

6.7 Transfers Incorporating Resonant Manifolds

Recall that the choice of the intermediate arc partly influences the cost-effectiveness of the transfer. Choosing an intermediate arc, whose Jacobi constant lies in between the departure and the arrival orbits, is more cost-effective than choosing an intermediate arc whose Jacobi constant lies outside the range of the departure and arrival orbits. Consequently, in this transfer scenario, an unstable resonant manifold of a 3:4 resonant orbit which has the same Jacobi constant as the departure NRHO is chosen as the intermediate arc. The departure NRHO, intermediate 3:4 resonant orbit and the arrival DRO are plotted together in the figure 6.16. The resonant orbit has a close encounter (flyby) with the Moon. The first Poincaré map is formed on the $y = 0$, and $\dot{y} > 0$ hyperplane using the unstable resonant manifolds of the 3:4 resonant orbit. The resonant orbit is first discretized into 20,000 points, and unstable manifolds are propagated for a time equivalent to two time periods of the resonant orbit, i.e., for 147 days. All the states and times of intersection with the hyperplane $y = 0$ in the positive direction, i.e., $\dot{y} > 0$ are recorded and plotted on the Poincaré map shown in the figure 6.17. The intersection of the representative DRO with the hyperplane is

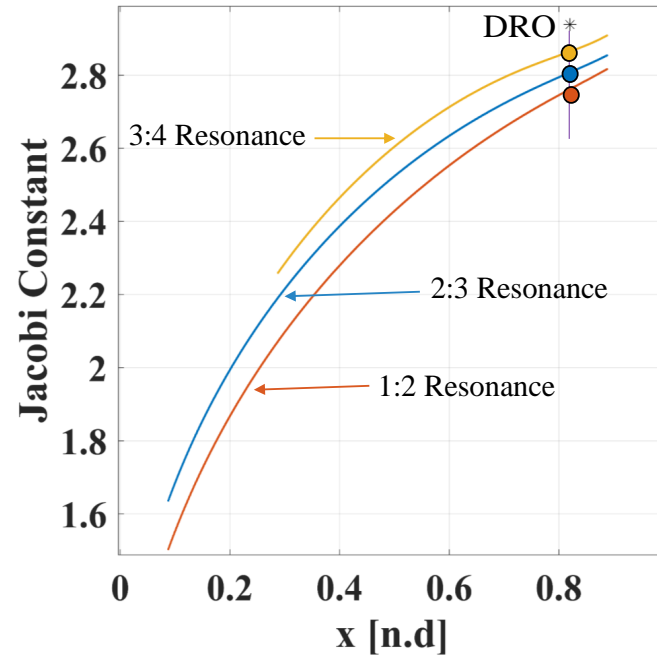


Figure 6.10. Potential resonant orbits for intermediate arcs.

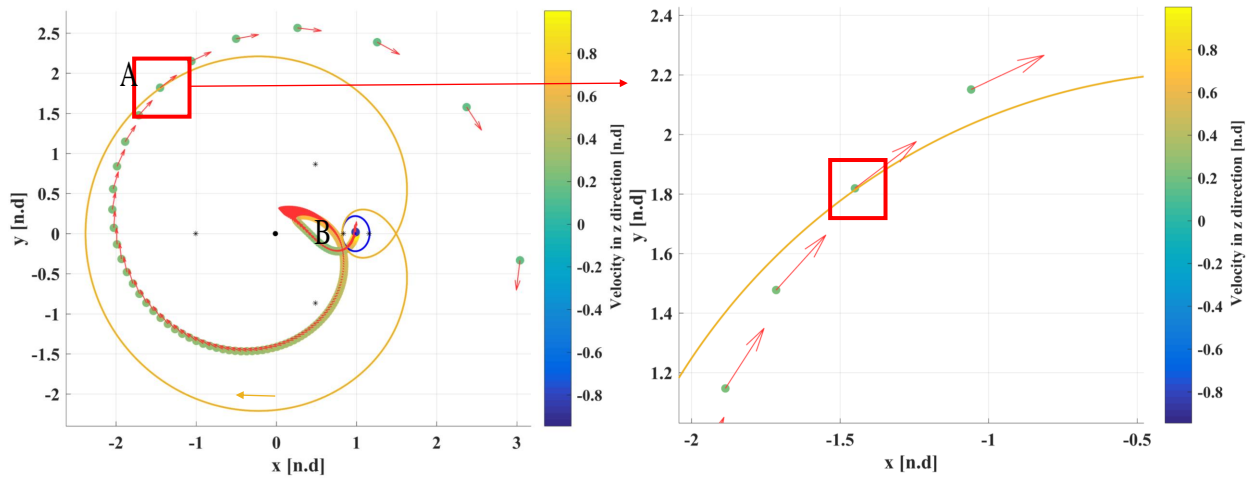


Figure 6.11. Transfer incorporating 1:2 resonant arc - Poincaré map $z = 0$, $\dot{z} > 0$.

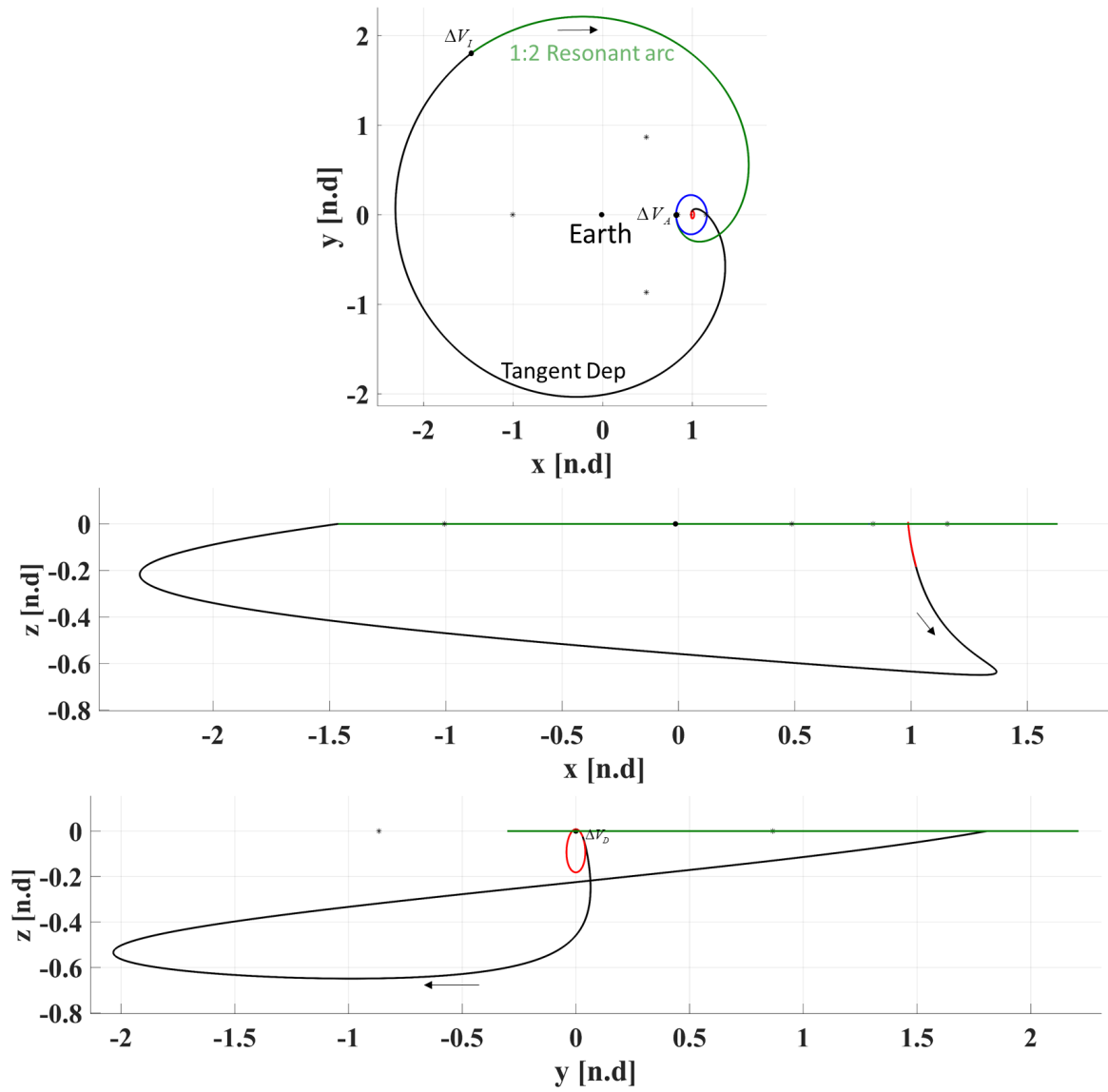


Figure 6.12. Transfer between NRHO and DRO using 1:2 resonant arc.

Table 6.4. Transfer using 1:2 resonant arc, transfer costs and TOF.

Parameter	Value
ΔV_D	0.181 km/s
ΔV_I	0.220 km/s
ΔV_A	0.156 km/s
ΔV_{tot}	0.557 km/s
TOF	50.70 days
Departure time from NRHO periapsis	0.198 days
Arrival time from DRO periapsis ($\dot{y} > 0$)	0 days

Table 6.5. Transfer using 2:3 resonant arc, transfer costs and TOF.

Parameter	Value
ΔV_D	0.176 km/s
ΔV_I	0.265 km/s
ΔV_A	0.119 km/s
ΔV_{tot}	0.560 km/s
TOF	76.80 days
Departure time from NRHO periapsis	0.289 days
Arrival time from DRO periapsis ($\dot{y} > 0$)	0 days

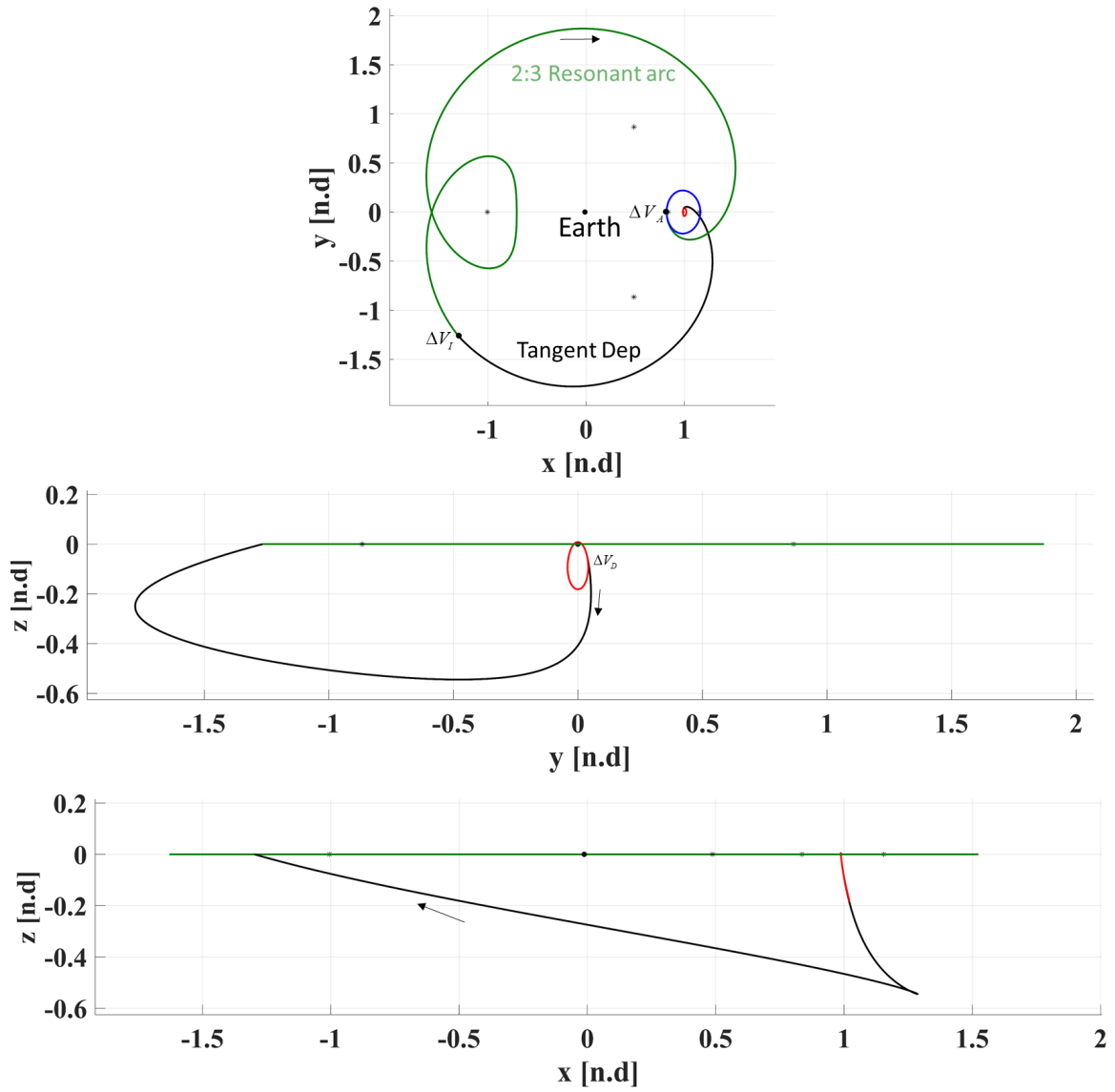


Figure 6.13. Transfer between NRHO and DRO using 2:3 resonant arc.

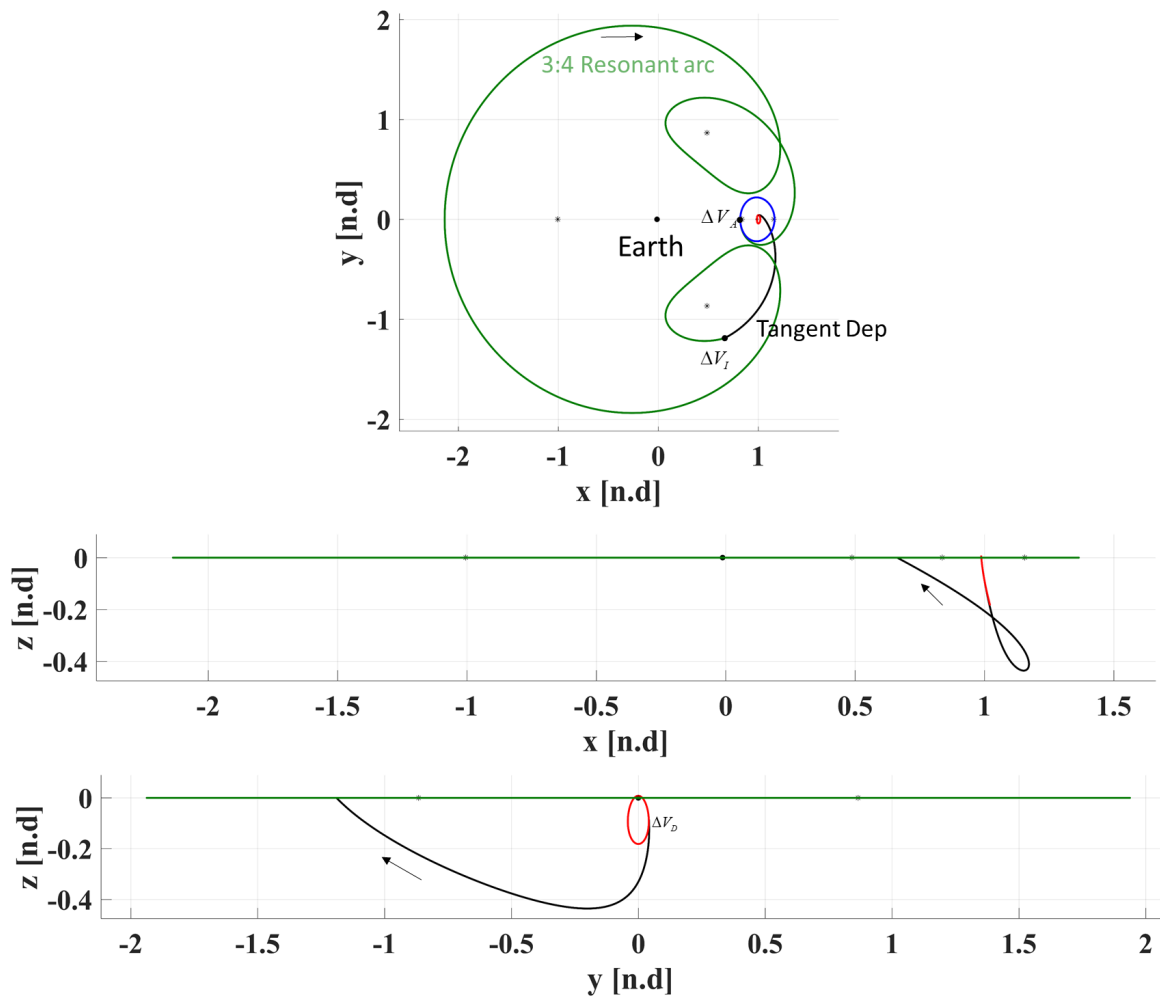


Figure 6.14. Transfer between NRHO and DRO using 3:4 resonant arc.

Table 6.6. Transfer using 3:4 resonant arc, transfer costs and TOF.

Parameter	Value
ΔV_D	0.174 km/s
ΔV_I	0.332 km/s
ΔV_A	0.070 km/s
ΔV_{tot}	0.576 km/s
TOF	106.15 days
Departure time from NRHO periapsis	0.551 days
Arrival time from DRO periapsis ($\dot{y} > 0$)	0 days

Table 6.7. Transfer using 4:3 resonant arc, transfer costs and TOF.

Parameter	Value
ΔV_D	0.489 km/s
ΔV_I	0.360 km/s
ΔV_A	0.190 km/s
ΔV_{tot}	1.039 km/s
TOF	78.20 days
Departure time from NRHO periapsis	3.34 days
Arrival time from DRO periapsis ($\dot{y} > 0$)	6.36 days

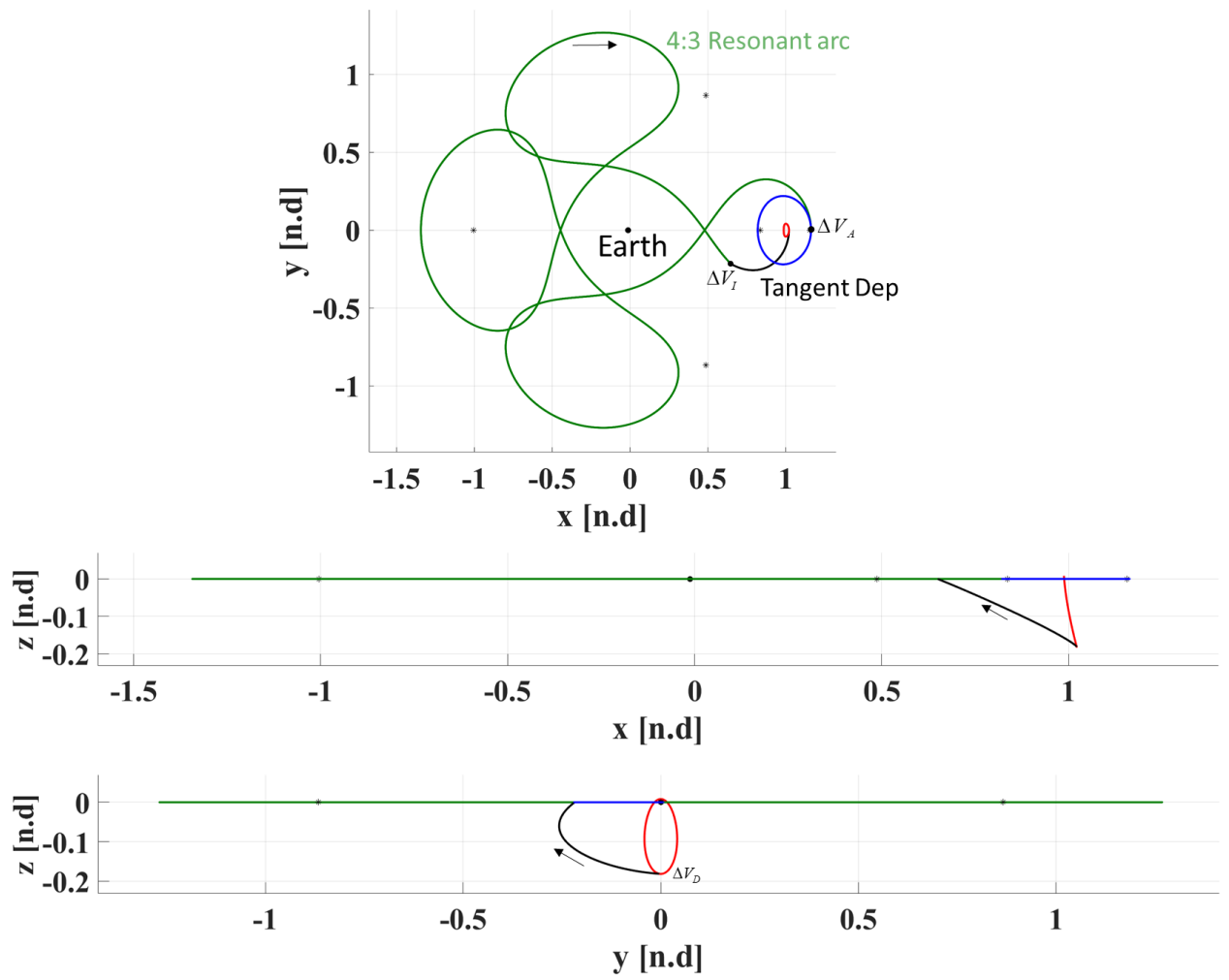


Figure 6.15. Transfer between NRHO and DRO using 4:3 resonant arc.

shown on the plot with a black asterisk mark. As an intermediate unstable manifold arc, the state on the Poincaré map closest to the DRO at point A is chosen. The state is propagated back to the resonant orbit, and while doing so, the intersections of the unstable resonant manifold with the hyperplane $y = 0$ and $\dot{y} > 0$ are recorded. To generate an initial guess for the departure leg, tangential burns with a small ΔV of 20 m/s are performed in the direction of the velocities on the discretized states of the NRHO. The new initial conditions on the NRHO are propagated forwards in time until they intersect the hyperplane $y = 0$ and $\dot{y} > 0$ for the 4th time as seen in figure 6.18. The intersections of the tangential departures and the integration times are recorded and plotted on the second Poincaré map as seen in figure 6.19, which will help to pick the departure leg from NRHO that connects to the unstable resonant manifold found using the 1st Poincaré map. The intersection of the selected unstable manifold with the second Poincaré map is marked with a red asterisk marker in figure 6.19. The nearest state of the departure leg to the unstable manifold intersection at point B is chosen and is integrated back to the NRHO to obtain the departure leg for the transfer. Having obtained the two, discontinuous departure and arrival intermediate arcs, patch points are distributed, and constraints are applied appropriately. A multiple shooting differential corrections process is used to blend in the initial guess to generate a continuous transfer as shown in figure 6.20. The ΔV and TOF for the transfer are shown in the table 6.8. Notice that the transfer cost is lesser than the ones obtained in the previous section. The transfer is not optimized. As the next step, transfer cost is reduced by reducing the arrival ΔV_A in the table 6.8, which will be adopted in the next section by using a slightly modified approach.

6.8 Transfers Using Tangential Departure and Arrival Arcs

The absence of natural dynamical structures makes the transfers between stable periodic orbits a challenging task in terms of finding a good initial guess. To overcome this problem, other periodic orbits or manifolds belonging to nearby trajectories have

Table 6.8. Transfer using 3:4 unstable resonant manifold, transfer costs and TOF.

Parameter	Value
ΔV_D	0.029 km/s
ΔV_I	0.119 km/s
ΔV_A	0.067 km/s
ΔV_{tot}	0.215 km/s
TOF	105 days
Departure time from NRHO periapsis	6.27 days
Arrival time from DRO periapsis ($\dot{y} > 0$)	0 days

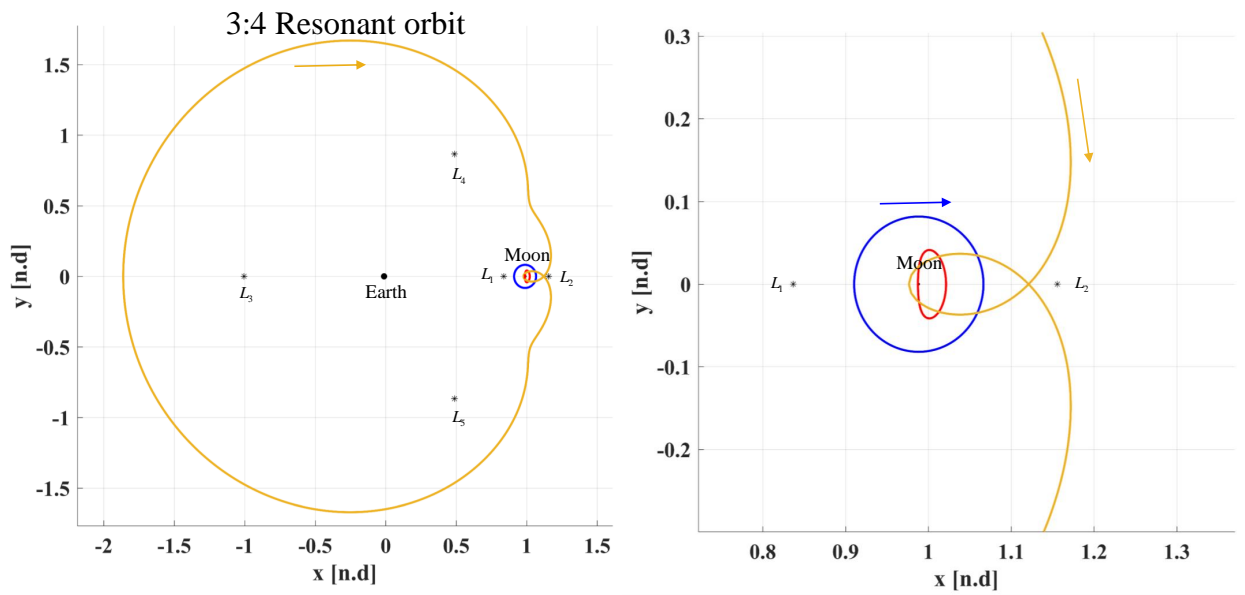


Figure 6.16. Transfer using resonant manifold - Representative orbits.

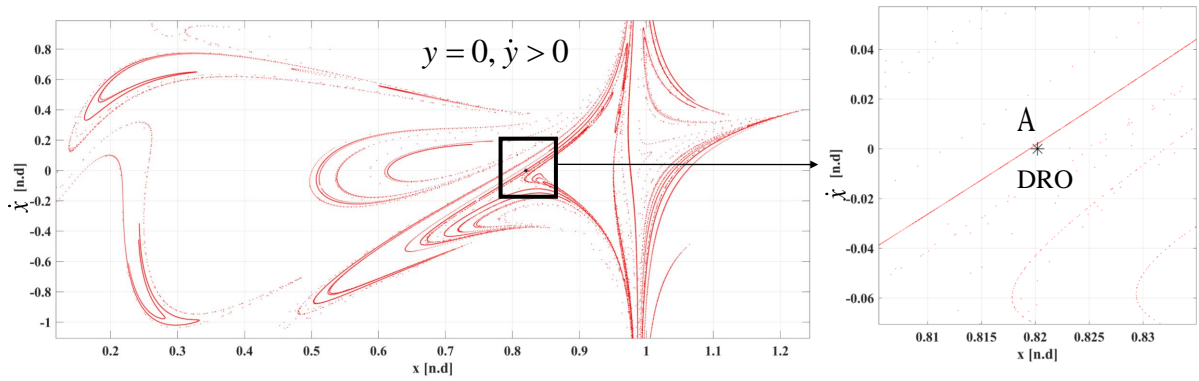


Figure 6.17. Transfer using resonant manifold - Poincaré map for arrival arc.

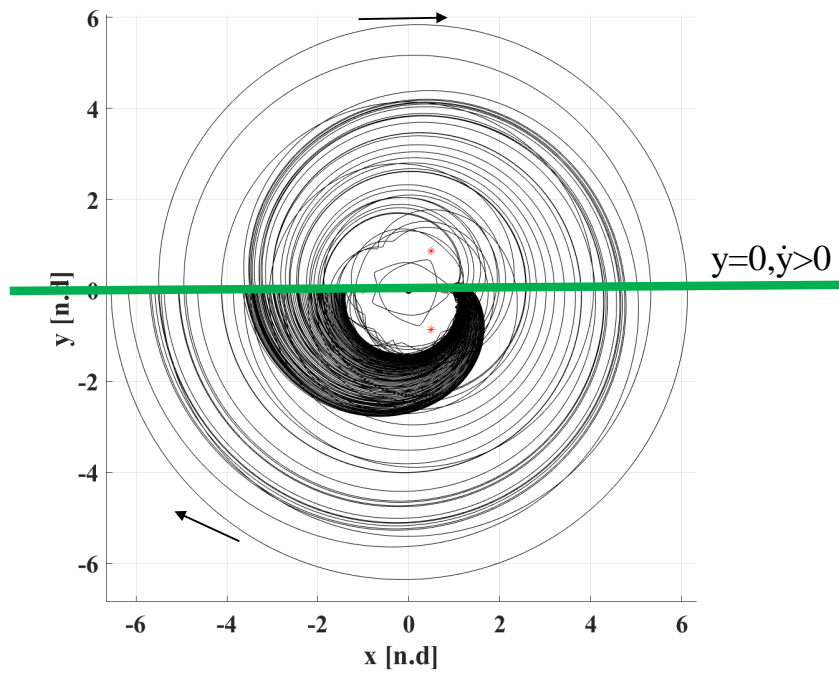


Figure 6.18. Transfer using resonant manifold - Tangential departures from NRHO with $\Delta V = 20$ m/s.

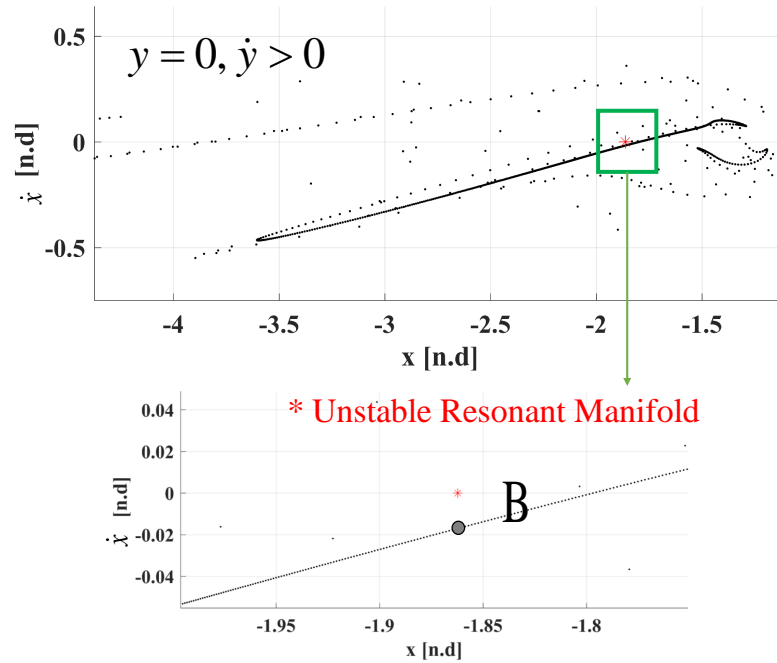


Figure 6.19. Transfer using resonant manifold - Poincaré map for departure arc.

been utilized as intermediate arcs to generate feasible transfer solutions to the representative periodic orbits. Tangential departure or arrival trajectories from the stable orbits, generated by executing a ΔV , can serve as a good substitute for transfers between stable periodic orbits. Similar to manifolds, connections to other intermediate arcs are sought by recording their intersections at various Poincaré maps. Even though the departure/arrival, from/to the periodic orbits can be chosen to be in many directions, departing/arriving tangentially is an easy way to formulate a good initial guess. This technique was partly used in previous transfers where the departure legs were tangential departures from the NRHO. In the transfers designed in sections 6.5, and 6.6, the tangential departure arcs reached the same Jacobi constant value for all the states on the NRHO. In the transfer type described in section 6.7 which uses an unstable manifold of a resonant orbit, to reduce the departure cost, a small $\Delta V = 20$ m/s was used to depart tangentially from all the states on the NRHO. The transfer cost is further brought down by reducing the arrival ΔV_A in table 6.8. To achieve

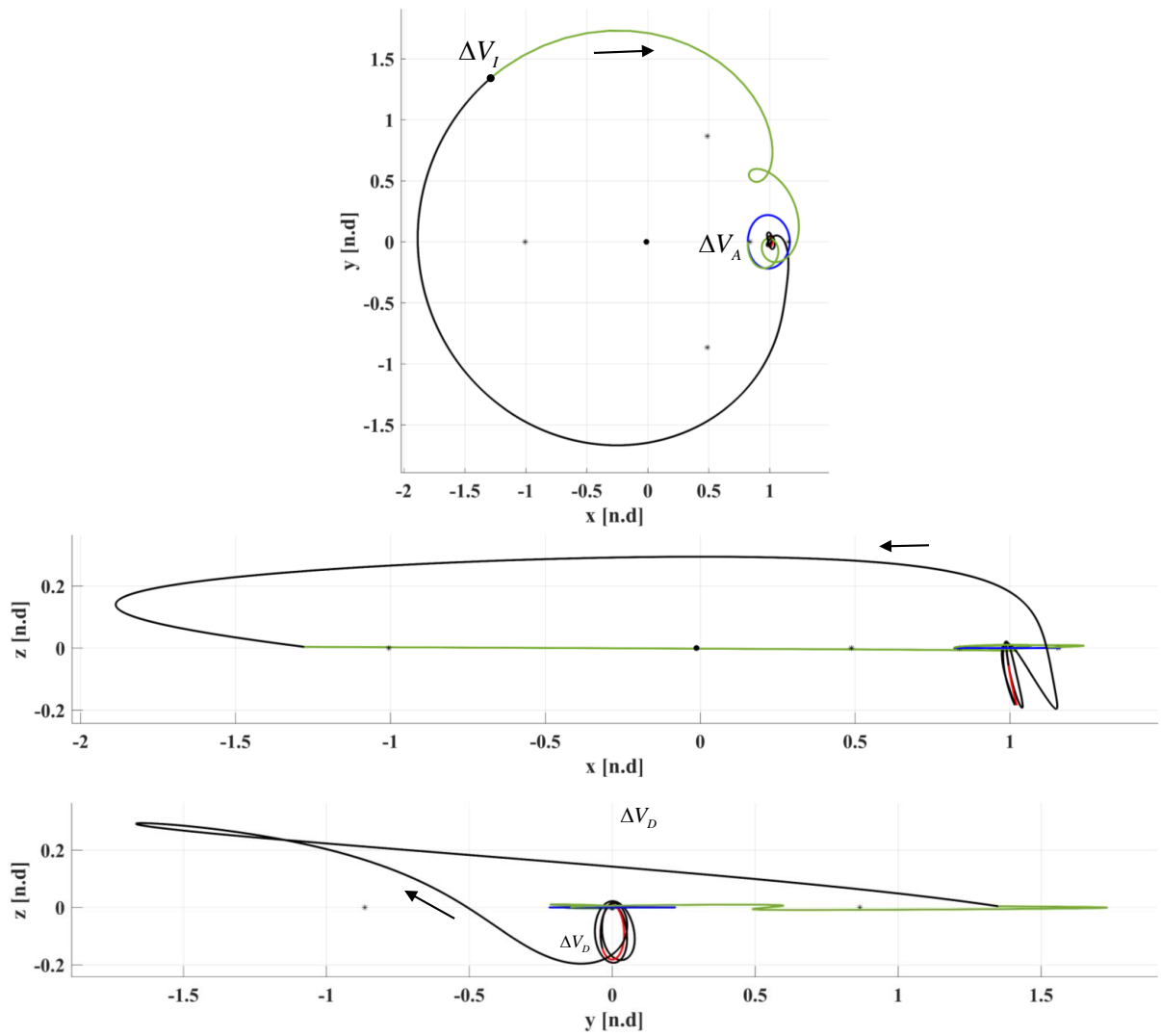


Figure 6.20. Transfer between NRHO and DRO using 3:4 resonant arc.

this, the technique of tangential arrivals is applied at the arrival DRO. Using a ΔV of 40 m/s (20 less than the arrival ΔV_A in table 6.8), the tangential burns are performed in the anti-velocity direction along the discretized states on the DRO. The new states are propagated backward in reverse time until they intersect the hyperplane $y = 0$ in the positive direction, i.e., $\dot{y} > 0$ for the 4th time. The intersections along with the integration times are stored and plotted on a Poincaré map in the figure 6.21 with blue dots. These trajectories are the potential arrival legs for the transfer. The departure leg from the NRHO is obtained in the same way as the previous section. A small ΔV of 20 m/s in the direction of velocity, is used to depart tangentially from all the states on the NRHO. The modified states are propagated until they intersect the hyperplane $y = 0$ in the positive direction $\dot{y} > 0$ for the 3rd time. The intersections are stored and plotted together with the potential arrival states in the Poincaré map shown in figure 6.21. The arrival and departure trajectories intersect distinctly at location A. When the states at point A are propagated back to their periodic orbits, they constitute the discontinuous initial guess for the transfer trajectory. Patch points are distributed, and constraints are enforced appropriately. A multiple shooting differential corrections process is used to blend in the initial guesses to generate a continuous transfer as shown in figure 6.22. This transfer is denoted as type A. The ΔV and TOF for the transfer are shown in the table 6.9. Notice that as intended, the transfer costs ΔV_D and ΔV_I are similar to section 6.7 and arrival ΔV_A is less by 20 m/s. The transfer is not optimized, but the Jacobi constants of the intermediate arcs lie in between the departure and the arrival orbits and decreases in an orderly fashion as shown in table 6.10.

The most expensive burn happens between the departure and the arrival legs which causes a significant plane change in the trajectory. Plane change maneuvers can be reduced by moving further away from the primaries. To search for trajectories which go further away from the primaries the hyperplane is modified to $y = 0$ and $\dot{y} < 0$. Tangential departures from NRHO which intersect the hyperplane 3rd

Table 6.9. Transfer type A, transfer costs and TOF.

Parameter	Value
ΔV_D	0.024 km/s
ΔV_I	0.118 km/s
ΔV_A	0.043 km/s
ΔV_{tot}	0.185 km/s
TOF	120.44 days
Departure time from NRHO periapsis	0.44 days
Arrival time from DRO periapsis ($\dot{y} > 0$)	3.91 days

Table 6.10. Transfer type A, Jacobi constant history.

Parameter	Jacobi constant
Departure orbit (NRHO)	3.047189
Departure arc (Tangential departure)	3.025508
Arrival arc (Tangential Arrival)	2.966086
Arrival orbit (DRO)	2.937908

time and the tangential arrivals of DRO which intersect the hyperplane for 4th time are plotted on the Poincaré map shown in figure 6.23. At the potential intersection point B, the two intermediate arc conditions are chosen and integrated backwards and forwards in time to form the departure and arrival guess for the transfer. Patch point are distributed and constraints are enforced appropriately. A multiple shooting differential corrections process is used to blend in the initial guesses to generate a continuous transfer as shown in figure 6.24. This transfer type is denoted as type B. The ΔV and TOF for the transfer are shown in the table 6.11. Notice that the plane change maneuver is now performed at a greater distance compared to the transfer in figure 6.22. Therefore comparing tables 6.11 and 6.9, the intermediate burn reduces by approximately 40 m/s with nearly similar ΔV_D and Δ_A . The TOF increase by 25

days. The transfer is not optimized but the Jacobi constants of the intermediate arcs lie in between the departure and the arrival orbits and decrease in an orderly fashion as shown in table 6.12.

Table 6.11. Transfer type B, transfer costs and TOF.

Parameter	Value
ΔV_D	0.029 km/s
ΔV_I	0.075 km/s
ΔV_A	0.052 km/s
ΔV_{tot}	0.156 km/s
TOF	145.28 days
Departure time from NRHO periapsis	0.55 days
Arrival time from DRO periapsis ($\dot{y} > 0$)	6.89 days

Table 6.12. Transfer type B, Jacobi constant history.

Parameter	Jacobi constant
Departure orbit (NRHO)	3.047189
Departure arc (Tangential departure)	3.040623
Arrival arc (Tangential Arrival)	2.974127
Arrival orbit (DRO)	2.937908

6.9 Designing Locally Optimal Transfers

All the transfers obtained in the previous sections are sub-optimal trajectories. In this section, locally optimal solutions are found using a constraint nonlinear optimization algorithm using Matlab's 'fmincon' function called Sequential Quadratic

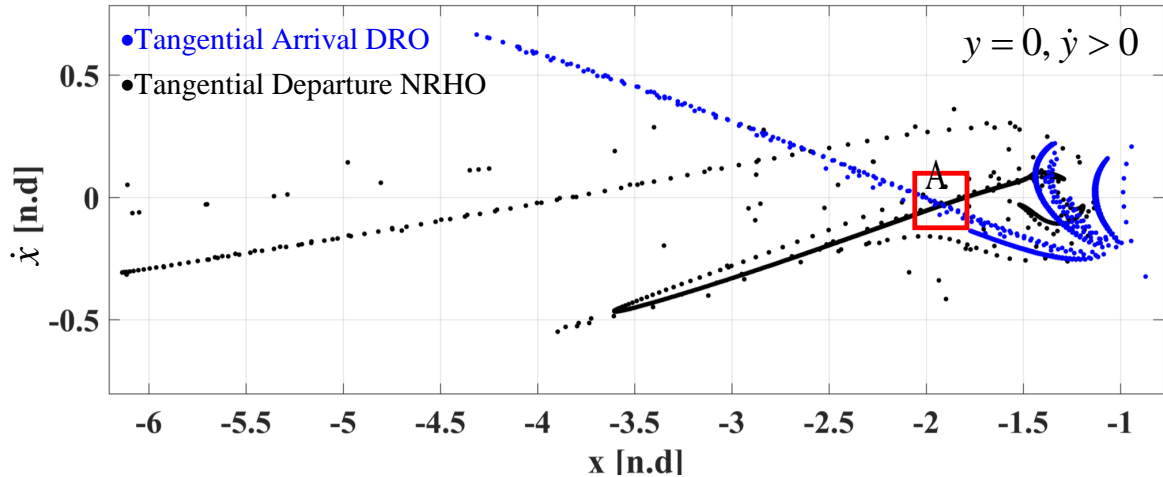


Figure 6.21. Transfer type A - Poincaré map for initial guess.

Programming (SQP). The SQP routine is a quasi-newton direct method of minimizing a continuous nonlinear objective function by solving a simpler quadratic programming sub-problem [22]. Similar to a differential corrections process, the optimization routine consists of a free variable vector which includes all the parameters of the trajectory which are free to vary in the optimization process. A nonlinear constraint function is defined, analogous to the constraint vector in the differential corrections method. The constraint function comprises of nonlinear equality constraints like continuity in states between patch points and nonlinear inequality constraints such as the closest approach to primaries, defined in terms of the elements in the free variable vector. A nonlinear objective function is defined which is the value to be minimized during the optimization routine. To illustrate the process, consider the transfer trajectory designed in figure 6.22. As the trajectory passes close to the Moon during the departure and arrival phases, the optimization process was found to be sensitive and did not show convergence when only the first states of the intermediate arcs were considered as elements in the design matrix. To reduce the sensitivity of the trajectory, the outbound and incoming legs are divided into sub-arcs by distributing sufficient patch points along the arcs including all the periapsis states. The patch

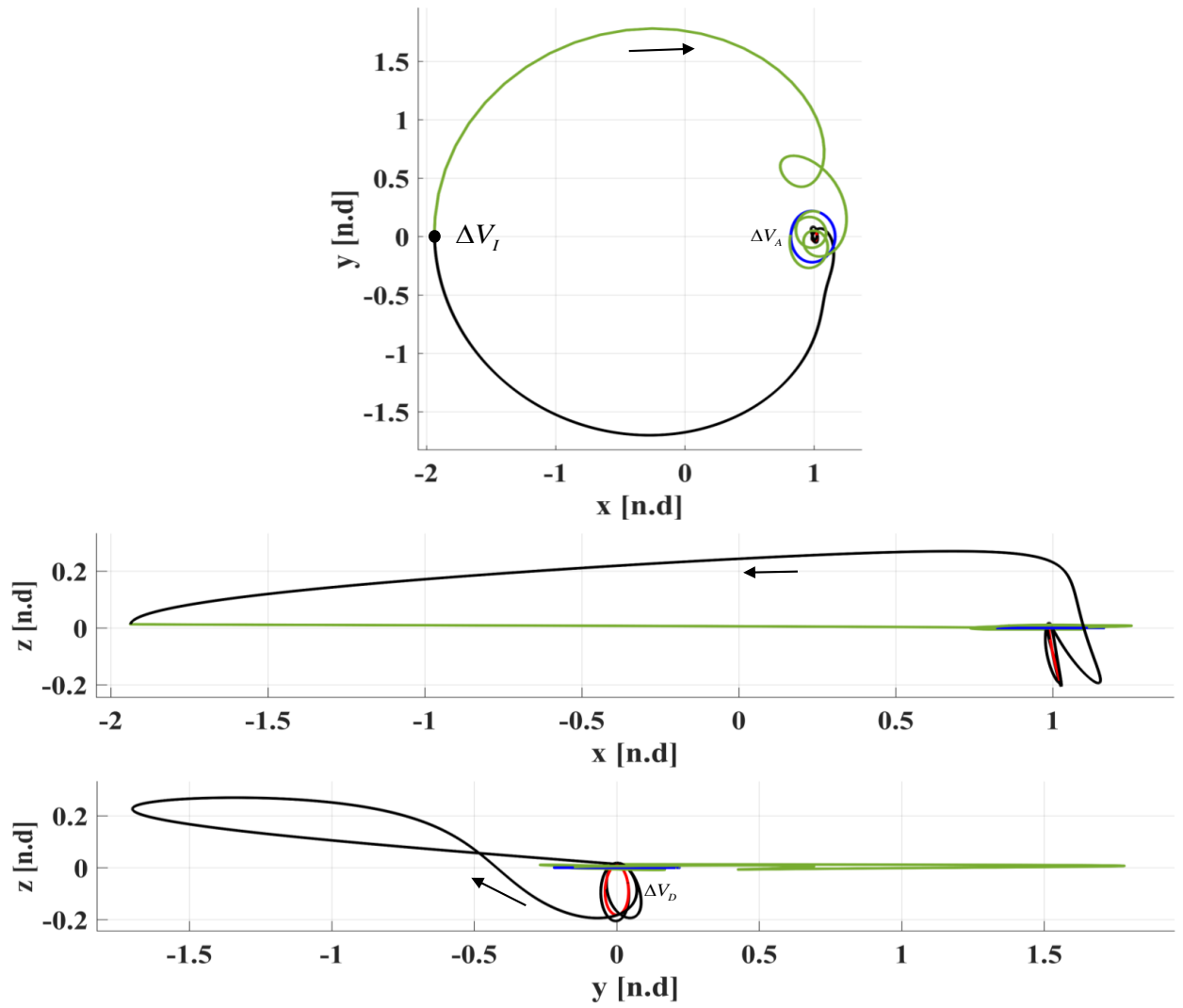


Figure 6.22. Transfer type A.

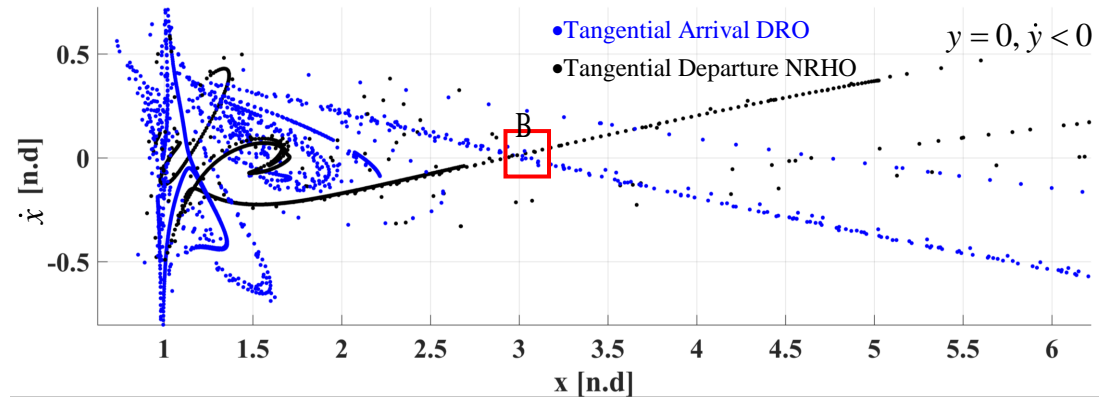


Figure 6.23. Transfer type B - Poincaré map for initial guess - Distant plane change.

points along with their respective integration times are included into the free variable vector. Another aspect of the optimization process is that the trajectory is free to vary on the initial and final orbit. This implies that the departure position on the NRHO and the arrival position on the DRO are allowed to change in order to minimize the objective function. Therefore, time periods T_1 and T_2 as shown in figure 6.6 are included into the free variable vector which indicate the departure time on NRHO from its periapsis location and arrival time on DRO from its positive \hat{x} -axis crossing. The nonlinear equality constraints include the following continuity constraints:

1. The first and last point of the trajectory are constrained to lie on the respective periodic orbits.
2. Continuity in both position and velocity is ensured across all the patch points except at the maneuver locations.
3. The total time of flight may or may not be constrained to be equal to that of the sub-optimal trajectory.

All the periapsis distances of the trajectory are constrained to be greater than 3200 km. This is included as nonlinear inequality constraint. Positive time of flights are ensured by setting the lower limits on time variables to be zero. As a human-

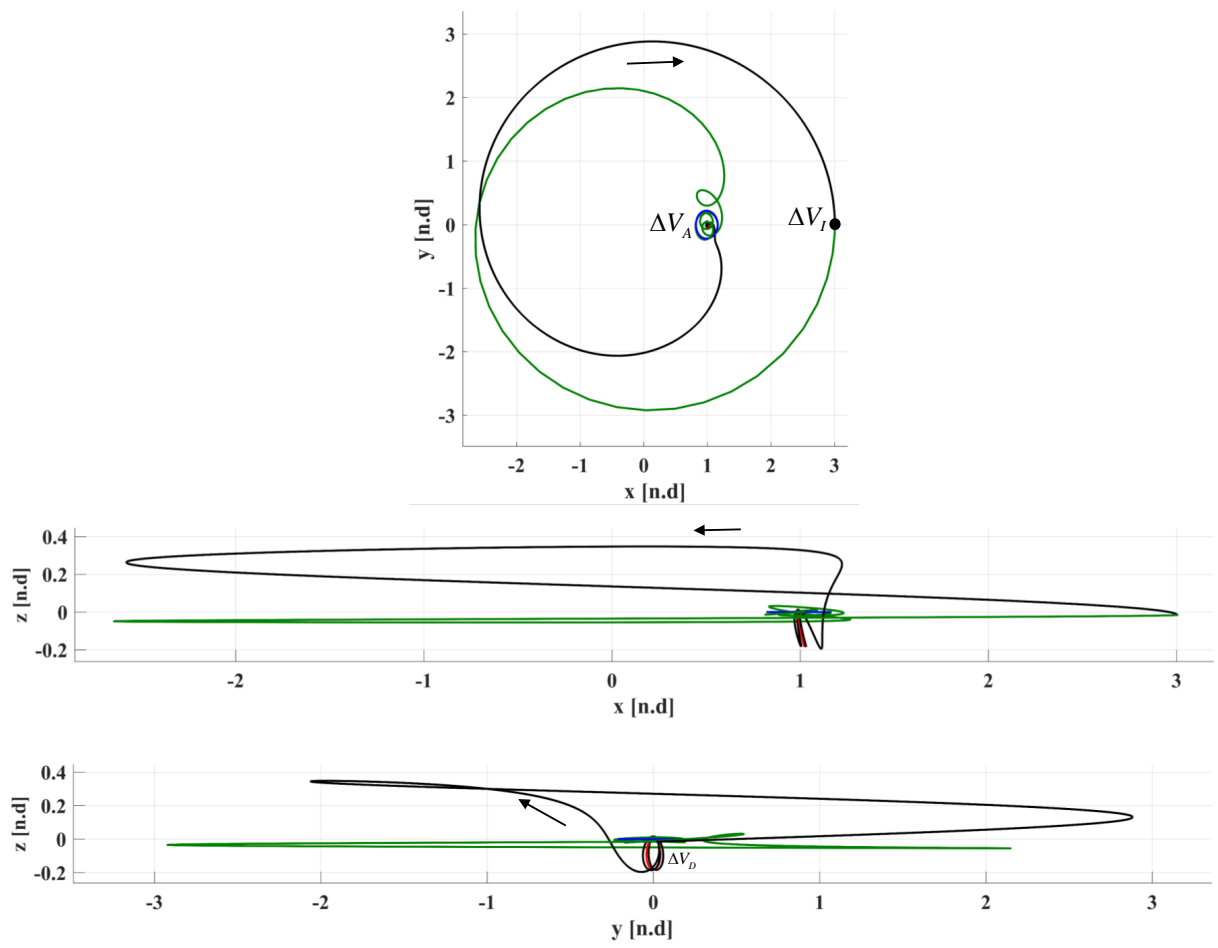


Figure 6.24. Transfer type B - Distant plane change.

spaceflight operational constraint the departure time on the NRHO is set to only vary between the sub-optimal initial departure time and the time until apoapsis on the departure orbit. This is done to ensure that the spacecraft does not burn close to the periapsis during the departure on NRHO. The objective function is written as,

$$J(\bar{X}) = \Delta V_D + \Delta V_I + \Delta V_A \quad (6.7)$$

Where ΔV_D is the departure burn at NRHO, ΔV_I is the intermediate plane change maneuver and ΔV_A is the arrival burn at DRO. In the optimization process numerical gradients are used and all constraints are met within the specified tolerances ($TolX = TolCon = TolFun = 10^{-12}$). When the first order optimality conditions are met and the algorithm is successful the exit flag output is returned as one. For the sub-optimal trajectory in figure 6.22, a local optimal with the same time of flight is found and is plotted together with the original sub-optimal trajectory in figure 6.25. The comparisons between the transfer costs and TOF between the two trajectories is seen in the table 6.13. For the same sub-optimal trajectory in figure 6.22, a better local optimal trajectory is found by letting the TOF to vary. The optimal and sub-optimal trajectories are shown together in figure 6.26. The comparisons between the transfer costs and TOF between the two trajectories is shown in the table 6.14. Similarly, for the sub-optimal trajectory in the figure 6.24, where the plane change maneuver is performed at a greater distance than the trajectory shown in figure 6.22, a local optimal with the same TOF is found and is plotted together with the original sub-optimal in figure 6.27. The comparisons between the transfer costs and TOF between the two trajectories is seen in the table 6.15. For the same sub-optimal trajectory in figure 6.24, a better local optimal trajectory is found by letting the TOF to vary. The optimal and sub-optimal trajectories are shown together in figure 6.28. The comparisons between the transfer costs and TOF between the two trajectories is seen in the table 6.16.

Table 6.13. ΔV and TOF comparison - fixed time optimal transfer - Transfer type A.

Parameter	Non-Optimum	Local Optimum
ΔV_D	0.024 km/s	0.016 km/s
ΔV_I	0.118 km/s	0.121
ΔV_A	0.043 km/s	0.035
ΔV_{tot}	0.185 km/s	0.172
TOF	120.44 days	120.44
Departure time from NRHO periapsis	0.44 days	0.44 days
Arrival time from DRO periapsis ($\dot{y} > 0$)	3.91 days	6.27 days

Table 6.14. ΔV and TOF comparison - variable time optimal transfer - Transfer type A.

Parameter	Non-Optimal	Optimal
ΔV_D	0.024 km/s	0.017 km/s
ΔV_I	0.118 km/s	0.099 km/s
ΔV_A	0.043 km/s	0.050 km/s
ΔV_{tot}	0.185 km/s	0.166 km/s
TOF	120.44 days	127.00 days
Departure time from NRHO periapsis	0.44 days	0.44 days
Arrival time from DRO periapsis ($\dot{y} > 0$)	3.91 days	8.23 days

Table 6.15. ΔV and TOF comparison - fixed time optimal transfer
-Transfer type B.

Parameter	Non-Optimal	Optimal
ΔV_D	0.029 km/s	0.026 km/s
ΔV_I	0.075 km/s	0.083 km/s
ΔV_A	0.052 km/s	0.031 km/s
ΔV_{tot}	0.156 km/s	0.0140 km/s
TOF	145.28 days	145.28 days
Departure time from NRHO periapsis	0.55 days	2.15 days
Arrival time from DRO periapsis ($\dot{y} > 0$)	6.89 days	5.64 days

Table 6.16. ΔV and TOF comparison - variable time optimal transfer
- Transfer type B.

Parameter	Non-Optimal	Optimal
ΔV_D	0.029 km/s	0.015 km/s
ΔV_I	0.075 km/s	0.084 km/s
ΔV_A	0.052 km/s	0.031 km/s
ΔV_{tot}	0.156 km/s	0.0130 km/s
TOF	145.28 days	148.88 days
Departure time from NRHO periapsis	0.55 days	0.55 days
Arrival time from DRO periapsis ($\dot{y} > 0$)	6.89 days	6.16 days

Overall, the local optimization process finds better trajectories in terms of the transfer costs for the implemented set of constraints. It should be noted that the optimized trajectories are only locally optimum, better solutions may be possible for a different set of constraint conditions or a different transfer geometry. The reduction in the transfer costs is however not large, which indicates that the initial guess for the transfer scenarios were close to the locally optimum solutions. To test the practical applicability of the computed optimum transfers, they must be transitioned into the higher fidelity ephemeris model. The next section describes this process and presents the results.

6.10 Higher-Fidelity Transfers from NRHO to DRO

Once an optimized transfer is obtained in the CR3BP, it needs to be transitioned into the higher fidelity ephemeris model to investigate the effects of additional gravitational perturbing forces on the overall transfer costs and time of flight. To illustrate this process, the time-varying optimal transfer type A as shown in the figure 6.26 is transitioned into the Earth-Moon ephemeris model in the presence of perturbing solar gravitational forces. The departure orbit (NRHO), transfer arcs and arrival orbit (DRO) are stacked together in the CR3BP in the following manner:

1. 10 revolutions of the departure orbit (NRHO) are stacked together starting from the \hat{x} - \hat{z} plane.
2. The departure and the arrival legs of the trajectory.
3. 10 revolutions of the arrival orbit (DRO) are stacked together starting from the insertion location on the arrival orbit (DRO).

Sufficient patch points are distributed across all the combined stacked orbits and are transitioned into the ephemeris model and corrected on each day of two representative months of the year 2020 using the ATD software [46]. During the corrections process, continuity in position and velocity are ensured between the sub-arcs except

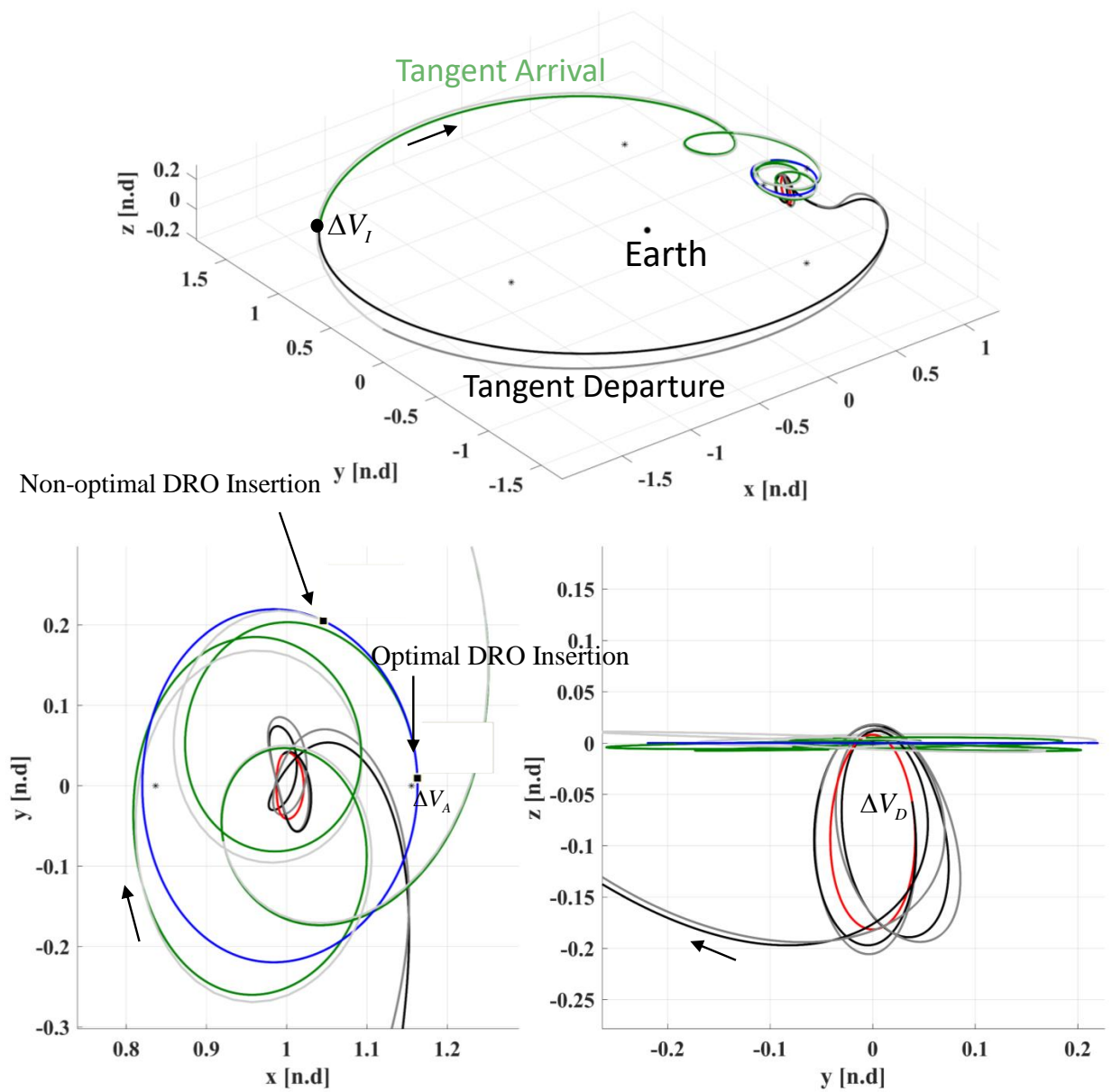


Figure 6.25. Fixed time optimized transfer - Transfer type A.

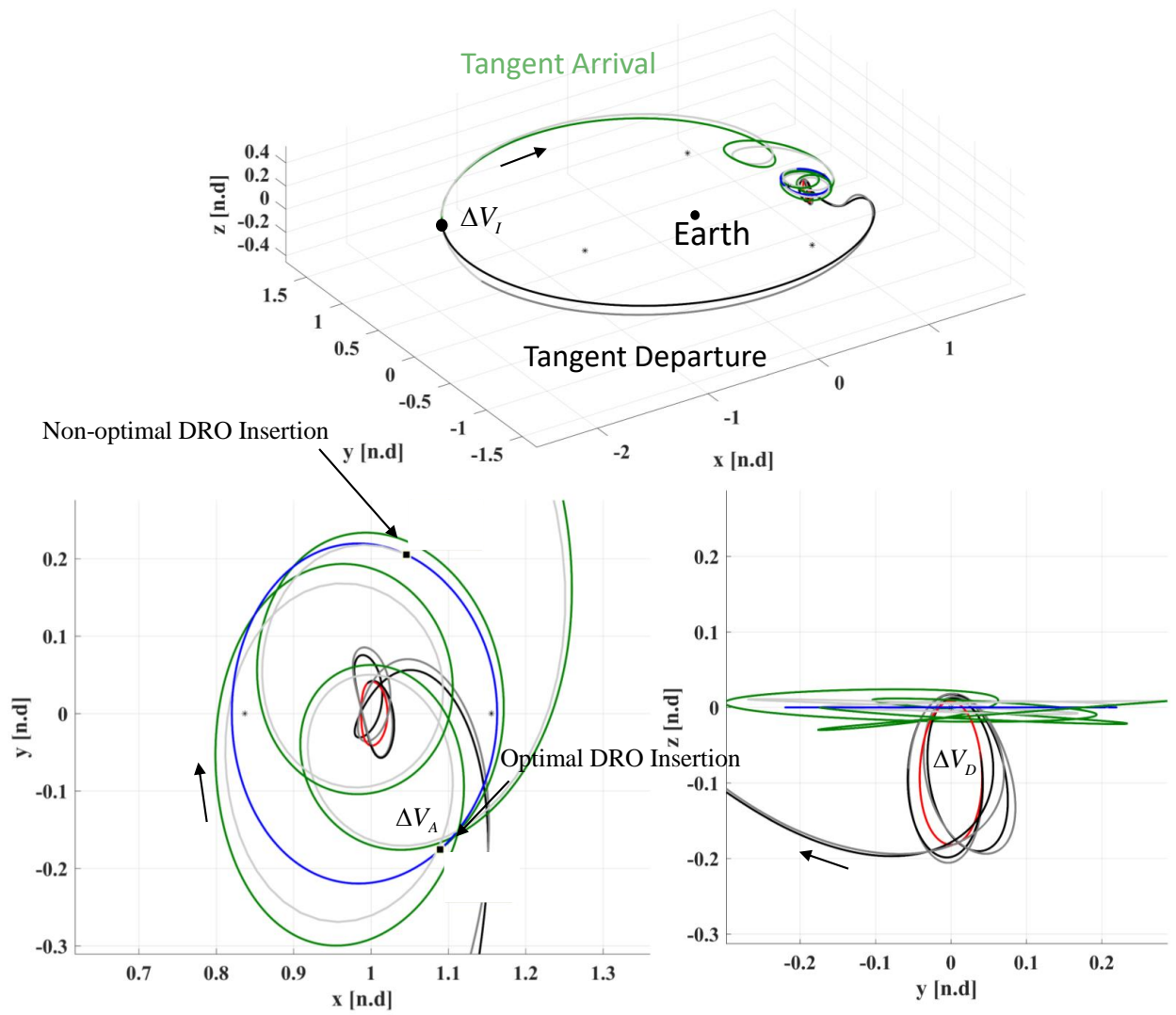


Figure 6.26. Variable time optimized transfer - Transfer type A.

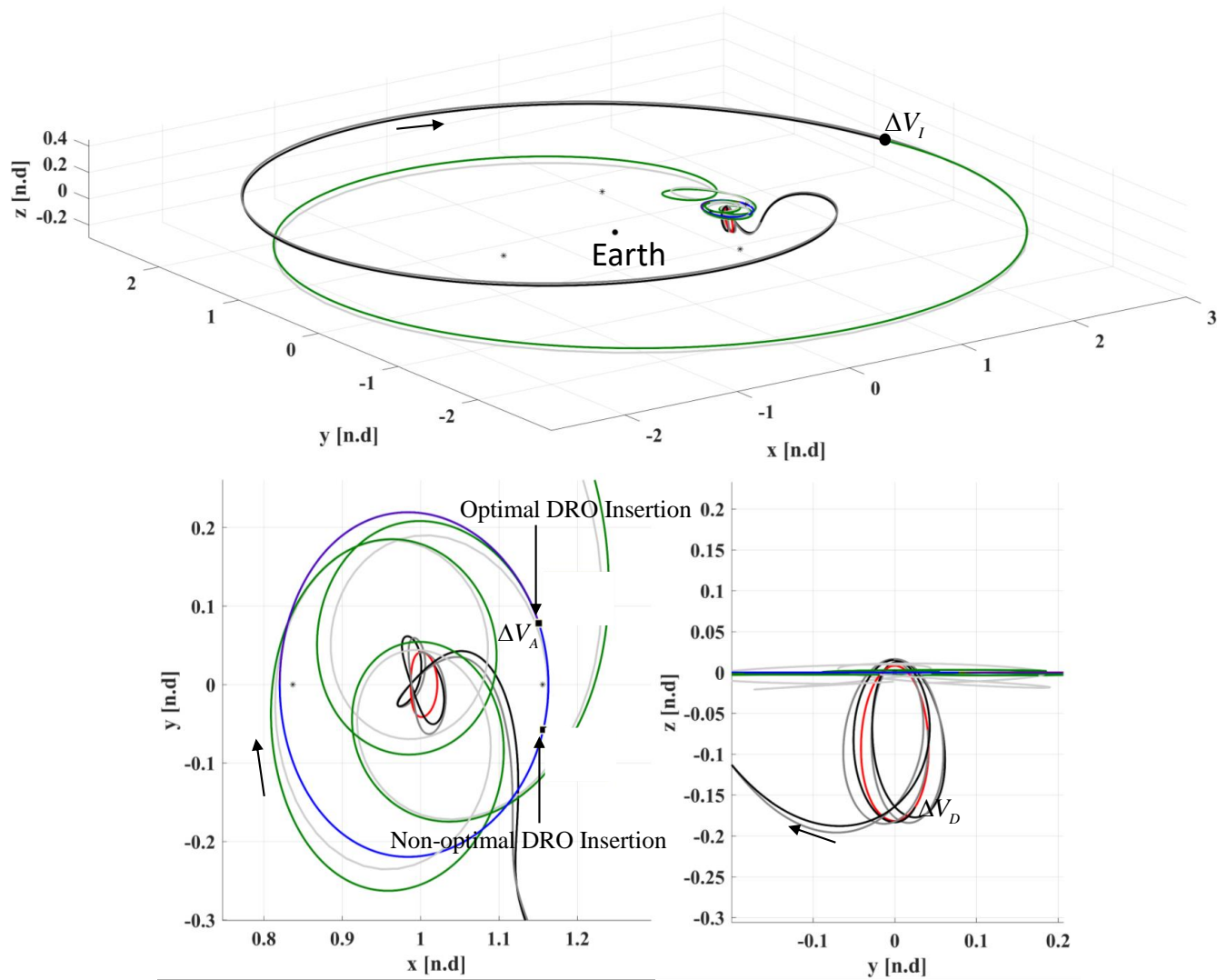


Figure 6.27. Fixed time optimized transfer - Transfer type B.

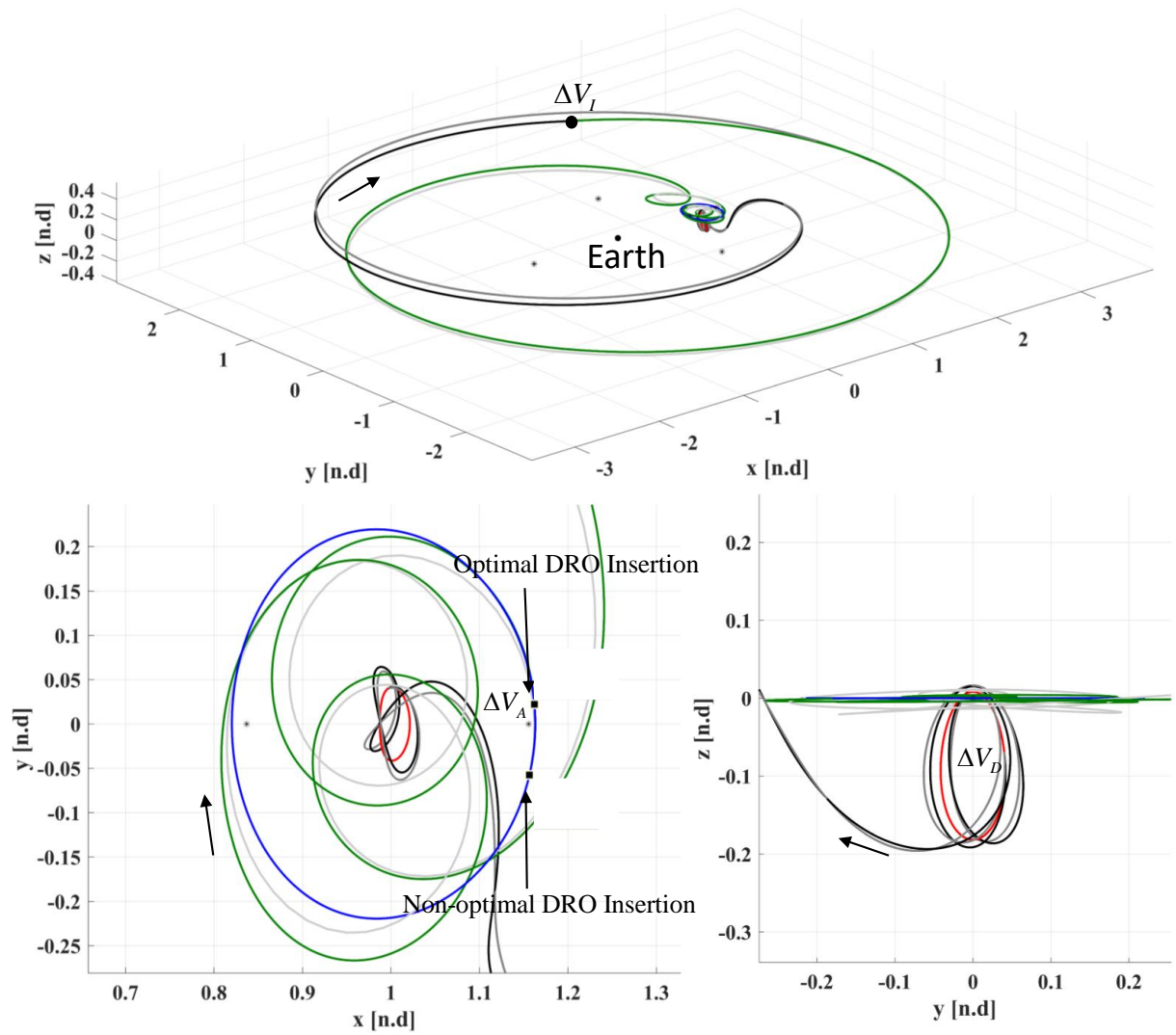


Figure 6.28. Variable time optimized transfer - Transfer type B.

at the maneuver locations. An attenuation factor equal to 0.2 is multiplied to the ephemeris update equation to ensure a steady decrease of the constraint vector. As the periodic orbits exist as quasi-periodic trajectories in higher fidelity model, the first and the last states of the transfer are constrained to lie on the quasi-periodic NRHO and DRO respectively. Figure 6.29 shows the ΔV variation for the variable time optimal transfer type A with respect to the days of the representative month. Note that the day corresponds to the first state on the stacked NRHO orbits and not the departure date. The red dots indicate the transfer costs during January (transfer departure from NRHO in the month of March). The blue dots indicate the transfer costs associated with May (transfer departure from NRHO in the month of July). The CR3BP equivalent ΔV is shown as a constant black line. Notice that during both the months, transfer cost is oscillatory and is dependent on the day of the departure. There are a few days during which the transfer costs in the ephemeris model is comparable to the CR3BP, while on some other days the transfer costs are very high. It should be noted that the converged trajectories are not optimal and cheaper ΔV transfers can be sought by optimizing these transfers.

Consider the ephemeris converged trajectory corresponding to the first red dot in figure 6.29, i.e., starting approximately on January 1st as shown in the figure 6.30. The total ΔV and TOF of the sub-optimal trajectory are 0.217 km/s and 126.51 days respectively. The epoch date of the converged trajectory is slightly less than Jan 1st, 2020. Sub-optimal trajectories are obtained by systematically working down the ΔV of the transfer by applying the ΔV constraint. While implementing the new constraint, the first state of the quasi-periodic NRHO and the first state of the quasi-periodic DRO are fixed, to only allow the patch points of the intermediate transfer arcs to vary. Also, the z coordinate of the departure point is constrained to prevent a departure from close to a periapsis location. Implementing this results in a sub-optimal trajectory and is shown together with the original ephemeris converged trajectory in figure 6.31. The initial trajectory is marked in gray, and the sub-optimal

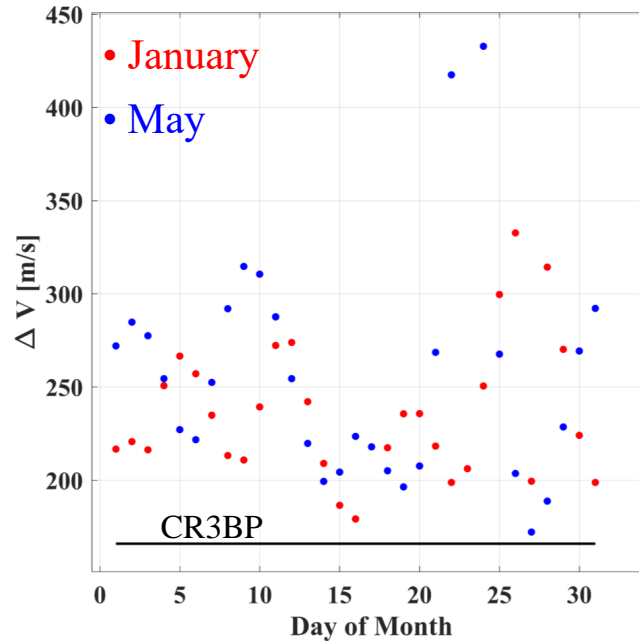


Figure 6.29. Variable time optimized transfer type A - ΔV vs ephemeris insertion epoch.

trajectory is shown with colors. The ΔV and TOF of the sub-optimal trajectory are 0.170 km/s and 126.27 days respectively. Further decrease in the transfer cost is possible by letting the DRO vary freely. DRO is allowed to vary in the plane by only constraining its z and \dot{z} coordinates and letting the positions and velocities in the \hat{x} - \hat{y} plane to change as opposed to fixing the entire six-dimensional state. Implementing this on the sub-optimal trajectory along with constraining the departure z coordinate results in a trajectory as shown in figure 6.32. Notice that while the NRHO is still similar to the initial ephemeris trajectory, the DRO shifts quite a lot compared to its initial counterpart. The ΔV and TOF of the transfer are 0.130 km/s and 130.37 days respectively. The epoch times of all the three transfers vary by a few hours while carrying out the ΔV reduction process. Overall the transfer geometry in the higher fidelity model stays similar to the CR3BP counterpart.

As an implication to the various transfer scenarios constructed in this chapter, it can be said that incorporating resonant arcs and their manifolds into the transfer design process may give rise to new transfer scenarios, particularly when the departure and the arrival orbits do not have any natural dynamical structures or manifolds associated with them. Tangential departure and arrival arcs also prove to be useful analogs to manifold structures in creating Poincaré maps to locate potential transfers between two stable periodic orbits.

Dec 31st 2019, 16:50:43.7326

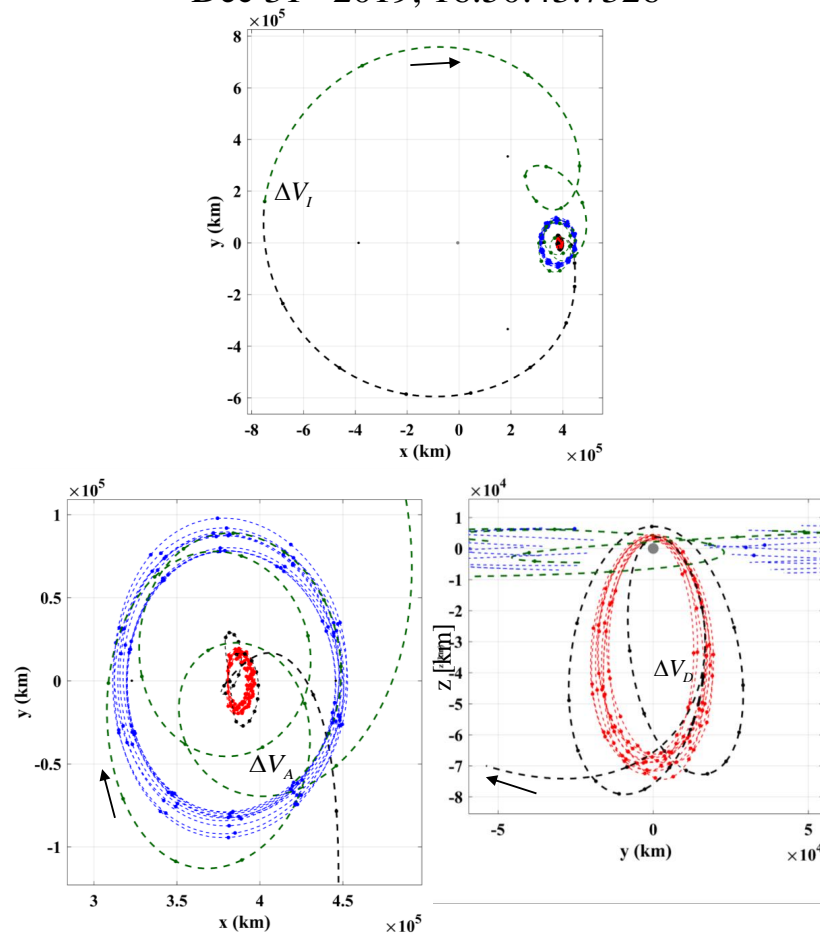


Figure 6.30. Variable time optimized transfer-type A - ephemeris converged trajectory.

Dec 31st 2019, 21:02:50.9702

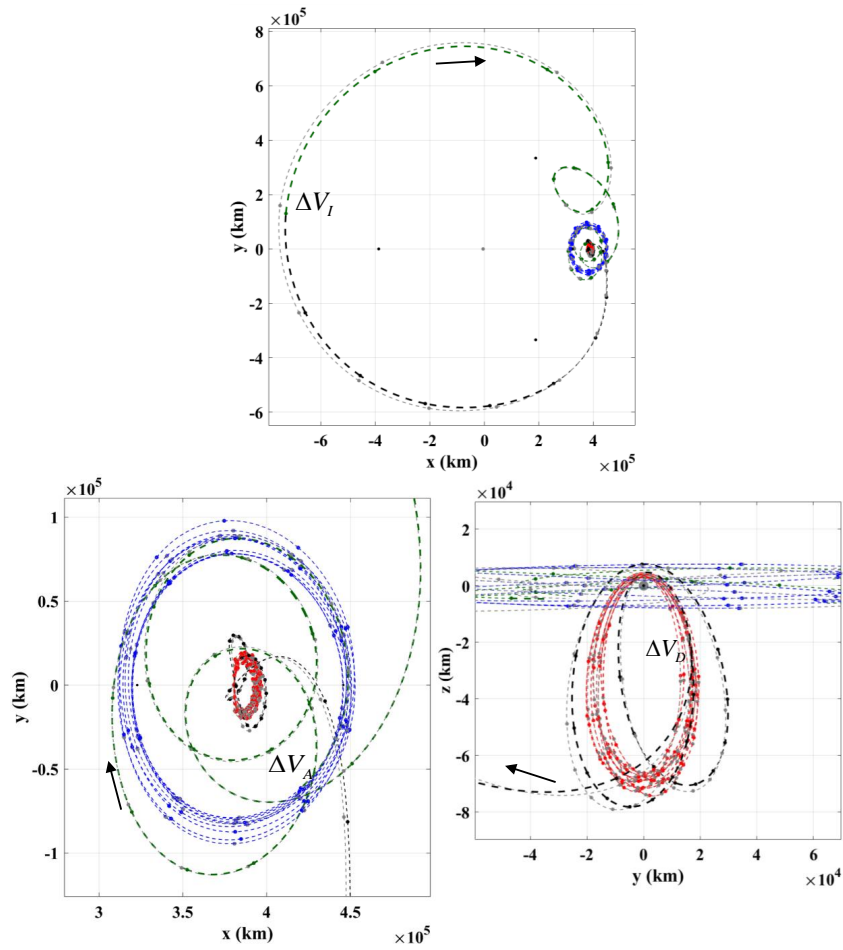


Figure 6.31. Variable time optimized transfer-type A - ephemeris trajectory with reduced ΔV .

Dec 31st 2019, 21:16:06.0912

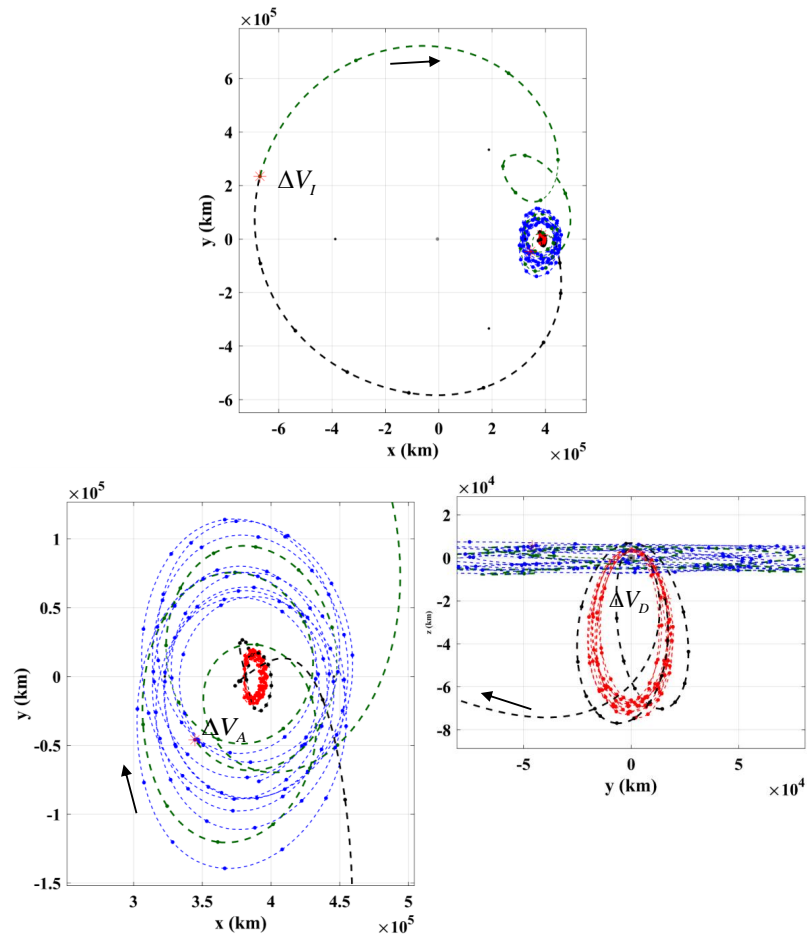


Figure 6.32. Variable time optimized transfer-type A - ephemeris trajectory with DRO free to vary.

7. SUMMARY

In this investigation, resonant orbits and manifolds in multi-body dynamical environments are introduced, and their applications to various aspects of trajectory design are established. Historically resonance phenomena and resonant orbits have been studied to understand the long-term stability and formation of the solar system. In recent years, it has been shown that resonant manifolds play a key role in undergoing resonance transitions when a spacecraft encounters a gravitational flyby. Resonant manifolds have been incorporated into the design of conceptual outer planet exploration missions such as JIMO [1] and JEO [2]. Resonant orbits which possess long-term stable characteristics are also being considered as nominal mission trajectories for the IBEX [3] and TESS [4] missions. However, they have not been leveraged as tools for multi-body trajectory design and therefore the overarching goals for this work are as follows: (1) to use resonant orbits in constructing ephemeris baseline solutions with desired properties and (2) to use resonant orbits and manifolds as intermediate arcs in transfer mechanisms connecting stable periodic orbits.

7.1 Resonant Orbits and Manifolds in CR3BP

To accomplish the above goals, all the design strategies are implemented in a multi-body CR3BP dynamical model. First, equations of motion for the CR3BP are derived and followed by the computation of the five planar equilibrium solutions in the system. Several numerical techniques which include various differential correction and continuation algorithms are developed and utilized to generate planar and spatial libration point orbits. The concept of linear stability analysis for periodic orbits was introduced which led to the detection of bifurcations on a periodic orbit family.

In the CR3BP, due to the gravitational influence of both the larger and the smaller primaries, definition, and computation of resonant orbits is not similar to the two-body model. Two categories of resonant orbits are shown to exist. The first type is two-body equivalent, planar and spatial periodic resonant orbits and the second category of resonant orbits are the libration point periodic orbits which are in resonance with the smaller primary. Methodologies to compute them are outlined in detail. Computation of manifolds for unstable resonant orbits is presented. A useful trajectory design practice namely the Poincaré mapping technique is described which forms an efficient design tool in different transfer scenarios.

7.2 Reference Ephemeris Trajectory Design Using Resonant Orbits

Periodic orbits in the CR3BP exist as quasi-periodic solutions in the higher fidelity models. In general, a quasi-periodic ephemeris trajectory is constructed by employing a traditional stacking process in which multiple revolutions of an identical periodic orbit in CR3BP are placed one behind another before transitioning them into the higher fidelity model. As the ephemeris model is non-autonomous, depending upon the epoch, the same set of periodic orbits in the CR3BP model converge to different quasi-periodic solutions in the ephemeris model. This may lead to the disappearance of specific useful properties depending upon on the transition epoch, some of them may include the ability to avoid eclipses and favorable periapsis conditions. Carefully altering the stacking sequence of the periodic orbits in the CR3BP, will lead to a nearby reference trajectories which are more consistent and maintain the favorable properties within the ephemeris model on any given transition epoch. Incorporating non-homogeneous periodic orbits with different time periods into the stacking sequence may offer better control of target periapsis in terms of their radii and epoch in the converged trajectory, thus aiding in avoiding short duration eclipse events caused due to the Earth and the Moon. Therefore to address the first overarching goal of this investigation a 3:1 synodic Near Rectilinear Halo orbit in the cislunar space is used

to develop an alternative, non-homogeneous stacking process to generate ephemeris reference trajectories with a better eclipse avoidance and periapsis control strategy.

7.3 Transfer Trajectory Design Using Resonant Orbits and Manifolds

The second goal of this investigation is to explore the possibility of incorporating resonant arcs and their manifolds in the transfer design process to aid the transfer initial guess generation between stable periodic orbits with no natural dynamical structures. The applicability of this idea is demonstrated between two stable cislunar periodic orbits namely a 9:2 NRHO and a DRO by constructing various transfer scenarios incorporating resonant arcs and manifolds as intermediate arcs. Poincaré mapping techniques are extensively used for selecting a variety of intermediate arcs thereby generating novel transfer geometries. An alternative approach to using manifolds as intermediate arcs between stable periodic destinations is to perform small propulsive maneuvers along the departure and arrival orbits in either direction of the velocity and generate tangential departure and arrival trajectories which are plotted on a Poincaré section to identify feasible transfers. Locally optimum transfers are generated in the CR3BP, and the practical validity of the optimal transfers are tested by transitioning them into a higher fidelity ephemeris model. The transfer costs when transitioned into the ephemeris model were found to vary depending on the epoch but retained the overall transfer geometry. The methodologies designed are general and can be used in transfer scenarios involving other stable periodic families.

7.4 Future Recommendations

To have a well connected cislunar environment, it is necessary to expand the transfer options to other stable locations like the L_4/L_5 SPOs, L_2 Halo orbits, Butterfly orbits, Low Lunar orbits and so on. Since the resonant orbits and manifolds travel across various locations in the CR3BP, the transfer design methodologies developed in this investigation can be extended to connect the above stable orbits. Implement-

ing a transfer continuation strategy on a transfer scenario between two representative orbits will lead to the generation of a transfer database between the nearby periodic orbits within the two families. In the present work, only a single maneuver is performed between the two intermediate arcs of a transfer. Incorporating multiple maneuver locations in between the transfer and its effect on the transfer cost can be investigated. Also, the use of primary bodies to decrease the plane change maneuver costs associated with the transfer can be explored in more detail. New transfer design methodologies and effects of adding more than two intermediate arcs, which can be other libration point or resonant orbits and associated manifolds, on the transfer geometries and cost can be developed. Therefore, expanding the transfer options and exploring different transfer geometries will help in making informed decisions about the type of transfer between two destinations in the dynamical region.

Further characterization and investigation of both the planar and spatial resonant families for spacecraft trajectory design is needed to achieve the above recommendations. The use of resonant orbits for trajectory design has thereby opened new doors for constructing cost efficient and novel transfer trajectories in multi-body dynamical systems.

REFERENCES

- [1] Jon A Sims. Jupiter icy moons orbiter mission design overview. 2006.
- [2] K Clark, J Boldt, R Greeley, K Hand, I Jun, R Lock, R Pappalardo, T Van Houten, and T Yan. Return to europa: overview of the jupiter europa orbiter mission. *Advances in space research*, 48(4):629–650, 2011.
- [3] DJ McComas, F Allegrini, P Bochsler, M Bzowski, M Collier, H Fahr, H Fichtner, P Frisch, HO Funsten, SA Fuselier, et al. Ibexinterstellar boundary explorer. *Space science reviews*, 146(1-4):11–33, 2009.
- [4] George R Ricker, Roland Kraft Vanderspek, David W Latham, and Joshua N Winn. The transiting exoplanet survey satellite mission. In *American Astronomical Society Meeting Abstracts# 224*, volume 224, 2014.
- [5] Isaac Newton. *The Principia: mathematical principles of natural philosophy*. Univ of California Press, 1999.
- [6] June Barrow-Green. *Poincaré and the three body problem*, volume 2. American Mathematical Soc., 1997.
- [7] Victory Szebehely. *Theory of orbit: The restricted problem of three Bodies*. Elsevier, 2012.
- [8] George William Hill. Researches in the lunar theory. *American journal of Mathematics*, 1(1):5–26, 1878.
- [9] Henri Poincaré. *Les méthodes nouvelles de la mécanique céleste: Méthodes de MM. Newcomb, Glydén, Lindstedt et Bohlin. 1893*, volume 2. Gauthier-Villars it fils, 1893.
- [10] Herbert B Keller. *Numerical solution of two point boundary value problems*. SIAM, 1976.
- [11] SM Roberts and JS Shipman. Continuation in shooting methods for two-point boundary value problems. *Journal of mathematical analysis and applications*, 18(1):45–58, 1967.
- [12] SM Roberts and JS Shipman. Justification for the continuation method in two-point boundary value problems. *Journal of Mathematical Analysis and Applications*, 21(1):23–30, 1968.
- [13] D Grebow. Generating periodic orbits in the circular restricted three-body problem with applications to lunar south pole coverage. *MSAA Thesis, School of Aeronautics and Astronautics, Purdue University*, 2006.
- [14] Robert Farquhar, Daniel Muhonen, and Leonard C Church. Trajectories and orbital maneuvers for the isee-3/ice comet mission. In *Astrodynamics 1983*, 1984.

- [15] Mark Woodard, David Folta, and Dennis Woodfork. Artemis: the first mission to the lunar libration orbits. In *21st International Symposium on Space Flight Dynamics, Toulouse, France*, 2009.
- [16] Martin W Lo, Bobby G Williams, Williard E Bollman, Dongsuk Han, Yungsun Hahn, Julia L Bell, Edward A Hirst, Robert A Corwin, Philip Hong, Kathleen C Howell, et al. Genesis mission design. *Journal of the Astronautical Sciences*, 49(1):169–184, 2001.
- [17] Rodney L Anderson. Low thrust trajectory design for resonant flybys and captures using invariant manifolds. 2005.
- [18] Wang Sang Koon, Martin W Lo, Jerrold E Marsden, and Shane D Ross. Heteroclinic connections between periodic orbits and resonance transitions in celestial mechanics. *Chaos: An Interdisciplinary Journal of Nonlinear Science*, 10(2):427–469, 2000.
- [19] WS Koon, MW Lo, JE Marsden, and SD Ross. Resonance and capture of jupiter comets. In *Dynamics of Natural and Artificial Celestial Bodies*, pages 27–38. Springer, 2001.
- [20] KC Howell, BG Marchand, and MW Lo. Temporary satellite capture of short-period jupiter family comets from the perspective of dynamical systems. *Journal of the Astronautical Sciences*, 49(4):539–558, 2001.
- [21] Tatiana Mar Vaquero Escribano. *Poincare sections and resonant orbits in the restricted three-body problem*. Purdue University, 2010.
- [22] M Vaquero. *Spacecraft Transfer Trajectory Design Exploiting Resonant Orbits in Multi-Body Environments*. PhD thesis, Ph. D. Dissertation, School of Aeronautics and Astronautics, Purdue University, West Lafayette, IN, 2013.
- [23] Mar Vaquero and Kathleen C Howell. Transfer design exploiting resonant orbits and manifolds in the saturn–titan system. *Journal of Spacecraft and Rockets*, 2013.
- [24] Mar Vaquero and Kathleen C Howell. Leveraging resonant-orbit manifolds to design transfers between libration-point orbits. *Journal of Guidance, Control, and Dynamics*, 2014.
- [25] Robert W Farquhar. The control and use of libration-point satellites. 1970.
- [26] John V Breakwell and John V Brown. The halofamily of 3-dimensional periodic orbits in the earth-moon restricted 3-body problem. *Celestial mechanics and dynamical astronomy*, 20(4):389–404, 1979.
- [27] Kathleen Connor Howell. Three-dimensional, periodic,haloorbits. *Celestial Mechanics*, 32(1):53–71, 1984.
- [28] Emily Zimovan. *Characteristics and design strategies for Near Rectilinear Halo Orbits within the Earth-Moon System*. Purdue University, 2017.
- [29] Lucia Capdevila, Davide Guzzetti, and K Howell. Various transfer options from earth into distant retrograde orbits in the vicinity of the moon. In *AAS/AIAA Space Flight Mechanics Meeting*, volume 118, 2014.

- [30] David C Folta, Thomas A Pavlak, Amanda F Haapala, and Kathleen C Howell. Preliminary design considerations for access and operations in earth-moon l1/l2 orbits. 2013.
- [31] Raymond Merrill, Patrick Chai, and Min Qu. An integrated hybrid transportation architecture for human mars expeditions. In *2015 AIAA Space Conference, Pasadena, CA*, 2015.
- [32] Ryan Whitley and Roland Martinez. Options for staging orbits in cislunar space. In *Aerospace Conference, 2016 IEEE*, pages 1–9. IEEE, 2016.
- [33] WS Koon, MW Lo, JE Marsden, and SD Ross. The three-body problem, and space mission design. *Dyn. Syst*, 2006.
- [34] Archie E Roy. *Orbital motion*. CRC Press, 2004.
- [35] Tony F Chan. Newton-like pseudo-arclength methods for computing simple turning points. *SIAM journal on scientific and statistical computing*, 5(1):135–148, 1984.
- [36] Natasha Bosanac. *Leveraging natural dynamical structures to explore multi-body systems*. PhD thesis, Purdue University, 2016.
- [37] Natasha Bosanac. *Exploring the influence of a three-body interaction added to the gravitational potential function in the circular restricted three-body problem: a numerical frequency analysis*. PhD thesis, Purdue University, 2012.
- [38] V Domingo, B Fleck, and Arthur I Poland. The soho mission: an overview. *Solar Physics*, 162(1):1–37, 1995.
- [39] Carl D Murray and Stanley F Dermott. *Solar system dynamics*. Cambridge university press, 1999.
- [40] M Vaquero. *Poincaré Sections and Resonant Orbits in the Restricted Three-Body Problem*. PhD thesis, MS Thesis, School of Aeronautics and Astronautics, Purdue University, West Lafayette, Indiana, 2010.
- [41] J Johannesen and L D’Amario. Europa orbiter mission trajectory design. 1999.
- [42] TS Parkerand and LO Chua. Numerical algorithms for chaotic systems, 1989.
- [43] Lawrence Perko. *Differential equations and dynamical systems*, volume 7. Springer Science & Business Media, 2013.
- [44] John Guckenheimer and Philip J Holmes. *Nonlinear oscillations, dynamical systems, and bifurcations of vector fields*, volume 42. Springer Science & Business Media, 2013.
- [45] Emily M Zimovan, Kathleen C Howell, and Diane C Davis. Near rectilinear halo orbits and their application in cis-lunar space. In *3rd IAA Conference on Dynamics and Control of Space Systems, Moscow, Russia*, 2017.
- [46] Davide Guzzetti, Natasha Bosanac, Amanda Haapala, Kathleen C Howell, and David C Folta. Rapid trajectory design in the earth–moon ephemeris system via an interactive catalog of periodic and quasi-periodic orbits. *Acta Astronautica*, 126:439–455, 2016.

- [47] Jacob Williams, David E Lee, Ryan J Whitley, Kevin A Bokelmann, Diane C Davis, and Christopher F Berry. Targeting cislunar near rectilinear halo orbits for human space exploration. 2017.
- [48] Amanda F Haapala. *Trajectory design in the spatial circular restricted three-body problem exploiting higher-dimensional Poincaré maps*. PhD thesis, Purdue University, 2014.